IFSA

Sergey Y. Yurish
Editor

Advances in OPTICS

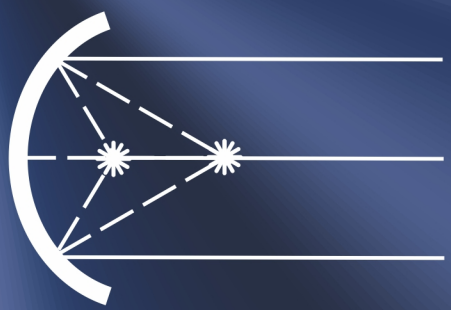

7

Advances in Optics

Book Series, Volume 7

Sergey Y. Yurish
Editor

Advances in Optics

Book Series, Volume 7

International Frequency Sensor Association Publishing

Sergey Y. Yurish
Editor

Advances in Optics
Book Series, Vol. 7

Published by International Frequency Sensor Association (IFSA) Publishing, S. L., 2024/25
E-mail (for print book orders and customer service enquires): ifsa.books@sensorsportal.com

Visit our Home Page at https://sensorsportal.com/ifsa_publishing.html

ISBN: 978-84-09-57871-9
DOI: 10.13140/RG.2.2.34181.87527
BN-20250619-XX
BIC: TTB

Acknowledgments

As Editor I would like to express my undying gratitude to all authors, editorial staff, reviewers and others who actively participated in this book. We want also to express our gratitude to all their families, friends and colleagues for their help and understanding.

Contents

Contributors

Abdenbi Bouzid

Moulay Ismail University, Laboratory of Optics, Information Processing, Mechanics, Energy and Electronics (OPTIMÉÉ), Meknes, Morocco

Anass Cherkaoui

Hassan I University, Faculty of Science and Technology, Higher Institute of Health Sciences, Settat, Morocco

Abdennacer El-Ouarzadi

Moulay Ismail University, Laboratory of Optics, Information Processing, Mechanics, Energy and Electronics (OPTIMÉÉ), Meknes, Morocco

Abdelaziz Essadike

Hassan I University, Faculty of Science and Technology, Higher Institute of Health Sciences, Settat, Morocco

Matthias Haupt

Jade University of Applied Sciences, Friedrich-Paffrath-Straße 101, 26389 Wilhelmshaven, Germany

Ricardo Oliveira

Instituto de Telecomunicações, University of Aveiro, 3810-193 Aveiro, Portugal

Antonio Parretta

Physics and Earth Sciences Department, Ferrara University, Via G. Saragat 1, 44122 Ferrara (FE), Italy
Academy of Sciences of Ferrara, Via del Gregorio 13, 44121 Ferrara (FE), Italy
E-mail: parretta@fe.infn.it, aparretta@alice.it

João Preizal

Instituto de Telecomunicações, University of Aveiro, 3810-193 Aveiro, Portugal

Sebastian Smarzyk

Jade University of Applied Sciences, Friedrich-Paffrath-Straße 101, 26389 Wilhelmshaven, Germany

Katharina Strathmann

Jade University of Applied Sciences, Friedrich-Paffrath-Straße 101, 26389 Wilhelmshaven, Germany

Preface

Optical science today stands at the intersection of numerous disciplines—bridging classical physics with cutting-edge applications in communications, biomedical imaging, environmental monitoring, and precision engineering. The '*Advances in Optics'* Book Series seeks to document these advances, providing a scholarly platform for disseminating innovative developments in optical materials, devices, and systems.

This seventh volume of the Series, *'Advances in Optics'*, Vol. 7, gathers five rigorously reviewed contributions from international research groups across Europe and North Africa. The diversity of topics reflects the breadth of contemporary optics research, spanning both fundamental studies and applied engineering solutions. This volume is intended to support university faculty, PhD students, and early-career researchers in optical engineering, photonics, materials science, applied physics, and biomedical optics.

Chapter 1 introduces new twist on microstructured polymer optical fibers. The authors present a detailed study of helically twisted microstructured polymer optical fibers (mPOFs) as novel optical components and sensors. The work describes the fabrication process, mechanical tuning of fiber properties, and the unique spectral characteristics resulting from twisting effects—offering new opportunities for wearable sensing, structural health monitoring, and flexible photonic devices.

Chapter 2 describes a comprehensive review on brain tumor detection and segmentation using optical scanning holography combined with active contour methods. The authors critically analyze various iterations of optical scanning holography systems and assess their potential for accurate, high-resolution 3D visualization of brain tumors. This chapter serves as a valuable reference for researchers in biomedical optics, medical imaging, and optical diagnostics.

Chapter 3 presents a combined theoretical and practical investigation on the design, simulation, and initial moldings of a concave polymer-based diffractive optical element for miniaturized spectroscopy. The chapter explores advanced fabrication techniques for curved diffractive gratings in polymer substrates, providing insights that will be of particular interest to those engaged in integrated optics, spectroscopic sensor design, and polymer photonics.

Chapter 4 details a holotomography approach for the detection and segmentation of amoebas in water samples. Combining holotomography imaging with active contour algorithms, the authors demonstrate a method for high-contrast visualization and quantitative analysis of microscopic biological samples—addressing pressing needs in water quality monitoring and microbiological diagnostics.

Chapter 5 explores optometry at dark with photoluminescent mires, a unique contribution focused on human visual performance under low-light conditions. The author propose new methodologies for assessing visual acuity and resolution in darkness, using photoluminescent targets. This chapter bridges physiological optics with experimental psychophysics, offering a foundation for future studies in vision science and clinical optometry.

Collectively, the works presented in this volume demonstrate both the diversity and depth of current research in optics. They offer valuable frameworks and experimental findings that will inform future studies and inspire new directions in academic and applied research.

As editor, I express my gratitude to the contributing authors for their high-quality submissions, and to the reviewers whose expertise ensured the rigor of the volume. I also extend thanks to the IFSA Publishing editorial team for their continued support of this series and their commitment to open-access academic publishing.

It is my sincere hope that '*Advances in Optics'*, Vol. 7 will prove a useful and stimulating resource for the academic community, and that it will encourage ongoing exploration and innovation in optical science and technology.

Dr. Sergey Y. Yurish

Editor
IFSA Publishing *Barcelona, Spain*

Chapter 1
A New Twist on Microstructured Polymer Optical Fibers

João Preizal and Ricardo Oliveira

1.1. Optical Fibers – An Introduction

Optical fibers have been the solution and the innovation key in diverse fields due to their advantages over conventional electronic devices. From telecom networks to optical fiber sensors, this technology has been proving its value thanks to its efficiency, low losses, and reliability in data transference and the measurement of physical parameters. The potential of optical fibers led also to its development, and nowadays, it is possible to find optical fibers with different structural designs and materials, allowing them to explore new properties and applications.

In this chapter, it will describe the use of helically twisted polymer optical fibers (POFs) with air-hole designs, also known as microstructured polymer optical fibers (mPOF), as a new tool to control the light properties and also work as flexible sensors. The helical structure created through the twisting of the mPOF over its central axis, allowed to generate a series of dips in the transmission spectrum. These were associated with the coupling of the core mode to the co-propagating cladding modes. The characterization of the structure to twist rate, revealed a linear dependency with the possibility to discriminate the twist direction. Also, the characterization of longitudinal strain showed the capability to easily tune the resonant wavelength. The interesting characteristics of this device, as is the case of its flexibility, elasticity, and low processing temperatures, pave the way for its use in flexible components with fields of application such as wearable sensors, structural health monitoring, spectral filters in telecom applications, etc.

1.1.1. History of Optical Fibers

The discovery of optical fibers dates back to the 19th century when scientists began studying the light-guiding properties in various materials. In 1870, John Tyndall revealed

João Preizal
Instituto de Telecomunicações, University of Aveiro, 3810-193 Aveiro, Portugal

that light traveling through a jet of water at a certain angle was able to be reflected several times at the water-air interface without being lost, as a consequence of the higher refractive index of water compared to that of air. At that time, it was suggested other transparent materials could also be used for the same effect [1]. Already in the early 20th century, there were several positive contributions to the creation of optical fibers, and in 1920, Arthur Korn developed a system for transmitting images using these optical waveguides. Ten years later, Heinrich Lamm invented the first optical fiber amplifier using zinc-selenide crystal. However, the generalized use of optical fibers only started in the 1960s when Elias Snitzer published the theoretical description of light propagation in glass fibers with low losses [2], opening the door to its widespread use in telecommunications. At the same time, Charles Kao was also working in this field, namely, to minimize transmission losses. Due to the quality and significance of his research in the tin telecommunications field, Kao received several awards, namely the Nobel Prize in Physics in 2009 [3]. Years later, Corning Glass Works first produced a high-quality glass optical fiber (GOF), made of pure silica and presenting losses reaching 20 dB/km at 633 nm [4]. Nowadays, information can be transmitted through a GO over tens of kilometers due to its low attenuation (0.2 dB/km at 1550 nm [5]). Because of that, they now form the backbone of our telecommunications infrastructure, which has a tremendous impact on our societies and on the way, we live and communicate [1].

Concerning POFs, they were first invented in the 1960s by DuPont, and later, Mitsubishi Rayon developed the POF manufacturing process. Despite its early-stage development, POFs produced at that time had high attenuation, making their use limited. However, after a few years of research, Mitsubishi Rayon was able to reduce the attenuation of POFs from 1000 dB/km to a value close to the theoretical loss limit of 100 dB/km at 650 nm [6]. Nowadays POFs have become a mature technology and it is not surprising to find POFs manufactured in multimode (MM) but also with single-mode (SM) behavior, with versions in the form of step-index (SI), graduate-index (GI), or even in microstructured designs [6]. Unfortunately, over the years, POFs have been overwhelmed by the popularity of GOFs. This occurred due to the higher attenuation of POFs compared to GOFs. Yet, the opportunities of POFs continue to soar and they still find applications in low to medium-distance communications and more importantly, in sensor applications, where polymers provide much more attractive features than silica.

1.1.2. Microstructured Optical Fibers

Microstructured optical fibers were first reported in silica fibers, and they have been termed photonic crystal fibers (PCFs) since they have the properties of photonic crystals. In these optical fibers, light is confined in the core region through air holes that are periodically arranged in the cladding region. The use of these fibers has shown several opportunities, such as the capability to propagate light with endlessly single-mode (ESM) behavior [7], the dispersion control [8, 9], the possibility to use them in high-power transmission systems [10], the capability to generate supercontinuum (SC) [11], or orbital angular momentum (OAM) modes [12], and the use in a wide range of sensor applications [13-16].

Microstructured fibers can be grouped in two main groups, namely index-guiding, and hollow-core. In Fig. 1.1, it is shown the air-hole structure of these microstructured fibers.

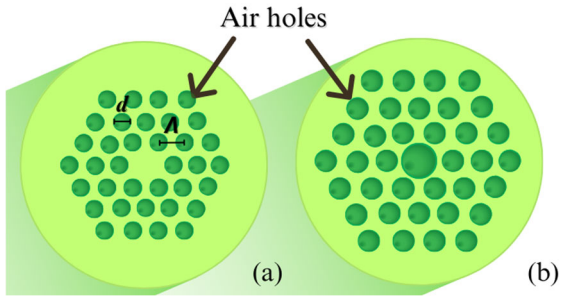

Fig. 1.1. Microstructured fibers with: (a) index-guiding; (b) hollow-core. d and Λ identify the diameter and the hole-to-hole distance, respectively.

For the index guiding microstructured fibers, the air holes are usually periodically distributed in a hexagonal arrangement. However, the central air hole is missing, leaving the fiber with a solid central core. The air hole structure is used to reduce the effective refractive index of the cladding while keeping the central solid core region with a higher refractive index. Because of this refractive index contrast, light can propagate in the core, similar to what happens with conventional SI fibers. Examples of the capabilities of these fibers are the possibility to propagate light with ESM behavior [7], zero-dispersion wavelength at the telecom region [8], generation of SC [11], and excitation of OAM modes [12, 17]. Regarding hollow core microstructured fibers, the cladding region is also filled with air holes periodically arranged along the radial distance, however, the central core is composed of a hollow region. In these fibers, the guidance mechanisms are ruled through the photonic bandgap effect, allowing light to be confined in the hollow-air central region, where the refractive index is approximately equal to 1. The biggest advantage of these fibers is the possibility to propagate light with ultra-low loss, avoiding problems associated with nonlinearities and allowing the propagation of high-power laser sources [10]. Additionally, they have lower latency as the light travels faster than in any other medium, and they provide low chromatic dispersion, and higher bandwidth, among others.

1.1.3. Endlessly Single-mode Property

One of the most attractive capabilities of microstructured fibers relates to their ability to be ESM, i.e., exhibit single-mode behavior at any wavelength. In standard SI optical fibers, the normalized frequency, commonly described as the V-parameter is generally used to identify the mode behavior of an optical fiber. For index-guiding microstructured fibers, it is possible to do an analogy. Assuming n_{SM} as the refractive index of the fundamental space-filling mode (FSM), it is possible to numerically describe the normalized frequency as [18]:

$$V_{PCF} = 2\pi \frac{\Lambda}{\lambda} \sqrt{n_{\text{Core}}^2 - n_{\text{SM}}^2}, \quad (1.1)$$

where d and Λ are the diameter and the hole-to-hole distance, respectively from a semi-analytical model performed in [18], it was identified that the V parameter does not depend on the wavelength for a certain fraction of the d and *Λ*. According to the numerical modeling performed in [18] and [19], it was shown that if the fiber has an air-filling fraction of d/Λ < 0.43, then, only one pair of degenerated modes can propagate in the solid core region, for all wavelengths. With this, the fiber is said to be ESM.

Microstructured fibers have been fabricated with silica glass, however, the advantages of polymers as is the case of their higher flexibility, non-brittle nature, easier functionalization, biocompatibility, higher thermal expansion coefficients (9×10^{-5} °C^{-1} vs. 5.5×10^{-7} °C^{-1}), lower thermo-optic coefficient (-1.1×10^{-4} K^{-1} vs. 9.2×10^{-6} K^{-1}), lower Young's modulus (i.e., 1.8 – 3.2 GPa vs. 72 GPa), higher failure strain (> 10 % vs. ≈1 %), and low processing temperatures (i.e., ≈ 100 °C vs. ≈ 1200 °C), brought the motivation for the development of POFs with microstructured designs [20]. Also, the capability to produce these fibers with technologies such as drilling [21], preform casting [22], and 3D printing [23], is much more attractive than the traditional stack and draw techniques used to produce PCFs. Because of this, POFs with microstructured designs have already been reported and are nowadays the subject of intense research in different scientific fields. Interesting to note is the easiness in achieving SM behavior at the visible spectral region where most of the POFs present lower losses. This reveals to be a great improvement compared to the SI-POF versions which are difficult to produce with SM behavior as this involves low refractive index contrasts and or small core diameters.

1.2. Helically Twisted Microstructured Optical Fibers

Depending on the internal composition of an optical fiber and on the changes that can be implemented after its production process, namely through post-processing techniques, it is possible to manipulate the light guiding mechanisms, such that it attends to the required needs for a specific application. Helically twisted optical fibers (HTOF) are some of these structures that can be manufactured through elegant and easy means, namely during the fiber drawing process or through fiber post-processing technologies.

1.2.1. Chiral Structures

The properties of light in chiral structures have been a hot topic in the photonics field, because of their qualities and applications. Any object, molecule, structure, etc. has some geometry associated and this geometry can be described as chiral or achiral. In chiral structures, their original image is not superposable on its mirror image even using any translations or rotations. This is in contrast with what occurs in achiral structures. In Fig. 1.2 it is shown an example of an achiral and chiral geometry.

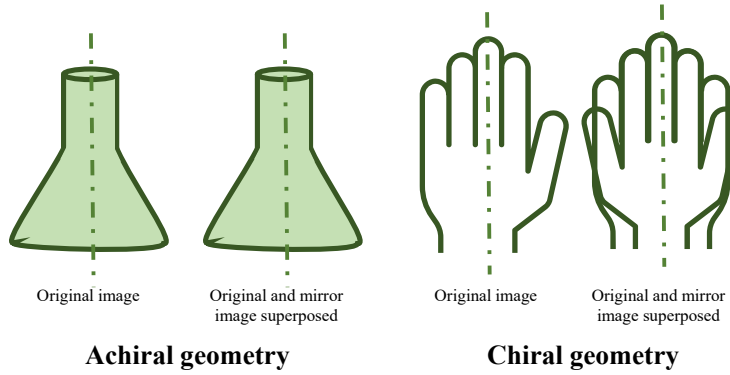

Fig. 1.2. Example of an achiral geometry (left side) and chiral geometry (right side).

Chiral structures have a specific geometry and this makes them unique. In general, they are associated with right- and left-hand geometry. This can be applied to molecules and any other structure as is the case of a twisted microstructured fiber shown in this chapter.

These structures have been applied in various fields, such as chemistry, biology, and physics. Examples to highlight regarding the use of these structures are: the use of chiral materials to manipulate light on a nanometric scale, allowing reach adaptive devices for photonic and electronic applications [24]; production of nanostructures made of graphene for polarization-enabled optoelectronic devices [25]; chiral carbon dots for biomedical applications such DNA rearrangement [26]; the use in optical tweezers, namely for the optical manipulation and trapping of optically active particles [27].

Beyond that, chiral structures have also been described in fiber optics. Victor Kopp et al. have been pioneering this technology using fibers with noncircular symmetry cross section [28] and with single- and double-helix symmetry [29], twisted in a helical path along the fiber principal axis. Therefore, due to the versatility of changing the air-hole arrangement in a PCF, it is not surprising to find their employment in the production of these structures [30, 31]. Philip Russell and his team have been leaders on this topic [32].

1.2.2. Theory behind Helically Twisted Optical Fibers

In an index-guiding microstructured fiber, such as the one shown in Fig. 1.3, the hexagonal hollow air cladding structure supports a fundamental space-filling mode where its axial Pointing vector (S_{SM}), points along the fiber principal axis. This mode has an effective axial refractive index greater than one, being the electromagnetic field at the antinodes trapped laterally by total internal reflection (TIR) at the silica- or polymer-air interface, depending if we are talking about GOFs or POFs, respectively. Considering the application of a gentle twist to the microstructured fiber (i.e., $\alpha\Lambda << 1$, being α the twist rate and Λ, the hole-to-hole distance), as is represented in Fig. 1.3(a), the field antinodes, represented in Fig. 1.3(c), will follow a helical path around the core central region [33].

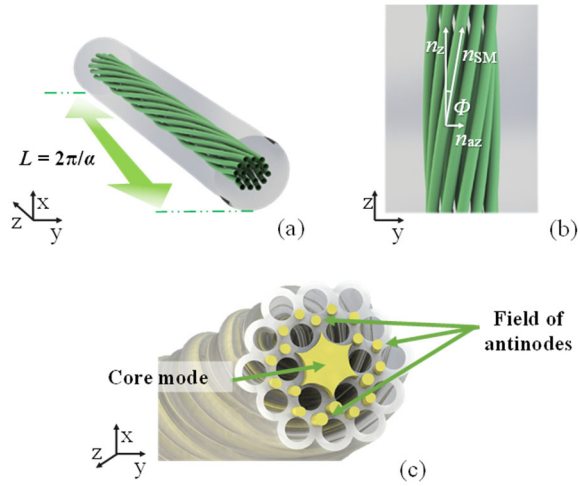

Fig. 1.3. (a) Representation of a microstructured optical fiber twisted one period in the clockwise (CW) direction. (b) Inset of the twisted hole structure. Φ describes the angle between the space-filling mode vector, $n_{SM,}$ and the z component, while n_Z and n_{az} define the refractive index along the fiber axis and in the azimuthal direction, respectively. (c) Representation of the core mode propagating at the fiber central region, and the satellite field antinodes at the cladding region.

As a consequence of the spiral path followed by the field antinodes, n_{SM} will point partially to the transverse direction of the optical fiber, being the angle between the fiber axis and the helical path shown in Fig. 1.3(b), and expressed at a given radius, ρ, by Eq. (1.2) [33]:

$$\Phi = sin^{-1}\left(\frac{\alpha\rho}{\sqrt{1+\alpha^2\rho^2}}\right) \approx \alpha\rho \tag{1.2}$$

This creates a component of momentum flow to the azimuthal direction, allowing the generation of orbital resonances at specific combinations of radius, twist rate, and wavelength.

As a consequence of the twisting process, the optical path length along the spiral path will increase. This rises the effective refractive index by a fractional amount, given in the form [31]:

$$\Delta n_x/n_0 = \sqrt{1+\alpha^2\rho^2} - 1 \approx \alpha^2\rho^2/2, \tag{1.3}$$

where n_x is the refractive index along of the hollow channels, the medium that composes the fiber and the space-filling mode, n_0 is the respective refractive index in the untwisted fiber, α is the twist rate and ρ is the cladding mode radius. For simplicity to the reader, in Fig. 1.4(a) and (b), it is represented the refractive index distribution inside the microstructured fiber before and after the twisting process, respectively. In this representation n_C represents the index of the core mode, n_a, the index of the hollow channels, n_S, the index of the medium that composes the fiber and n_{SM}, the space-filling mode refractive index.

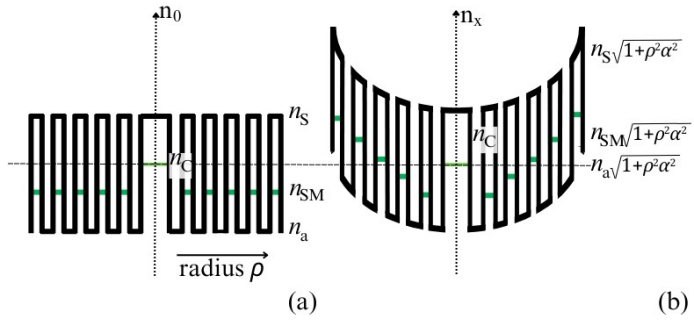

Fig. 1.4. (a) Representation of the refractive index distribution of: (a) raw microstructured optical fiber, and (b), its twisted version. Adapted from [31].

As observed from Fig. 1.4, there is an increase in the effective refractive index when the fiber is twisted. Therefore, the fundamental core mode, with a modal index n_C, can phase match with the fundamental space-filling mode, with a phase index n_{SM}, in the untwisted fiber at a radius given by:

$$\rho = \alpha^{-1}\sqrt{(n_C/n_{SM})^2 - 1} \tag{1.4}$$

As a result of this phase match, the guided core mode can couple to the modes propagating in the hollow air region. Because of this, the appearance of a set of dips in the transmission spectrum occurs. This is a consequence of the anti-crossings between the core mode and the leaky cladding modes that carry OAM, where each dip corresponds to an OAM mode with a different mode order. Thanks to the altered path of light traveling through the air holes helical path, the azimuthal component of its wavevector must take values that produce a roundtrip phase advance which is an integer multiple l of 2π, being l the OAM order. In this way, this produces the following general relation [31]:

$$\frac{l\,\lambda_l}{2\pi} = n_{az}\rho = n_{SM}\,\rho\,sin(\Phi) \approx n_{SM}\alpha\,\rho^2, \tag{1.5}$$

where λ_l is the wavelength of the dip corresponding to the l^{th} order of the OAM mode and n_{az} is the azimuthal component of the refractive index. As the axial effective refractive index evolves quadratically with the radius, light will refract outwards the fiber making the cladding resonances highly leaky, causing attenuation dips in the transmission spectrum with high losses. One important thing to notice in Equation (1.5) is that the resonant wavelengths scale linearly with the reciprocal of L, where $L = 2\pi/\alpha$. This is different from the phenomenon observed in fiber gratings, where the resonant wavelength scales with L [32]. Although Equation (1.5) does not refer to the phase-match condition between the core mode and the cladding mode, such correspondence seems essential. The increase in the effective refractive index makes the phase-matching condition more likely to happen. However, it does not imply that this correspondence happens either. According to Russell and his colleagues, the explanation derives from the high loss of the cladding resonances, which widens the coupling bandwidth and relaxes the phase-matching condition [31].

One of the biggest advantages of HTOFs is the generation of OAM modes. OAM is a light property that explains the angular momentum associated with a specific light path, containing a different spatial field distribution compared to conventional plane wave light beams. In other words, OAM is the quantity of rotation of a light beam around the central axis. Light with OAM is set with an azimuthal phase dependency, giving the light a helical path. This enables the development of brand-new optical components that can be used for instance in space division multiplexing applications in optical telecommunications [34].

1.2.3. Optical Sensing with Helically Twisted Optical Fibers

Optical fiber sensors work on the principle that changes induced on their intrinsic properties allow the modification of the light guiding properties, such as phase, amplitude, wavelength, polarization, intensity, etc., These changes can then be transduced to the parameter under study, such as temperature, pressure, strain, vibration, refractive index, humidity, among many others. These types of sensors have the potential to replace some of the conventional sensors like electronic sensors, and the reason for such relates to their advantages such as small size, immunity to electromagnetic interference, resilience, and multiplexing capabilities.

Nowadays, there is a variety of fiber optic technologies that can be used for sensor applications. The most well-known examples are fiber gratings, as is the case of fiber Bragg gratings (FBGs), long-period gratings (LPGs), and tilted fiber Bragg gratings /TFBGs). Other commonly referred technology is the fiber optic interferometers, as is the case of the Fabry-Perot interferometer (FPI) or, the multimode interferometer (MMI). In all these examples, light traveling in the optical fiber will be affected by any changes in the refractive index of the media and also, on its physical length. Despite their versatility, they still find obstacles to the measurement of special parameters, as is the case of torsion, curvature, electric current, etc. On top of this, the simplicity and cost are mandatory in every sensor technology. HTOFs are structures that handle all these properties and therefore, they can pave the way for a bright future in the fiber sensor technology.

1.2.4. Twist and Strain Effects

To understand what happens when an HTOF is subjected to an external load, it is necessary to go back to Eq, (1.5). This equation shows that the resonant wavelength has a proportional relationship with the applied twist rate, the effective refractive index of the space-filling mode, and the radius of the cladding mode resonance. To obtain a relation of the resonant wavelength shift, $\Delta\lambda_R$, with an external load, such as strain and twist, it is possible to differentiate Eq. (1.5), allowing to obtain [35]:

$$\Delta\lambda_R = \lambda_{R0}\left(\frac{\Delta n_{SM}}{n_{SM0}} + \frac{\Delta\alpha}{\alpha_0} + \frac{2\Delta\rho}{\rho_0}\right), \quad (1.6)$$

with λ_{R0}, n_{SM0}, α_0, and ρ_0, the parameters of the optical fiber without external loads. When an axial strain, ε, is applied to the HTOF, it is predicted an increase in the fiber length and therefore an increase in the twist period. On the other hand, when a positive mechanical

torsion is applied (with a twisted rate $\alpha_M > 0$), the period will decrease. Combining both effects, it is possible to describe the resulting net change as [35]:

$$\Delta\alpha = \alpha_{\mathrm{M}} - \alpha_0\varepsilon \tag{1.7}$$

Now let's consider the study of the variation of the effective refractive index of the space-filling mode, n_{SM} when the HTOF is subjected to an external load. Knowing that the Poisson ratio, υ, indicates the degree of deformation in the transverse direction when a longitudinal strain is imposed in the material, and knowing that this generates three orthogonal components of strain that change the polarizability of the material, and thus, its effective refractive index, it is possible to write [35]:

$$\Delta\left(\frac{1}{n_{\mathrm{T}}^2}\right) = [-\nu(p_{11} + p_{12}) + p_{12}]\varepsilon, \tag{1.8}$$

where n_{T} is the refractive index seen by the transversely polarized light, and p_{11} and p_{12} are the photoelastic coefficients of the material. Finally, ρ can be estimated from the Poisson's ratio, which results in [35]:

$$\Delta\rho = -\rho_0\nu\varepsilon \tag{1.9}$$

Noting still that for slow twist rates, the hollow air holes represent a small fraction of the total cladding region, it is possible to approximate n_{T} to n_{SM} and in this way, from Eq. (1.8), it is possible to obtain the dependence of n_{SM} with the axial strain, such as [35]:

$$\Delta n_{\mathrm{SM}} = \left(\frac{n_{\mathrm{SM0}}^3}{2}\right)[\nu(p_{11} + p_{12}) - p_{12}]\,\varepsilon \tag{1.10}$$

Substituting Equations (1.7), (1.9), and (1.10), into Equation (1.6), yields:

$$\frac{\Delta\lambda_{\mathrm{R}}}{\lambda_{\mathrm{R0}}} = \left(\frac{\alpha_{\mathrm{M}}}{\alpha_0} - \varepsilon\right) - 2\nu\varepsilon + \left(\frac{n_{\mathrm{SM0}}^2}{2}\right)[\nu(p_{11} + p_{12}) - p_{12}]\varepsilon, \tag{1.11}$$

Considering the case where the HTOF is subjected to twist while keeping the strain constant, the variation in the resonant wavelength will show a proportional relationship between the twist rate and the wavelength shift.

1.3. Fabrication and Characterization of Helically Twisted mPOFs

Silica fibers are well established in the telecom industry and all the optical fiber laboratory equipment has been developed on top of this type of optical fiber. Because of that, the implementation of POFs requires the use of GOFs and for that, the splicing between these fibers is needed. Due to the glass transition temperature between GOFs and POFs, conventional hot splicing processes cannot be used, and thus, "cold" splicing methods, based on the use of photopolymerizable resins at the GOF-POF junction as a common laboratory practice, an example of it is shown in Fig. 1.5.

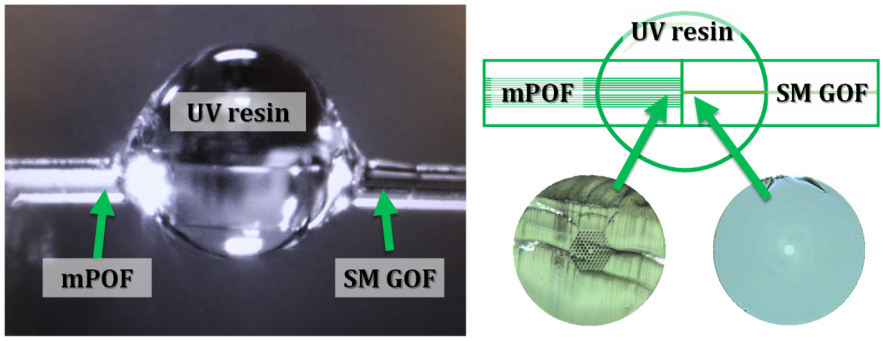

Fig. 1.5. Image of the cold fusion between the fiber terminals (left side) and a scheme of it, with a microscope image of the mPOF and a standard single mode fiber (SMF) (right side).

After creating a permanent splice between the GOF and the mPOF, an experimental setup needs to be implemented to post-process the POF with a helical shape. A literature review regarding the production of HTOFs indicates the requirement of three key components. The first, is the heating element, designed to soften the fiber material, enabling its post-processing. The second component involves the linear movement of the fiber related to the heat source. This requires linear positioners responsible for moving the fiber along the heating element, ensuring uniform heating along the fiber length. Finally, the third necessary component is the rotational positioner. This is used to twist the fiber during the fabrication process, allowing the hollow air holes to reach a permanent helical profile along the central axis of the fiber.

1.3.1. Heating Region

One of the biggest advantages of POFs compared to their glass counterparts relates to their lower glass transition temperature. This allows their post-processing using low-cost, easier to handle, and safer to use, heat sources. Several possibilities could be explored to attain this, such as the use of resistive wires, heating coils, hot air, etc. However, due to the simplicity of thermoelectric coolers (TECs), they are the preferred choice as already reported in [36]. To reach temperatures above 100 °C, dual-stage TECs are an option as is the case of the TEC2D model from Thorlabs Inc. These temperatures are needed to soften the polymer material that composes the POF, which considering the most well-known polymer fiber material (i.e., polymethyl methacrylate (PMMA)) is ≈ 110 °C. The TEC needs to be mounted with its cold face on top of a heat dissipative element and its hot region facing the fiber region. To evenly distribute the temperature around the mPOF, a heat conductive metal containing a hollow region for the mPOF passage, can be placed on top of the TEC. For the correct TEC temperature control, a thermistor needs to be placed in the vicinity of the hollow region where the fiber will pass. This will serve as the input for the correct loop temperature control performed at the temperature controller. In Fig. 1.6 it is shown a picture of a setup used to heat the mPOF to its softening point.

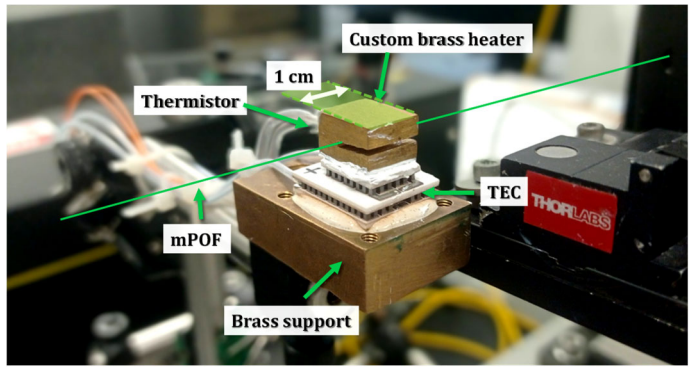

Fig. 1.6. Detailed picture of the heating region used to heat the mPOF to its softening point using a TEC element and a custom brass support [36].

1.3.2. Linear and Rotational Movements

To twist the mPOF a dedicated setup needs to be implemented, namely, to move the POF along the heating region during the twisting process. To move the heating region to the vicinity of the mPOF, a linear positioner is used. The elements composing the heating regions are mounted on top of the positioner and aligned related to the fiber, such that the hollow region of the heat conductive metal covers ~1 cm section of the mPOF, as is shown in Fig. 1.6, through the green line drawn to exemplify the location of the mPOF. This positioner is allowed to move forward to the vicinity of the POF at the beginning of the fabrication process, and after the fiber post-processing, it is moved backward.

To heat the mPOF along its length, the heat source is kept fixed, while the fiber is passed through the heat region with the help of two linear positioners that hold the fiber terminals. On top of one of the positioners (defined here as positioner 1) it is located a rotational positioner used to rotate the fiber during the production process. The mPOF was secured using two fiber clamps, one solidary with the linear positioner 2, and another solidary to the rotational positioner sitting on top of positioner 1. Fig. 1.7 illustrates the schematic of the experimental setup used to produce the HTOFs.

The coordination movement of the positioners is centralized in a universal motion controller, which requires a trajectory file with all the necessary positions and velocities. This allows the controller to synchronously move all the positioners involved in the setup. The necessary positions and velocities are based on the twist period, L, the number of twists (number of periods), N, and the heating time per twist period, T_Λ. Thus, the rotational speed needed for the rotational positioner is set to $V_\theta = 2\pi/T_\Lambda$, and the linear speed of the right positioners in Fig. 1.7 is set to $V_1 = L/T_\Lambda$. It is worth mentioning that the velocity of linear positioner 2, V_2 needs to be higher than V_1 (e.g., $\approx$ 1 %). This allows the fiber to be under tension during the twisting process, eliminating possible curvatures arising from gravity forces. Considering the above velocities, the twist rate can be easily calculated as $\alpha = V_\theta/V_1$. In this case, and in order to achieve a twist rate of α = 9.7 rad/mm as reported in prior studies based on twisted PCFs [31, 33], the theoretical

twist period is equal to, $L = 2\pi/\alpha \approx 650$ μm. Considering $T_\Lambda = 0.8$ seconds, this results in $V_\theta = 7.9$ rad/s, $V_1 = 0.81$ mm/s and $V_2 = 0.82$ mm/s. It is worth mentioning that sharp resonance dips require a high number of helical periods. However, the coupling strength can also be compromised, meaning that a compromise between both needs to be found.

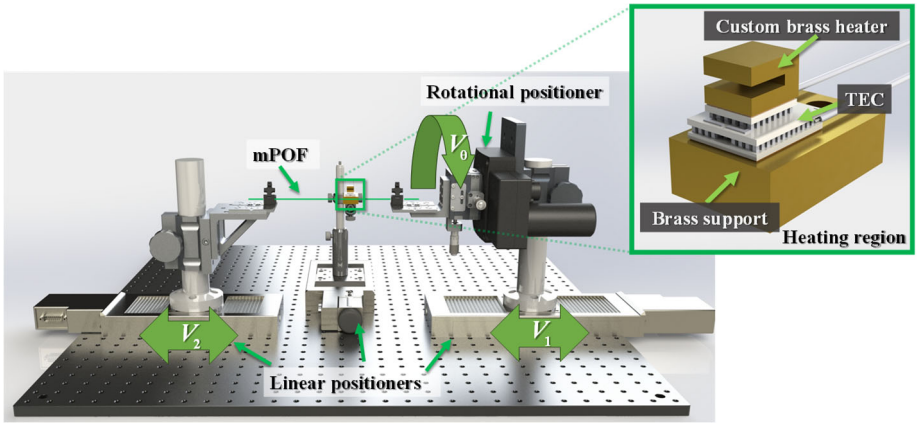

Fig. 1.7. Illustration of the experimental setup used to helically twist mPOFs. The inset shows the heating region composed of the TEC and the heat conductive metal used to soften the fiber. (Adapted from [36]).

At the beginning of the twisting process, the heat source is moved to the vicinity of the POF as is exemplified in Fig. 1.8(a), this allows preheating of the mPOF ensuring that the mPOF is soft enough to be molded. This preheat process is achieved by moving the heat source a couple of times at low velocities i.e., 5 to 6 mm/s, backward and forward along the last 4 mm POF length. This fabrication step can be seen in Fig. 1.8(b). Then, the positions and velocities inside the trajectory file are executed, allowing the synchronous movement of the linear positioners (1 and 2) and rotational positioner. This step is shown in Fig. 1.8(c). At the end of the process, the heat source solidary to the linear positioner is moved backward to a region away from the fiber as is shown in Fig. 1.8(d).

1.3.3. Torsion Characterization

To perform the torsion characterization, two 3-axis translation stages, and a high-precision fiber rotator, can be implemented. These are used to secure the fiber and to induce torsion steps to the HTOF, respectively. During the characterization, the fiber needs to be kept straight. This is done through the application of a small tension to the fiber, before the characterization tests. The distance between the two fiber clamps needs to be the same during the experiment while the torsion is applied through the high-precision fiber rotator. A supercontinuum light source (SCS), and an optical spectrum analyzer (OSA), are used to characterize the transmission spectra of the HTOF. To connect the POF to the OSA a 127 μm bore ferrule connector can be employed. In Fig. 1.9 it is shown a schematic representation of the setup used in this characterization. The inset shows the mechanical setup used to apply the twist.

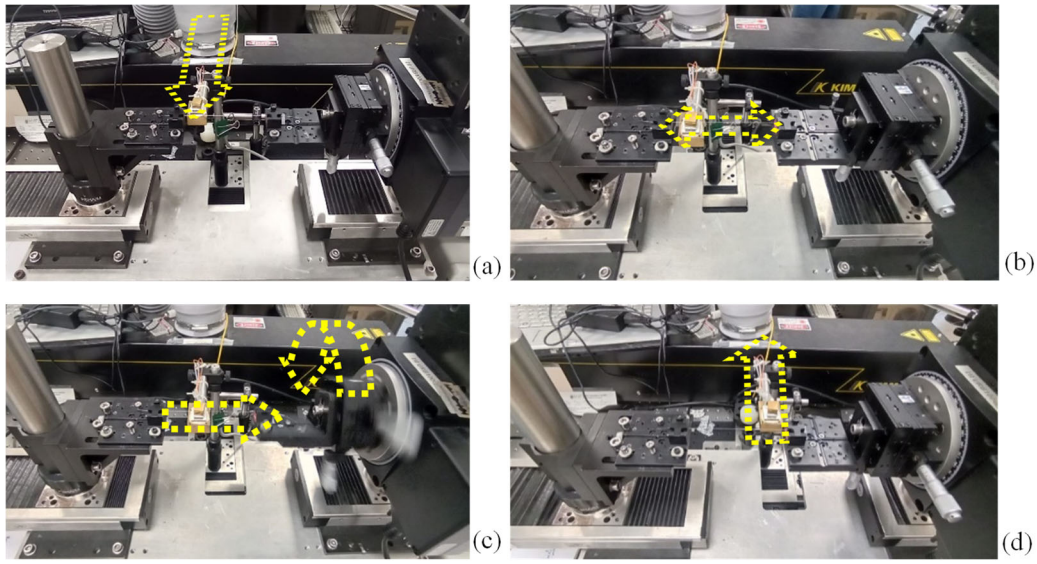

Fig. 1.8. Images taken during the manufacturing process of an HTOF: (a) positioning of the heat source (b) preheating, (c) HTOF production, (d) movement of the heat source to a region away from the HTOF.

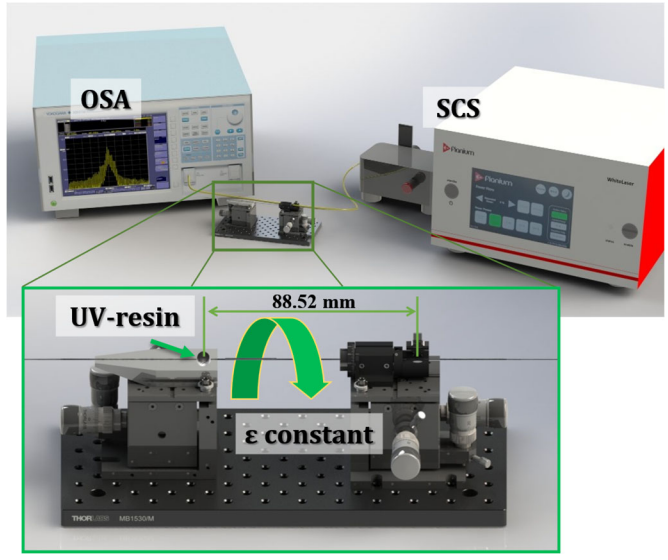

Fig. 1.9. Schematic representation of the experimental setup used for the strain and torsion characterizations of the HTOF.

The twist characterization is done in predefined rotations steps. The characterization is done in the clockwise (CW) and counterclockwise (CCW) directions.

1.3.4. Strain Characterization

The setup used for the strain characterization can also be used for the torsion characterization, namely the one shown in Fig. 1.9. However, in this characterization, the fiber rotator needs to be static while one of the translation stages is used to apply strain to the HTOF. This is achieved by displacing one of the fiber terminals in predefined steps of strain. The maximum strain imposed on the fiber needs to be taken into account when performing this type of characterization, ensuring that the fiber is working within the linear regime.

1.4. Helically Twisted Microstructured Polymer Optical Fibers

To excite the helical modes, the mPOF needs to operate with single-mode behavior. Fig. 1.10 shows a typical example of a PMMA mPOF composed of a set of 6 layers of air holes hexagonally arranged in the cladding and surrounding the central solid core region. This fiber has an attenuation of 3.8 dB/m at 650 nm wavelength region.

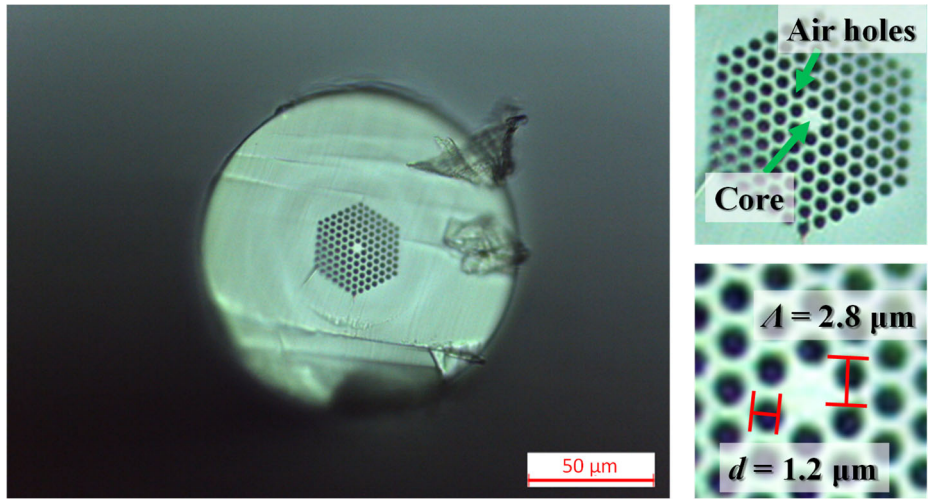

Fig. 1.10. Microscope image of a Kyriama Pty mPOF (left side). The inset of the air hole structure is shown in the top right, and the magnified image of the core central region is shown on the bottom right image, the dimensions are also included for reference.

The mPOF presented in Fig. 1.10 has an air hole diameter and a hole-to-hole distance of 1.2 and 2.8 µm, respectively. This gives an air-filling fraction of $d/\Lambda \approx 0.43$, being within the reference value needed to support endlessly single-mode behavior, (i.e., 0.43) [18, 19]. For clarity purposes, a simulation based on the finite element method in Fig. 1.11 shows the electric field distribution of this fiber for a simulation made using finite element methods and considering the working wavelength of 650 nm and the host material as PMMA with a refractive index of 1.4902.

As observed from Fig. 1.11, the fundamental mode is confined within the solid core central region. The simulation estimates an effective refractive index of n_{eff} (@ 650 nm) = 1.487.

To analyze the structural changes in the mPOF after the spirally twisting process, microscope images were captured before and after the twisting process. The pictures are shown in Fig. 1.12(a) and (b), respectively.

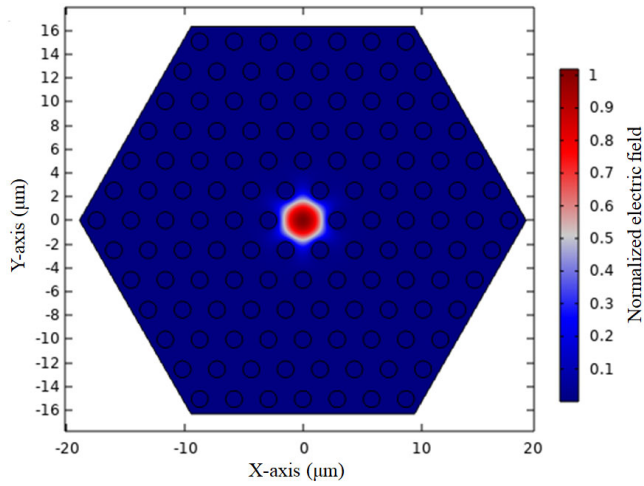

Fig. 1.11. Electric field distribution of the fundamental core mode found at the mPOF central region, propagating with an effective refractive index of 1.487 for 650 nm.

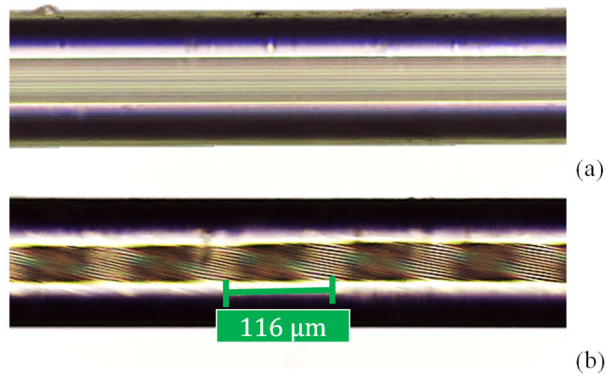

Fig. 1.12. Longitudinal microscope images of a: (a) raw mPOF and (b), after being post-processed with α = 9.7 rad/mm.

As can be seen in Fig. 1.12 (a), a longitudinal pattern of lines running along the fiber length is found in the innermost part of the raw mPOF. These correspond to the hollow air-hole channels that compose the air-hole cladding region of the fiber. After post-processing the fiber with twist and heat, it is possible to obtain a periodic pattern of bright

lines (tilted related to the fiber axis), see Fig. 1.12 (b). Considering the six-fold symmetry of the air hole structure that composes the cladding region of the mPOF, the observed period corresponds to 1/6 of the full twist of the air hole structure around the central axis of the mPOF. Fig. 1.13 was created to easily interpret the results, showing that for one full rotation, a periodic pattern of more translucent zones appears at each π/3, similar to what happens with Fig. 1.13 (b).

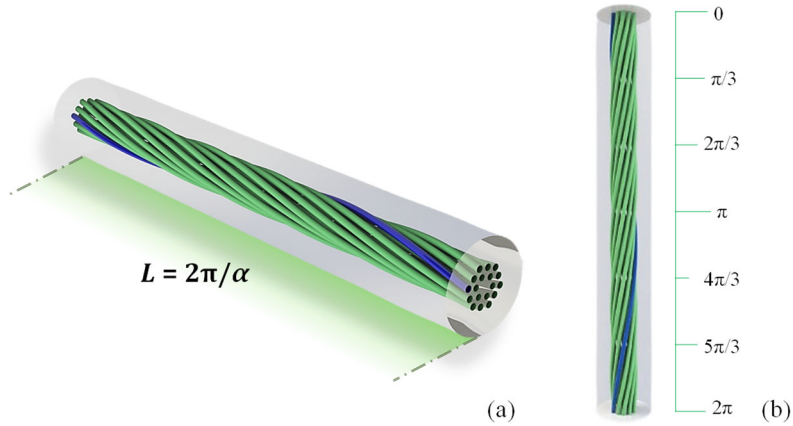

Fig. 1.13. (a) Simplified representation of an mPOF with one full turn and (b), pattern created at each π/3 rotation. The blue color was added to one of the air holes to simplify the image interpretation.

Considering the periodic pattern of ~116 μm shown in Fig. 1.12 (b), and the six-fold symmetry of the hexagonal air hole lattice, the experimental twist period corresponds to ~696 μm or in other words, to a twist rate of $\alpha \sim 9$ rad/mm. The result was confirmed through the measurement of several samples processed under the same conditions, showing similar experimental twist periods. The slight difference between the twist periods observed experimentally and the ones defined on the trajectory files, namely $\alpha = 9.7$ rad/mm, was attributed to the mPOF soft nature. This occurs because of the flexible nature of the mPOF, allowing it to twist in the unheated regions during the fabrication procedure. Therefore, the twist accumulated on the unheated regions will be released after releasing the mPOF from the fiber clamps. This originates a post-processed fiber with a twist rate smaller than the one predicted, or in other words, with a higher twist period, which is exactly what was observed.

In Fig. 1.14, it is shown the transmission spectrum of the HTOF shown on the microscope image shown in Fig. 1.12 (b).

The graph displayed in Fig. 1.14 shows a series of sharp spectral dips, identified by the ordered numbers (i.e., 1 – 5). These spectral resonances present a linewidth of ≈ 2 nm and are located between 420 nm and 500 nm wavelength region, matching the low loss region of the host material that composes the mPOF, namely PMMA. According to the literature [37], each dip resonance corresponds to the wavelength where the fundamental core mode

phase matches the fundamental space-filling cladding mode propagating along the spirally twisted cladding region of the HTOF. To observe the excited cladding modes, the near-filed modes need to be observed at the far-end terminal of the fiber, close to the helical structure. This requires a laser source at the visible region cable to be tuned to the resonant wavelength of the dip.

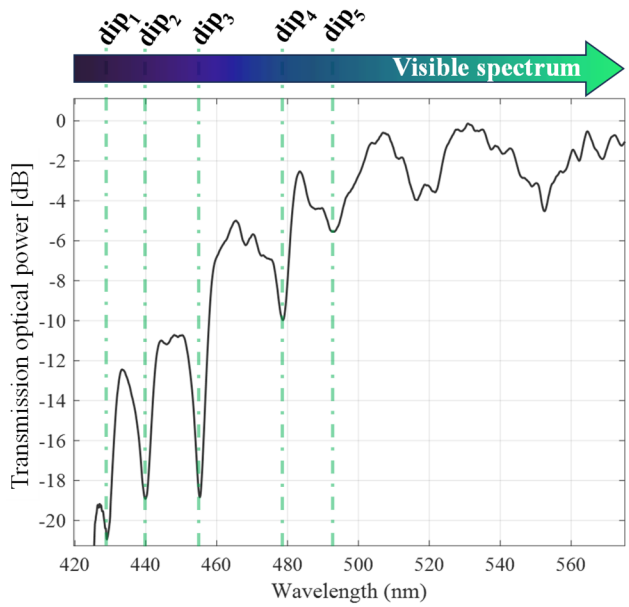

Fig. 1.14. Spectrum of an HTOF with L = 696 µm (α = 9 rad/mm), showing a series of spectral dip resonances, as indicated by the ordered dashed green lines.

At first look, the spectral result presented in Fig. 1.14 agrees well with those obtained for silica PCFs [33, 35], namely due to its similar spectral signature and also due to the spectral location of the resonant wavelengths, specifically for α ranging between 9 rad/mm and 18 rad/mm. Furthermore, since the axial effective refractive index increases quadratically with the fiber radius, ρ, as expressed by Equation (1.5), light propagating in the core region is allowed to phase match the cladding modes propagating in the spiral cladding region. These resonant modes are highly leaky, leading to obtain strong attenuation dips in the transmission spectrum [31]. Moreover, it is possible to see that the dip strength is highest for shorter wavelengths, which corresponds to the higher effective refractive index. This was in agreement with what is observed in [31]. However, it is also seen that the out-of-band losses are quite high in this region, and an explanation for such could be due to the bandwidth of the cladding resonances which can overlap due to the tight wavelength separation between the wavelength resonances. This could result in losses outside the resonant wavelength.

During the HTOF characterizations, it was also observed a high amount of light leakage along the spiral structure. An example of this phenomenon is shown on the left side of Fig. 1.15. Another interesting detail is the light filtering action that the twisted structure

is performing to the input light. This can be easily observed by the top and bottom right pictures shown in Fig. 1.15, obtained for the raw and post-processed mPOF, respectively. These show that the output light at the mPOF was greenish before the twisting process and turned reddish after the post-processing. This is in agreement with the results presented on the spectral characterizations since the spectrum is strongly attenuated for wavelengths below 500 nm as a consequence of the strong core to cladding mode couplings found at those wavelengths.

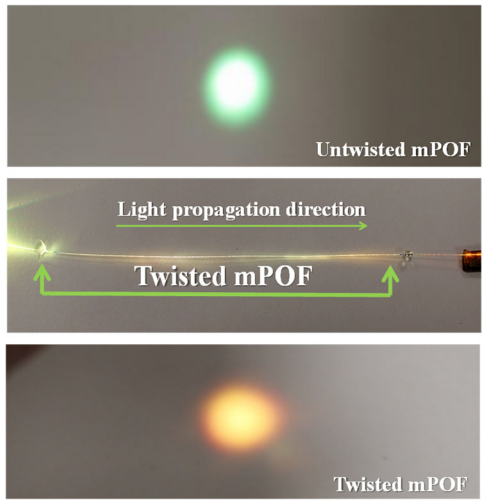

Fig. 1.15. Light from an SC source is injected into an HTOF and leaks out as it travels along the fiber length (middle image). The top and bottom pictures show the far-field images observed at the terminal of an untwisted and twisted mPOF, respectively.

1.4.1. Production Repeatability

The repeatability of a test is always a good indicator of quality performance. Because of that, the transmission spectra of two more samples were taken and compared with the one observed in Fig. 1.14. The results concerning the transmission spectra of the three HTOF samples prepared with $\alpha = 9.7$ rad/mm are shown in Fig. 1.16.

The resonance pattern shown in each HTOF spectrum presented in Fig. 1.16, is similar across all post-processed samples, showing similar spectral signatures. Despite the similarities, it can be seen that the resonant wavelength location is slightly different. Again, the results are associated with the soft nature of the POF, causing the final twist period to vary slightly between the samples, and thus, the spectrum can be slightly red- or blue-shifted depending on the final twist period. In addition, errors can arise due to temperature fluctuations, homogeneity of the mPOF along its length, incorrect position of the mPOF on the heating platform, and differences in fiber pre-tension, which may require further optimization. Regarding the difference between the out-of-band losses obtained for each of the three samples analyzed, it is important to notice that the measurements were performed in a POF spliced to a silica fiber (using UV resin) and using a ferrule

connector to attach the terminal of the mPOF to the OSA. Thus, small misalignments in these fiber sections can induce losses. Considering that the fiber is moved from the measurement setup to the fabrication setup and later again to the characterization setup, it is reasonable to consider some degree of inaccuracy across the sample measurements. Nevertheless, the noise level in all the spectra is too high, and therefore, applications of these spectral filters can only be seen in the sensor field, since the measurements could be wavelength encoded.

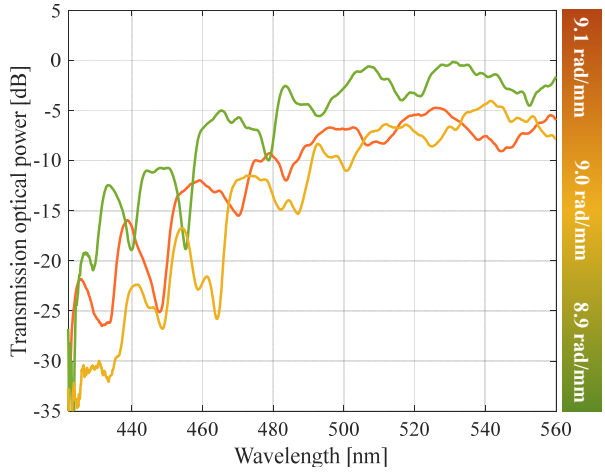

Fig. 1.16. Spectra of three HTOF samples with an experimental helical twist of ~ 9 rad/mm. The spectral resonances are indicated by the ordered numbers.

1.4.2. Torsion Characterization

One great advantage of HTOFs, when compared to other fiber optic sensors, is related to the capability to measure torsion. Furthermore, since the wavelength of the spectral resonance is related to the twist rate, as is described by Equation (1.5), they can also distinguish the direction in which the twist is being imposed. Therefore, the sample with $\alpha = 9.0$ rad/mm, presented in Fig. 1.16, was characterized by torsion in the CW and CCW directions, following the descriptions above. In Fig. 1.17 it is shown all the spectra collected for twist rates done in intervals of 0.0059 rad/mm, for the CCW direction (green to red marked) and CW direction (green to blue marked).

According to Equation (1.5), it is expected that a pure axial twist would change the twist rate, α, and consequently, the resonant wavelength λ_R would change proportionally. This was observed experimentally as seen in Fig. 1.17, presenting a linear blue- and red-wavelength shift when the HTOF is twisted CCW and CW, respectively. To monitor the spectral wavelength shift in Fig. 1.17, it was calculated the central wavelength taken through the center-of-mass method performed at 1 dB above the minimum dip loss. The results are shown in Fig. 1.17, by the markers labeled with "■" and "⧫", namely for the CCW and CW directions, respectively. With these data, it was possible to create the graph of the dip wavelength shift as a function of torsion. The results are shown in Fig. 1.18.

Beyond that, the analytical result predicted from Equation (1.11) is also plotted. For this, it was assumed $\varepsilon = 0$ με, $\lambda_{R0} = 472$ nm, and $\alpha_0 = 9$ rad/mm for a range of values of α_M between −0.08 rad/mm and +0.08 rad/mm. The calculated data is presented in Fig. 1.18 for the dashed purple line.

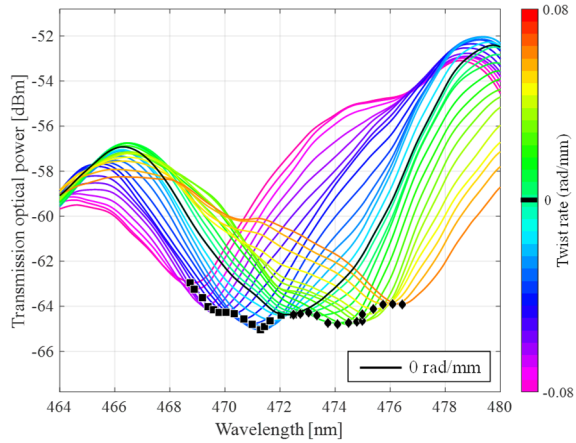

Fig. 1.17. Spectra obtained at different twist rates for the dip wavelength located at ≈472 nm. The minimum dip wavelength is indicated by the ■ and ♦ markers, for the CCW and CW direction, respectively. The reference spectrum (untwisted fiber) is marked with a black trace.

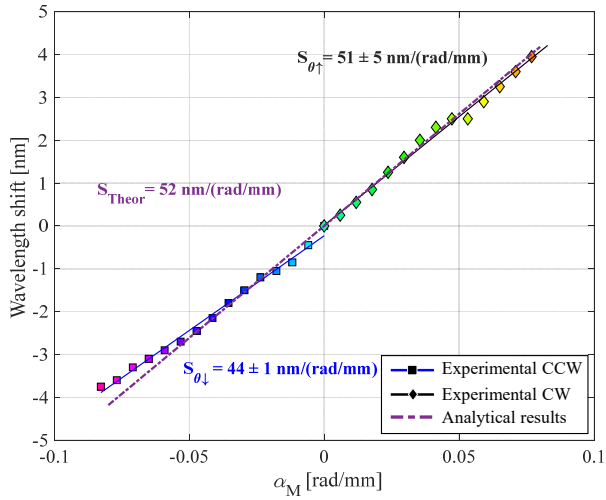

Fig. 1.18. Dip wavelength shift as a function of the twist rate for the CCW and CW characterization directions, obtained from the dips found in Fig. 1.16. The numerical result is also included, assuming $\lambda_{R0} = 472$ nm, $\varepsilon = 0$ με and $\alpha_0 = 9$ rad/mm. On the same graph, it is shown the first-order linear regressions obtained for each data set.

The results presented in Fig. 1.18 show a proportional behavior between the dip wavelength shift and the twist rate. Thus, a first-order linear regression model was applied

to each set of data points. The sensitivities obtained from the absolute value of the slope were 44 ± 1 nm/(rad/mm) and 51 ± 5 nm/(rad/mm), for the CCW and CW directions, respectively. The values were close to each other, being the slight differences associated with the detection method used to calculate the dip wavelength, i.e. center of the mass at 1 dB above the minimum. This occurs because the spectral dips slightly change their shape (optical power over wavelength) when the twist rate increases. This originates errors in the identification of the dip wavelength. In order to understand the accuracy of the results the analytical data shown in Fig. 1.18 was calculated recurring to Equation (1.11) and considering, λ_{R0} = 472 nm, α_0 = 9.0 rad/mm, and ε = 0 με. The obtained results for the analytical sensitivity are close to the experimental sensitivities, namely 52 nm/(rad/mm). Comparing the results reached in this work with the ones found for silica fiber sensors [38], which report sensitivity values on the order of tens or hundreds of pm/(rad/mm), it is possible to infer that the results of the HTOF are much more attractive. Furthermore, the sensitivity values reached for the polymer HTOF closely match the ones observed for the same twisted structures in silica PCF, i.e. ≈56 nm/(rad/mm) [35]. However, it is important to stress that POFs are more flexible, non-brittle, compliant, and offer higher elastic limits, meaning that they can extend the limits and range of applications.

1.4.3. Strain Characterization

Considering the longitudinal strain characterization of the HTOF, it was obtained the spectral results shown in Fig. 1.19.

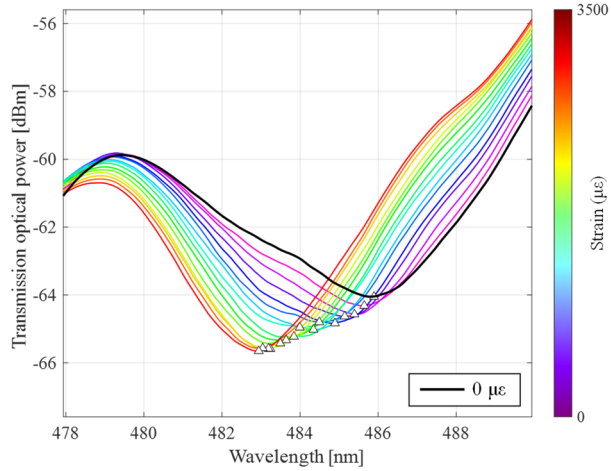

Fig. 1.19. Spectra acquired for different strain steps for the loading tests. The minima dip wavelengths are indicated by △ markers. The reference spectrum is marked in black for the unstrained condition.

As seen in Fig. 1.19, the spectra were blue-shifted with increasing strain. Furthermore, the dip wavelengths calculated from the center-of-mass method at 1 dB above the minima are also shown with "△" markers for the increasing strain steps. The corresponding dip

wavelength and the analytical result are shown in Fig. 1.20. For the analytical result, it was used Equation (1.11), assuming λ_{R0} = 486 nm, n_{SM} = 1.49, υ = 0.35, p_{11} = 0.121, p_{12} = 0.270 [39], and α_M constant.

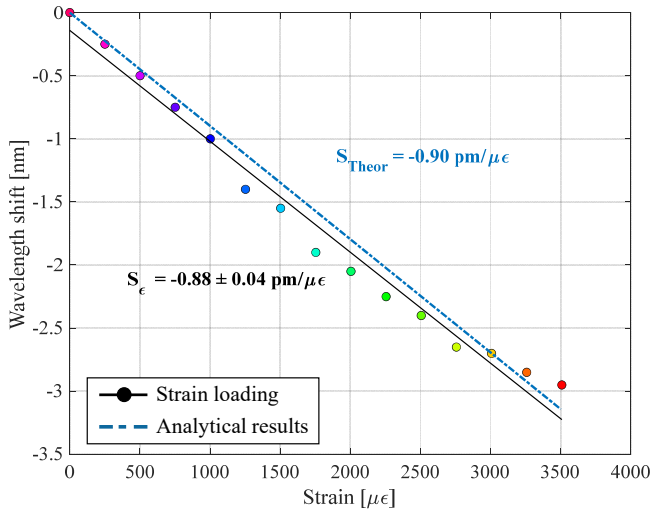

Fig. 1.20. Corresponding dip wavelength shifts of the transmission spectra shown in Fig. 1.19, as a function of strain, for the ≈486 nm dip resonance. On the same graph, it is shown the first-order linear regressions obtained for each of the experimental data points and the curve estimated from the analytical model assuming λ_{R0} = 486 nm and n_{SM} = 1.49, υ = 0.35, p_{11} = 0.121 and p_{12} = 0.270.

Looking at Fig. 1.20, it is possible to see a linear relationship between the dip wavelength shift and the applied strain. A 1st order linear regression model was applied to the experimental data revealing sensitivities of −0.88 ± 0.04 pm/με. Comparing these results with the ones reported in [35] for silica PCFs, it can be seen that the negative slope response was also present. From the analytical results, it was obtained a sensitivity that closely match the one obtained in the experimental results, namely −0.90 pm/με. Furthermore, the sensitivity reached is similar to the one reported in the literature for twisted PCFs, i.e., −1.18 pm/με [35], being the slight differences associated with the lower dip wavelength used in this work, i.e. 470 – 485 nm vs. 800 nm, for the work reported in [35]. Also, the absolute values of the sensitivities are within the same values reported for polymer FBGs [40]. These results prove that the HTOF can be used for longitudinal strain sensing applications, giving good prospects regarding the high tunable range associated with the high elastic limits of POFs and their easy fabrication.

1.5. Conclusion

In this chapter, it was described the theory as well as the production of helically twisted microstructured polymer optical fibers. The use of polymer fibers brings the benefit of working at lower temperatures, making the helically twisting process easier to do when

compared to their glass counterparts. Additionally, the use of polymer optical fibers allows to development new stretchable and flexible optical fiber devices.

The work reports the post-processing of a PMMA mPOF with a helical period of ~696 μm. The process was repeatable, showing similar helical periods for different post-processed samples. The spectral characterization revealed a series of attenuation dips in the low-loss region of the mPOF. These attenuation dips correspond to the coupling of the fundamental core mode with the highly leaky cladding modes propagating in the spiral path at the hollow air hole region.

Results obtained from the torsion characterization revealed that the spectrum is wavelength shifted, presenting a sensitivity close to 50 nm/(rad/mm), with the capability to distinguish between CW and CCW directions. The responses were close to the analytical calculations and also similar to those reported for similar structures in PCFs.

Strain characterization results revealed a wavelength shift sensitivity of −0.90 pm/μm. This was slightly lower than the one reached for similar structures in PCFs, however, this was a consequence of the lower wavelength range used for the characterizations. Comparisons with FBGs in POFs, working at the same wavelength region revealed similar absolute values. Furthermore, the sensitivity achieved in this work was close to the one obtained through the analytical calculations.

In conclusion, the production and characterization of HTOF in polymer optical fibers were successfully accomplished. The results presented in this work will pave the way for the implementation of this new class of fiber optic structure in compliant materials. The simplicity of production allied to the relevant qualities of the polymers will for sure increase the attention of the research community to this fiber optic technology, opening the doors for their use in smart flexible sensor applications.

Acknowledgements

This work was funded by Fundação para a Ciência e a Tecnologia (FCT) and FEDER funds through the COMPETE 2020 Programme and under the projects UIDB/50008/2020-UIDP/50008/2020 and by FCT/MEC under the project (PTDC/EEI-TEL/1511/2020). R. Oliveira acknowledges the FCT contract CEECIND2021.01066.

References

[1]. J. Hecht, City of Light: The Story of Fibre Optics, *Oxford University Press*, 2004.
[2]. J. W. Hicks, E. Snitzer, H. Osterberg, Optical Energy Transmitting Devices and Method of Making Same, U.S. Patent 3,157,726, *USA*, 1960.
[3]. C. K. Kao, W. S. Boyle, G. E. Smith, The Masters of Light, https://www.nobelprize.org/prizes/physics/2009/summary/
[4]. F. P. Kapron, D. B. Keck, R. D. Maurer, Radiation losses in glass optical waveguides, *Appl. Phys. Lett.*, Vol. 17, Issue 10, 1970, pp. 423-425.

[5]. ITU-T G.652: Characteristics of a Single-Mode Optical Fibre and Cable, https://www.itu.int/rec/T-REC-G.652-201611-I/en
[6]. K. Bhowmik, G.-D. Peng, Polymer optical fibers, in Handbook of Optical Fibers, *Springer Singapore*, 2019, pp. 1-51.
[7]. A. Upadhyay, S. Singh, D. Sharma, S. A. Taya, A highly birefringent bend-insensitive porous core PCF for endlessly single-mode operation in THz regime: an analysis with core porosity, *Appl. Nanosci.*, Vol. 11, Issue 3, Mar. 2021, pp. 1021-1030.
[8]. H. Pakarzadeh, M. Taghizadeh, M. Hatami, Designing a photonic crystal fiber for an ultra-broadband parametric amplification in telecommunication region, *J. Nonlinear Opt. Phys. Mater.*, Vol. 25, Issue 0, Jun. 20162, 1650023.
[9]. S. M. A. Razzak, Y. Namihira, Proposal for Highly Nonlinear Dispersion-Flattened Octagonal Photonic Crystal Fibers, *IEEE Photonics Technol. Lett.*, Vol. 20, Issue 4, Feb. 2008, pp. 249-251.
[10]. Y. Wang, *et al.*, Hollow-core photonic crystal fibre for high power laser beam delivery, *High Power Laser Sci. Eng.*, Vol. 1, Issue 1, Mar. 2013, pp. 17-28.
[11]. J. M. Dudley, G. Genty, S. Coen, Supercontinuum generation in photonic crystal fiber, *Rev. Mod. Phys.*, Vol. 78, Issue 4, Oct. 2006, pp. 1135-1184.
[12]. C. Fu *et al.*, High-order orbital angular momentum mode generator based on twisted photonic crystal fiber, *Opt. Lett.*, Vol. 43, Issue 8, 2018, pp. 1786-1789.
[13]. R. Beravat, G. K. L. Wong, X. M. Xi, M. H. Frosz, P. St. J. Russell, Current sensing using circularly birefringent twisted solid-core photonic crystal fiber, *Opt. Lett.*, Vol. 41, Issue 7, 2016, pp. 1672-1675.
[14]. X. Cao, Y. Liu, L. Zhang, Y. Zhao, T. Wang, Characteristics of chiral long-period fiber gratings written in the twisted two-mode fiber by CO_2 laser, *Appl. Opt.*, Vol. 56, Issue 18, 2017, pp. 5167-5171.
[15]. K. E. Carroll, C. Zhang, D. J. Webb, K. Kalli, A. Argyros, M. C. Large, Thermal response of Bragg gratings in PMMA microstructured optical fibers, *Opt. Express*, Vol. 15, Issue 14, 2007, pp. 8844-8850.
[16]. J. N. Dash, R. Jha, SPR Biosensor Based on Polymer PCF Coated With Conducting Metal Oxide, *IEEE Photonics Technol. Lett.*, Vol. 26, Issue 6, Mar. 2014, pp. 595-598.
[17]. C. Fu, Y. Wang, Z. Bai, S. Liu, Y. Zhang, Z. Li, Twist-direction-dependent orbital angular momentum generator based on inflation-assisted helical photonic crystal fiber, *Opt. Lett.*, Vol. 44, Issue 2, 2019, pp. 459-462.
[18]. N. A. Mortensen, J. R. Folkenberg, M. D. Nielsen, K. P. Hansen, Modal cutoff and the V parameter in photonic crystal fibers, *Opt. Lett.*, Vol. 28, Issue 20, 2003, pp. 1879-1881.
[19]. X. M. Xi, G. K. L. L. Wong, T. Weiss, P. S. J. Russell, Helically Twisted Solid-Core Photonic Crystal Fibres, *Phil. Trans. R. Soc. A*, Vol. 375, Issue 2087, 2013, 20150440.
[20]. M. C. J. Large, L. Poladian, G. W. Barton, M. A. van Eijkelenborg, Microstructured Polymer Optical Fibres, *Springer US*, Boston, MA, 2008.
[21]. M. van Eijkelenborg, *et al.*, Microstructured polymer optical fibre, *Opt. Express*, Vol. 9, Issue 7, 2001, pp. 319-327.
[22]. Y. Zhang, *et al.*, Casting preforms for microstructured polymer optical fibre fabrication, *Opt. Express*, Vol. 14, Issue 12, 2006, pp. 5541-5547.
[23]. K. Cook, *et al.*, Air-structured optical fiber drawn from a 3D-printed preform, *Opt. Lett.*, Vol. 40, Issue 17, 2015, pp. 3966-3969.
[24]. J. Li, *et al.*, Tunable Chiral Optics in All-Solid-Phase Reconfigurable Dielectric Nanostructures, *Nano Lett.*, Vol. 21, Issue 2, Jan. 2021, pp. 973-979.
[25]. N. Suzuki, *et al.*, Chiral Graphene Quantum Dots, *ACS Nano*, Vol. 10, Issue 2, 2016, pp. 1744-1755.

[26]. F. Li, *et al.*, Chiral Carbon Dots Mimicking Topoisomerase I To Mediate the Topological Rearrangement of Supercoiled DNA Enantioselectively, *Angew. Chemie – Int. Ed.*, Vol. 59, Issue 27, 2020, pp. 11087-11092.
[27]. F. Patti, *et al.*, Chiral optical tweezers for optically active particles in the T-matrix formalism, *Sci. Rep.*, Vol. 9, Jan. 2019, 29.
[28]. X. Kong, K. Ren, L. Ren, J. Liang, H. Ju, Chiral long-period gratings: fabrication, highly sensitive torsion sensing, and tunable single-band filtering, *Appl. Opt.*, Vol. 56, Issue 16, 2017, pp. 4702-4707.
[29]. V. I. Kopp *et al.*, Single- and double-helix chiral fiber sensors, *J. Opt. Soc. Am. B*, Vol. 24, Issue 10, 2007, pp. A48-A52.
[30]. V. I. Kopp, V. M. Churikov, J. Singer, N. Chao, D. Neugroschl, A. Z. Genack, Chiral fiber gratings, *Science*, Vol. 305, Issue 5680, 2004, pp. 74-75.
[31]. P. S. J. Russell, R. Beravat, G. K. L. Wong, Helically twisted photonic crystal fibres, *Philos. Trans. R. Soc. A Math. Phys. Eng. Sci.*, Vol. 375, Issue 2087, 2017, 20150440.
[32]. P. Russell, Photonic crystal fiber, *Science*, Vol. 299, Issue 5605, 2003, pp. 358-362.
[33]. G. K. L. Wong, *et al.*, Excitation of Orbital Angular Momentum Resonances in Helically Twisted Photonic Crystal Fiber, *Science*, Vol. 337, Issue 6093, 2012, pp. 446-449.
[34]. A. M. Yao, M. J. Padgett, Orbital angular momentum: origins, behavior and applications, *Adv. Opt. Photonics*, Vol. 3, Issue 2, 2011, pp. 161-204.
[35]. X. Xi, G. K. L. Wong, T. Weiss, P. S. J. Russell, Measuring mechanical strain and twist using helical photonic crystal fiber, *Opt. Lett.*, Vol. 38, Issue 24, 2013, pp. 5401-5404.
[36]. J. Preizal, L. Bilro, R. Nogueira, R. Oliveira, Helically twisted microstructured polymer optical fiber and its application as a torsion and strain sensor, *J. Light. Technol.*, Vol. PP, 2023, pp. 1-8.
[37]. X. Xi, Helically twisted solid-core photonic crystal fibers, PhD Thesis, *National University of Defense Technology*, 2015.
[38]. V. Budinski, D. Donlagic, Fiber-Optic Sensors for Measurements of Torsion, Twist and Rotation: A Review, *Sensors*, Vol. 17, Issue 3, 2017, 443.
[39]. R. M. Waxler, D. Horowitz, A. Feldman, Optical and physical parameters of Plexiglas 55 and Lexan, *Appl. Opt.*, Vol. 18, Issue 1, Jan. 1979, pp. 101-104.
[40]. R. Oliveira, L. Bilro, R. Nogueira, Polymer Optical Fiber Bragg Gratings: Fabrication and Sensing Applications, 1st Ed., *CRC Press*, Aveiro, Portugal, 2019.

Chapter 2
Brain Tumor Detection and Segmentation: A Review of Optical Scanning Holography Method Using Active Contour

Abdelaziz Essadike, Anass Cherkaoui, Abdennacer El-Ouarzadi and Abdenbi Bouzid

2.1. Introduction

A brain tumor is a mass of abnormal cells engaged in a chaotic process of driver somatic mutations [1], where they cause various symptoms, increasing the risk of damaging the brain. Indeed, the secondary tumor infiltrates neighboring healthy tissues and proliferates within the brain or its membranes, making it crucial to determine its shape and volume to ensure effective management of patients at an early stage of cancer. Magnetic resonance imaging (MRI) is commonly used as a non-invasive imaging modality for brain tumor detection [2]. MRI employs radio waves and a strong magnetic field to acquire a set of cross-sectional brain images. In other words, the 3D anatomical details of a tumor are presented as a set of parallel 2D cross-sectional images. Representing 3D data as projected 2D sections results in information loss and can raise questions about tumor prognosis. Furthermore, 2D cross-sectional images do not accurately represent the complexities of brain anatomy. Therefore, interpreting 2D images requires specialized training. This is why the reconstruction of volumes from sequential parallel 2D cross-sectional slices is a necessity for 3D visualization of tumors [3].

The 3D reconstruction of tumors initially requires appropriate segmentation of the region of interest. This 3D reconstruction helps radiologists better diagnose patients and subsequently eradicate the entire tumor when surgical intervention is considered. Techniques presented in [4, 5] are based on preprocessing, image enhancement, and contouring before reconstruction. In 2012, authors in [6] utilized a technique based on phase contrast projection tomography to calculate the 3D density distribution in bacterial

Abdelaziz Essadike
Hassan I University, Faculty of Science and Technology, Higher Institute of Health Sciences, Settat, Morocco

cells. In 2013, authors in [3] proposed an improved interpolation technique to estimate missing inter-slices, and the Marching Cubes (MC) algorithm for meshing the tumor. For surface rendering, they applied the Phong shading and lighting model to better calculate the tumor's volume. Furthermore, an approach in [7], in 2019, offers a technique for segmenting brain tumors throughout the 3D volume using a 2D convolutional neural network to predict tumors. Authors in [8] conducted a comparison between conventional machine learning-based techniques and deep learning-based techniques. The latter are further categorized into 2D-CNN and 3D-CNN techniques. However, the results of techniques based on deep convolutional neural networks outperform those of machine learning techniques. As for authors in [9], they introduced a two-stage optimal mass transport technique (TSOMT) that involves transforming an irregular 3D brain image into a cube with minimal deformation for segmenting medical 3D images. Automatic segmentation, facilitated by convolutional neural networks, of a brain tumor from two-dimensional slices (coronal, sagittal, and axial) [10], significantly aids in delineating the region of interest in 3D.

Conventional holography, as we know it today, owes its inception to Hungarian-British physicist Dennis Gabor in 1948 [11]. His groundbreaking research aimed at enhancing the resolution of electron microscopes paved the way for this revolutionary technique. In the 1960s, with the emergence of lasers, holography saw significant development. Holograms were originally recorded on plates or photosensitive films, primarily relying on silver ions that darkened when exposed to light. The advent of high-resolution matrix detectors in 1994, championed by U. Schnars and W. Jüptner [12], heralded the era of digital holography. This development opened doors to a multitude of applications, including holographic microscopy [13, 14], quantitative phase imaging [15-18], color holography [19-21], metrology [22-24], holographic cameras [25], 3D displays [26-28], and head-up displays [29, 30]. An innovative breakthrough came with the introduction of phase-shifting holography by Yamaguchi and Zhang [31], aiming to eliminate unwanted diffraction orders from holograms. They employed spatial phase shifting using a piezoelectric transducer with a mounted mirror, and minor frequency adjustments of acousto-optic modulators (AOM), a technique closely related to heterodyne detection methods. Optical Scanning Holography (OSH) stands out as an intelligent application for processing pupillary interaction [32-35]. In 1979, Korpel and Poon introduced optical heterodyne scanning to implement the pupillary interaction scheme, while in 1992, Indebetouw and Poon innovated by incorporating this scheme into a scanning illumination mode. A pivotal moment occurred in 1985 [36] when Poon, through a clever adjustment of one lens relative to another (one serving as an open mask and the other as a pinhole mask), and by deliberately defocusing the optical system, developed an optical scanning system capable of holographically recording scanned objects. This ingenious technique marked the birth of optical scanning holography (OSH), which has since found diverse applications, including optical scanning microscopy, 3D shape recognition, 3D holographic TV, 3D optical remote sensing, and more. OSH's early forays into preprocessing can be traced back to 1985 [37]. Subsequent research indicated that replacing a flat lens with a Gaussian annular aperture was beneficial for recovering the edges of cross-sectional images in holograms [38]. In 2010, Xin Zhang and Edmund Y. Lam [39] showcased the efficiency of selecting a pupil function such as the Laplacian of

Gaussian for extracting the edges of 3D scanned objects using the OSH system. Furthermore, authors in reference [40] proposed a 1D image capture system for autostereoscopic displays, comprising a cylindrical lens, a focusing lens, and an imaging device. By scanning an object across a wide angle, they successfully synthesized 3D stereoscopic images, adding a unique dimension to the OSH technology landscape.

Progress in Optical Scanning Holography (OSH) represents a significant leap in the field of medical imaging and tumor detection. This progress is achieved through the strategic integration of innovative features and techniques that collectively enhance the capabilities of the method. One pivotal enhancement is the combination of off-axis optical scanning with a heterodyne fringe pattern [41-44]. This combination significantly improves the accuracy of tissue imaging. Off-axis scanning, which involves capturing data from multiple angles, allows for more precise 3D structure reconstruction. The heterodyne fringe pattern plays a crucial role in phase retrieval, making it easier to extract valuable information from the holographic data. The introduction of a Spatial Light Modulator (SLM) for MRI image display is another significant innovation. This technology enables the direct correlation of holographic data with anatomical MRI images, enhancing the precision of tissue visualization. By fusing the holographic and MRI data, this feature provides a more comprehensive and informative representation of the biological tissues under examination. Moreover, there is a dedicated focus on extracting the in-phase component of the scanned data. This precise component is essential for accurate tumor localization. The peak of the in-phase component serves as a reliable indicator of the tumor's position, reducing the likelihood of false positives and false negatives in diagnostic assessments [45, 46]. Generalized Optical Scanning Holography (GOSH) represents a significant leap in data collection efficiency. GOSH can acquire a single on-axis hologram, significantly expediting the process while minimizing the risk of motion artifacts. This is particularly advantageous for 3D imaging, where efficiency is paramount. Furthermore, the method incorporates a cylindrical lens for line-by-line scanning, enhancing the speed and accuracy of data collection [47]. This approach contributes to more efficient data acquisition, reducing the time required for the scan while enriching the dataset. The utilization of an Active Contour Model (ACM) for segmentation is another crucial addition. ACMs are efficient in delineating complex shapes and contours, making them well-suited for identifying abnormal tissue regions [48]. By automating the segmentation process and incorporating the tumor's position, the method ensures that the area of interest is precisely encompassed. Transitioning active contour theory from semi-automatic to fully automatic status with reliable tumor detection, our method's effectiveness is demonstrated through tests using the well-known BraTS 2019 and BraTS 2020 databases. Ultimately, the goal of this methodology is to reconstruct 3D brain tumors from segmented areas of interest, offering a comprehensive view of tumor size and location. These added features and enhancements are of utmost significance, as they collectively contribute to faster, more accurate, and more informative assessments of biological tissues. By enabling early and precise tumor detection, this methodology holds the potential to significantly improve patient outcomes, making it a valuable asset in the realm of medical diagnostics and research.

2.2. Materials and Methods

2.2.1. The First Iteration: Off-axis Optical Scanning Holography

Fig. 2.1 illustrates the Optical Spatial Heterodyne (OSH) system used for the extraction of the in-phase and quadrature components of scanned current information. The system configuration is as follows: A laser source emits light with temporal frequencies ω. This light is split into two beams using a Beam Splitter BS_1, and the laser source in use operates at two wavelengths, $532\ nm$ and $1064\ nm$. The first beam, following reflection from Mirror M_1, illuminates the first pupil, designated as $p(x,y)$. In contrast, the second beam undergoes a frequency shift through an acousto-optic modulator. After reflecting off Mirror M_2, the frequency of the laser illuminating the second pupil, $p(x,y)$, becomes $(\omega + \psi)$. Both pupils are then combined using Beam Splitter BS_2, focusing the light onto $2D$ scanning mirrors located at the rear focal plane of Lenses L_1. These optical beams are further directed to a Spatial Light Modulator (SLM), which imparts spatially varying modulation based on MRI data onto the light. The SLM used here is known as LC 2012, featuring a resolution of 1024 × 768 pixels. This SLM is responsible for displaying the brain tumor image, denoted as $I(x,y,z)$, located at a specific distance z from the $2D$ scanning mirrors. It's not worthy that SLMs have historically encountered issues related to diffraction efficiency because of phase shift limitations. However, the selected SLM effectively overcomes this challenge. It can achieve a phase shift range approaching 2π, resulting in significantly enhanced diffraction efficiency. Furthermore, the LC 2012 SLM offers the capability to modulate the blazing function, thereby improving grating efficiency and overall diffraction performance. The system is completed by Lens L_3, which focuses transmitted light onto a photo-detector, producing an output current, $i(x,y)$. An electronic bandpass filter (BPF), tuned to the heterodyne frequency ψ, provides an output of a swept current, denoted as $i_\psi(x,y)$.

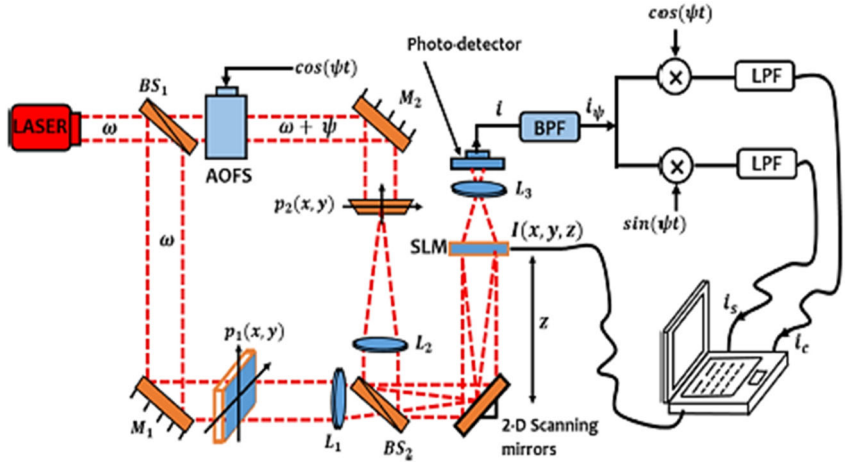

Fig. 2.1. Two-pupil optical heterodyne scanning image processor for the in-phase component extraction of brain tumor.

$$i_{\psi_Q}(x,y,z+z_0) = P^1_{z+z_0}\left(\frac{k_0 x'}{f},\frac{k_0 y'}{f}\right) P^{2\,*}_{z+z_0}\left(\frac{k_0 x'}{f},\frac{k_0 y'}{f}\right) \otimes |O(x,y,z+z_0)|^2 \qquad \text{F.1)}$$

Afterward, we are able to define the optical transfer function (OTF) of the system by:

$$OTF_\Psi(k_x,k_y,z+z_0) = \frac{F\{i_{\psi_Q}(x,y,z+z_0)\}}{F\{|O(x,y,z+z_0)|^2\}} \qquad (2.2)$$

As a result, we obtain the following equations:

$$\mathrm{i_c(x,y)} = \mathrm{Re}\{\int \mathrm{F^{-1}\{F\{|O(x,y,z+z_0)|^2\}.OTF_\Psi\}\,dz\}}, \qquad (2.3)$$

$$\mathrm{i_s(x,y)} = \mathrm{Im}\{\int \mathrm{F^{-1}\{F\{|O(x,y,z+z_0)|^2\}.OTF_\Psi\}\,dz\}} \qquad (2.4)$$

These two currents are respectively representing the In-phase component $\mathrm{i_c(x,y)}$ and the quadrature component $\mathrm{i_s(x,y)}$ of the extracted heterodyne current from the scanned MR image. the temporal frequency shift is inserted between the two pupils by assuming:

$P^1_{z+z0}(x,y) = 1$ and $P^2_{z+z0}(x,y) = \delta(x,y)$ Thus, the optical transfer function becomes:

$$\mathrm{OTF_\Psi(k_x,k_y,z+z_0)} = \exp\left[\frac{-j(z+z_0)}{2k_0}\left(k_x{}^2 + k_y{}^2\right)\right], \qquad (2.5)$$

and the two streams become:

$$\mathrm{i_c(x,y)} = \int\left\{|O(x,y,z+z_0)|^2 * \frac{k_0}{2\pi(z+z_0)}\sin\left[\frac{k_0}{2(z+z_0)}(x^2+y^2)\right]\right\}dz, \qquad (2.6)$$

$$i_s(x,y) = \int\left\{|O(x,y,z+z_0)|^2 * \frac{k_0}{2\pi(z+z_0)}cos\left[\frac{k_0}{2(z+z_0)}(x^2+y^2)\right]\right\}dz \qquad (2.7)$$

2.2.2. The Second Iteration: In-line Optical Scanning Holography

In the progression of our Optical Scanning Holography (OSH) setup (Fig. 2.2), the transition from the off-axis holography structure to inline holography marked a pivotal shift in our methodology. Off-axis holography, characterized by a physical separation of the object and reference beams at an angle, was succeeded by inline holography, where these beams are aligned. This alteration bears significant implications. Off-axis holography excels in extracting precise phase information, and its sensitivity to phase variations is conducive to accurate $3D$ reconstruction. However, it can be susceptible to speckle noise and is more sensitive to vibrations. In contrast, inline holography simplifies the optical setup, supports real-time imaging, and offers a more streamlined approach, significantly enhancing the speed of data acquisition. By virtue of its direct correlation of holographic and MR image data through the spatial light modulator (SLM), inline holography enhances the accuracy of tissue visualization, a fundamental feature for our diagnostic objectives. This transition has not only expedited data acquisition but also ensured greater precision and efficiency in our holographic imaging, setting the stage for subsequent enhancements.

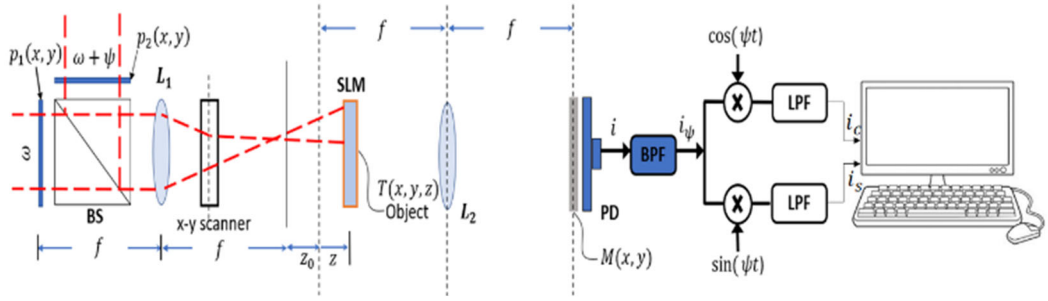

Fig. 2.2. Generalized two-pupil heterodyne scanning image processing system for the In-phase component extraction of brain tumor.

In this section, we present the transition to an inline holography setup for our imaging process, departing from the previous off-axis configuration. Our primary focus is on the automatic detection of tumors, utilizing the In-phase component of the scanned current. To maintain this crucial component during data acquisition, we adopt a novel optical heterodyne approach. For instance, we implement acousto-optic modulators to manipulate the laser beam frequency. The heart of our inline holography system involves the merging of two laser beams through a beam splitter (BS). These combined beams are directed by an $x-y$ scanner towards a $3D$ object positioned at a distance of $z+z_0$ from the back focal plane of lens L_1. This object is placed within a spatial light modulator, which plays a pivotal role in our holographic imaging process. Each slice of the object is represented by an amplitude transmittance $T(x,y,z)$, and the spatial light modulator displays the brain tumor image, labeled as $I(x,y,z)$, situated at a distance of $z+z_0$ away from the back focal plane of lens L_1. Moreover, as we transition to this inline setup, we encounter challenges related to diffraction efficiency, particularly associated with phase shift loss. This transition is essential because the MRI image is binary, and our chosen spatial light modulator can effectively achieve an offset range of nearly 2π, resulting in exceptional diffraction efficiency. Additionally, the spatial light modulator stands out as a modern device, allowing us to modulate blazing functions to attain maximum grating efficiency and significantly enhance diffraction performance. These adjustments are critical in our pursuit of precise holographic imaging.

In the context of our study, we define the in-phase component, $i_c(x,y)$, and the quadrature component, $i_s(x,y)$, of the extracted heterodyne current from the scanned MR image as follows:

$$i_c = \int \left\{ |T(x,y;z)|^2 * \frac{k_0}{2\pi z} sin\left[\frac{k_0(x^2+y^2)}{2z}\right] \right\} dz = H_{\sin(s,y)}, \tag{2.8}$$

$$i_s = \int \left\{ |T(x,y;z)|^2 * \frac{k_0}{2\pi z} cos\left[\frac{k_0(x^2+y^2)}{2z}\right] \right\} dz = H_{\cos(s,y)} \tag{2.9}$$

2.2.3. The Third Iteration: Cylindrical Lens-integrated Optical Scanning Holography

To enhance the precision and efficiency of our approach, we leverage the invaluable benefits of cylindrical lens L_1 in the context of optical scanning holography for the automated segmentation of $3D$ brain tumors from MRI data. L_1 plays a pivotal role in optimizing our method in several ways. Firstly, it enables meticulous line-by-line scanning, which is crucial for capturing intricate details within the MRI images. The cylindrical lens L_1 configuration ensures that each section of the image is consistently and accurately scanned, reducing the likelihood of information loss or distortion. Secondly, the integration of cylindrical lens L_1 in our system enhances the depth perception and spatial accuracy of the captured data. By focusing on specific areas of interest within the MRI images, L_1 ensures that the relevant tumor structures are precisely imaged and analyzed. This level of precision not only accelerates the segmentation process but also reduces the risk of misinterpretation, which can occur in manual delineation. Moreover, cylindrical lens L_1 is instrumental in optimizing the digitization of the phase component of the scanned data. This digital representation is critical for pinpointing the exact location of the tumor within the brain, as the peak of the phase component reliably indicates its position. This information serves as the foundation for rapid segmentation and subsequent $3D$ tumor reconstruction. In summary, the inclusion of cylindrical lens L_1 in our approach significantly enhances the overall accuracy, speed, and reliability of tumor segmentation, making it an indispensable component in our quest to streamline neuroimaging and improve patient care. L_1 allows for a higher level of precision and detail, reducing the margin of error and contributing to the system's efficacy in advancing medical diagnostics and treatment planning.

Fig. 2.3 displays the optical scanning holography system used for our method. A laser beam of frequency ω is shifted in frequency to ψ and $\psi + \Delta\psi$ through acousto-optic modulators ($AOM_{1,2}$), respectively. The beams from AOMs are then collimated by collimators BE_1 and BE2. The outgoing beam from BE_2 is considered a plane wave of frequency $\omega + \psi + \Delta\psi$, which is projected onto the object through the $x - y$ scanner. Our novel method involves integrating into the chosen imaging system a cylindrical lens L_1, which provides a cylindrical wave at $\omega + \psi$, projected onto the object. A focusing lens is also used to capture a large number of elemental images containing extensive parallax data. These elemental images are transformed into a matrix of elemental images, where each captured elemental image corresponds to a vertical line in the ray space [46]. The utilization of this linear scanning technology involves capturing object images in a single pass rather than point by point, while adjusting the shape of the surface after each iteration, resulting in computational time savings. Accordingly, following appropriate sampling for viewing conditions, we achieved fully automatic segmentation through the improved algorithm and the arrangement of color filters. This allowed the transformation of two-dimensional elemental images into three-dimensional ($3D$) images.

The $x - y$ scanner is used to uniformly scan the $3D$ object, line by line. As a result, each scan line of the object corresponds to a line in the hologram at the same vertical position. Along each scan line, photodetectors PD_1 and PD_2 are employed to capture the optical

signal scattered by the object and the heterodyne frequency information $\Delta\psi$ as a reference signal, respectively, and convert them into electrical signals for the lock-in amplifier. The in-phase and quadrature-phase outputs of the lock-in amplifier circuit produce a sine hologram, $H_{\sin}(x,y)$, and a cosine hologram, $H_{\cos}(x,y)$, to achieve a full $2D$ scan of the object, as illustrated below:

$$H(x,y) = H_{cos}(x,y) + jH_{sin}(x,y) = \sum_{k=0}^{N-1} H_k(x,y;\, z_k) \tag{2.10}$$

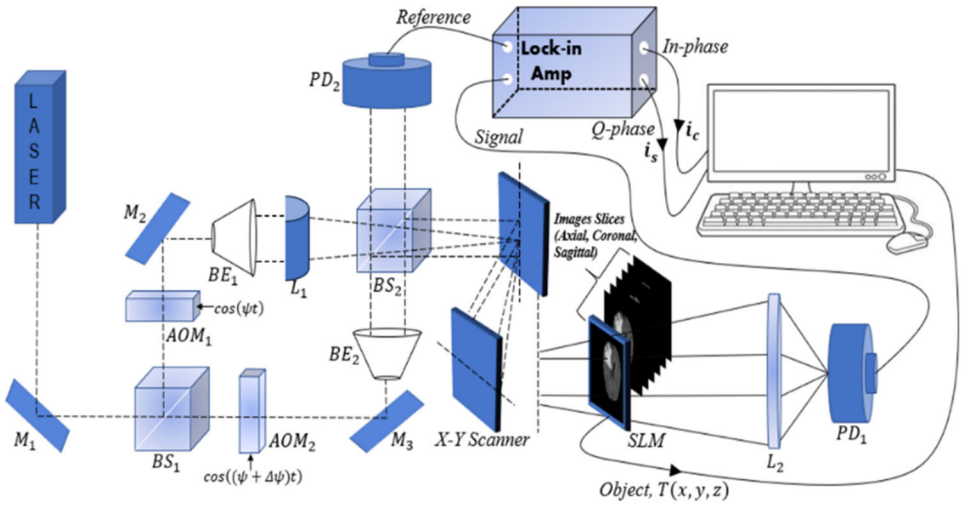

Fig. 2.3. Schematic setup of the optical scanning holography (OSH).

2.2.4. Core Principle of OSH

The central premise of our proposed approach centers on harnessing the In-phase component (denoted as $i_c(x,y)$) within MR images to discern abnormal tissue. In Figs. 2.1-2.2-2.3, the optical system yields an output illustrating the distribution of the In-phase component via heterodyne current. We designate the prominent points in this output as "In-phase component peaks." Fig. 2.4 furnishes visual illustrations of these In-phase component peaks, detected using the OSH method. Consequently, we can accurately locate brain tumors by identifying these peaks in the In-phase component distribution.

Armed with knowledge about the positions of these In-phase component peaks, as depicted in Fig. 2.5, we can establish the initial contour (C_i) for tumor segmentation within the affected tissue. This initial contour serves as a critical foundation for further analysis and refinement of the tumor's boundaries. Our proposed method is highly adaptable, capable of effectively detecting multimodal tumors by pinpointing the positions of two maxima within the In-phase component peaks. This feature proves invaluable in cases involving tumors with multiple characteristics or modalities, enhancing our ability to provide tailored and precise diagnoses and treatment strategies for patients facing complex tumors.

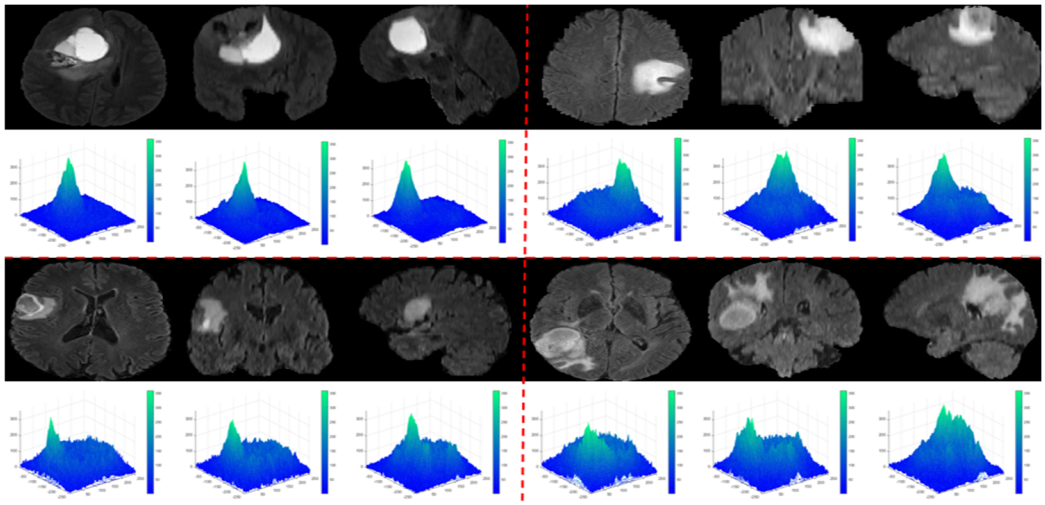

Fig. 2.4. In-phase component peaks at the proposed OSH method's tumor position: examples of image slices (Axial, Coronal, Sagittal) from BRATS 2019 database.

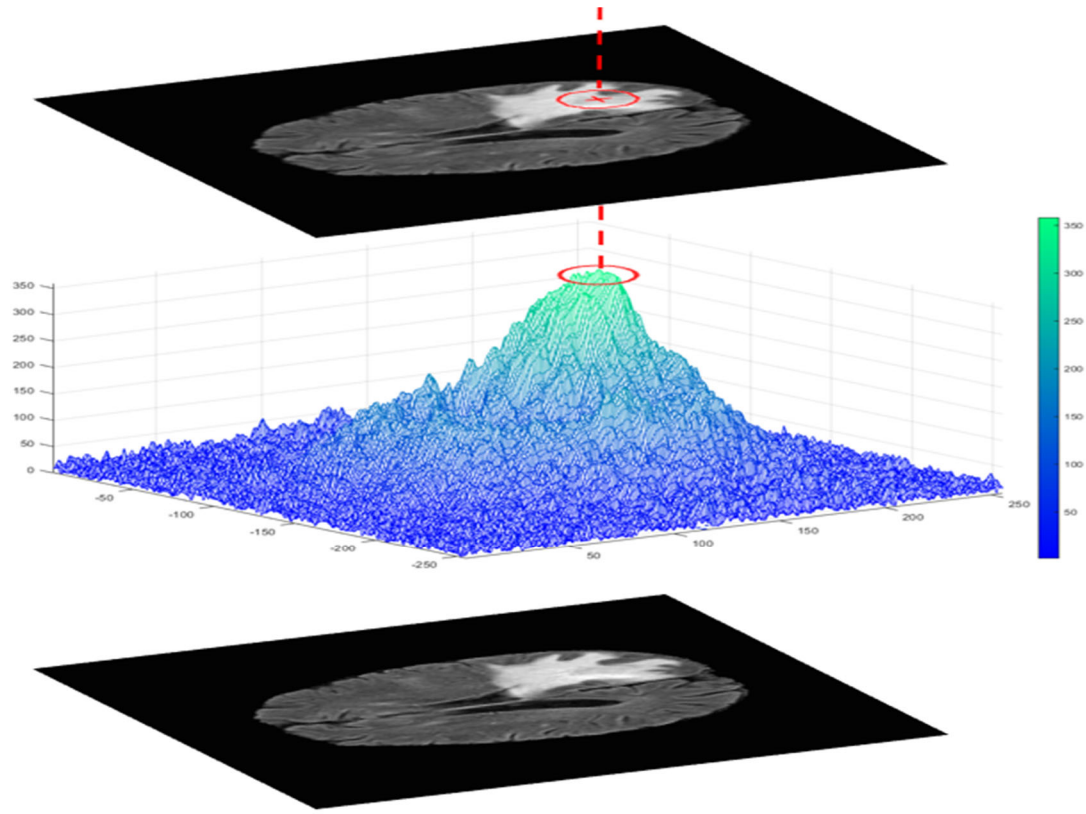

Fig. 2.5. Preliminary extraction of the initial contour Ci inside the tumor tissue by OSH-based phase component peaks.

2.3. Results and Discussion

2.3.1. Evaluation of Detection Phase

Various methods are used to detect tumor contours, including derivative methods, which are based on evaluating the variation at each pixel by identifying maxima. determining the brain tumor's position by searching the peaks given by the maximum values of the In-phase component distribution. With the peaks position of the In-phase component, as shown in Fig. 2.4, we extract the initial contour C_i of the tumor segmentation within the tumor tissue. The proposed method can be adapted to detect multimodal tumors by detecting the two maxima's two positions of the In-phase component peaks.

The output results of the OSH optical process are digitally implemented to extract the following parameters: c the center of the tumor, L the amplitude of the In-phase component peak, and C_i the initial contour formed using the principal in Fig. 2.5. the suggested method detects tumor tissue and facilitates the energy calculation of active contours. Using the initially detected contour C_i, we calculate the averages of the image $I(x, y)$ inside C_i and outside C_i to define the active contour model:

$$\mathrm{E_{i,j}} = \alpha.\mathrm{C_{i,j}} + \beta.\left|\mathrm{I} - \mathrm{M_{i,j}}\right|^2 + \gamma.\left|\mathrm{I} - \mathrm{m_{i,j}}\right|^2, \tag{2.11}$$

where $\alpha = \beta = \gamma = 1$ are fixed parameters. $\mathrm{C_{i,j}}$ is the initial contour detected by the proposed method. $\mathrm{m_{i,j}}$ is the average of the input RM image $I(x, y)$ inside the initial contour $\mathrm{C_{i,j}}$. $\mathrm{M_{i,j}}$ is the average of the input RM image $I(x, y)$ outside the initial contour $\mathrm{C_{i,j}}$. Besides, the evolution of the initial contour detected by the OSH system is realized through the programming of the proposed active contour pattern, based on finite differences obtained after linearization and discretization of the equation energy (2.11).

In our system in Fig. 2.3, the phase component enables us to extract the phase current after line-by-line scanning of the object images, as shown in Fig. 2.4. The maximum values characterizing this output are called phase component peaks. Contours delimiting these peaks are drawn, creating the regions of interest within the tumor tissue.

As the decision of the existence of a brain tumor on an MR image is based on the parameter L, we have studied L values for MR images of healthy and tumor brains. Fig. 2.6 represents the statistical distribution of the L parameter in the two cases mentioned. Evidently, in the case of the tumor, L values are large compared to the healthy brain. In the images of healthy brains, the average L in the images used was 110, and in the images of brain tumors was 325. It should be noted that the maximum peaks of In-phase components given by the OSH process, which localized the tumors, were within the margin of $[300; 350]$. This margin increases to over 255 due to the multiplication of the MRI images in equation 10. Moreover, due to the uniform distribution of pixel intensity in images of the healthy brain, all the maximum peaks of the In-phase component in cases of healthy brains being within $[100; 120]$. Therefore, the parameter L given by the OSH process is a reliable parameter to decide the existence of a tumor in the MR images.

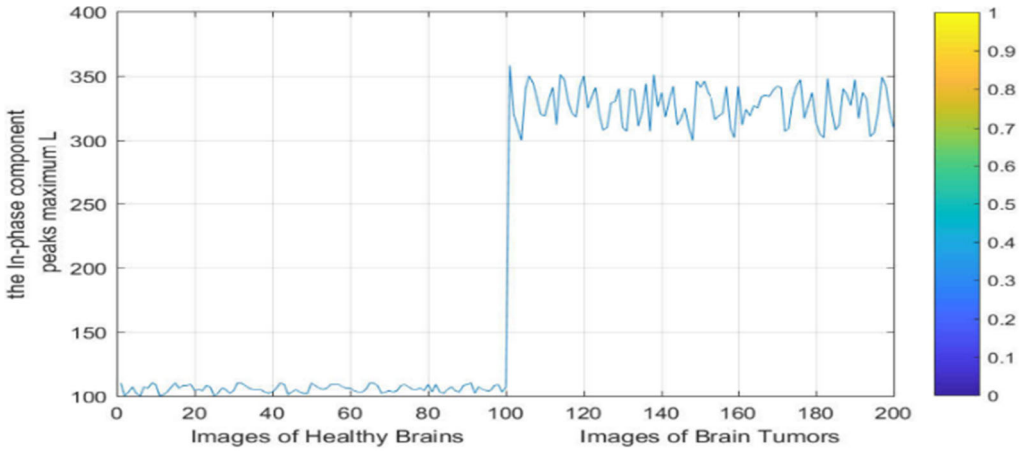

Fig. 2.6. Distribution of the L parameter in the healthy and tumorous brain images.

Similarly, the brain tumor position's decision is based on the parameter c given by the OSH. Therefore, we have estimated the precision of the proposed method regarding the detection of c inside of the tumor tissue. As a comparison, we have also calculated the percentage rate of the potential field segmentation (PFS) algorithm in [49] regarding tumor centers' detection. This approach is founded on potential field analogy in detecting brain tumors by assuming the intensity of a pixel as a mass, creating a potential field. It should be pointed out that the center used is obtained from the maximum peaks of the In-phase component. Table 2.1 reveals the high accuracy of detecting the center of the tumor tissue by the proposed method. In 98.5 % of the patients (from both databases), the maximum peaks of In-phase components given by the proposed method are located in the tumor tissue center. In the remaining 1.5 %, the OSH returned parameter c to the border of this tumor. Two principal reasons explain these results; firstly, owing to the modalities used in MR images to separate tumors from healthier tissue, contrast provides an almost unique signature for each type of tissue, particularly the type of tumor, which appears in most cases with the white color. Secondly, the high value of the maximum peaks of the In-phase component in tumoral regions. Therefore, the proposed method is a promising technique for detecting anomalous tissue in MR images, comparing with recently published methods. The proposed method is more accurate and quicker. It should be noted that the center used is determined by the maximum peak of the In-phase component.

Table 2.1. Percentage of the proposed method in terms of the c parameter return within the tumor tissue and the meantime, comparing to the method in [49].

Method	**Accuracy (%)**			**Time average (seconds)**
	Inside tumor	**Edge tumor**	**Outside tumor**	
Potential Field [29]	95 %	0	5 %	38.1643
Proposed method	98.5 %	1.5 %	0 %	0.2009

2.3.2. Evaluation of Segmentation Phase

Following our previous works [41-47], we explored the use of OSH in automatizing tumor tissue detection in MRI, enhanced framework for optical scanning holography (OSH) to detect abnormal tissue regions Fig. 2.7. We improve [41] in terms of acquisition speed, accuracy, and data size. In addition, the Generalized Optical Scanning Holography (GOSH) of recording holographic information is advantageous as on-axis holograms are acquired simultaneously, unlike standard phase-shifting holography where their holograms are acquired sequentially. To test the last proposed method in a very demanding way and link it to clinical imaging applications, we have used 20 images of patients with the most challenging segmentation conditions. These images contain different shapes, sizes, and contrasts of tumors, Tables 2.2 compare the performance reported from these 20 images and reached by the GOSH method with the Geodesic Active Contour model (GAC) [50], the Localized Active Contour (LAC) [51], the Active Contours by Cuckoo Search (ACCS) [52] and our previous work [41]. Compared to other ACMs, the proposed method performs better in terms of Sen, D, H, and Spe parameters. For evidence, the sensitivity value of 0.9961 reached by the proposed method was the highest obtained, and its Hausdorff distance of 2.0000 was the lowest. Besides, its highest average specificity value of Spe = 1.0000 indicates that it can correctly classify healthy tissue more than other ACM-based methods. It should be noted that the highly efficient performance of all methods in terms of the Spe parameter is explained by the fact that all the initial contours detected by the proposed OSH technique are located inside the tumor tissue. Following these methods' development, the optimal segmentation contours remain inside the tumor tissue, making the FP parameter very close to zero.

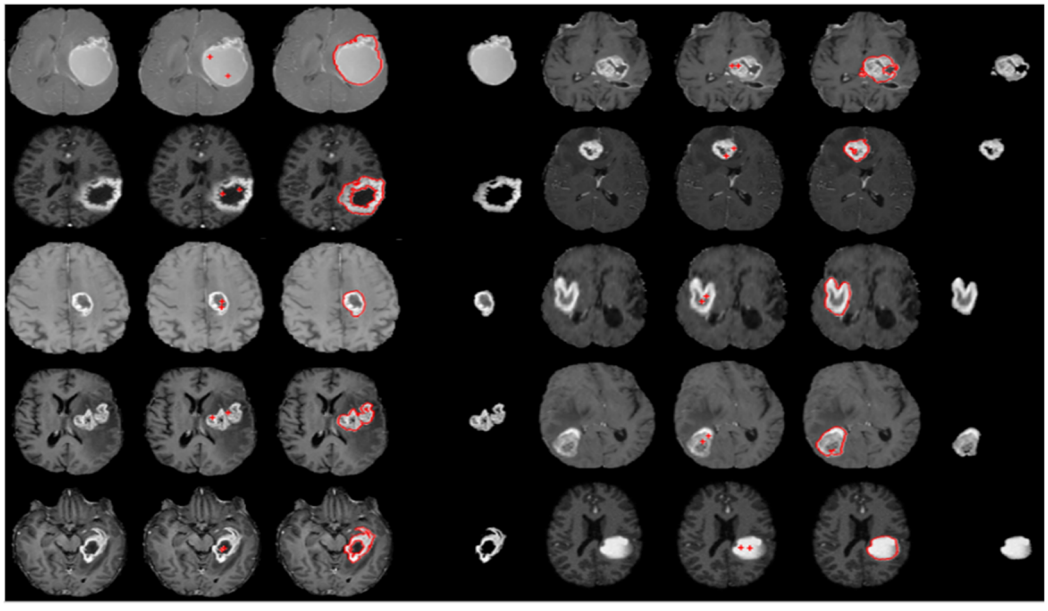

Fig. 2.7. Segmentation Results by Our Method on BRATS 2012 and 2013 Databases.

Also, it can be observed from Table 2.2 shows that our proposed method [47] reduces the calculation time (in seconds) as illustrated in Fig. 2.8, our method achieves a reduction in computation time compared to existing methods (expressed in seconds). The OSH method is faster compared to our previous approach because it recognizes the initial tumor contour in real time, which reduces the computational time required to evolve the active contour.

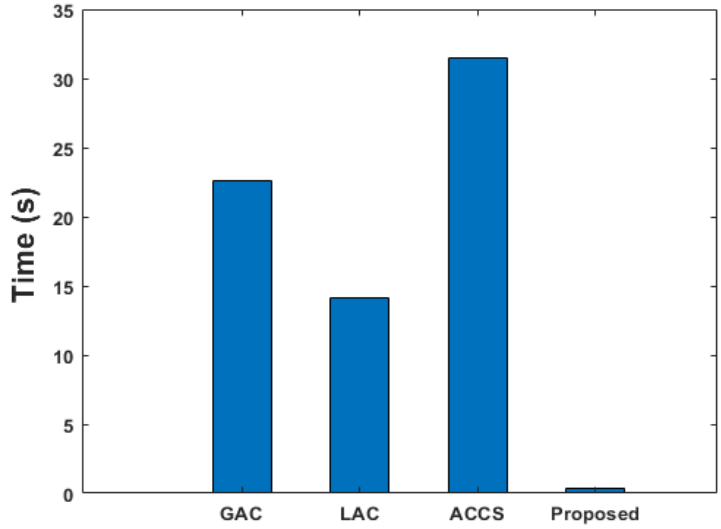

Fig. 2.8. Evaluation of Computation Time: Comparing Geodesic Active Contour, Localized Active Contour, Active Contour with Cuckoo Search, OSH-ACM, and the Proposed Method.

2.3.3. Evaluation of Reconstruction Phase

This new technique improves computational efficiency and pixel selection accuracy, which are essential for the reconstruction of 3D object shapes. The results of 3D object image reconstruction, based on real patients' dataset, are shown in Table 2.3.

The data, in Table 2.3, enable us to obtain the tumor volume for each patient with very respectable accuracy, making it easier to estimate the degree of cancer. These tables also provide useful information such as brain volume and mean intensity for each patient label (brain label and tumor label). The 3D reconstruction of the brain tumor is based on a given set of two-dimensional brain slices. The tumor areas of interest were extracted by the improved process of optical scanning holography (OSH) by extracting the maximum phase component, and the application, at the same time, of an active contour model (ACM) for faster segmentation of the region corresponding to the tumors in each slice. The results of this reconstruction are shown in Fig. 2.9.

Table 2.2. Sensitivity, Dice, Hausdorff distance, Specificity, and elapsed time rates obtained from the optimal contour of the BRATS 2012 databases images reached by using the Geodesic Active Contour (GAC), the Localized Active Contour (LAC), the Active Contour driven by Cuckoo Search (ACCS), our previous work (OSH-ACM) and our proposed method (Proposed).

Patients	Method	Sen	D (AVG±SDx10^{-4})	H_d	Spe	Time (s)
Patient 1 (BRATS 2012)	GAC	0.7194 ±1.2	0.7650±6.3	4.1200 ±2.6	0.9945±0.0	14.9945±1.2
	LAC	0.9016 ±2.6	0.9482±3.3	2.7488 ±2.6	0.9975±2.3	14.2406±1.9
	ACCS	0.9502 ±7.5	0.9495±9.0	2.6488 ±5.2	0.9980±1.0	48.1200±2.0
	OSH-ACM	0.9772 ±0.5	0.9838±0.3	2.0458 ±0.0	0.9987±4.5	0.2937±3.1
	Proposed	0.9809 ±0.7	0.9896±0.1	2.0402±0.1	0.9989±2.5	0.2463±2.1
Patient 2 (BRATS 2012)	GAC	0.7844 ±0.0	0.7377 ±4.2	4.3589 ±6.1	0.9903 ±4.5	26.1737 ±2.5
	LAC	0.8250 ±5.4	0.9041 ±4.8	4.0010 ±2.0	0.9957 ±2.8	17.1943 ±9.5
	ACCS	0.9347 ±1.5	0.9605 ±0.8	3.0050 ±2.5	0.9989 ±1.1	46.9430 ±9.0
	OSH-ACM	0.9752 ±0.2	0.9753 ±0.1	2.1623 ±0.0	0.9980 ±0.0	0.3540 ±7.2
	Proposed	0.9879 ±0.4	0.9802 ±0.6	2.1597 ±0.2	0.9987 ±0.1	0.3232 ±8.2
Patient 3 (BRATS 2012)	GAC	0.6804 ±6.3	0.7489 ±5.6	5.7823 ±2.4	0.9902 ±0.3	27.7494 ±2.8
	LAC	0.6715 ±2.3	0.8417 ±5.3	4.8990 ±7.5	0.9914 ±0.0	17.3898 ±7.0
	ACCS	0.9274 ±3.8	0.9410 ±4.1	3.5560 ±7.1	0.9992 ±0.9	59.2705 ±2.7
	OSH-ACM	0.9898 ±0.1	0.9897 ±0.1	2.0623 ±1.0	1.0000 ±0.1	0.2530 ±3.8
	Proposed	0.9899 ± 0.0	0.9898 ±0.0	2.0596 ±3.0	1.0000 ±0.1	0.2498 ±2.4
Patient 4 (BRATS 2012)	GAC	0.5751 ±3.7	0.6456 ±0.1	4.1231 ±8.7	0.9976 ±1.7	37.9528 ±8.7
	LAC	0.6346 ±2.0	0.7765 ±1.0	4.3589 ±5.7	0.9950 ±4.6	17.6072 ±8.0
	ACCS	0.8892 ±3.9	0.9395 ±1.0	3.3940 ±3.3	0.9989 ±7.4	25.7492 ±5.4
	OSH-ACM	0.9867 ±0.1	0.9834 ±0.1	2.0056 ±1.0	0.9997 ±0.7	0.2212 ±1.5
	Proposed	0.9884 ±0.0	0.9905 ±0.6	2.0024 ±5.0	0.9999 ±0.2	0.2200 ±1.0
Patient 5 (BRATS 2012)	GAC	0.7247 ±3.4	0.6902 ±2.8	5.7958 ±3.9	0.9906 ±5.5	22.1867 ±9.6
	LAC	0.7678 ±2.0	0.7243 ±0.0	4.0001 ±1.0	0.9907 ±0.5	16.6965 ±0.8
	ACCS	0.9192 ±2.1	0.9380 ±0.2	3.5437 ±1.0	0.9984 ±6.6	18.4792 ±0.8
	OSH-ACM	0.9894 ±0.2	0.9757 ±0.1	2.5826 ±1.0	0.9997 ±4.4	0.2165 ±2.6
	Proposed	0.9899 ±0.1	0.9864 ±0.2	2.459 ±3.0	0.9997 ±0.3	0.2130 ±0.6
Patient 6 (BRATS 2012)	GAC	0.7800 ±5.4	0.8096 ±1.7	3.0010 ±2.0	0.9950 ±2.2	9.3899 ±7.4
	LAC	0.7473 ±0.3	0.7181 ±0.1	3.0000 ±0.0	0.9975 ±7.9	10.5313 ±0.9
	ACCS	0.9247 ±2.0	0.9400 ±2.3	2.8947 ±9.7	0.9998 ±2.3	15.3692 ±5.0
	OSH-ACM	0.9898 ±1.7	0.9887 ±1.2	2.0620 ±0.0	0.9995 ±3.8	0.1730 ±2.6
	Proposed	0.9902 ±0.8	0.9942 ±5.8	2.0329 ±0.5	0.9998 ±9.7	0.1710 ±4.6
Patient 7 (BRATS 2012)	GAC	0.5154 ±0.4	0.6069 ±0.4	5.3852 ±0.0	0.9963 ±2.7	26.4020 ±4.0
	LAC	0.6850 ±0.4	0.6436 ±0.2	4.9904 ±0.3	0.9975 ±7.0	14.1543 ±6.6
	ACCS	0.8995 ±1.2	0.9364 ±5.6	2.9634 ±2.3	0.9986 ±0.9	28.3751 ±5.9
	OSH-ACM	0.9789 ±1.5	0.9871 ±1.1	2.0458 ±0.0	0.9997 ±0.0	0.1356 ±1.8
	Proposed	0.9808 ±5.6	0.9894 ±6.2	2.0389 ±1.0	0.9996 ±0.0	0.1310 ±2.9
Patient 8 (BRATS 2012)	GAC	0.5471 ±0.4	0.5565 ±0.3	5.8990 ±1.0	0.9904 ±0.5	24.9600 ±1.3
	LAC	0.7693 ±0.6	0.7895 ±0.5	4.3852 ±1.0	0.9985 ±2.8	16.8878 ±1.0
	ACCS	0.9599 ±0.6	0.9601 ±4.0	2.7945 ±0.0	0.9950 ±3.3	36.7810 ±1.8
	OSH-ACM	0.9886 ±2.4	0.9749 ±1.0	2.0827 ±1.1	0.9987 ±4.6	0.1321 ±3.6
	Proposed	0.9888 ±1.4	0.9780 ±2.0	2.0684 ±2.5	0.9996 ±2.4	0.1329 ±4.7
Patient 9 (BRATS 2012)	GAC	0.6878 ±0.2	0.6558 ±0.0	5.0915 ±0.2	0.9967 ±0.0	15.7585 ±4.5
	LAC	0.8095 ±0.0	0.8947 ±0.1	3.1623 ±2.0	0.9974 ±7.7	8.5422 ±8.9
	ACCS	0.9097 ±3.0	0.8997 ±0.4	3.1597 ±5.3	0.9988 ±9.6	17.1467 ±2.4
	OSH-ACM	0.9877 ±1.4	0.9782 ±0.5	2.1284 ±0.0	0.9996 ±0.8	0.1879 ±0.3
	Proposed	0.9899 ±0.9	0.9842 ±0.2	2.0084 ±0.2	0.9997 ±1.5	0.1479 ±1.9
Patient 10 (BRATS 2012)	GAC	0.5499 ±0.3	0.4998 ±0.1	6.7823 ±0.0	0.9945 ±9.1	20.8182 ±6.2
	LAC	0.6867 ±0.3	0.6577 ±0.1	5.1644 ±0.1	0.9959 ±2.2	8.0357 ±9.8
	ACCS	0.9002 ±4.2	0.9147 ±2.5	2.9846 ±7.3	0.9979 ±0.4	18.7666 ±0.0
	OSH-ACM	0.9868 ±1.0	0.9786 ±0.2	2.0628 ±1.0	0.9997 ±2.0	0.2429 ±4.7
	Proposed	0.9961 ±6.0	0.9882 ±4.2	2.0304 ±9.0	0.9997 ±0.0	0.2099 ±8.2

Table 2.3. 3D Segmentation results of real patient data from the BRATS 2019 database.

Patients	Labels	Voxel count	Volume (mm^3)	Intensity Mean ±SD
Patient 1	Clear Label	8 812 673	8.812673×10^6	32.4629 ± 76.7841
	Label with tumor	115 327	1.15327×10^5	434.7898 ± 75.9586
Patient 2	Clear Label	8 908 742	8.908742×10^6	31.0648 ± 66.3003
	Label with tumor	19 258	1.9258×10^4	424.8549 ± 65.4917
Patient 3	Clear Label	8 896 112	8.896112×10^6	24.4006 ± 649036
	Label with tumor	31 888	3.1888×10^4	451.9312 ± 57.2040
Patient 4	Clear Label	8 893 509	8.893509×10^6	36.5984 ± 90.5500
	Label with tumor	34 491	3.4491×10^4	1137.5650 ± 202.0132
Patient 5	Clear Label	8 874 450	$8.874450\ x10^6$	34.4983 ± 78.4227
	Label with tumor	53 550	5.3550×10^4	432.8664 ± 75.4400
Patient 6	Clear Label	8 815 463	$8.815463\ x10^6$	31.0447 ± 74.2778
	Label with tumor	112 537	1.12537×10^5	451.1814 ± 65.6239
Patient 7	Clear Label	8 800 705	8.800705×10^6	21.7560 ± 56.5531
	Label with tumor	127 295	1.27295×10^5	305.4569 ± 57.3601
Patient 8	Clear Label	8 872 783	8.872783×10^6	29.3676 ± 68.4357
	Label with tumor	55 217	5.5217×10^4	334.1023 ± 48.2186
Patient 9	Clear Label	8 920 644	8.920644×10^6	11.8151 ± 32.1527
	Label with tumor	7 356	7.356×10^3	198.0174 ± 38.5634
Patient 10	Clear Label	8 911 678	8.911678×10^6	23.9592 ± 59.2099
	Label with tumor	16 322	1.6322×10^4	454.6847 ± 83.4070
Patient 11	Clear Label	8 900 834	8.900834×10^6	35.1428 ± 75.6676
	Label with tumor	27 166	2.7166×10^4	344.4761 ± 46.2303
Patient 12	Clear Label	8 833 615	8.833615×10^6	64.3847 ± 39.4228
	Label with tumor	94 385	9.4385×10^4	580.9401 ± 36.3711
Patient 13	Clear Label	8 876 743	8.876743×10^6	68.8470 ± 153.2978
	Label with tumor	51 257	5.1257×10^4	698.3368 ± 120.9774
Patient 14	Clear Label	8 698 867	8.698867×10^6	25.9308 ± 57.5036
	Label with tumor	229 131	2.29131×10^5	304.6895 ± 70.7478
Patient 15	Clear Label	8 778 460	8.778460×10^6	44.1679 ± 112.9932
	Label with tumor	149 540	1.49540×10^5	442.8497 ± 45.4427
Patient 16	Clear Label	8 801 474	8.801474×10^6	18.6908 ± 43.6618
	Label with tumor	126 526	1.26526×10^5	241.1445 ± 36.7579
Patient 17	Clear Label	8 690 176	8.690176×10^6	16.6104 ± 39.7039
	Label with tumor	237 824	2.37824×10^5	213.0597 ± 45.3580
Patient 18	Clear Label	8 833 752	8.833852×10^6	16.8981 ± 43.7038
	Label with tumor	94 248	9.8248×10^4	270.6864 ± 44.3378
Patient 19	Clear Label	8 699 808	8.699808×10^6	16.7930 ± 41.8654
	Label with tumor	228 192	2.28192×10^5	227.5470 ± 37.6771
Patient 20	Clear Label	8 902 965	8.902965×10^6	47.3972 ± 115.0547
	Label with tumor	25 035	2.5035×10^4	477.4638 ± 28.0403

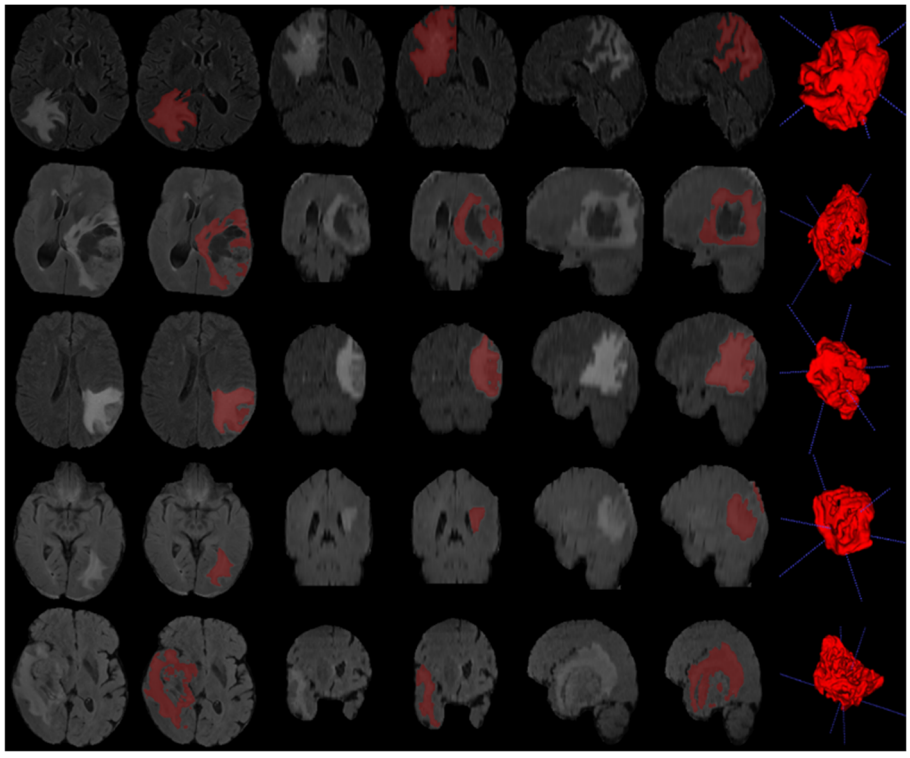

Fig. 2.9. 3-D reconstruction results of real patient data
from the MICCAI 2019-2020 databases.

2.4. Conclusion

In conclusion, this review underscores the significant advancements in our system for automating tumor tissue detection in MRI using Optical Scanning Holography (OSH). Our enhanced framework combines elements of in-line digital holography, a heterodyne fringe pattern, and the integration of an MR image display facilitated by a spatial light modulator (SLM). The result is a system that not only improves acquisition speed, accuracy, and data size but also introduces the concept of Generalized Optical Scanning Holography (GOSH), which allows the simultaneous acquisition of two on-axis holograms, reducing artifacts in reconstruction. This upgraded system takes advantage of line-by-line scanning with a cylindrical lens and leverages the precise collection of the outgoing phase component of the scanned current. This component reliably pinpoints the tumor's location, enabling faster and more accurate segmentation through an active contour model (ACM). The culmination of these advancements enables the reconstruction of 3D brain tumors from segmented regions of interest in each MRI slice. The continuous evolution of our system showcases its potential for significantly improving the efficiency and accuracy of tumor detection and segmentation in MRI, offering promising prospects for the medical field and underscoring the potential of holographic technologies in medical imaging.

Acknowledgment

We would like to express our gratitude to the organizers of the Brain Tumor Segmentation (BraTS) challenge for providing us with the BRATS 2019 and 2020 databases. These datasets are instrumental in our research and contribute significantly to our work in the field of medical image analysis. Thank you for your valuable support [29-31].

References

[1]. The International Cancer Genome Consortium, International network of cancer genome projects, *Nature*, Vol. 464, April 2010, pp. 993-998.

[2]. R. Ranjbarzadeh, A. B. Kasgari, S. J. Ghoushchi, S. Anari, M. Naseri, M. Bendechache, Brain tumor segmentation based on deep learning and an attention mechanism using MRI multi-modalities brain images, *Sci. Rep*., Vol. 11, Issue 1, 2021, 10930.

[3]. M. P. Arakeri, G. Ram Mohana Reddy, An Effective and Efficient Approach to 3D Reconstruction and Quantification of Brain Tumor on Magnetic Resonance Images, *International Journal of Signal Processing, Image Processing and Pattern Recognition*, Vol. 6, Issue 3, June 2013, pp. 111-128.

[4]. M. Bartels, M. Priebe, R. N. Wilke, S. Kruger, K. Giewekemeyer, S. Kalbfleisch, C. Olendrowitz, M. Sprung, T. Salditt, Low-dose three-dimensional hard x-ray imaging of bacterial cells, *Optical Nanoscopy*, Vol. 1, Nov 2012, 10.

[5]. K. Pawar, Z. Chen, N. Jon Shah, G. F. Egan, An Ensemble of 2D Convolutional Neural Network for 3D Brain Tumor Segmentation, in *Proceedings of the International MICCAI Brainlesion Workshop (BrainLes'19)*, 2019, pp. 359-367.

[6]. K. K. Al-Shayeh, M. S. Al-Ani, Efficient 3D Object Visualization via 2D Images, *International Journal of Computer Science and Network Security*, Vol. 9, Issue 11, Nov. 2009, pp. 234-239.

[7]. Q. K. Al-Shayea, M. S. Al-Ani, An Efficient Approach to 3D Image Reconstruction, *International Journal of Computer Science and Network Security*, Vol. 16, Issue 8, August 2016, pp. 35-41.

[8]. H. Khan, S. F. Alam Zaidi, A. Safi, S. Ud Din, A Comprehensive Analysis of MRI Based Brain Tumor Segmentation Using Conventional and Deep Learning Methods, in *Proceedings of the International Symposium on Intelligent Computing Systems (ISICS'20)*, 2020, pp. 92-104.

[9]. W.-W. Lin, C. Juang, M.-H. Yueh, T.-M. Huang, T. Li, S. Wang, S.-T. Yau, 3D brain tumor segmentation using a two-stage optimal mass transport algorithm, *Scientific Reports*, Vol. 11, 2021, 14686.

[10]. P. Li, W. Wu, L. Liu, F. M. Serry, J. Wang, H. Han, Automatic brain tumor segmentation from Multiparametric MRI based on cascaded 3D U-Net and 3D U-Net++, *Biomedical Signal Processing and Control*, Vol. 78, September 2022, 103979.

[11]. D. Gabor, A new microscopic principle, *Nature*, Vol. 161, 1948, pp. 777-778.

[12]. U. Schnars, W. Jüptner, Direct recording of holograms by a CCD target and numerical reconstruction, *Applied Optics*, Vol. 33, Issue 2, 1994, pp. 179-181.

[13]. W. Xu, M. H. Jericho, I. A. Meinertzhagen, H. J. Kreuzer, Digital in-line holography for biological applications, *Proceedings of the National Academy of Sciences*, Vol. 98, Issue 20, 2001, pp. 11301-11305.

[14]. J. Garcia-Sucerquia, W. Xu, S. K. Jericho, P. Klages, M. H. Jericho, H. J. Kreuzer, Digital in-line holographic microscopy, *Applied Optics*, Vol. 45, Issue 5, 2006, pp. 836-850.

[15]. E. Cuche, F. Bevilacqua, C. Depeursinge, Digital holography for quantitative phase-contrast imaging, *Optics Letters*, Vol. 24, Issue 5, 1999, pp. 291-293.
[16]. B. Rappaz, P. Marquet, E. Cuche, Y. Emery, C. Depeursinge, P. J. Magistretti, Measurement of the integral refractive index and dynamic cell morphometry of living cells with digital holographic microscopy, *Optics Express*, Vol. 13, Issue 23, 2005, pp. 9361-9373.
[17]. B. Kemper, G. von Bally, Digital holographic microscopy for live cell applications and technical inspection, *Applied Optics*, Vol. 47, Issue 4, 2008, pp. A52-A61.
[18]. N. Demoli, D. Vukicevic, M. Torzynski, Dynamic digital holographic interferometry with three wavelengths, *Optics Express*, Vol. 11, Issue 7, 2003, pp. 767-774.
[19]. J. Zhao, H. Jiang, J. Di, Recording and reconstruction of a color holographic image by using digital lensless Fourier transform holography, *Optics Express*, Vol. 16, Issue 4, 2008, pp. 2514-2519.
[20]. P. Tankam, P. Picart, D. Mounier, J.-M. Desse, J. C. Li, Method of digital holographic recording and reconstruction using a stacked color image sensor, *Applied Optics*, Vol. 49, Issue 3, 2010, pp. 320-328.
[21]. F. Charrière, J. Kühn, T. Colomb, F. Montfort, E. Cuche, Y. Emery, K. Weible, P. Marquet, C. Depeursinge, Characterization of microlenses by digital holographic microscopy, *Applied Optics*, Vol. 45, Issue 5, 2006, pp. 829-835.
[22]. J.-M. Desse, P. Picart, P. Tankam, Digital three-color holographic interferometry for flow analysis, *Optics Express*, Vol. 16, Issue 8, 2008, pp. 5471-5480.
[23]. P. Tankam, Q. Song, M. Karray, J.-C. Li, J.-M. Desse, P. Picart, Real-time three-sensitivity measurements based on three-color digital Fresnel holographic interferometry, *Optics Letters*, Vol. 35, Issue 12, 2010, pp. 2055-2057.
[24]. K. Kim, H. Yoon, M. Diez-Silva, M. Dao, R. R. Dasari, Y. K. Park, High resolution three-dimensional imaging of red blood cells parasitized by plasmodium falciparum and in situ hemozoin crystals using optical diffraction tomography, *Journal of Biomedical Optics*, Vol. 19, Issue 1, 2013, 011005.
[25]. F. Yaras, H. Kang, L. Onural, Real-time phase-only color holographic video display system using LED illumination, *Applied Optics*, Vol. 48, Issue 34, 2009, pp. H48-H53.
[26]. P.-A. Blanche, A. Bablumian, R. Voorakaranam, C. Christenson, W. Lin, T. Gu, et al., Holographic three-dimensional telepresence using large-area photorefractive polymer, *Nature*, Vol. 468, 2010, pp. 80-83.
[27]. J. Geng, Three-dimensional display technologies, *Advances in Optics and Photonics*, Vol. 5, Issue 4, 2013, pp. 456-535.
[28]. M. Kujawinska, T. Kozacki, C. Falldorf, T. Meeser, B. M. Hennelly, P. Garbat, W. Zaperty, M. Niemelä, G. Finke, M. Kowiel, T. Naughton, Multiwavefront digital holographic television, *Optics Express*, Vol. 22, Issue 3, 2014, pp. 2324-2336.
[29]. H. Mukawa, A full color eyewear display using holographic planar waveguides, *SID Dig*., Vol. 39, Issue 1, 2008, pp. 89-92.
[30]. C. Jang, C.-K. Lee, J. Jeong, G. Li, S. Lee, J. Yeom, K. Hong, B. Lee, Recent progress in see-through three-dimensional displays using holographic optical elements, *Applied Optics*, Vol. 55, Issue 3, 2016, pp. A71-A85.
[31]. I. Yamaguchi, T. Zhang, Phase-shifting digital holography, *Optics Letters*, Vol. 22, Issue 16, 1997, pp. 1268-1270.
[32]. I. Yamaguchi, J. Kato, S. Ohta, J. Mizuno, Image formation in phaseshifting digital holography and applications to microscopy, *Applied Optics*, Vol. 40, Issue 34, 2001, pp. 6177-6186.
[33]. F. Le Clerc, L. Collot, M. Gross, Numerical heterodyne holography with two-dimensional photodetector arrays, *Optics Letters*, Vol. 25, Issue 10, 2000, pp. 716-718.

[34]. E. Absil, G. Tessier, M. Gross, M. Atlan, N. Warnasooriya, S. Suck, M. Coppey-Moisan, D. Fournier, Photothermal heterodyne holography of gold nanoparticles, *Optics Express*, Vol. 18, 2010, pp. 780-786.

[35]. B. Samson, F. Verpillat, M. Gross, M. Atlan, Video-rate laser Doppler vibrometry by heterodyne holography, *Optics Letters*, Vol. 36, Issue 8, 2011, pp. 1449-1451.

[36]. T.-C. Poon, Three-dimensional image processing and optical scanning holography, *Advances Imaging & Electron Physics*, Vol. 126, 2003, pp. 329-350.

[37]. B. W. Schilling, T.-C. Poon, Real-time preprocessing of holographic information, *Opt. Eng.*, Vol. 34, Issue 11, Nov 1995, pp. 3174-3180.

[38]. G. Indebetouw, W. Zhong, D. Chamberlin-Long, Point-spread function synthesis in scanning holographic microscopy, *J. Opt. Soc. Am. A*, Vol. 23, Issue 7, Jul 2006, pp. 1708-1717.

[39]. X. Zhang, E. Y. Lam, Edge detection of three-dimensional objects by manipulating pupil functions in an optical scanning holography system, in *Proceedings of the IEEE 17th International Conference on Image Processing (ICIP'10)*, 2010, pp. 3661-3664.

[40]. Y. Momonoi, K. Taira, Y. Hirayama, Scan-type image capturing system using a cylindrical lens for one dimensional integral imaging, *Proceedings of SPIE*, Vol. 6490, 2007, 649017.

[41]. A. Essadike, E. Ouabida, A. Bouzid, Optical scanning holography for tumor extraction from brain magnetic resonance images, *Optics Laser Technology*, Vol. 127, 2020, 106158.

[42]. A. Essadike, et al., Optical based approach for brain tumor segmentation, in *Proceedings of the 1st International Conference on Innovative Research in Applied Science, Engineering and Technology (IRASET'20)*, 2020, pp. 1-5.

[43]. E. Ouabida, A. Essadike, A. Bouzid, Optical correlator based algorithm for driver drowsiness detection, *Optik*, Vol. 204, 2020, 164102.

[44]. A. Essadike, E. Ouabida, A. Bouzid, Brain tumor segmentation with Vander Lugt correlator based active contour, *Computer Methods and Programs in Biomedicine*, Vol. 160, 2018, pp. 103-117.

[45]. E. Ouabida, A. Essadike, A. Bouzid, Automated segmentation of ophthalmological images by an optical based approach for early detection of eye tumor growing, *Physica Medica*, Vol. 48, 2018, pp. 37-46.

[46]. E. Ouabida, A. Essadique, A. Bouzid, Vander Lugt Correlator based active contours for iris segmentation and tracking, *Expert Systems with Applications*, Vol. 71, 2017, pp. 383-395.

[47]. A. Cherkaoui, A. El-Ouarzadi, A. Essadike, A. Bouzid, Automatic Brain Tumor Detection, Segmentation Using Enhanced Optical Scanning Holography and Active Contour Model in MRI, *Sensors & Transducers*, Vol. 262, Issue 2, 2023, pp. 13-22.

[48]. A. Essadike, E. Ouabida, A. Bouzid, Medical Image Segmentation by Active Contour Improvement, *American Journal of Software Engineering and Applications*, Vol. 6, Issue 2, 2017, pp. 13-17.

[49]. I. Cabria, I. Gondra, MRI segmentation fusion for brain tumor detection, *Information Fusion*, Vol. 36, 2017, pp. 1-9.

[50]. V. Caselles, R. Kimmel, G. Sapiro, Geodesic active contours, *International Journal of Computer Vision*, Vol. 22, Issue 1, 1997, pp. 61-79.

[51]. E. Ilunga-Mbuyamba, J. G. Avina-Cervantes, A. Garcia-Perez, R. J. Romero-Troncoso, H. Aguirre-Ramos, I. Cruz-Aceves, C. Chalopin, Localized active contour model with background intensity compensation applied on automatic MR brain tumor segmentation, *Neurocomputing*, Vol. 220, 2017, pp. 84-97.

[52]. E. Ilunga-Mbuyamba, J. M. Cruz-Duarte, J. G. Avina-Cervantes, C. R. Correa-Cely, D. Lindner, C. Chalopin, Active contours driven by cuckoo search strategy for brain tumour images segmentation, *Expert Systems with Applications*, Vol. 56, 2016, pp. 59-68.

Chapter 3
Design, Simulation, and Initial Moldings of a Concave Polymer-based Diffractive Optical Element for Spectroscopy Applications

Matthias Haupt, Sebastian Smarzyk and Katharina Strathmann

3.1. Introduction

Diffractive Optical Elements (DOEs) are advanced optical components that utilize light diffraction to achieve specific light modulations. This technology finds a wide range of applications in fields such as telecommunications, sensing, medical technology, and illumination. DOEs allow for precise control over light distribution and direction, making them an indispensable tool in modern optical systems. With the growing demand for cost-effective and flexible optical solutions, polymer-based DOEs have gained significant research interest. Polymers offer several advantages, including low manufacturing costs, simple replication processes, and the ability to create complex three-dimensional structures. One of the key applications of DOEs is in spectrometry. Analyzing the optical spectrum of matter provides critical insights into its chemical and molecular composition. In various scenarios, such as analyzing food, blood, or pharmaceuticals, miniaturized mobile spectrometers can serve as efficient alternatives or valuable supplements to traditional stationary laboratory spectrometers. At Jade University of Applied Sciences in Wilhelmshaven, we are developing a miniaturized spectrometer under the "MiniSpectral" project. The primary goal of this project is to realize a polymer-based optic in a single manufacturing step using modern injection molding technology and innovative tools. This Chapter aims to provide a comprehensive overview of the fundamental functions and the current development status of the miniaturized spectrometer. The basic principles of the spectrometer were introduced at the Opal Conference 2024 [1] and in the corresponding conference proceedings. Additionally, the first steps in designing and fabricating a stamp suitable for hot embossing to create the DOE for the spectrometer was published in

Matthias Haupt
Jade University of Applied Sciences, Friedrich-Paffrath-Straße 101, 26389 Wilhelmshaven, Germany

Sensors & Transducers [2]. The first two sections of this Chapter will summarize the basic functionality of the spectrometer and provide an overview of the design, simulation, and fabrication of the initial master grating for the DOEs. Subsequent sections will discuss the first molding experiments using silicone and provide an outlook on the hot embossing process in PMMA.

3.2. Fundamental Principles of the Miniaturized Spectrometer

3.2.1. Spectral Analysis and Its Applications

Spectroscopy is a critical analytical method used to examine the interaction between light and matter, providing valuable insights into the chemical and molecular composition of a given sample. Through the analysis of light's spectral properties, it becomes possible to identify the composition of a material, making spectroscopy an essential tool in fields such as chemistry, physics, biology, and material science. Traditionally, spectrometers have been large, complex instruments predominantly used in laboratory settings for precise measurements. However, the demand for portable and miniaturized spectrometers has significantly increased in recent years due to advancements in material science, optical technologies, and manufacturing processes. These smaller spectrometers enable real-time, on-site analysis in diverse environments, such as quality control in food industries, medical diagnostics for blood analysis, and environmental monitoring. Miniaturized spectrometers, particularly those based on DOEs, offer the potential for cost-effective, portable, and highly adaptable solutions. These devices provide a practical alternative to their larger counterparts, combining flexibility with the precision necessary for real-world applications. As a result, miniaturized spectrometers are becoming essential tools in various domains, contributing to rapid, decentralized testing and diagnostics.

3.2.2. Basic Concept of the Spectrometer

As part of the "MiniSpectral" project at Jade University of Applied Sciences Wilhelmshaven, an innovative spectrometer is being developed based on the Rowland circle concept [3]. The primary goal of this project is to create a cost-effective, compact, and high-performance solution for spectral analysis, particularly suited for applications in health and environmental technologies. By utilizing polymer-based optical elements, the system is designed to be not only lighter and more flexible but also easier to integrate into various application scenarios. The core of this spectrometer is its three-dimensional dome-shaped optical component, which enhances light guiding efficiency, significantly improving the signal-to-noise ratio (S/N) [4]. This innovative geometry, in combination with a concave diffraction grating, allows the spectrometer to perform all essential functions efficiently, eliminating the need for conventional complex lens systems. The operation of the spectrometer is based on the interaction of light with these optical elements. Light enters the system through an input fiber, specifically a polymer-based optical fiber (POF), which guides the light into a polymer dome with a radius denoted as "r". At the far end of the dome is a mirrored concave diffraction grating with a radius of 2r. This grating disperses the incoming light into its individual wavelengths and reflects

it back into the dome. Due to the 2:1 radius ratio of the Rowland circle geometry, the dispersed light is focused onto the surface of the dome, where a detector array is placed to capture and analyze the decomposed light for spectral analysis [5]. For a clearer understanding of the system, Fig. 3.1 shows a detailed layout of the optical components, with dimensions provided in millimeters. The grating sphere has a radius of 20 mm, while the input dome has a radius of 10 mm. Although the grating is depicted as a spherical section, only a specific, finely calibrated portion of the surface will be covered with the diffraction grating material to optimize the interaction between the light and the grating for effective dispersion. The input dome, with a radius of 10 mm, serves as the light entry point. The light is coupled into the system using an optical polymer fiber, which ensures precise alignment and minimizes optical losses.

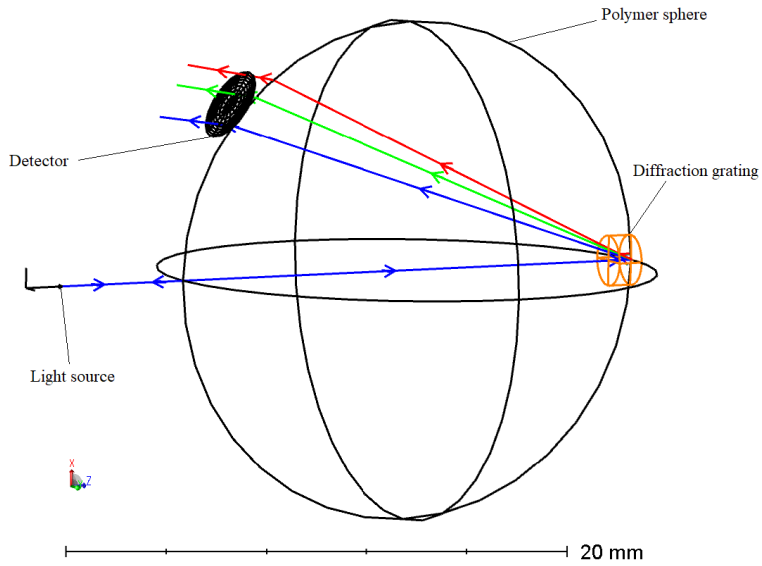

Fig. 3.1. The simulation was created with Ansys Zemax to illustrate the spectrometer concept: The optics of the spectrometer are based on a polymer-based dome with a radius of r. A mirrored grating is applied to this dome, featuring a curvature radius of 2r.

This coupling mechanism not only enhances the accuracy of the analysis but also simplifies the overall system design by eliminating the need for complex external optics. Additionally, the technical drawing includes a rectangular mounting bracket at the center of the structure, providing a robust integration point for incorporating the spectrometer into larger frameworks. This strategic design allows for easy handling and installation across a range of application scenarios. The “MiniSpectral” spectrometer presents a novel solution for spectroscopic applications, focusing on an efficient, compact, and cost-effective approach. The polymer-based dome and diffraction grating system streamline the manufacturing process while maintaining high optical performance for precise spectral measurements. Through advanced polymer materials and a well-engineered layout, the spectrometer offers a versatile platform that can be adapted

for various specific requirements in fields ranging from health diagnostics to environmental monitoring.

3.3. Design and Simulation of the Diffractive Optical Element

The design of a DOE for a miniaturized spectrometer presents a unique set of challenges and opportunities. The goal is to achieve high spectral resolution and efficiency while maintaining a compact form factor, low cost, and ease of manufacturing. In the context of the "MiniSpectral" project, a polymer-based concave DOE is utilized due to its ability to diffract and focus light, enhancing the performance of the miniaturized spectrometer. This section provides an in-depth overview of the design process, including the selection of design parameters, the simulation tools and methods employed, and the initial results of the optimization process.

3.3.1. DOE Design Parameters and Requirements

The design of the diffractive optical element must meet several critical performance criteria to be viable for use in the "MiniSpectral" spectrometer. Key design parameters include the wavelength range, diffraction efficiency, spectral resolution, and physical dimensions of the DOE. Each of these factors plays a crucial role in the overall performance of the spectrometer.

The DOE is designed to operate in the visible spectrum, typically from 400 nm to 700 nm. This range is chosen because it aligns with the most common applications of spectroscopy, such as analyzing chemical compositions, food safety, and medical diagnostics [6]. The material choice of the DOE, PMMA, supports high transparency within this wavelength range, making it ideal for polymer-based optical elements. One of the primary functions of the DOE is to efficiently diffract light over a wide range of angles, depending on the wavelength. Achieving high diffraction efficiency is essential to maximize the signal-to-noise ratio in the spectrometer and to ensure that the detected light is sufficiently strong for precise analysis. The surface structure of the DOE must be carefully optimized to achieve high efficiency, especially for the first diffraction order, which is the main contributor to the spectrometer's performance. Additionally, considerations have been made to explore the use of the second diffraction order, which could offer further enhancements in specific applications. The spectral resolution of the DOE-based spectrometer is directly related to the angular separation of different wavelengths of light after diffraction. In the case of a concave DOE, the geometry of the element helps to focus the diffracted light onto the detector, enabling high resolution while maintaining a compact optical path. The design process involves careful consideration of the grating period and the curvature of the DOE, as these factors influence the separation of spectral components. Since the spectrometer is miniaturized, the DOE itself must have small physical dimensions while still being capable of performing the necessary diffraction and focusing tasks. The compact design places additional constraints on the curvature and the spacing of the diffractive structures, as these need to be optimized for a short optical path without sacrificing performance. The DOE is designed to be fabricated using injection

molding, a process that allows for mass production at low cost. This requirement imposes limitations on the complexity of the surface features that can be reliably produced. The grating must have a structure that can be molded accurately, with a surface roughness that does not interfere with optical performance.

3.3.2. Simulation Methods and Software Tools

The design and simulation of the DOE for the "MiniSpectral" spectrometer require a combination of advanced optical simulation techniques to balance accuracy and efficiency. Due to the complexity of curved optical gratings, various mathematical models can be applied to simulate their behavior. Among these, methods like Finite Difference Time Domain (FDTD) and Finite Element Method (FEM) are commonly considered. However, Rigorous Coupled-Wave Analysis (RCWA) proves to be the most effective solution for this application, given its precision in solving Maxwell's equations while maintaining computational efficiency. Compared to FDTD and FEM, RCWA stands out for its accuracy, computational speed, and flexibility in handling various geometries and materials. These qualities make RCWA particularly well-suited for simulating complex curved grating systems such as the DOE used in the "MiniSpectral" spectrometer. By embedding RCWA within the Ansys Zemax environment using Dynamic Link Libraries (DLLs), we can dynamically adjust and simulate key parameters like the curvature radius and blazing of the grating. This integration enables efficient exploration of parameter spaces to fine-tune the optical performance of the spectrometer. The grating for the DOE in this design is anticipated to have a line density of up to 1000 lines/mm, with the objective of achieving a spectral resolution of less than 1 nm. This high line density is critical for separating closely spaced wavelengths, ensuring the spectrometer's capability to resolve fine spectral details. The overall layout and optical path of the spectrometer were modeled in Ansys Zemax OpticStudio, a leading ray tracing software used for designing intricate optical systems. Ansys Zemax enables simulation of light propagation through the entire spectrometer, including diffractive and refractive components. The software allows for precise modeling of how light interacts with the DOE, propagates through the system, and focuses onto the detector. The initial optical path simulation considered various combinations of wavelengths and radii, with a particular focus on the Rowland circle configuration. In the baseline configuration, the optical path was simulated for wavelengths of 400 nm, 550 nm, and 650 nm, with a Rowland circle radius of 10 mm. The grating, with a line density of 1000 lines/mm, was modeled with a reflective aluminum coating, chosen for its superior reflectivity in the visible spectrum [7]. An entrance aperture of 1 mm diameter was used, corresponding to the typical diameter of a standard polymer optical fiber (POF), ensuring compatibility with polymer-based light delivery systems [8].

The detailed behavior of the DOE, particularly its diffraction efficiency and angular separation of wavelengths, was modeled using RCWA. RCWA is a robust method for solving Maxwell's equations for periodic structures, such as the grating used in this DOE. It offers exceptional accuracy in predicting how light will be diffracted across various wavelengths, making it ideal for optimizing the grating's design parameters, such as line density, blazing angle, and curvature. The RCWA model allowed dynamic adjustments of

the DOE's parameters within the Zemax simulation, thanks to the use of DLLs. This approach enabled iterative tuning of key parameters, such as the curvature radius and line density, to achieve optimal diffraction efficiency and spectral resolution. By integrating RCWA calculations directly into Zemax's ray tracing framework, we ensured that the spectrometer's overall optical performance, including focusing and aberration control, was accurately simulated.

The combined use of ray tracing and RCWA simulations allowed for a comprehensive evaluation of the spectrometer system. RCWA was used to model the diffraction behavior of the DOE, calculating how different wavelengths are separated and how efficiently light is diffracted. The results were then fed into the Zemax ray tracing model, which simulated the light's propagation through the rest of the system and it focusing onto the detector. In this configuration, ray tracing simulations examined the influence of system-level factors such as the alignment of optical elements, aberration control, and the impact of dome diameter variations. This hybrid simulation approach was crucial in optimizing the overall system performance, particularly in achieving high spectral resolution and minimizing optical aberrations like spherical aberration. By combining RCWA and Zemax, we ensured a holistic understanding of both the DOE's microstructure and the macroscopic behavior of the spectrometer. Extensive parametric studies were conducted in Ansys Zemax to explore a wide range of design variables. These studies evaluated the performance of different grating materials, including aluminum, as the reflective coating for its high efficiency in the visible spectrum. Other parameters, such as the dome diameter and grating line density, were also varied to identify the optimal configuration for the desired performance. The simulations played a critical role in refining the design, particularly in achieving the targeted resolution of less than 1 nm. Adjustments to the grating curvature and blazing angles were explored to enhance spectral efficiency and optimize light collection at the detector. Additionally, parametric studies helped identify potential trade-offs, such as balancing resolution with diffraction efficiency or managing the size of the spectrometer versus its performance. These insights were vital in making informed design decisions and improving the overall system.

Fig. 3.2 shows the light path through the spectrometer. Compared to Fig. 3.1, the PMMA optics have been reduced and minimized in this view. This diagram illustrates the complete optical system, detailing how light enters the spectrometer, interacts with the DOE, and is subsequently focused onto the detector. The orange-highlighted section in the diagram represents the DOE, which plays the crucial role in diffracting and focusing the incoming light. The optical path demonstrates the interplay between the refractive and diffractive components within the compact design of the spectrometer, ensuring precise wavelength separation and efficient light collection.

In Fig. 3.3, the DOE itself is depicted in greater detail. This figure shows a visual representation of the DOE simulation in Zemax, utilizing the RCWA-DLL. The grid structure of the DOE is modeled layer by layer, with key design parameters such as a lattice constant of 1 μm, a blaze angle of 63°, and a grid depth of 0.5 μm. The RCWA simulation divides the DOE into 20 uniformly decreasing layers, systematically replicating the physical structure and optical properties of the grating.

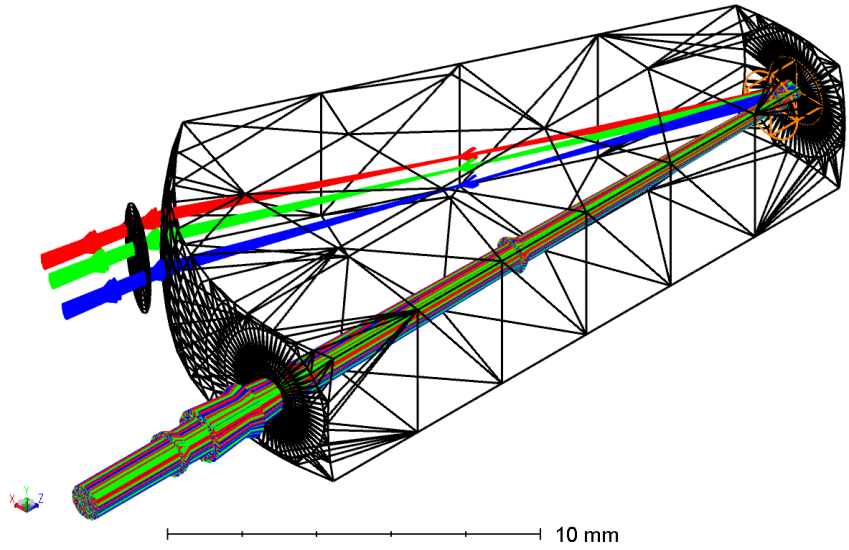

Fig. 3.2. Simulated optical path of the miniaturized spectrometer in Zemax for wavelengths of 400 nm, 550 nm, and 600 nm, focused on the reduced optics where rays of the first diffraction order are guided. The DOE, highlighted in orange, is responsible for diffraction and focusing.

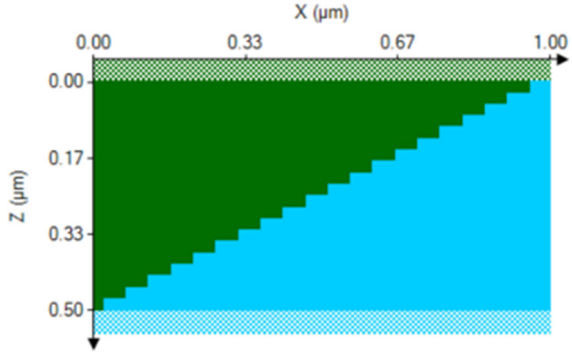

Fig. 3.3. Illustration of the optical grating simulation in Zemax using the Rigorous Coupled Wave Analysis Dynamic Link Library (RCWA DLL). The grating structure is modeled in a layer-by-layer approach, showcasing parameters such as a lattice constant of 1 µm, a blaze angle of 63°, and a grating depth of 0.5 µm. The simulation calculates 20 evenly decreasing layers to systematically replicate and validate the measured optical structures.

This detailed simulation allows for precise prediction of the diffraction efficiency and spectral resolution, validating the design and ensuring that the fabricated DOE will perform as expected. The combination of Figs. 3.1 and 3.2 provides a comprehensive view of both the system-level optical design and the microstructural details of the DOE, highlighting how these elements work together to achieve the desired performance in the spectrometer.

3.3.3. Challenges of Curved Gratings Compared to Flat Gratings in Polymer-based DOEs

Curved gratings in polymer-based DOEs introduce unique challenges but also offer distinct advantages over flat gratings, particularly in their ability to exploit focal effects. Unlike flat gratings, curved gratings are designed to focus light at specific points or along particular paths, enabling enhanced manipulation and control of light. This focal effect is especially beneficial in applications such as beam shaping, spectral focusing, and correcting optical aberrations. In the field of spectroscopy, curved gratings offer significant potential to improve the resolution and sensitivity of optical systems by precisely controlling the dispersion of light. Through careful adjustment of the grating's curvature and geometry, the dispersion characteristics can be optimized to achieve superior spectral resolution and efficiency. However, the fabrication of curved gratings in polymer-based DOEs presents notable challenges compared to flat gratings, primarily related to the complexity of the manufacturing processes. While flat gratings can be relatively straightforward to produce using standard techniques like photolithography or electron beam lithography on planar substrates, curved gratings demand more intricate approaches. A major difficulty lies in achieving precise and uniform curvature profiles across the polymer substrate. Traditional lithographic methods struggle to accurately pattern curved surfaces, which can result in deviations from the desired geometry and, consequently, reduced optical performance. To address these challenges, advanced manufacturing techniques such as nanoimprint lithography, hot embossing, and ultraprecision machining (UPM) have been developed. Nanoimprint lithography and hot embossing are particularly effective for replicating complex curvature profiles with high precision. These techniques allow for the mass production of curved grating structures, ensuring the accurate replication of both curvature and fine features. UPM, on the other hand, offers a direct machining solution for creating curved surfaces with submicron accuracy, making it an ideal method for fabricating high-precision optical elements. Despite the advancements in these manufacturing methods, challenges remain, particularly in terms of material compatibility and scalability. Ensuring that the polymer materials maintain their optical properties while undergoing the replication process is critical. Moreover, scaling these techniques for large-scale production can be difficult, as maintaining consistency in the curvature and feature replication becomes more complex. Overall, while curved gratings offer substantial advantages in terms of optical performance, their fabrication requires specialized techniques and careful attention to the limitations of existing methods. Continued developments in manufacturing technologies will be essential to fully harness the potential of curved gratings in polymer-based DOEs for applications such as spectroscopy.

3.4. Manufacturing and Characterization

Following the completion of simulations and preliminary laboratory tests, the production of the initial demonstrators will begin. The process starts with the fabrication of a planar stamp using UPM, a method that removes extremely thin layers of material with diamond tools. This technique allows for the creation of highly precise structures with

sub-micrometer tolerance deviations. The planar stamp will be used for initial replication methods, such as hot embossing, to test the viability of the grating structures. After successful tests with the planar stamp, UPM will be employed to manufacture a highly precise mold that will serve as the basis for the subsequent injection molding process. This mold will be used to form the polymer dome in a single process step, integrating the complex grating structures directly onto the surface. The demonstrators produced through these processes will be thoroughly examined and characterized in the laboratory. To verify the accuracy of the grating structures, an Atomic Force Microscope (AFM) will be used. AFM offers high-resolution imaging and precise nanometer-scale measurements, enabling detailed analysis of surface features. This validation step ensures that the manufactured gratings closely match the intended specifications with minimal deviations. The results will be compared to simulation data to further optimize the process. Building on these findings, the optical parameters and production workflows will be refined, leading to the next generation of miniaturized spectrometers. This iterative development process will focus on enhancing performance, reliability, and manufacturability. In parallel, advancements in material science and manufacturing technologies will be explored to push the limits of spectrometer miniaturization and functionality.

3.4.1. Fabrication of Initial Gratings in Nickel Phosphorus

Nickel-phosphorus is particularly advantageous for the fabrication of optical gratings due to its amorphous nature, which reduces scattering and interference effects, enabling the creation of high-precision gratings with minimal optical distortions. Its uniform refractive index across the surface of the grating ensures accurate dispersion of light into different wavelengths, which is critical for optical applications. Additionally, the material's mechanical stability and excellent chemical resistance enhance the durability of the gratings, making nickel-phosphorus an ideal choice for high-resolution optical elements [9]. Fig. 3.4 displays the planar nickel-phosphorus stamp, which features three distinct grating segments with lattice constants of 1 µm, 1.5 µm, and 2 µm. These segments were fabricated using UPM, a process that ensures high structural accuracy [10]. The stamp serves as the basis for initial replication processes, such as hot embossing, to test the performance of the grating designs. Each of the three grating segments underwent thorough analysis using AFM and Scanning Electron Microscopy (SEM). AFM provided precise measurements of surface topography, including pitch and depth, which are essential for assessing the optical functionality of the gratings. SEM analysis complemented these measurements by examining the internal structure and ensuring consistency across the grating surfaces.

Fig. 3.5 present the SEM and AFM images of the grating with a 1 µm lattice constant. AFM confirmed a depth of approximately 0.5 µm and precise pitch, while the SEM images revealed a uniform grating structure across a large area, demonstrating the robustness of the fabrication process. For the gratings with lattice constants of 1.5 µm and 2 µm (Figs. 3.6 and 3.7), similar results were obtained, with both SEM and AFM confirming structural consistency and precision. However, a slight undulation was observed at the apex of the grating grooves, which could potentially influence the optical performance. Further verification of the 60° blazing angle is required, as this parameter is

crucial for optimizing diffraction efficiency. Ensuring consistent blazing angle measurements will be an essential focus for refining the fabrication process and improving the optical performance of future grating designs.

Fig. 3.4. Displays the planar nickel-phosphorus stamp, featuring three distinct grating segments with lattice constants of 1 µm, 1.5 µm, and 2 µm, each with a blazing angle of 60°. These segments were produced using Ultra-Precision Machining (UPM); compare the angle and orientation of the grating grooves with Fig. 3.2.

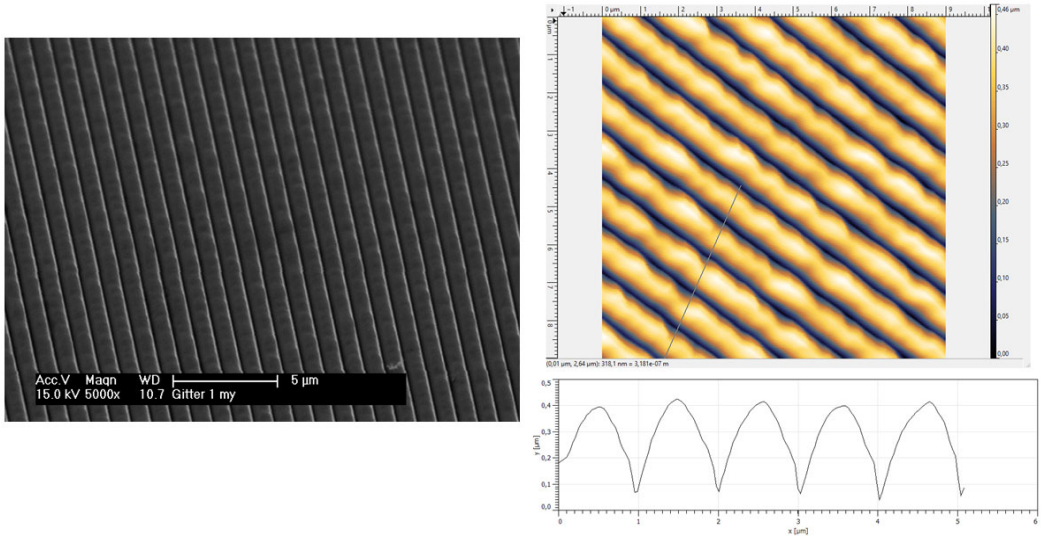

Fig. 3.5. Left: SEM image at 5000× magnification showing a grid structure with a precise 1 µm lattice constant, highlighting the uniformity and high-quality fabrication of the microscale pattern over a large area. Right: AFM image of the same grid structure, illustrating its 3D topography with evident surface fluctuations along the grooves, further confirming the 1 µm lattice constant.

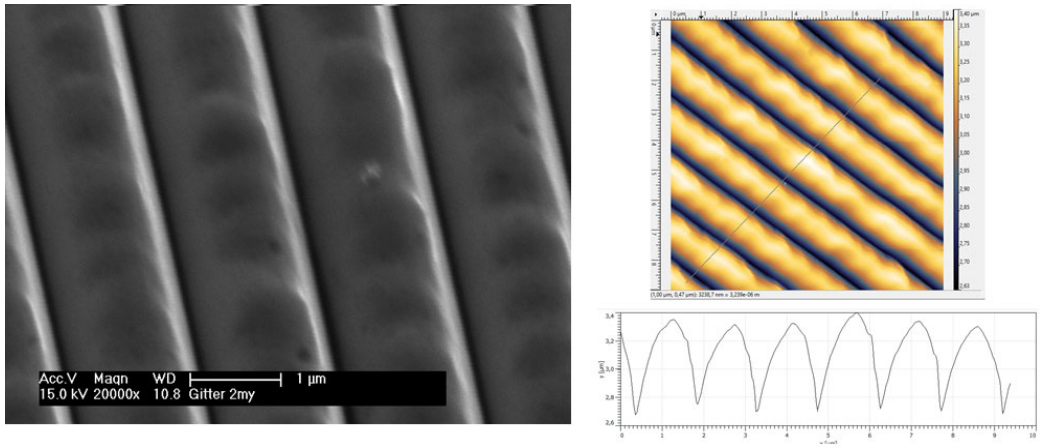

Fig. 3.6. Left: SEM image at 20000× magnification showing a grid structure with a precise 1.5 µm lattice constant, highlighting the uniformity and high-quality fabrication of the microscale pattern over a large area. Right: AFM image of the same grid structure, illustrating its 3D topography with evident surface fluctuations along the grooves, further confirming the 1.5 µm lattice constant.

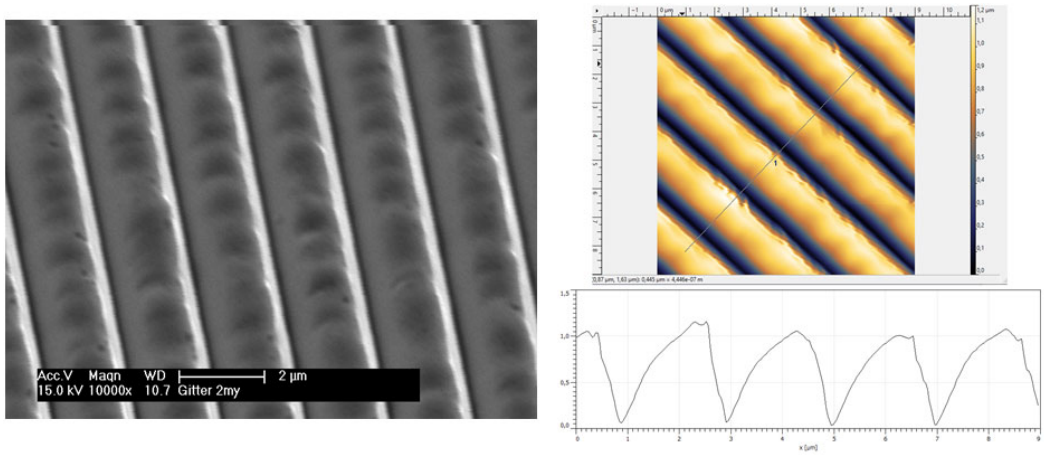

Fig. 3.7. Left: SEM image at 10000× magnification showing a grid structure with a precise 2 µm lattice constant, highlighting the uniformity and high-quality fabrication of the microscale pattern over a large area. Right: AFM image of the same grid structure, illustrating its 3D topography with evident surface fluctuations along the grooves, further confirming the 2 µm lattice constant.

3.4.2. First Molding Experiments Using Silicone

The next step involves transferring the fabricated nickel phosphorus grids into silicone molds. This process is essential to accurately replicate the intricate grid patterns. The grids are carefully embedded in the silicone, which captures the fine details of the nickel phosphorus structure due to its moldability. Once molded, the grids undergo thorough optical inspection to evaluate their diffraction properties as transmissive gratings. This analysis ensures that the silicone replication process accurately preserves the intended

diffraction orders and spatial characteristics of the original grids. After this transmissive examination, the grids are enhanced by coating them with a layer of silver. This silver coating serves to increase the reflectivity of the grids and provides additional durability, protecting against environmental factors and ensuring long-term optical performance. Once coated, the grids undergo further analysis using advanced microscopy techniques such as Scanning Electron Microscopy (SEM). This inspection ensures that the silicone molding process was precise and that the silver coating adheres uniformly across the grid surfaces, maintaining the necessary precision for optimal optical functionality. After confirming structural integrity and uniform coating, the grids are reevaluated for their optical properties, this time as reflective gratings. Reflectance efficiency, spectral response, and overall optical quality are carefully assessed during this phase. This evaluation is crucial to validate the grids' performance as reflective optical components for various optics and photonics applications. In conclusion, the process of transferring nickel phosphorus grids into silicone molds, followed by optical inspection, silver coating, and reflective evaluation, highlights the careful attention to detail necessary to ensure these grids perform reliably as high-quality optical components.

In Fig. 3.8, the left side shows the grid structures successfully molded into silicone and mounted in an optical holder, while the right side displays the illuminated grid. The 1 μm grid is irradiated with a 515 nm laser diode, and the separation of the individual diffraction orders is clearly visible. This demonstrates the precise replication of the grid structure in silicone. The distinct separation between the diffraction orders confirms the high fidelity of the silicone molding process, preserving the fine details of the original grid structure and verifying its suitability for optical applications.

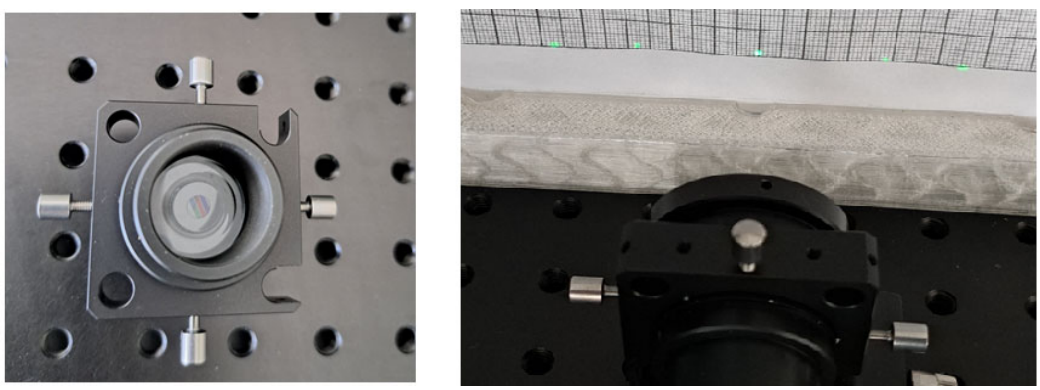

Fig. 3.8. Left: Grid structures molded into silicone and mounted in an optical holder; Right: 1 μm grid illuminated with a 515 nm laser diode, displaying distinct diffraction orders that confirm the high fidelity of the silicone replication process and the preservation of fine structural details.

3.4.3. Hot Embossing in PMMA

Hot embossing of Polymethylmethacrylate (PMMA) is an effective method for producing high-precision microstructures, especially when heated near its glass transition temperature (Tg). PMMA has a Tg of approximately 105-110° C, which enables it to enter

a viscoelastic state that allows fine structural replication without compromising the material's integrity. At this temperature, PMMA softens enough for precise molding while retaining sufficient strength, making it ideal for producing intricate microstructures essential for DOEs [11, 12]. Operating near Tg is critical, as PMMA below this temperature remains brittle and limits plastic deformation. Above Tg, PMMA transitions into a rubber-like state with viscoelastic properties that facilitate accurate embossing. Studies demonstrate that PMMA's behavior near Tg can be modeled by viscoelastic frameworks that incorporate multiple relaxation times and viscous deformation components, which are useful for structure replication in optical applications like spectroscopy. Precise control of temperature and pressure during embossing is essential to maintain consistent viscoelastic behavior, which allows for the accurate replication of complex microstructures with minimal defects [13]. Pressure is also essential, as it ensures that microstructures are fully transferred to the PMMA surface. Inadequate or uneven pressure can lead to incomplete embossing, particularly detrimental in high-resolution applications like optical gratings, where precision is paramount [14].

To implement the hot embossing of PMMA, a specialized aluminum mold was fabricated to fit the design requirements of the diffractive optical element. This mold serves as the primary form into which a precision-etched stamp is placed, designed to transfer the microstructure onto the polymer surface. During the embossing process, a PMMA sheet is placed atop this mold and then heated to a temperature slightly above its glass transition temperature, allowing the material to achieve the necessary viscoelastic state for accurate microstructure replication. This setup ensures that the embossed PMMA plate precisely captures the intricate details of the DOE design, creating a high-resolution optical component suited for spectroscopy and other advanced applications.

3.5. Conclusion and Outlook

This Chapter presents the initial design, simulation, and first molding trials of a concave polymer-based DOE intended for compact and efficient spectroscopy applications. By employing polymer materials and advanced simulation methods, the project addresses the need for cost-effective and portable spectroscopic solutions with high performance. The DOE's unique concave geometry, paired with advanced design parameters, has been optimized to deliver effective spectral dispersion and focus, making it suitable for use in miniaturized spectrometers. Using tools like Rigorous Coupled-Wave Analysis (RCWA) and ray tracing simulations in Ansys Zemax, key attributes such as grating line density, blaze angle, and curvature were finely tuned, achieving a high diffraction efficiency and a spectral resolution of under 1 nm. A significant achievement within this study has been the precise replication of initial DOE structures using a planar nickel-phosphorus stamp fabricated through ultra-precision machining. Nickel-phosphorus, known for its stability and minimal scattering, was utilized exclusively for this initial stamp due to its ability to create detailed and reproducible microstructures. These early molding trials used silicone to capture the grid pattern and validate replication fidelity. While these trials confirmed the structural potential of the DOE, they also underscored the limitations of planar stamps. Moving forward, a key goal will be the development and fabrication of a curved grating structure tailored to DOE applications, which is anticipated to further improve light

management and resolution in the final spectrometer design. The next phase will focus on manufacturing the concave DOE directly through methods such as hot embossing in PMMA and injection molding, aiming to streamline production for practical implementation. While hot embossing in PMMA has not yet been tested, it will be essential to validate this technique's effectiveness in reproducing the complex DOE structures and preserving surface fidelity. Injection molding offers additional advantages, as it supports scalable manufacturing and is particularly suited for the three-dimensional shaping required by the DOE. This progression from planar to curved gratings will be critical in aligning the DOE's design with the compact spectrometer requirements, providing high resolution within a small form factor. Further planned developments will enhance the integration of the DOE with sensor arrays to allow for real-time spectral analysis, facilitating diverse applications in fields such as environmental monitoring, food safety, and medical diagnostics. Additionally, implementing anti-reflective coatings and exploring new materials for the DOE could enhance overall efficiency and robustness. The ultimate objective is to advance from prototype demonstrations to a fully functional, commercially viable spectrometer that offers precise, rapid, and on-site spectral analysis. In summary, this project highlights the potential of polymer-based DOEs in miniaturized spectrometry. By refining both the manufacturing process and optical performance, this technology holds promise for broad application, bridging laboratory-grade precision with the accessibility and portability needed for modern, decentralized testing.

Acknowledgements

This Project is supported by the Federal Ministry for Economic Affairs and Climate Action (BMWK) on the basis of a decision by the German Bundestag.

References

[1]. M. Haupt, S. Smarzyk, K. Strathmann, Design and development of a miniature spectrometer for the visible wavelength region, in *Proceedings of the 7th International Conference on Optics, Photonics and Lasers (OPAL'24)*, 2024, pp. 58-61.

[2]. M. Haupt, S. Smarzyk, K. Strathmann, Design and development of a miniature spectrometer for the visible wavelength region., *Sensors & Transducers Journal*, Vol. 266, Issue 3, August 2024, pp. 1-8.

[3]. H. A. Rowland, On concave gratings for optical purposes, *American Journal of Science*, Vol. s3-26, Issue 152, 1883.

[4]. S. Höll, M. Haupt, U. H. P. Fischer, Design and development of an injection-molded demultiplexer for optical communication systems in the visible range, *Appl. Opt*., Vol. 52, 2013, pp. 4103-4110.

[5]. S. Smarzyk, et al., Entwicklung eines miniaturisierten Spektrometers für den optischen Wellenlängenbereich, online at https://www.dgao-proceedings.de/download/124/124_p5.pdf (in German).

[6]. D. A. Skoog, F. J. Holler, S. R. Crouch, Principles of Instrumental Analysis, *Cengage Learning*, 2018.

[7]. G. Hass, J. E. Waylonis, Optical constants and reectance and transmittance of evaporated aluminum in the visible and ultraviolet, *Journal of the Optical Society of America*, Vol. 51, Issue 7, 1961, 719.

[8]. K. Strathmann, O. Lass, S. Smarzyk, M. Haupt, Simulationsberechnungen eines Spektrometers mit Rowlandkreis und Simulation einer Eintrittsöffnung mit großer NA, Tagungsband der NWK 2023, https://www.hs-harz.de/dokumente/extern/Forschung/NWK2023/TagungsbandNWK2023.pdf (in German).

[9]. H. Nazari, G. Darband, R. Arefinia, A review on electroless Ni-P nanocomposite coatings: effect of hard, soft, and synergistic nanoparticles, *Journal of Materials Science*, Vol. 58, 2023, pp. 4292-4358.

[10]. W. B. Lee, B. C. F. Cheung, Surface Generation in Ultraprecision Diamond Turning: Modelling and Practices, *Wiley*, 2003.

[11]. G., Palm, R. B., Dupaix, J. Castro, Large strain mechanical behavior of poly(methyl methacrylate) (PMMA) near the glass transition temperature, *ASME. J. Eng. Mater. Technol*., Vol. 128, Issue 4, 2006, pp. 559-563.

[12]. P. Gilormini, L. Chevalier, G. Régnier, Thermoforming of a PMMA transparency near glass transition temperature, *Polymer Engineering and Science*, Vol. 50, Issue 10, 2010, pp. 2004-2012.

[13]. A. Ghatak, R. Dupaix, Material characterization and continuum modeling of poly (methyl methacrylate) (PMMA) above the glass transition, *Int. J. Struct. Chang. Solids. Mech. Appl*., Vol. 2. 2010, pp. 53-63.

[14]. Y. Xu, C. Wang, Y. Wang, J. Liu, Design and application of diffractive optical element: a review, *Proceedings of SPIE*, Vol. 12910, 2024, 129100O.

Chapter 4
Holotomography Approach for the Detection and Segmentation of Amoebas in Water Samples Using Active Contour

Anass Cherkaoui, Abdelaziz Essadike and Abdenbi Bouzid

4.1. Introduction

Holotomography is a technique that combines holography with tomography to create cross-sectional images of an object [1]. It involves capturing multiple holograms from different angles and using computer algorithms to reconstruct a three-dimensional image of the object [2]. This allows for detailed analysis of the object's internal structure and can be used to visualize objects that are transparent or otherwise difficult to image using other methods [3]. In biology, holographic tomography has been used to study the internal structure of cells and other biological samples, such as visualizing the three-dimensional structure of cells and their organelles and tracking the movement of molecules within cells. Overall, holographic tomography is a valuable tool for studying the internal structure of objects and has a variety of applications in biology and other fields.

Amoebas are a type of single-celled organism that are found in a variety of aquatic environments, including freshwater, marine, and soil. While most amoebas do not pose a significant threat to humans, some types of amoebas can cause serious infections if they enter the human body through the nose, mouth, or other openings. For example, the amoeba Naegleria fowleri, which is commonly found in warm freshwater environments, can cause a rare and often fatal brain infection called primary amebic meningoencephalitis (PAM) if it is inhaled through the nose. In addition to the dangers posed to humans, some types of amoebas can also be harmful to other aquatic organisms and can affect the overall quality of the water. It is important to be aware of the potential risks associated with amoebas and to take appropriate precautions to avoid exposure. Amoebas are a type of eukaryotic organism that are traditionally classified under the Kingdom Protista. They are characterized by their ability to change shape, a trait that is facilitated by their flexible cell walls. Some amoebas, such as Naegleria fowleri, are capable of entering the human body

Anass Cherkaoui
Hassan I University, Faculty of Science and Technology, Higher Institute of Health Sciences, Settat, Morocco

through the nose and feeding on neurons, leading to destruction of brain tissue. This type of amoeba is often referred to as the brain-eating amoeba, and it has a very high fatality rate of 97 %. It is important to be aware of the potential risks posed by this type of amoeba [4, 5].

Holotomography is a technique that combines holography with tomography (a method for creating cross-sectional images of an object) to create detailed, three-dimensional images of objects [2, 7]. It involves capturing multiple holograms of an object from different angles and using computer algorithms to reconstruct a three-dimensional image of the object's internal structure and properties [8]. Holographic tomography has a wide range of applications, including the study of biological samples such as cells and microorganisms [9, 10], as well as non-biological objects such as materials and engineering structures [11]. One of the key advantages of holographic tomography is that it is non-invasive and does not require the use of stains or chemical agents, making it a safe and reliable method for studying objects in their natural state [5]. In this paper, we will describe our use of holographic tomography to extract and segment amoebas from liquids.

The study of amoebas, single-celled organisms that are found in a variety of aquatic environments, is of great interest due to their diverse roles in ecosystems and their potential impacts on human health [1]. To accurately and precisely study the behavior and characteristics of amoebas, it is important to be able to extract and segment them from liquids, such as water samples. In this study, we used holographic tomography, a technique that involves capturing multiple holograms of an object from different angles and using computer algorithms to reconstruct a three-dimensional image [12], to extract and segment amoebas from liquids. By analyzing the three-dimensional images of the amoebas, we were able to study their size, shape, and movement in detail [9]. Holographic tomography is a non-invasive technique that does not require the use of stains or chemical agents, making it a safe and reliable method for studying amoebas in their natural habitat [12]. In this paper, we will describe our use of holographic tomography to extract and segment amoebas from liquids and discuss the benefits of this approach.

Overall, the use of holotomography technique to extract and segment amoebas from liquids allows for detailed, three-dimensional analysis of these organisms and can provide valuable insights into their behavior and characteristics. By visualizing and tracking the movement of amoebas in real-time, it is possible to study their interactions with their environment and understand how they may be affected by different factors. Additionally, the non-invasive nature of holographic tomography makes it a safe and reliable method for studying amoebas in their natural habitat. In the following sections, we will present our results and discuss the implications of our findings for the study of amoebas and their role in ecosystems and human health.

4.2. Materials and Methods

4.2.1. Experimental Setup

In our experimental setup, we harnessed the technique of holotomography to examine water samples containing amoebas. We initiated the process with a sophisticated doubled YAG laser, operating at a precise wavelength of 532 nm, characterized by an ultra-short pulse width of 10 nanoseconds and an impressive pulse energy of 100 millijoules. This powerful laser system played a pivotal role in capturing holograms of our water samples, with a unique twist. Rather than employing a traditional single-angle holography approach, we took a multi-angle approach. We recorded holograms at six specific angles: 0°, 30°, 60°, 90°, 120°, and 150°. This multi-angle strategy was instrumental in enhancing our holographic recordings by providing a comprehensive view of the amoebas within the water samples. It significantly boosted both the resolution and contrast of our holographic imagery. The key advantage of employing a pulsed laser in our setup lay in its ability to eliminate motion blur. As we recorded the dynamic water droplets containing amoebas, the pulsed laser's ultra-short duration ensured that even rapidly moving objects were imaged with precision, guaranteeing accuracy in the representation of amoebas. Subsequent to hologram acquisition, we took a post-processing approach. We meticulously extracted the phase component for each recorded slice based on our previous work [13-21]. The purpose of this phase extraction was to isolate the characteristic features of the amoebas. To achieve this, we turned to active contour theory. This advanced image segmentation technique proved highly effective in distinguishing the amoebas from the background, substantially enhancing the interpretability of the holographic data. Now, the heart of our approach lay in the application of holotomography. This technique allowed us to reconstruct detailed three-dimensional structural information and study the dynamic behaviors of the amoebas with an exceptional degree of precision. Holotomography, with its capacity for volumetric reconstruction, provided invaluable insights into the amoebas' morphology and their interactions within their aquatic environment. Lenses in our setup were instrumental in precisely directing and focusing the laser beam, ensuring optimal beam quality. Furthermore, a beam splitter and six CCD cameras, each equipped with its own lens, facilitated simultaneous hologram recording from multiple angles, enabling comprehensive imaging of amoebas within water samples. In summary, our experimental setup, which seamlessly integrated holotomography with a high-powered pulsed laser, multi-angle holographic recording, and advanced image segmentation techniques, enabled us to effectively extract and segment amoebas from water samples. This comprehensive approach offered a profound understanding of amoeba behavior, their intricate three-dimensional structure, and their interactions within their aquatic habitat, thus advancing our scientific analysis in the field.

4.2.2. Detection Phase

Fig. 4.2 showcases inline holograms of water samples containing amoebas recorded at various angles (0 degrees, 30 degrees, 60 degrees, 90 degrees, 120 degrees, and

150 degrees) using our experimental setup. These holograms were instrumental in our endeavor to detect the presence of amoebas through the phase component.

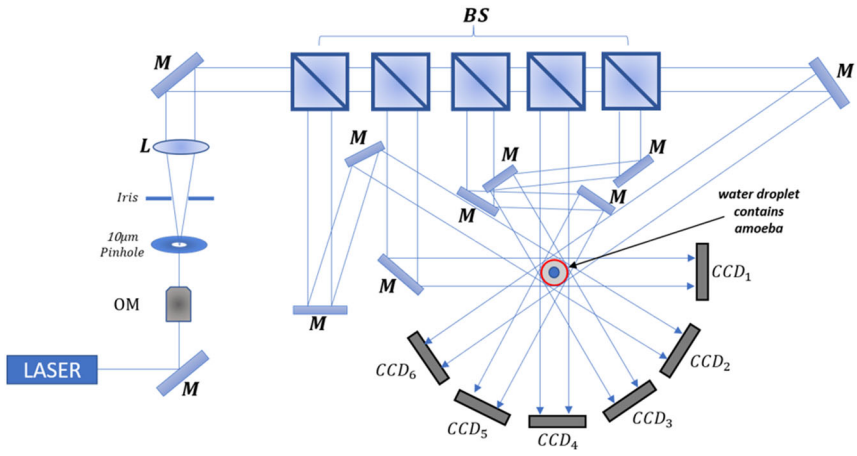

Fig. 4.1. Holotomography Setup for the detection Amoebas from Liquids samples.

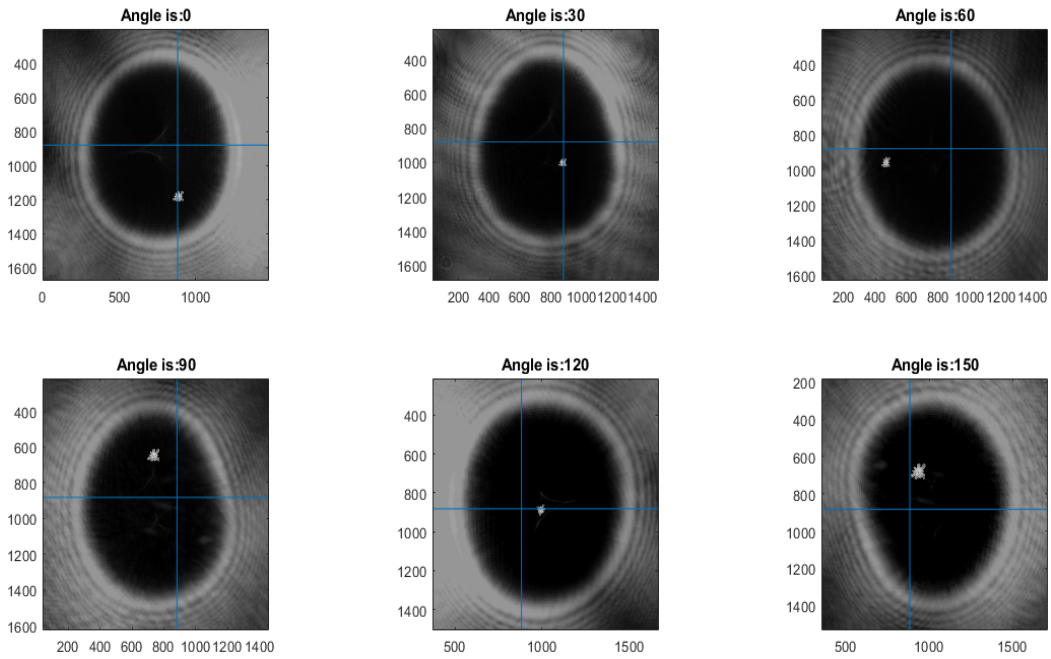

Fig. 4.2. Recorded Inline Holograms of Water Samples Containing Amoebas.

To elaborate on the scientific aspect, the detection of amoebas relied on the variation in the phase component caused by the refractive index differences between the amoebas and their surrounding water medium. The extraction of the phase component for each recorded

slice provided valuable data regarding these refractive index disparities, ultimately enabling the identification and localization of amoebas within the holograms. This phase-based detection approach not only offers high sensitivity but also allows for label-free and non-destructive analysis, making it a powerful tool in the realm of biological imaging and analysis.

The integration of holotomography with phase extraction techniques in our study represents a cutting-edge approach to the detection of amoebas in water samples. Holotomography provided us with the capability to acquire detailed three-dimensional information about the specimens. This technique was instrumental in capturing inline holograms from multiple angles, giving us a comprehensive view of the amoebas within the samples. Concurrently, phase extraction served as the key to unveil the amoebas within the holographic data.

Through phase extraction [15], we deciphered the specific phase changes induced by the presence of amoebas in the laser light. These phase variations were intricately linked to refractive index differences between the amoebas and the surrounding water medium. By combining holotomography and phase extraction, we could localize amoebas with a high degree of precision, leveraging the remarkable sensitivity of phase-based detection. The resulting combination allowed us to not only observe the three-dimensional structure of the amoebas but also accurately pinpoint their positions within the samples. This synergy between holotomography and phase extraction represents a significant advancement in biological imaging, providing a holistic approach for the detection, localization, and detailed study of amoebas in their natural aquatic habitat.

In Fig. 4.3, we delve into the critical phase of detection in our holographic tomography setup. This phase illustrates the results of our method applied to all the recorded slices at different angles. The primary objective here is to showcase the effectiveness and reliability of our proposed approach for detecting amoebas within liquid samples using our system. To understand this process scientifically, consider the object of interest as a small 3D structure situated at a distance "d" from the CCD camera. In our holographic tomography setup, we employ the Fresnel approximation formula, a well-established mathematical approach in optics. The core of this method involves utilizing an inverse Fourier-transform formula, as expressed in Equation (4.1). This mathematical procedure allows us to computationally reconstruct the holograms recorded at different angles, thereby generating a comprehensive view of the object's three-dimensional characteristics. In this case, it enables us to visualize and analyze the presence and location of amoebas within the liquid samples with a high degree of accuracy, highlighting the robustness of our detection method.

$$\begin{aligned}\Gamma(\xi,\eta) \;&=\; j\frac{1}{\lambda d}exp\left(-j\frac{2\pi d}{\lambda}\right)exp\left[-j\frac{\pi}{\lambda d}(\xi^2+\eta^2)\right]\times \\ &\times\int_{-\infty}^{+\infty}\int_{-\infty}^{+\infty}h(x,y)\,E_R^*(x,y)exp\left[-j\frac{\pi}{\lambda d}(x^2+y^2)\right]\times \\ \times\, exp\left[j\frac{2\pi}{\lambda d}(x\xi+y\eta)\right]dxdy \;&=\equiv \hat{z}(\xi,\eta)\Im_{x,y}[hE_R^*w]|_{k_x\,=\,2\pi\xi/\lambda d,k_x\,=\,2\pi\eta/\lambda d},\end{aligned} \tag{4.1}$$

where $\Im_{x,y}[hE_R^*w]$ is the Fourier transform operator. The intensity is calculated by squaring the optical field, i.e., $I(\xi,\eta) = |\Gamma(\xi,\eta)|^2$, and the phase is calculated using $\phi(x,y) = \arctan(Im[\Gamma(\xi,\eta)]Re[\Gamma(\xi,\eta)]$. If x, y are discretized on a rectangular raster of N_x,× N_y points (corresponding to the number of pixels in the CCD camera in the x and y dimensions, respectively) with step sizes Δx, Δy, which are the pixel-to-pixel distances on the CCD in the x and y directions, respectively.

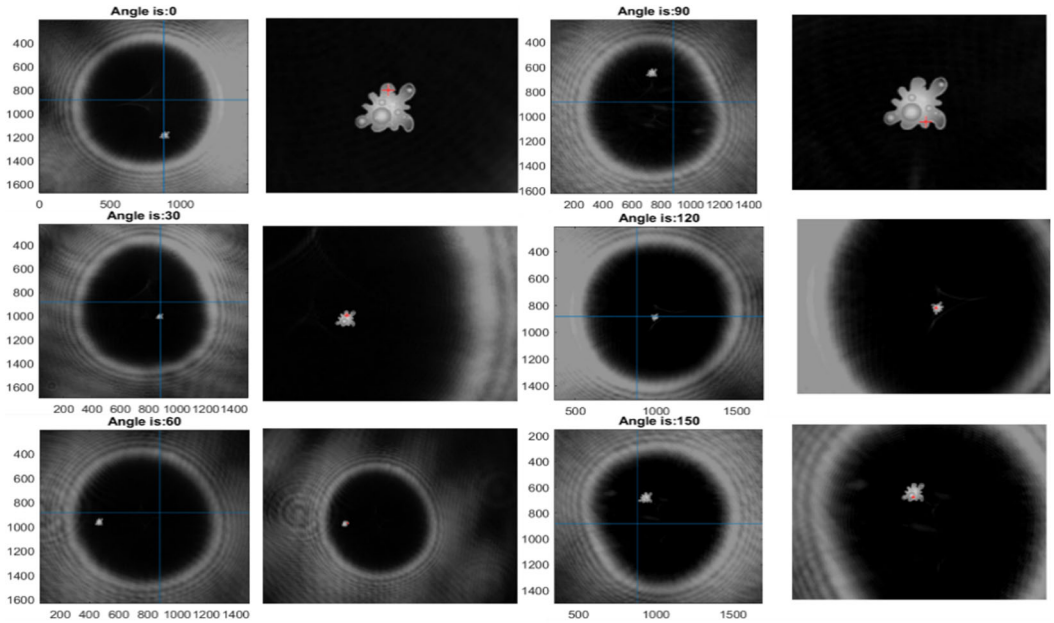

Fig. 4.3. Holographic Detection of Amoebas: Phase Analysis at Diverse Angles.

Fig. 4.4 provides a visual representation of the distribution of phase component peaks at amoeba positions according to the proposed method. These peaks, crucial for identifying amoeba presence, are recognized using our method and clearly highlighted in the figure using the red color. This distribution map facilitates a comprehensive comparison of phase values across various angles, underscoring the efficacy of our proposed technique for reliable amoeba detection and segmentation in liquid samples. In a manner similar to its application in our study [15, 19], Fig. 4.4 underscores the importance of parameter "L" as a reliable indicator for amoeba detection within the liquid medium. It's worth noting that in the case of amoebas, the average L value in our healthy water sample images stands at 130, while in water samples contain amoebas, it significantly rises to 427. Moreover, the in-phase component peaks consistently fall within the [400, 450] range for amoebas, highlighting their presence. Conversely, in images of healthy water samples with uniform pixel intensity distribution, the in-phase component peaks remain confined to the [110, 150] range.

Fig. 4.5a presents the 3D reconstruction of amoebas in liquids using our proposed setup. The figure includes multiple views of the reconstructed 3D image, including top, bottom,

front, and side views. This figure provides a detailed and comprehensive view of the 3D structure of the amoebas and allows for the visualization of their internal features. this figure helps to illustrate the capabilities of our proposed setup for 3D reconstruction of sample of water. this figure helps to illustrate the capabilities and potential of our proposed setup for 3D reconstruction. The Fig. 4.5b provides a detailed and comprehensive view of the multiple projections of the volume from different angles and allows for the visualization of the internal features and relationships within the volume.

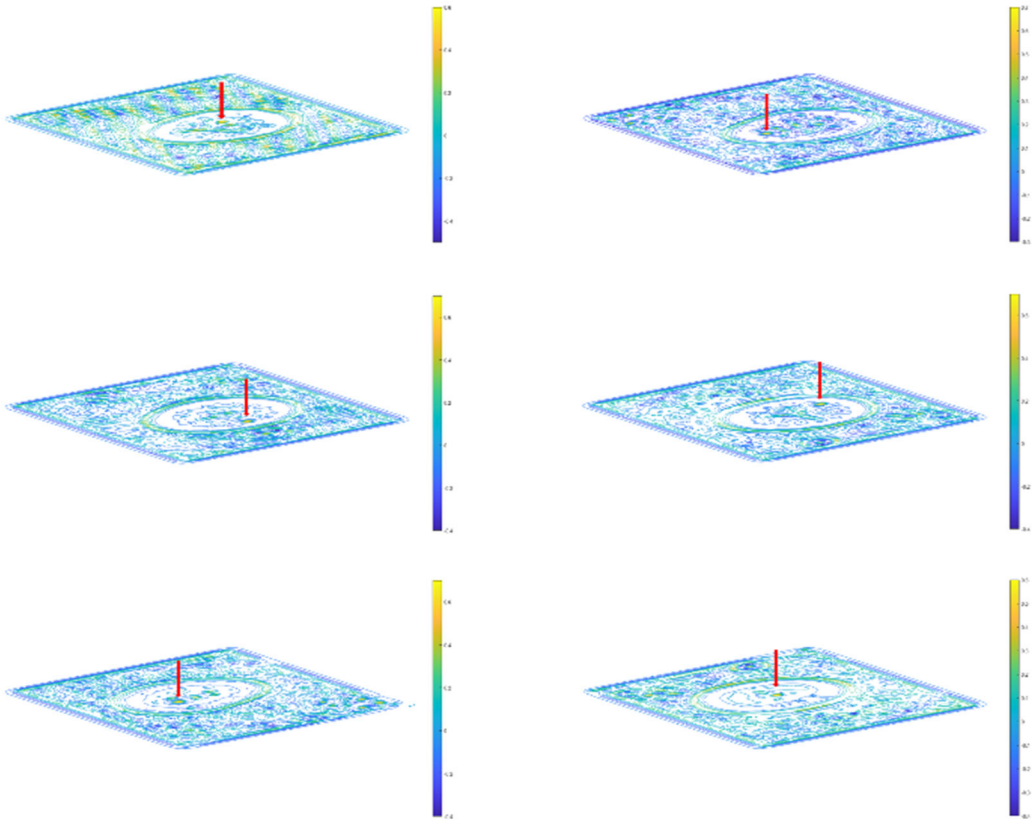

Fig. 4.4. Phase component peaks at the amoeba position according to the proposed method.

After the initial contour has been optimized using the proposed active contour model, the 3D shape of the object can be reconstructed by numerically reconstructing the function $h(x, y)$ and computing the intensities I on multiple planes at various angles and at distance d surrounding the test volume. This process involves using the discretized form of the Fresnel diffraction formula and performing some coordinate transformations. The resulting reconstructed intensities are then multiplied along each angular projection to obtain a 3D reconstruction of the object Equation (4.2).

$$I = \prod_1^M I_j \tag{4.2}$$

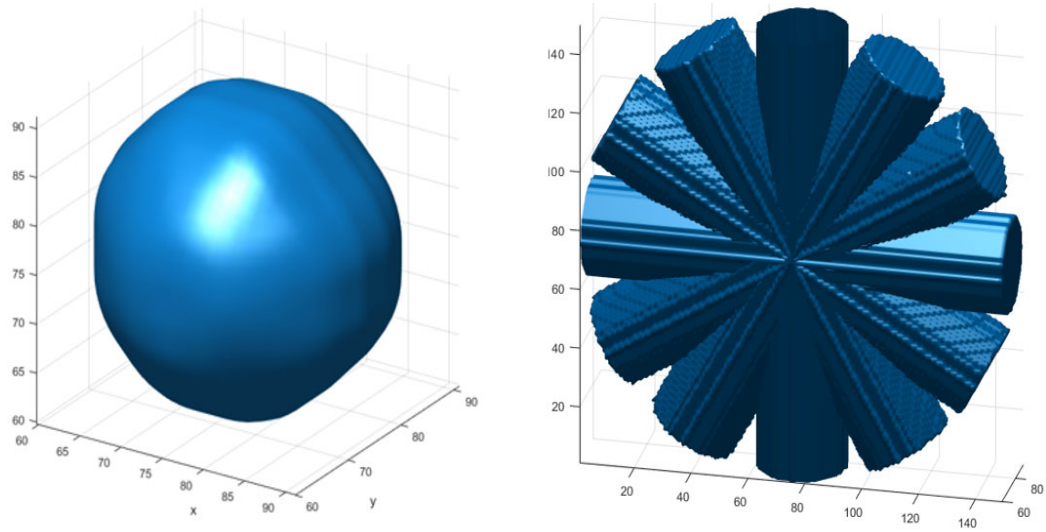

a) b)

Fig. 4.5. 3D Reconstruction and Multiplication of Projections from Different Angles for our Sample.

4.3. Results and Discussion

4.3.1. Detection Evaluation

To evaluate the performance of our proposed method for detecting and segmenting amoebas in liquids using holotomography, we measured the accuracy of the method in terms of its ability to correctly identify the position of the amoeba based on the value of the c parameter returned by our setup (Table 4.1). To compare the performance of our method with other state-of-the-art methods, we also calculated the percentage of accuracy for the Potential Field Segmentation (PFS), Edge Detection, Template Matching, and Clustering methods in detecting the centers of the amoebas. The results of these comparisons provide insight into the relative effectiveness of these different approaches for detecting and segmenting amoebas in liquids. Potential Field Segmentation (PFS) is a method used in image processing and computer vision to segment an image into different regions or objects [23]. It works by creating a potential field for each pixel in the image, with the strength of the field determined by the pixel's intensity or color. Pixels with similar intensities are attracted to each other, causing them to cluster together and form a segment. Edge detection is a method used to identify the boundaries of objects in an image. It works by detecting sudden changes in pixel intensity or color, which typically occur at the edges of objects. There are many different edge detection algorithms, each with its own strengths and weaknesses [20]. Template matching is a method used to find a template or pattern in an image [24]. It works by sliding the template over the image and comparing the template to each subregion of the image. If the template and subregion match, the method records the location of the match. Template matching can be used for

object recognition, image registration, and many other applications. Clustering is a method used to group data points into clusters based on their similarity. It is often used in image processing and computer vision to segment an image into different regions or objects. In image segmentation, the principle of clustering algorithms involves partitioning an image into meaningful regions or objects based on similarities in pixel values, colors, textures, or other visual features. Clustering algorithms such as K-Means, DBSCAN, or hierarchical clustering can be applied to group pixels with similar characteristics into distinct clusters, effectively segmenting the image into semantically meaningful regions. This process aids in tasks like object detection, image recognition, and computer vision by isolating and identifying objects or regions of interest within the image [21, 22].

Table 4.1. Proposed method percentage in returning the parameter c inside the amoeba and the average time compared the state of art.

Methods	Accuracy (%)			Time average (seconds)
	Inside Amoeba	Edge Amoeba	Outside Amoeba	
Edge detection method [20]	80 %	19 %	1 %	9.1007
Template matching method [24]	90,5 %	5,5 %	4 %	7.4689
Clustering method [21, 22]	96 %	2 %	2 %	13.1247
Potential field method [23]	95 %	0	5 %	38.1643
Proposed method	98 %	2 %	0 %	1.4322

4.3.2. Segmentation Evaluation

Image segmentation techniques such as the Geodesic Active Contour (GAC) [25], Localized Active Contour (LAC) [24], and Active Contour driven by Cuckoo Search (ACCS) [28] have been widely used for their ability to extract objects of interest from images. GAC is a fast method that can handle topological changes well but may struggle with noisy or concave objects. On the other hand, LAC is more sensitive to local features and less sensitive to global features than GAC but may be more prone to getting stuck in local minima [27]. ACCS combines the principles of active contours with the Cuckoo Search optimization algorithm, allowing it to more effectively escape local minima and find the global minimum energy solution. However, ACCS may be slower due to the added computational cost of the Cuckoo Search algorithm. Each of these methods has its own strengths and limitations, and the appropriate method to use may depend on the specific needs of the application.

In comparison (Table 4.2) to the Geodesic Active Contour (GAC) method, our method showed improved sensitivity and specificity, as well as a lower average time for image

processing. The Dice coefficient was similar between the two methods, but our method had a slightly smaller Hausdorff distance. The Localized Active Contour (LAC) method had similar sensitivity and specificity to our method, but a lower Dice coefficient and a larger Hausdorff distance. The Active Contour driven by Cuckoo Search (ACCS) method had the highest sensitivity and Dice coefficient, but the longest average processing time and the largest Hausdorff distance. Overall, our method strikes a good balance between accuracy and efficiency, making it a strong contender in image segmentation tasks.

Table 4.2. Sensitivity, Dice, Hausdorff distance, Specificity, and elapsed time rates obtained from the optimal contour of the images of our sample reached by using the Geodesic Active Contour (GAC), the Localized Active Contour (LAC), the Active Contour driven by Cuckoo Search (ACCS), and the proposed method (Proposed).

Patients	Method	Sen	D (AVG± ±SD×10^{-4})	H_d	Spe	Times (s)
Captured image at 0°	GAC	0.7083 ±1.1	0.7539 ±6.2	3.2311 ±2.5	0.9645±0.6	12.8450 ±1.2
	LAC	0.8905 ±2.5	0.9371 ±3.2	2.6478 ±2.6	0.9772±2.1	11.2406 ±1.9
	ACCS	0.9391 ±7.4	0.9384 ±9.0	2.7448 ±5.2	0.9240±1.2	18.1200 ±2.0
	Proposed	0.9798 ±0.6	0.9876 ±0.1	2.7902±0.1	0.9969±1.5	1.4321 ±0.1
Captured image at 30°	GAC	0.6854 ±0.0	0.7978 ±4.3	4.3569 ±6.1	0.9913 ±4.5	12.8352 ±1.0
	LAC	0.8152 ±5.4	0.9241 ±2.2	4.5010 ±2.0	0.9907 ±2.8	11.2316 ±1.1
	ACCS	0.9243 ±1.5	0.9685 ±0.8	3.6050 ±2.5	0.9969 ±1.1	18.1340 ±2.6
	Proposed	0.9849 ±0.3	0.9792 ±0.6	2.1597 ±0.2	0.9987 ±0.1	1.4401 ±0.3
Captured image at 60°	GAC	0.6804 ±5.3	0.8689 ±5.2	6.5823 ±2.5	0.9702 ±0.3	12.7052 ±1.4
	LAC	0.6915 ±1.3	0.7917 ±4.2	5.7490 ±3.5	0.8914 ±0.1	10.1016 ±2.1
	ACCS	0.9574 ±2.8	0.9620 ±4.1	3.8760 ±5.1	0.9892 ±0.7	18.1340 ±3.1
	Proposed	0.9978 ±0.1	0.9898 ±0.0	2.0194 ±1.1	0.9987 ±0.0	1.4301 ±0.5
Captured image at 90°	GAC	0.5435 ±3.6	0.6842 ±0.2	4.5432 ±7.7	0.9976 ±1.7	12.9528 ±8.7
	LAC	0.6951 ±2.2	0.7845 ±1.3	4.0214 ±3.7	0.9850 ±4.6	9.8972 ±8.0
	ACCS	0.8785 ±3.5	0.9456 ±1.4	3.0145 ±2.3	0.9679 ±7.4	17.8972 ±5.4
	Proposed	0.9876 ±0.1	0.9934 ±0.5	2.0124 ±1.1	0.9899 ±0.2	1.4401 ±1.0
Captured image at 120°	GAC	0.8267 ±3.4	0.7382 ±2.8	4.8558 ±3.9	0.9804 ±3.5	12.5467 ±8.6
	LAC	0.8678 ±2.0	0.8243 ±0.0	6.5701 ±1.2	0.9906 ±0.5	10.1245 ±2.8
	ACCS	0.9242 ±2.1	0.9780 ±0.2	3.6437 ±1.1	0.9881 ±4.6	18.7682 ±1.8
	Proposed	0.9896 ±0.1	0.9964 ±0.2	2.3559 ±1.1	0.9967 ±0.3	1.4330 ±0.6
Captured image at 150°	GAC	0.7952 ±5.4	0.8256 ±2.7	3.2310 ±2.0	0.9920 ±2.2	12.3899 ±7.4
	LAC	0.8645 ±0.3	0.7981 ±0.7	3.2453 ±0.0	0.9965 ±7.9	10.5313 ±0.9
	ACCS	0.9145 ±2.0	0.9680 ±3.3	2.8947 ±6.7	0.9988 ±2.3	17.3692 ±5.0
	Proposed	0.9956 ±0.8	0.9962 ±2.2	2.0420 ±0.1	0.9998 ±1.7	1.4310 ±4.6

The evolution of the initial contour detected by our system is performed using the proposed active contour model, which is programmed using finite differences after the energy function has been discretized and linearized. This allows us to track the evolution of the contour as it moves towards the optimal solution for the given energy function Eq. (4.3). The finite difference approach enables us to approximate the derivatives of the energy function in a computationally efficient manner, and the linearization allows us to solve for the update to the contour at each iteration using a set of linear equations. By iteratively updating the contour according to the optimized solution, we are able to accurately extract the object of interest from the image.

$$E_{i,j} = \alpha C_{i,j} + \beta|I - m_{i,j}|^2 + \gamma|I - M_{i,j}|^2, \quad (4.3)$$

where $\alpha = \beta = \gamma = 1$ are fixed parameters, $C_{i,j}$ is the initial contour detected by the proposed method. $m_{i,j}$ is the average of the input RM image I(x,y) inside the initial contour $C_{i,j}$. $M_{i,j}$ is the average of the input RM image I(x,y) outside the initial contour $C_{i,j}$ and

$$0 \le Sen = \frac{TP}{TP+FN} \le 1, 0 \le D = \frac{TP}{TP+\frac{FP+FN}{2}} \le 1,$$
$$0 \le Sep = \frac{TN}{TN+FP} \le 1, H_d(G,S) = \max\left\{\max_{a\in G}\min_{b\in S}\|a-b\|, \max_{b\in S}\min_{a\in G}\|b-a\|\right\}$$

4.4. Conclusion

In summary, our use of holographic tomography to extract and segment amoebas from water samples has allowed us to visualize the three-dimensional structure and movement of these organisms in detail, study their behavior and interactions with their environment. The use of multiple CCD cameras to record holograms at different angles has improved the resolution and contrast of the images, resulting in clearer and more detailed visualization of the amoebas. The extraction of the maximum value from the in-phase component of the scanned data allows for the reliable and precise localization of amoeba positions. Concurrently, the application of active contour theory enables the meticulous delineation and segmentation of amoebas from their surrounding environment. This synergistic approach ensures a scientifically rigorous methodology for amoeba detection and analysis. Simultaneously, 3D reconstruction of amoebas provides critical insights into their structure and behavior, enhancing our understanding of their ecological roles and potential impacts on human health. Overall, our results demonstrate the effectiveness of holographic tomography as a powerful tool for studying the internal structure and properties of biological samples and have important implications for understanding the behavior and interactions of amoebas in aquatic environments. This knowledge is instrumental in assessing water quality and safety for human consumption, contributing to essential public health considerations.

Acknowledgment

We would like to express our gratitude to the organizers of the Brain Tumor Segmentation (BraTS) challenge for providing us with the BRATS 2012 and 2013 databases. These datasets are instrumental in our research and contribute significantly to our work in the field of medical image analysis. Thank you for your valuable support [29].

References

[1]. C. Depeursinge, P. Marquet, L. Magaud, Digital holographic microscopy: a review, *Advances in Optics and Photonics*, Vol. 2, Issue 2, 2010, pp. 238-278.

[2]. D. Kim, Y. Kim, D. Kim, Digital holographic microscopy, *Optics Letters*, Vol. 30, Issue 22, 2005, pp. 3033-3035.

[3]. P. Gu, H. Chen, L. Zeng, Digital holographic microscopy for three-dimensional imaging and analysis of biological cells, *Chinese Physics Letters*, Vol. 28, Issue 4, 2011, 044202.
[4]. J. Xu, W. Chen, J. Li, X. Wang, Detection and identification of free-living amoebae in water environments: A review, *Environmental Science and Pollution Research*, Vol. 27, Issue 24, 2020, pp. 29791-29801.
[5]. R. Bhojwani, D. Bhojwani, V. Khanna, Amoebiasis: An overview, *Journal of Global Infectious Diseases*, Vol. 11, Issue 1, 2019, pp. 1-7.
[6]. L. Zeng, C. Ma, Optical tomography for imaging and sensing, *Laser Photonics Reviews*, Vol. 7, Issue 1, 2013, pp. 94-119.
[7]. Bazow B, Lam VK, Phan T, Chung BM, Nehmetallah G, Raub CB. Digital Holographic Microscopy to Assess Cell Behavior. *Methods Mol Biol.,* 2644, 2023, pp. 247-266.
[8]. Gu, J. Pan, L. Chen, Digital holographic microscopy: a review, *Journal of Biomedical Optics*, Vol. 16, Issue 11, 2011, 111401.
[9]. Wang, K., Song, L., Wang, C. et al., On the use of deep learning for phase recovery, *Light Sci Appl.,* 13, 2024, 4.
[10]. Zhang, H. Chen, Digital holographic microscopy for cells and tissues, *Journal of Biomedical Optics,* Vol. 19, Issue 8, 2014, 086008.
[11]. Y. Kim, J. Kim, S. Kim, Three-dimensional imaging of transparent objects by digital holographic microscopy, *Optics Letters*, Vol. 30, Issue 24, 2005, pp. 3382-3384.
[12]. E, Ouabida, A. Essadique, A. Bouzid, Vander Lugt Correlator based active contours for iris segmentation and tracking, *Expert Systems with Applications*, Vol. 71, 2017, pp. 383-395.
[13]. A. Essadike, E. Ouabida, A. Bouzid, Brain tumor segmentation with Vander Lugt Correlator based active contour, *Computer Methods and Programs in Biomedicine*, Vol. 160, 2018, pp. 103-117.
[14]. A. Essadike, E. Ouabida, A. Bouzid, Optical scanning holography for tumor extraction from brain magnetic resonance images, *Optics Laser Technology*, Vol. 127, 2020, 106158.
[15]. E. Ouabida, A. Essadike, A. Bouzid, Optical correlator based algorithm for driver drowsiness detection, *Optik*, Vol. 204, 2020, 164102.
[16]. E. Ouabida, A. Essadike, A. Bouzid, Automated segmentation of ophthalmological images by an optical based approach for early detection of eye tumor growing, *Physica Medica*, Vol. 48, 2018, pp. 37-46.
[17]. El-Ouarzadi, Abdennacer, et al., Brain Tumor Detection and Segmentation Using a Hybrid Optical Method by Active Contour, Preprint, Available at *SSRN 4629062*, 2023.
[18]. A. Cherkaoui, A. El-Ouarzadi, A. Essadike, A. Bouzid, Automatic brain tumor detection and segmentation using enhanced optical scanning holography and active contour model in MRI, *Sensors & Transducers*, Vol. 262, Issue 2, 2023, pp. 13-22.
[19]. J. Canny, A computational approach to edge detection, *IEEE Transactions on Pattern Analysis and Machine Intelligenc*e, Vol. 8, Issue 6, 1986, pp. 679-698.
[20]. A. K. Jain, Data clustering: 50 years beyond K-means, *Pattern Recognition Letters*, Vol. 31, Issue 8, 2010, pp. 651-666.
[21]. Xu, Rui, and Donald Wunsch, Survey of clustering algorithms, *IEEE Transactions on neural networks,* 16, 3, 2005, pp. 645-678.
[22]. J. A. Lee, Image segmentation by potential field computation, *Computer Vision and Image Understanding*, Vol. 55, Issue 1, 1991, pp. 7-27.
[23]. L. Zhang, A survey of thresholding techniques, *Computer Vision and Image Understanding*, Vol. 104, Issue 1, 2004, pp. 59-78.
[24]. V. Caselles, R. Kimmel G. Sapiro, Geodesic active contours, *International Journal of Computer Vision*, Vol. 22, 1997, pp. 61-79.
[25]. I. Cabria, I. Gondra, MRI segmentation fusion for brain tumor detection, *Information Fusion*, Vol. 36, 2017, pp. 1-9.

[26]. E. Ilunga-Mbuyamba, J. G. Avina-Cervantes, A. Garcia-Perez, et al., Localized active contour model with background intensity compensation applied on automatic MR brain tumor segmentation, *Neurocomputing*, Vol. 220, 2017, pp. 84-97.

[27]. U. Baid, et al., The RSNA-ASNR-MICCAI BraTS 2021 Benchmark on Brain Tumor Segmentation and Radiogenomic Classification, *arXiv preprint*, *arXiv:2107.02314*, 2021.

[28]. B. H. Menze, A. Jakab, S. Bauer, J. Kalpathy-Cramer, K. Farahani, J. Kirby, et al., The multimodal brain tumor image segmentation benchmark (BRATS), *IEEE Transactions on Medical Imaging*, Vol. 34, Issue 10, 2015, pp. 1993-2024.

[29]. S. Bakas, H. Akbari, A. Sotiras, M. Bilello, M. Rozycki, J. S. Kirby, et al., Advancing the cancer genome atlas glioma MRI collections with expert segmentation labels and radiomic features, *Nature Scientific Data*, Vol. 4, 2017, 170117.

Chapter 5
Optometry at Dark with Photoluminescent Mires

Antonio Parretta

5.1. Introduction

The use of photoluminescent stickers is widespread among people, particularly the youngest, when reproducing sky constellations on the ceilings of houses to be admired in the dark [1, 2]. They are also used in fixed warning systems (obstacles on the roads) or mobile ones (bicycles, motorcycles), to ward off the dangers of accidents. The main task of this work is to explore human vision in the dark when using photoluminescent materials as targets. There is no dark optometry based on the use of these materials, and therefore it has been possible to work in a little explored field, which allowed me to find new results in the context of different types of optometric tests. Traditional optometric techniques were a reference to adapt the techniques used in the dark, in an artisanal laboratory, to the more sophisticated ones available in a modern optometric laboratory. For this purpose, all the tests chosen for working in the dark with logMAR optometric charts and PL optotypes, illuminated with UVA light, were replicated in the light with logMAR optometric charts and white optotypes, illuminated with LED lamps in white light indoors and sunlight outdoors. In a few cases decimal tables on paper or on monitors in negative contrast were used. In this work, the books [3, 4] will be considered as the main references for optometry, and will be cited together with the page number.

The incipit of this work is an occasional event experienced one night by myself, observing the spectacle, well known to children, of the starry sky drawn on the ceiling by putting together many PL stickers in the shape of stars to form well known sky constellations. Finding myself no more than a meter away with my eyes from the stars, and having my sight already adapted to the dark, I noticed with great surprise that, by staring at one of these stars, after a very short fraction of time, it disappeared from sight and only the dark background of the ceiling remained. At the same time, the other adjacent stars remained visible in the background of the visual field, even if they were not in focus. If I then moved my gaze to a nearby star, it too suddenly disappeared, while the previous one became visible in the background of the visual field. This is schematically pictured in Fig. 5.1.

Antonio Parretta
Physics and Earth Sciences Department, Ferrara University, Ferrara (FE), Italy

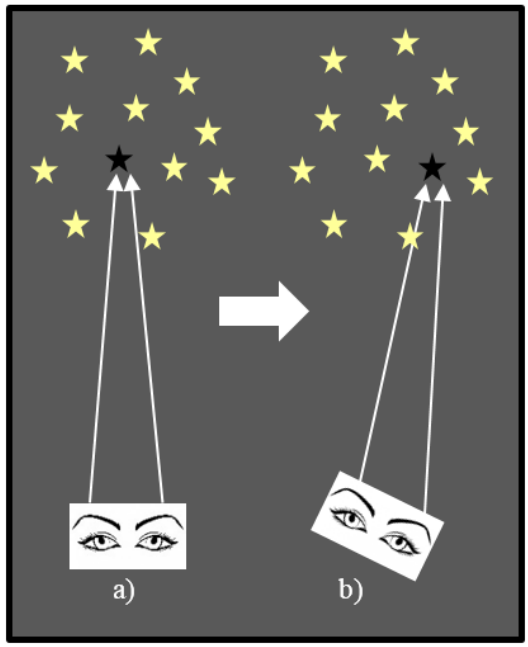

Fig. 5.1. Schematic representation of a ceiling covered by a group of photoluminescent star stickers. If we fix a photoluminescent star sticker, previously illuminated by white or UVA light, with eyes adapted to the dark, the sticker disappears from view (a). The same thing happens by moving the view on another sticker (b). Of course, the eyes-sticker distance and the luminosity of the stickers must be appropriate (see the text).

This phenomenon occurred both when looking at the stars with both eyes, and when looking at them with each of them separately. As I said, my eyes were about a meter away from the stars, and these were of 1-cm diameter, so I was observing them under an angle of ~0.5°. It should be noted that the stars had remained in the dark for more than an hour after being illuminated by the room light, and therefore their brightness had reduced considerably. If we were to do this experiment with very bright stars, the phenomenon would not be repeated, even with dark-adapted sight.

The explanation of this phenomenon can be summarized as follows. When one has dark-adapted vision, each eye behaves like a source emitting outwards a cone of “black light” or “darkness”, that is a shadow, which can darken everything inside, and then also the PL sticker. The linear angular amplitude of this cone, that I call “angle of view”, is of ~1° (this is precisely the value that I measured on my eyes). In the dark, the faint photoluminescent stars at ~1m distance are virtually "seen" within a cone of linear angle of ~0.5°, and then are included in this "shadow cone", and no longer visible, that is, they are completely darkened (see Fig. 5.2 (a)). If I bring my eyes close to a star, it would remain completely darkened until the shadow cone coincides with the virtual cone of view of the star (see Fig.5.2 (b)). Continuing to get closer to the star, it will appear to the sight, initially faint, and then increasingly brighter as getting closer to it (see Fig. 5.2(c)).

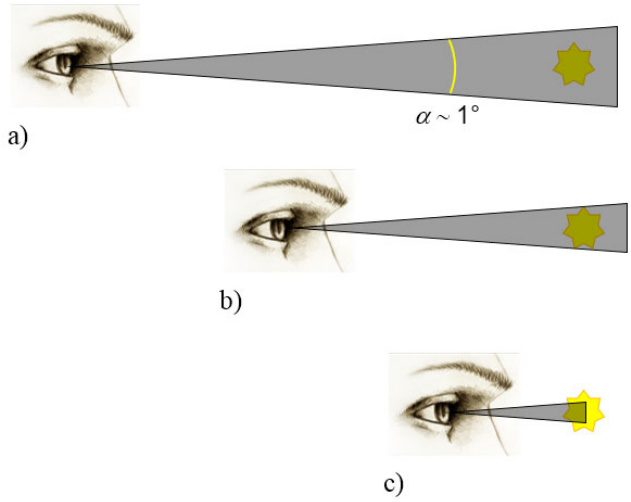

Fig. 5.2. The figure shows an observer who, in the dark, emits from his eye a shadow cone equal to ~1°. (a) The cone includes the star, which is not visible; (b) the cone grazes the edge of the star, which is not yet visible; (c) the cone of shadow intercepts only a part of the star, which thus becomes partially visible.

What I have illustrated describes exactly the "angle of view test", apart from the fact that the star was replaced by a PL disk of well-defined diameter, finalized to a precise determination of the critical angle of view at dark, α_D, where the subscript D stay for "dark". It is generally found by slowly moving away from the star, and recording the distance at which it darkens, that is moving from (c) to (b) in Fig. 5.2; this measurement is then repeated several times by moving back and forth with respect to the star, to get a more precise value of α_D. The described phenomenon can be attributed to the almost complete deactivation, in the dark, of the cone photoreceptors, and the absence of rod photodetectors in the foveal area involved by the direct view of a luminous object [3, p. 19; 4, p. 77]. The darkening of a circular PL target occurs therefore only when it subtends to the sight of the tested eye an angle smaller than the critical angle α_D, which is a parameter related to the extension of the foveolar area (macula), as we will see later. The "test of the angle of view" allows therefore to know this parameter by observing the target at different distances and recording the minimum distance at which it can be darkened. The described test of the angle of view at dark can be considered a new, original test, precisely because derived from the use of PL sights, which are not foreseen in the traditional photometric methods [4, p. 14].

The phenomenon described is the same as that occurring when looking the sky on a moonless night with no other terrestrial illumination. These are the conditions in which our sensitive capacity becomes clearer and more perfect in the peripheral regions of the retina. It is known that, if we observe the brightest stars in a constellation, we cannot see the fainter ones. To see these, we must turn our gaze to the side of them, so that the parts of the retina that are most sensitive to darkness, those around the fovea, are activated. This fact was discovered for the first time by the Swiss astronomer J. H. Lambert in 1779 [5].

In practice, the central fovea is the area of the eye with the greatest visual acuity (VA), but in dark conditions, when most of the conical photoreceptors are deactivated, the direct vision of the star is obscured, while, moving our gaze away from it, the light of the star is perceived by the peripheral retinal cells, more sensitive to darkness. According to French physicist Francoise Arago [6]: "to see a dimly lit object, you must not look at it."

There is another optometric test which allows the darkening of a target at dark, and is the well-known “Mariotte’s blind spot test” [3, p. 143; 4, p. 149; 7; 8; 9]. Generally applied at light, this test allows to obscure the first of a pair of targets by focusing the sight of one eye on the second target and closing the other eye. The Mariotte’s test requires a particular arrangement of the eyes with respect to the two targets kept horizontal. This test can be applied at both light and dark, and the results are information on the position of the terminal part of the optic nerve on the retina, that is on the angular orientation of the papilla with respect to the visual axis of the eye. We will see that, due to the extension of the papilla, the darkening of the target will involve the determination of an angular interval, and not just a single angular value, as done with the angle of view test. The Mariotte’s test, if applied at dark, can be suitably combined with the angle of view test to darken simultaneously two PL stickers. This fact, in principle, does not give rise to any new information, but nevertheless remains interesting as it arouses a double surprise compared to that which the two single tests are able of arousing. I named this new type of test “Two Blind Spots Test” (TBST), precisely because it involves the darkening of two targets together. The TBST too is a new, original test, precisely because it derives from the use of PL mires, which are not foreseen in the traditional photometric practice.

The other test taken into consideration in this work, and which involved a large number of optometric measurements, is the “morphoscopic visual acuity” test, which is well known to all of us, as it is the one we must pass if we want to drive a motor vehicle. A large part of this work is dedicated to this test, which will be applied both in the light, using decimal charts, and logMAR charts realized by hand drawing white optotypes by brush and white paint, and in the dark, using logMAR charts realized by hand drawing the optotypes by brush and PL paint. The results of these tests will be compared to those provided by a private optometric laboratory. Very important insights were made with the VA morphoscopic test concerning measurement outdoors in sunlight with a cloudy sky, as a function of the illuminance on the logMAR chart. A second, and important insight was also that of the VA morphoscopic test done in indoor with UVA light, as a function of the luminance of the logMAR chart optotypes.

The last test considered in this work is the “resolution acuity test”, performed by looking at a slit in the light or in the dark, and whose results should be closely linked to those of the morphoscopic vision acuity test.

To summarize, these are the tests which will be discussed in this work in order of presentation, carried out at light and/or dark conditions:

a) The morphoscopic visual acuity (VA) test (light and dark).

b) The morphoscopic visual acuity (VA) test in a private laboratory (light).

c) The test of the angle of view (dark).

d) The Mariotte's blind spot test (light and dark).

e) The combined test of the angle of view and the Mariotte's blind spot test, or TBST (dark).

f) The test of resolution acuity or of the minimum angle of resolution, *MAR* (light and dark).

As will be evident reading this paper, the realization of this work required only a few commercial materials and low-medium cost instrumentation, which makes it very suitable to be replicated by students who want to deepen not only the art of optometry, but also the knowledge of human eye, which is the most sophisticated sense organ we have: if comparing neural input, the cochlear division of the acoustic nerve contains ~31,000 neurons, against the 1,200,000 ones of the optic nerve.

In addition to the description of optometric tests, this work also addresses the problem of measuring the luminance of the optotypes in the used tables. Ignoring the decimal tables, which are of little importance, as regards the logMAR charts read in the light, they are characterized by optotypes drawn with white paint and illuminated with white light indoors and outdoors. Their luminance has been derived by measuring the illuminance on the surface of the table, and using calibration curves, traced in the laboratory by characterizing white disk samples prepared like the optotypes themselves. As regards, instead, the logMAR charts read in the dark, they are characterized by optotypes drawn with photoluminescent (PL) yellow-green paint, and illuminated with UVA light indoors. Their luminance has been derived by measuring the illuminance on the surface of the table, and using calibration curves, traced in the laboratory by characterizing PL disc samples prepared like the optotypes themselves. The experimental part of this methodology is preceded by a theoretical part.

A further part of this work has been an experimental study of the decay of the photoluminescence light emitted by the PL optotypes and stickers, or targets. This part had the aim of quantifying the luminance of the PL targets, when these were suitable to be darkened during the angle of view test. As we will see, this objective is very complex to achieve without having a photomultiplier, and therefore I will limit myself to describing all the steps I carried out to try to overcome this lack. I believe, however, that this study deserves further investigation, and will be addressed in a future work [10]. Another aspect that has been addressed in this work was to find which other light sources, of weak intensity, showed the property of being obscured like the PL light targets. Here I will limit myself to listing some of the samples that showed this property and others that did not, believing, however, that this study is susceptible to further investigation.

Finally, I would like to point out that most of the measurements relating to the morphoscopic visual acuity test, both outdoors at sunlight with white optotypes, and indoors at dark with white or photoluminescent optotypes, were performed by me by reading, and recording in real time the individual optotypes on all the lines, starting from

the most visible ones to those on which the identification of the characters was no longer possible. It can therefore be said that the procedure I adopted for reading the optotypes was a self-test procedure. Although this procedure is not reported in the optometric measurement protocol, which requires the distinction between a subject who reads and a subject who directs, judges and records the VA result, it was adopted necessarily due to the lack of collaborators to commit for such a long time to such a large number of results. This procedure allowed me to record a considerable amount of reading in a very short time, even if listening to it again, transcribing them on the logMAR chart, assigning the correct VA value, and finally reporting it on the computer took much longer. In defense of this method, I can only say that I concentrated myself to the maximum to free the memory at the beginning of each new reading, trying not to read a character because it was previously recognized, but only because it was effectively recognized at that moment.

5.2. The Physiology of Human Eye

Before proceeding to describe the experiments and fully understanding their meaning, it is important to report here the main morphological and functional properties known about this organ, which is the result of the vast existing literature on vision, starting from the monumental work of H. von Helmholtz [11-20]. Fig. 5.3 (a) shows a detailed horizontal section of the human right eye bulb, in which all the main components of this organ have been reported. Fig. 5.3 (b) shows a schematic representation of the same section, in which some optical quantities have been highlighted, which will be soon after discussed.

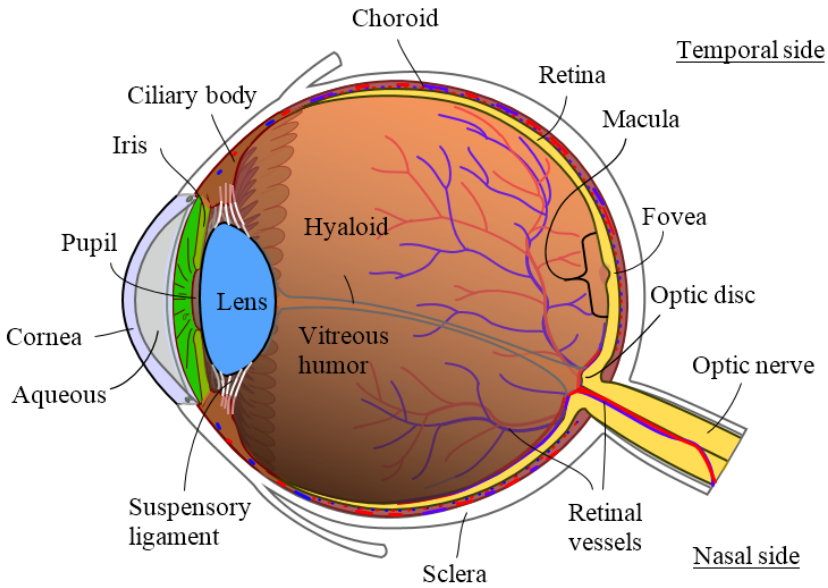

Fig. 5.3 (a). Horizontal section of the right human eye, with the main elements underlying vision.

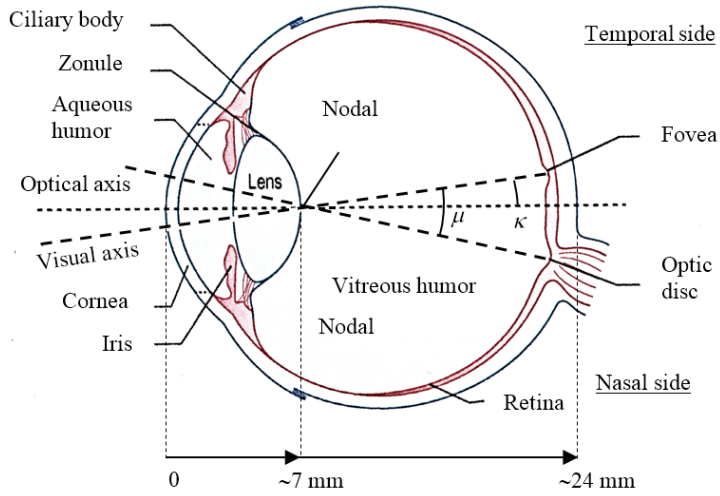

Fig. 5.3 (b). Schematic horizontal section of the right eye, with the bar giving the approximate scale. The angle between the visual and optical axes is indicated as angle κ. The angle between the visual axis and the axis crossing the optic nerve is indicated as angle μ. Both angles are measured starting from the nodal point, placed near the posterior surface of the lens. The distance from the cornea surface and the nodal point is approximately one third of the longitudinal axial length *LAL*~24mm of an emmetropic eye.

The human eye is composed of two positive lenses, the cornea and the crystalline lens, that project images of the object space onto the retina [4, p. 5]. We distinguish two axes in the eye: the optical axis, or main ocular axis, which passes in an average position between the centers of the individual media (cornea, lens) and through the nodal point and falls eccentrically at the macula; the visual axis, which connects the fovea with the nodal point and with the observed object. We call κ the angular divergence between these two axes, and its value is 3°-5° in the horizontal direction and 2° in the vertical direction. Rosenfield & Logan [3, p.9] call this angle α, but we prefer to call it κ so as not to confuse it with the visual angle α. Regarding the dimensions of the human eye, until the 1970s it was established that the longitudinal axial length (*LAL*) is different in cases with myopia ~24.6 mm, emmetropia ~23.4 mm, and hypermetropia ~22.5 mm. At present, researches describe a more complicated picture indicating that there are considerable individual variations of shape and size in myopic eyes and that there may be different types of myopia [21]. The average *LAL* of an adult human is of ~24mm (see Fig. 5.3 (b)), and, for most of emmetropic eyes, the nodal point is located ~7mm far from the cornea, slightly behind the lens [3, p. 161]. For simplicity, we have placed the position of the nodal point, and therefore of the corresponding nodal plane, on the internal face of the crystalline lens (see Fig. 5.3(b)). In adult humans, then, the distance between the nodal point and the retina is ~17mm. The iris is the vascular membrane of the eye, pigmented and with the shape and function of diaphragm, perforated by the pupil, whose aperture is changing as function of the ambient light intensity, and shows a diameter from 2mm in bright light to 8mm in the dark [3, p. 8]. The light, refracted by the cornea, a lens with a fixed optical power $P \sim 43$D and refraction index $n \sim 1.37$, crosses the aqueous humor (index $n \sim 1.33$), and is refracted

again by the crystalline, an active optical element able to modify its optical power between ~20D and ~33D (peripheral index $n \sim 1.38$ and central index $n \sim 1.40$) [4, p. 8]. After, the light crosses the vitreous humor (index $n \sim 1.33$) and reaches the central area of the optical retina [3, p. 17]. Fig. 5.4(a) shows a photo of the central area of the optical retina, with, on the left, the optic disc (papilla), the point of convergence of the nerve fibers for the formation of the optic nerve and also the point of emergence of the retinal vessels [3, p. 280; 4, p. 77]. Here, more than 1,200,000 retinal optical fibers converge, each single fiber corresponding to a small area of the retina, themselves divided into approximately 200 bundles, each bundle corresponding to a larger retinal region. In Fig. 5.4(a), at right of the optic disc, it can be seen the central macula (macula lutea), so called because of yellow color due to the presence of the lutein and zeaxanthin pigments, an avascular area responsible of the sharp and detailed vision [3, p. 280-88; 4, p.76]. A schematic overview of the inner parts of the macula is reported in Fig. 5.4 (b). Inside the central macula, of ~5.5mm diameter, we find the fovea, distinguished into different concentric areas: the parafovea (with ~2.5mm diameter), the fovea (with ~1.5mm diameter), and the foveola (with ~0.35 mm diameter). The angular divergence of the different regions of the macula is ~1° for the foveola, ~5° for the fovea, ~8° for the parafovea and ~18° for the perifovea [23].

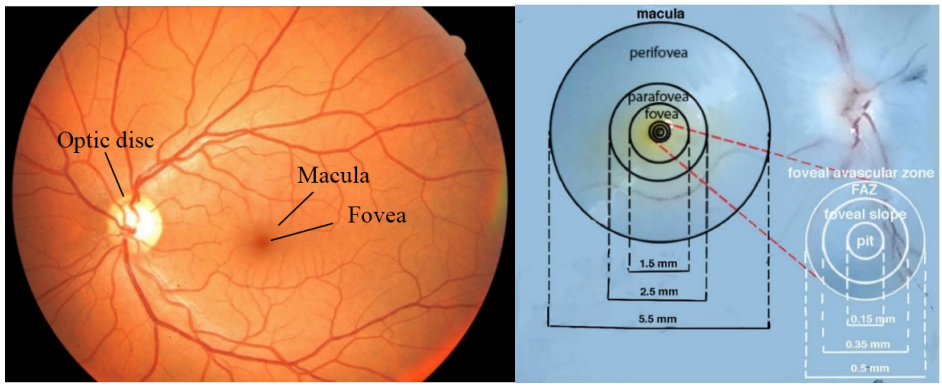

(a) (b)

Fig. 5.4. (a) Photo of the fundus of the human retina, showing the optic disc on the left with the blood vessels, and the macula with the fovea on the right; (b) A schematic overview of the inner parts of the macula, with their mean dimensions [22].

The fovea is an avascular zone where the photoreceptors, cones, specialized for vision in the light (photopic vision), are densely packed and provide an image of the object space with the highest resolution. Cones are divided into three types for different wavelengths, namely L-cones (long wavelengths), M-cones (medium wavelengths) and S-cones (short wavelengths), also indicated as cones for red light (R), green light (G) and blue light (B), respectively. The cones are on average 6.3-6.4 million and are concentrated in the fovea, the region of eye where light is focused by the process of accommodation [4, p. 183]. The peripheral part of the retina contains the rods, photoreceptors specialized for lower light condition and dark (scotopic vision), and renders lower resolution. At scotopic levels,

absolute sensitivity is high but since rods provide achromatic signals only, colors cannot be perceived. They are much more numerous (120 million on average) and are specialized in movement and object detection in the visual field. In contrast, at photopic levels, sensitivity is dramatically lower but colors can be perceived due to the trichromatic nature of the cone cells. The region where both receptor types play a role is denoted as mesopic vision. Fig. 5.5 shows the distribution pattern of the rods and cones photoreceptors.

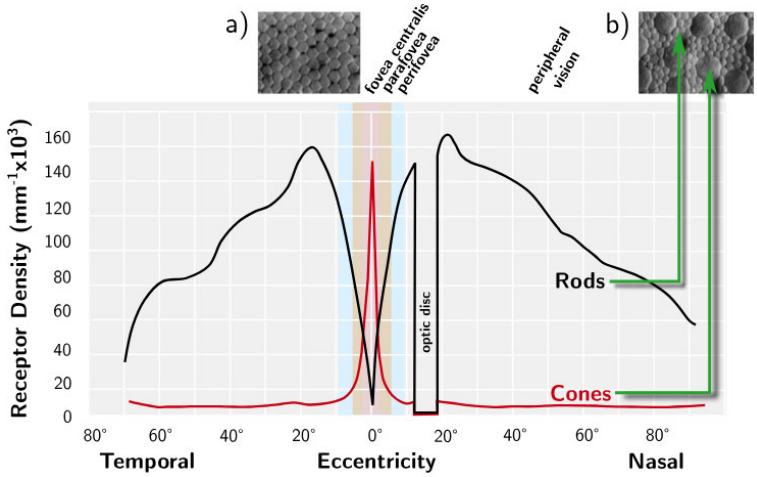

Fig. 5.5. Retinal photoreceptor distribution. Illustration adapted from Goldstein [24, p. 51]. Retinal microscopic recordings (a) and (b) from Curcio et al. [23].

The highest density of rods and cones is found in the macula. The central area of the macula, the fovea, consists entirely of cones. The center of the fovea, the foveola, consists of M-cones and R-cones, and represents the center of our visual field, with ~1° divergence. Starting from the fovea, the cone density drops significantly with increasing eccentricities (the angular distance to the visual axis). The inner parts of the macula constitute central vision, while areas further away are referred to as peripheral vision. Also, the density of the L-, M- and S-cones types differ. There are less S-cones (7% of the cone population) than M- and L-cones [24, p. 69]. Thus, humans are much less sensitive to short 'blueish' wavelengths than to the 'reddish' and 'greenish'. However, the S-cones are more spread out outside of the fovea. The highest density of rods is approximately 15°-20° around the fovea, this then decreases almost linearly. Fig. 5.6(a) shows a section of retina near the fovea, in which we distinguish the rods and cones photoreceptors, oriented perpendicular to the retinal surface, as well as the ganglion and bipolar cells. The horizontal and amacrine cells are instead oriented horizontally respect to the plane of the retina. What is shown in Fig. 5.6(a) is only the optical part of the retina. The retina, as a whole, forms the entire internal lining of the eyeball, from the point of entry of the optic nerve to the pupillary margin of the iris. The retina then comprises three portions: the optical part (applied to the choroid), the ciliary part (adherent to the ciliary body), and the iris part. The ciliary and iris components form the blind retina, with no receptors and exclusively epithelial in nature. Fig. 5.6(c) shows the schematic structure of the individual rods and

cones in detail, whereas Fig. 5.6(b) shows the natural shape of the two photoreceptors. In rods, the outer segment is cylindrical and elongated, while in cones it is pyramidal and shorter. The outer segment of the two photoreceptors has a layered structure, and contains specialized membranes in which the photosensitive pigments are located; as a result of light radiation, these pigments undergo biochemical transformations from which the nervous impulse originates. The red arrows in Fig. 5.6(a) show the path of the nervous impulse through the retina towards the optic nerve.

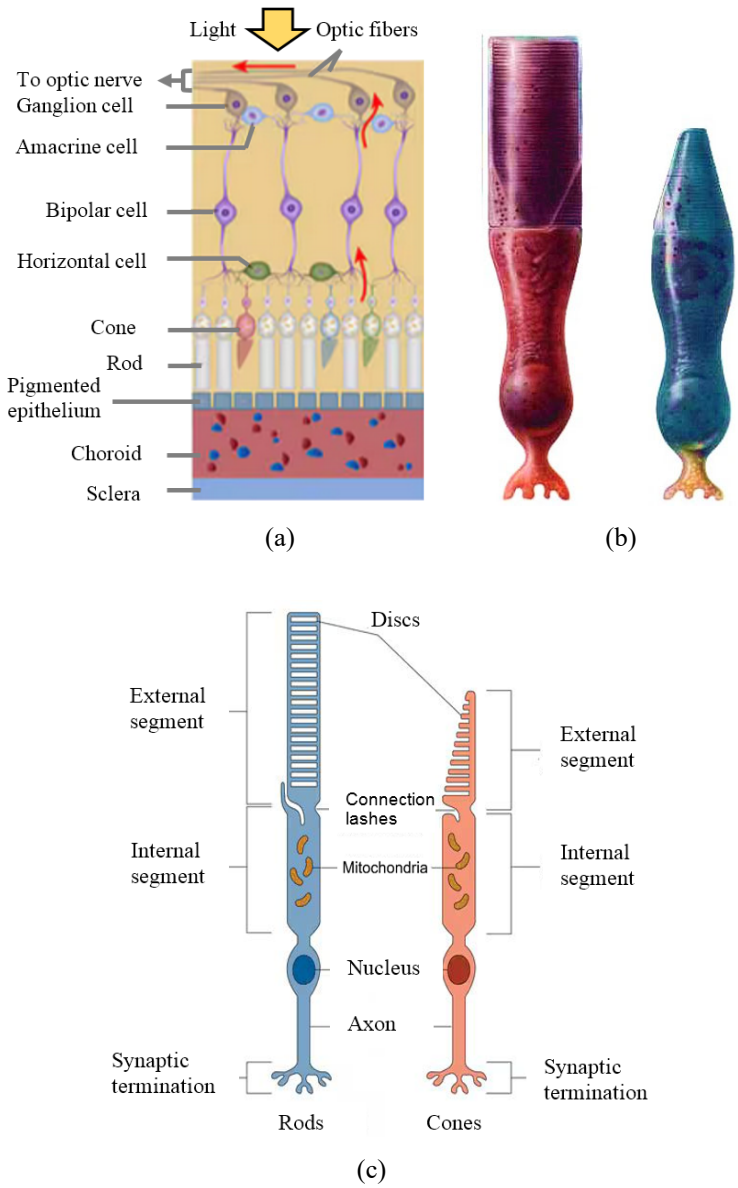

Fig. 5.6. (a) Schematic representation of a section of the retina near the fovea; (b) Natural shape of rods and cones photoreceptors; (c) Schematic structure of rods and cones photoreceptors.

As regards the choroid, we know that it is a highly vascularized tissue that supports the trophism of photoreceptors and eliminates catabolites. Being made up of blood vessels, its thickness can vary. His important optical function is containing pigmented cells that absorb the light passed through the retina, thus preventing the light from being reflected and diffused inside the eye. This does not happen, for example, in the cat's eye, which has a membrane (tapetum lucidum), reflecting into the eye the light that has not been absorbed by the retina, thus increasing the eye's sensitivity. Thanks to this structure, cats can see in low light conditions, and the tapetum lucidum also gives cats' eyes a characteristic green or yellowish shine that is especially noticeable in the dark.

In the cones there are pigments (iodopsin) sensitive to three different frequencies of electromagnetic waves (red, blue and green). The main photosensitive pigment present in rods is instead rhodopsin. Rhodopsin is inactivated by light and is activated in the dark. For this reason, rods are responsible for night vision, and because of their location in the external portion of the retina, in the dark we perceive an object as brighter if we “look” at it out of the corner of our eye. In fact, by staring at a bright object in the dark, the rays hit the central part of the retina more populated by cones, whose efficiency in responding to light stimuli in the dark is lower than that of rods.

The visual system relies largely on a self-regulating system: to ensure that the image of the object is always clearly formed on the surface of the retina, the crystalline lens changes its shape in relation to the distance of the observed object (accommodation); the iris is able to widen or narrow the diameter of the pupil, thus regulating the amount of light falling on the eye, and the optical characteristics of the visual system adapt to the luminance of the visual field or the spectral distribution of the light stimulus (adaptation). The ocular muscles have the function of aiming the visual field and of making both eyes converge on the same point so that the images arrive on the part of the retinal surface where there is maximum resolution (fovea) and merge, allowing the evaluation of the size, three-dimensionality and distance of the observed object.

As we have already discussed, the image of the object space on the retina is formed at the fovea, which is a concave area of about 1.5 mm in diameter (see Fig. 5.7), showing an extremely high concentration of photoreceptor cells: the cones in the fovea are packed so tightly together that they are almost touching, allowing for a very high level of detail and clarity in the central vision. Fig. 5.7(a) shows a section of the retina at the fovea. The thickness of the retina is here greatly reduced due to the lateral displacement of the ganglion and bipolar cells, and therefore the focused light arrives directly on the cones. The other reason why the fovea has such a high resolution of vision is that the cones here are much smaller (~1.5μm-diameter) than those distributed throughout the rest of the retina (~4μm-diameter). If we then consider that the maximum resolution in the fovea occurs when two illuminated cones are separated by a third non-illuminated cone, we find that, for a focal distance of ~17mm (distance between the nodal point and the retina), the *MAR* becomes approximately equal to 1’: $MAR = 60 \cdot tg^{-1}(3 \cdot 1.5 \cdot 10^{-3} / 17)$, which corresponds to an *AV* of 10/10 (see Table 5.5).

Furthermore, in contrast to the rest of retina, the human fovea contains midget ganglion cells, which are connected in a one-to-one ratio with midget bipolar cells. Then, the channel from midget bipolar to midget ganglion cell carries information from a single cone, thus relaying a point-to-point image from the fovea to the brain. The message going to the brain carries, therefore, both spatial and spectral information of the finest resolution. It must be considered, in fact, that half of the optic nerve fibers originate from the fovea, a very small region on the retina, which however becomes very large in the cortex, where half of the neurons of the primary visual cortex processes the information coming from the fovea. Fig. 5.7(b) shows the foveal pit, the deepest part of the foveola, with a diameter of approximately 0.15 mm.

As we have seen, we distinguish two axes for the eye: the optical axis, perpendicular to the cornea and intersecting the center of the entrance pupil, and the visual axis, connecting the fixation point in the object space to the nodal point and to the fovea (see Fig. 5.3(b)). The angular distance between these axes is, for an average eye, around 4° horizontally in the temporal direction and 2° vertically [3, p.9; 25]. The two axes meet on the nodal point, located approximately 7 mm from the cornea surface.

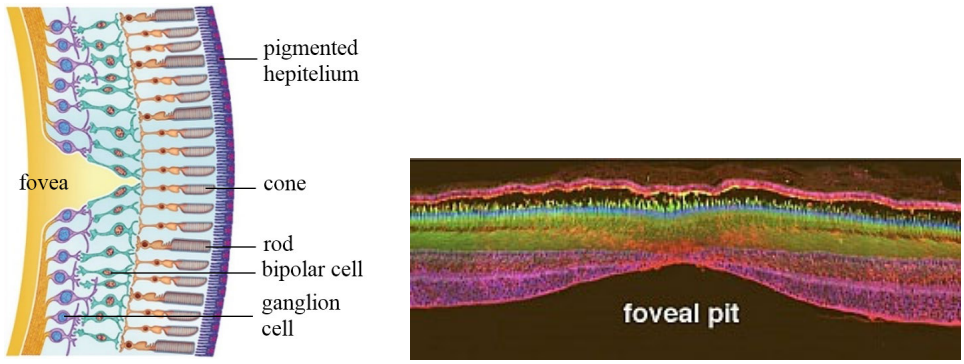

Fig. 5.7. (a) Schematic representation of a section of the retina at the fovea; (b) An immunostained human retina section covering the foveal pit. Adapted from Cuenca, et al. [22].

There is another important axis inside the eye to be considered. It connects the nodal point with the center of the optic disc. This axis, being involved with the phenomenon known as the Mariotte's blind spot, will be indicated here with the Greek symbol μ. From Fig. 5.3 we see that, on the right eye, the optic nerve is oriented toward the nasal part of the head, diverging on average by ~15°±2° from the visual axis, as resulted from my tests (see next section D). The optic nerve of the left eye, also, is oriented toward the nasal side of the head, as well known. The two eyes, therefore, are symmetrical with respect to a vertical plane crossing the center between the two eyes. This property has many interesting consequences, some of which will be discussed in Section 5.4.4.

The last topic of eye physiology concerns the accommodation mechanism, by which the eye, starting from a state of relaxation corresponding to long-distance vision, called also

unaccommodated state, is subject to a modification of its refractive part when it has to focus on a nearby object. As we will see, this topic is of fundamental importance when we discuss the results of Mariotte's blind spot test (see Section 5D). The activity of accommodation allows the eye to create focused images of objects at various distances on the retinal plane. The topic of accommodation has occupied scientists for almost 300 years [26-28], during which various theories have been presented, starting with the first demonstrations by Scheiner [29] at the beginning of the seventeenth century. Even Descartes addressed this topic, speculating that changes in the refractive power and shape of the crystalline lens might be responsible for the ability of the human eye to see objects at varying distances. The most accredited theory remains today the theory proposed by Helmholtz [30, 31], called relaxation theory of accommodation (see Fig. 5.8) [32]. He observed that when the eye is in the unaccommodated state and focused for distance, the ciliary muscle is relaxed and the elastic zonular fibers are in a state of tension, pulling the crystalline lens outwards at the equator and maintaining the lens in a flattened state. He further observed that during accommodation, the ciliary muscle contracts, causing a reduction in the zonular tension that allows for the increase in curvature of the crystalline lens, a decrease in its equatorial diameter, and increased lens thickness; an increase in the curvature of the anterior surface of the crystalline lens with only a small change in the curvature of the posterior surface of the crystalline lens; a forward movement of the anterior surface of the crystalline lens whilst the posterior surface showed no appreciable movement; and an increase of 0.5 mm in the axial thickness of the lens during accommodation. Given that the lens volume is constant, Helmholtz [30] concluded that the lens equatorial diameter decreased during accommodation. Helmholtz's relaxation theory of accommodation [30] has received support and modifications from other researchers [26]. The efficiency of this process declines with age. Usually, the range of power change that the eye is capable of, or amplitude of accommodation, diminishes to zero by the age of ~50 years (a maximum 2D residue is measured) [3, p. 12].

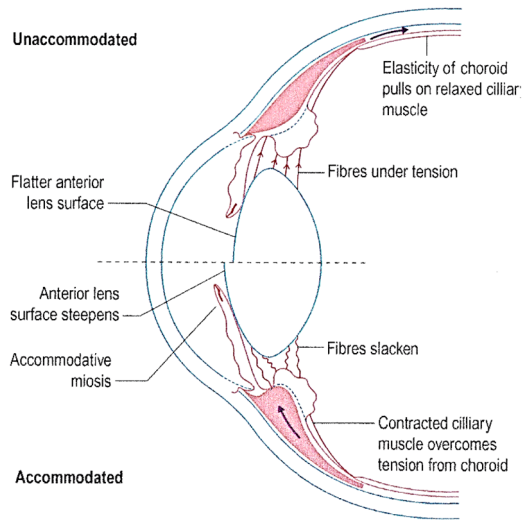

Fig. 5.8. Changes in the anterior eye during accommodation. (After Pipe & Rapley, [33]).

5.3. Experimental Section

5.3.1. Materials and Instrumentation

The mires used for the various tests in the dark, in positive contrast (black background), were made using photoluminescent stickers or paints. The mires used for the various tests in the light, in positive contrast, were made using white paints; those used in negative contrast were black optotypes printed on white paper sheets or projected by a monitor screen. All tests were associated with luminance measurements of the marks and/or their background, and of the environment with two luxmeters: the LUTRON LX-1108 (lx1) and the LUTRON LX-1102 (lx2) [4, p. 108]. The lighting in the dark of the PL marks was carried out with UVA light by using LED torches or panels, while in the light the marks were illuminated with white light LED lamps or flat panels, or with sunlight. The PL stickers used were of two types. The first ones were preformed circular stickers of light green color from Becho, used for living room decoration. They were used mainly for the test of the angle of view in the dark as dots of 10 and 20-mm diameter. The second ones were made from light green PVC adhesive tapes from Ontwie (Furnrubden), used for realizing the PL slit in the test of the minimum angle of resolution (MAR). A PL paint of light yellow-green color, Aurora Bright Green, from the SpaceBeams company, was used to draw the PL optotypes for the morphoscopic vision acuity tests in the dark. For the excitation of the stickers and PL paint with UVA light, Wood lamps with LED sources were used. The first one was a torch of the Youthink company, mod. YT-UL03, operating at λ = 395nm and the second one was a torch of the company Alonefire, mod SV53 15W, operating at λ = 365 nm. These two UVA torches were initially used to illuminate the logMAR PL chart during the first morphoscopic visual acuity measures in the dark, but their limited angular extension required the presence, during the test, of an operator directing the beam of light on the optotypes that were gradually read by the subject, taking care to orient the beam at the correct angle and distance, according to what previously resulted from the calibration measurements. Furthermore, this type of battery-powered LED sources were unable to keep a constant intensity beam during long times, so the morphoscopic VA tests were subsequently performed using mains-powered UVA-LED sources, consisting of a pair of 10 × 20 cm^2 flat LED lamps from Createstar, mod. CHX-FL-A-100W, operating in the wavelength band 395-405 nm. These sources were also used to measure the luminance of the PL optotypes and of its decay.

This work was initially tackled using easily available materials (see Fig. 5.9 (a)), some low-cost tools, such as those shown in Fig. 5.9 (b), and a series of spotlights not shown, commonly used for lighting up the house. In the course of the work, however, to simplify the set-up of the experiments and make the measurements quicker, other sources were added, like two luxmeters, LUTRON LX-1102 and LX-1108, this last shown in Fig. 5.9 (c)-(d), the two extended sources of UVA light (see Fig. 5.9 (e)) and an extended source of white light, the LED panel from Parko, Mod. IP54 (35 W, 5000 lm, 4000 K), whose intensity can be dimmed to 100 %, 50 % and 20 % (see Fig. 5.9 (f)). As it can be deduced from Fig. 5.9, this work can be replicated either by students with a small investment, or by professionals with a higher investment.

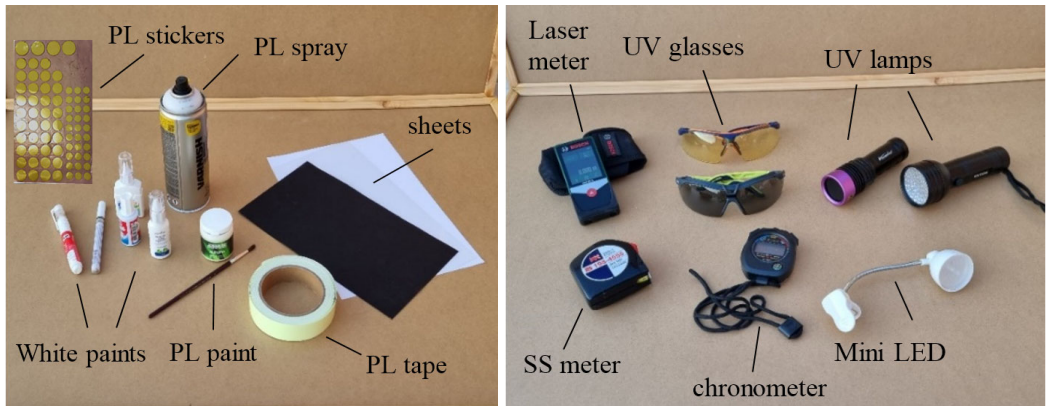

(a) (b)

(c) (d) (e) (f)

Fig. 5.9. (a) The basic materials used for carrying out the experiments in the dark; (b) Some instruments for measuring distance and time, various lamps and protective glasses; (c) The luxmeter LX-1108, and (d) its sensor; (e) One of the UVA LED light panels; (f) The white light LED panel.

The use of UVA lamps was always done by protecting the operator and the collaborator with safety glasses. Two types of Uvex glasses were used; the first, mod. i-vo, with clear yellow-orange lenses (indicated also as LG, light glasses), and the second, mod. i-5, with dark anthracite/lime lenses (indicated also as DG, dark glasses) (see Fig. 5.9 (b)). The attenuation factor, F, operated by the glasses with respect to the UVA light source of the LED panels was first measured. Fig. 5.10 shows the sensor (se2) of the luxmeter (lx2) facing the UVA LED panels and one of the glasses (gl) used for the test. By alternating a measurement with the naked sensor, with one with the two lenses, we obtain the attenuation factor F. By placing the LED sources at various distances from (se2), the average value, reported in Table 5.1, is obtained for the two glasses, together with the corresponding transmittance $T = 1/F$. As it can be seen, both glasses are very effective in blocking UV radiation, with a factor $F = 10$ for the Uvex i-vo lenses and $F = 30$ for the Uvex i-5 lenses. A second measurement concerned the attenuation factor of the Uvex glasses with respect to the photoluminescence light emitted by the optotypes of the

logMAR chart in the dark. For this purpose, a 10cm-dia disc was prepared, painted with PL paint, the same used to paint the PL optotypes (see Fig. 5.11 (a)). The disc is then illuminated with the UVA LED panels, and is flanked by the sensor (se2) of the luxmeter (lx2), positioned so as not to intercept the direct UVA light (see Fig. 5.11 (b)).

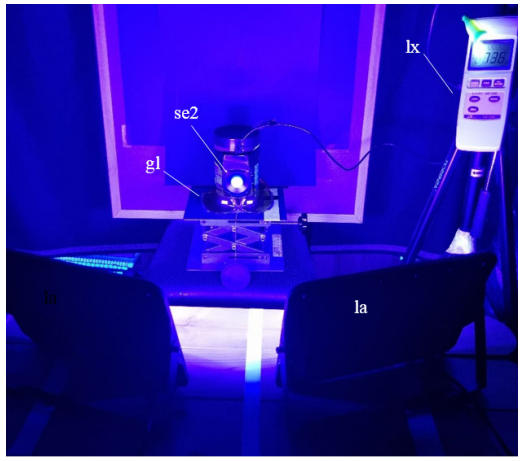

Fig. 5.10. Photo of the apparatus used to measure the attenuation factor by Uvex glasses of the UVA light from the two LED panels. The sensor (se2) with or without glasses lenses (gl) are faced to the two LED lamps (la). The light intensity is measured by luxmeter (lx2).

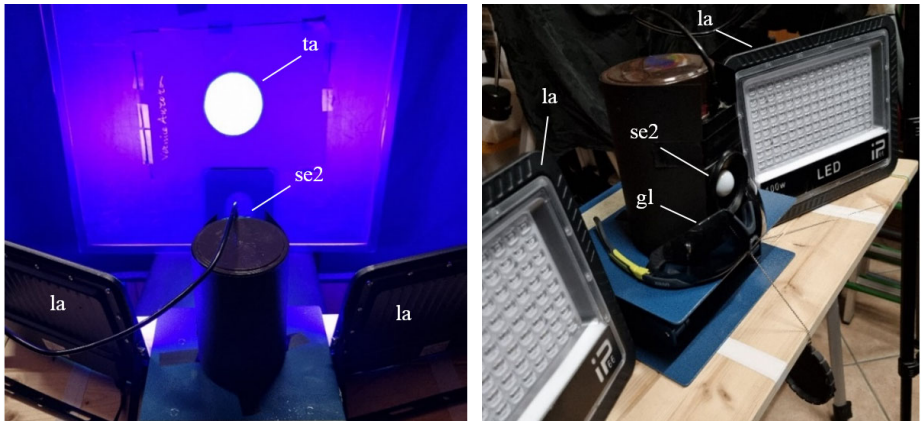

(a) (b)

Fig. 5.11. Photos of the apparatus used to measure the attenuation factor by Uvex glasses lenses (gl) respect to the photoluminescent light emitted by the target disc (ta) illuminated by two LED UVA lamps (la). (a) The apparatus during the measurements; (b) The sensor (se2) is positioned in such a way to not see the direct light from the panels (la).

The measurement of the attenuation factor F (and the corresponding transmittance $T = 1/F$) of the lenses is carried out in the following way:

i) Measurement on the bare sensor (se2) exposed to the illuminated target (disc);
ii) Measurement on the bare sensor with the target masked by a black paddle. The difference between the two measurements provides the light emitted only by the disc;
iii) Measurement on the sensor covered by a lens and exposed to the illuminated target;
iv) Measurement on the sensor covered by a lens, with the target masked by a black paddle.

The difference between the two measurements provides only the light transmitted to the sensor through the lens. The ratio between the two differences provides the attenuation factor F of the lens (i.e. its transmittance $T = 1/F$). This sequence of measurements is then repeated at least ten times. The Uvex glasses, LG and DG, are used both for protecting the eyes from UVA light and for reading the PL optotypes at dark. The attenuation factor of the Uvex Glasses for the two uses is reported in Table 5.1.

Table 5.1. Results of Attenuation Factor F (Transmittance $T = 1/F$) of the Uvex Glasses at UVA and PL Light.

Glasses	UVA source	PL light
Uvex i-vo (LG)	$F = 10\pm2$ $T = 0.1\pm0.02 = 10\pm2\%$	$F = 1.14\pm0.04$ $T = 0.88\pm0.03 = 88\pm3\%$
Uvex i-5 (DG)	$F = 30\pm5$ $T = 0.03\pm0.005 = 3\pm0.5\%$	$F = 4.3\pm0.4$ $T = 0.23\pm0.02 = 23\pm2\%$

The two glasses behave differently also with respect to PL light; it is transmitted, in fact, at almost 90% for the light glasses (LG), which therefore appear quite transparent to the eye, while it is transmitted at about 20% for the dark glasses (DG). This data will be taken into account when discussing the results of the morphoscopic AV test made in presence of the glasses and as function of the target luminance. The white light sources used for the indoor VA tests were a series of LED lamps arranged around the tables to have a fairly constant luminous flux, or a single flat light source (25x15 cm^2) of 5000 lm, from Parko S.r.l., dimmable on three positions: 20%, 50% and 100% (see Fig. 5.9 (f)). The LUTRON LX-1102 and LX-1108 luxmeters were used for luminance measurements of optotypes and their background, and for indoor and outdoor illuminance measurements on surfaces. The sensor of the luxmeters has a dome with a diameter of 21.5 mm, and area A_d = 363 mm^2. The digital laser BOSCH PLR 50 C was used for optical distance measurements (see Fig. 5.9 (b). Although the materials and instrumentation used were easy to acquire and cost-effective, much manual work was required for the preparation of the logMAR charts with PL or white optotypes. Lacking of a series of normographs covering the entire range of font sizes (factor 20), in fact, all those optotypes were drawn manually.

The white characters were drawn by using white paint pencils easily found in a stationery shop, the PL ones were drawn by using a brush and the Aurora PL paint. Moreover, for the preparation of the logMAR charts to test the morphoscopic acuity, being particularly difficult to prepare the smallest optotypes, those relative to highest visual acuity (VA), by using painting methods, it was decided to operate at the distance of 6 m, to have the

smallest characters with height not less than ~5 mm. Furtherly, being difficult to have 6m indoor distance in the laboratory, a mirror was interposed between the observing subject and the chart, having so an optical path of 3+3 m, compatible with a small environment. The use of a mirror naturally involves the drawing of inverted characters on the chart. The mirror reflectance was measured at the red light of a laser and resulted to be of ~90 %. This data has been used to correct the luminance measured in front of the PL targets in the dark, into the luminance effectively perceived by eyes through the mirror.

The optometric charts were prepared as follows. The base of the chart is a large black cardboard (70x50cm). The chart could not be drawn directly on it, but individual parts of it, already prepared on the computer with the correct dimensions, were printed on sheets of transparent A4 paper; these were then turned over and new sheets of transparent paper were placed on them. Finally, on this paper the white or the photoluminescent characters were painted by a brush, which obviously appeared inverted (left exchanged with right) (see Figs. 5.12 (a), (b)).

The morphoscopic VA tests were also performed by using a computer monitor (see Fig. 5.12 (c)). Fig. 5.12 (a) shows the logMAR chart with the white optotypes drawn on the back of transparent sheets, placed on a black cardboard bottom and lightened by white light lamps or sunlight. Fig. 5.12 (b) shows the logMAR chart with the PL optotypes drawn on the front of transparent sheets, placed on a black cardboard bottom and lightened by UVA lamps. Fig. 5.12 (c) shows the logMAR chart projected by a PC monitor in negative contrast. With tests carried out in the dark, the subject is made to observe differently colored cards; if he has truly achieved scotopic vision, he will not distinguish colors because the cones photodetectors are deactivated. The scotopic vision is reached after about twenty minutes [3, p. 71; 4, p. 125].

(a) (b) (c)

Fig. 5.12. (a) LogMAR chart realized in positive contrast on black cardboard, by using white paint; (b) LogMAR chart realized in positive contrast on black cardboard, by using photoluminescent (PL) paint; (c) LogMAR chart projected in negative contrast by the monitor of a PC. The chart in (a) is lightened with white light lamps or with sunlight; the chart in (b) is lightened by UVA Wood lamps. The characters are inverted because viewed through a mirror.

5.3.2. Luminance Measurements

The luminance measurements described below refer to the morphoscopic visual acuity charts, of decimal or logMAR type, and concern the luminance of the fundus, in the case of charts with negative contrast, such as the decimal ones on white paper sheets, and the logMAR ones on monitor, or the luminance of the optotypes, in the case of logMAR charts with white or PL optotypes. For the test of morphoscopic VA in the light by using the monitor of a PC, the logMAR chart was drawn in negative format, i.e., with the bright background and black characters. It was then a matter of measuring the luminance of the background by removing the characters.

The measurement of monitor (mo) luminance is simple, because it is homogeneous over the entire surface. It was masked with a black cardboard sheet (sh) with a hole of known diameter $D = 2R = 12$ cm, as illustrated in Fig. 5.13. In front of the monitor, a tripod (tr) supports the sensor head (se) of the luxmeter (lx) and is moved back and forth to change its distance d from the monitor (mo). For having the luminance L_v of the monitor at normal direction, it is simply a matter of measuring the illuminance E_v recorded on the luxmeter as a function of distance d. To limit the influence of ambient light, it is preferable to work in the dark, making two measurements, a first one with the light from the naked monitor, and the second one covering the monitor by a black paddle, making in this way the background light to be subtracted from the first measurement.

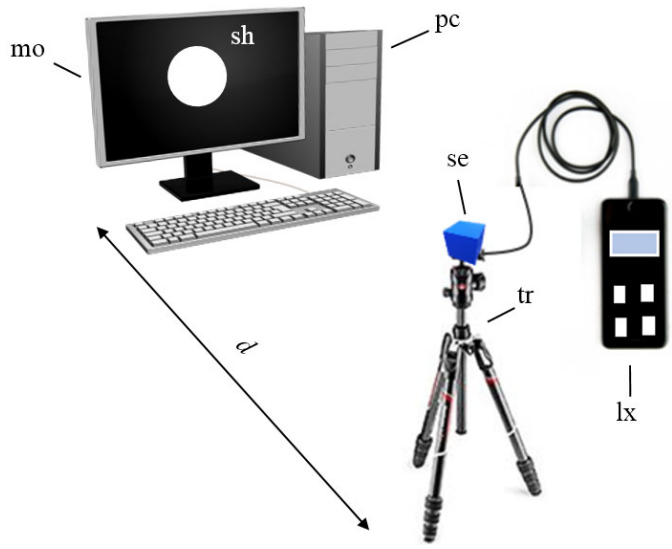

Fig. 5.13. A schematic experimental set up for measuring the monitor luminance.

To understand how to derive luminance from illuminance measurements vs. d, we refer to the scheme of Fig. 5.14. We select, on the monitor disk, a portion of area, $dA = 2\pi\,\rho \cdot d\rho$, corresponding to a circular crown, of radius $\rho < R$, subtending the angle α respect to the sensor center.

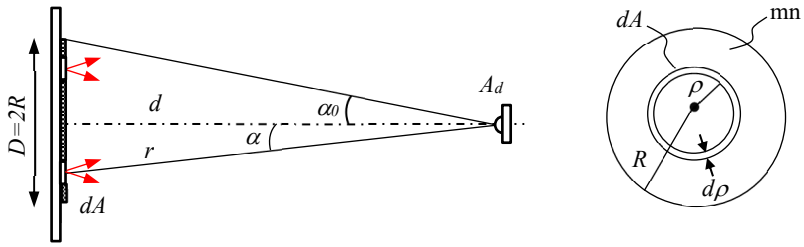

Fig. 5.14. Schematic of the measure of monitor luminance. The sensor area is A_d = 363 mm^2.

The elementary luminous flux $d\Phi$, emitted by the elementary area dA, can be expressed as:

$$d\Phi = \frac{L_v \cdot A_d}{d^2} \cdot cos\alpha^4 \cdot 2\pi\rho \cdot d\rho \tag{5.1}$$

The total emitted flux, Φ, becomes:

$$\Phi = \frac{2\pi\, L_v \cdot A_d}{d^2} \cdot \int_0^R d\rho \cdot \rho \cdot cos^4\alpha \tag{5.2}$$

Moving from variable ρ to variable α, we have:

$$\Phi = \frac{2\pi\, L_v \cdot A_d}{d^2} \cdot \int_0^{\alpha_0} d\alpha \cdot sin\alpha \cdot cos\alpha = \pi\, L_v \cdot A_d \cdot sin^2\alpha_0 = \pi\, L_v \cdot A_d \cdot \{sin[tg^{-1}(R/d)]\}^2 \tag{5.3}$$

Being the total flux measured by the luxmeter:

$$\Phi = E_v \cdot A_d \tag{5.4}$$

from Eqs. (5.3) and (5.4), we obtain finally for the luminance of the monitor:

$$L_v = \frac{E_v}{\pi\{sin[tg^{-1}(R/d)]\}^2} \tag{5.5}$$

Eq. (5.5) provides the correct luminance of the target at normal direction if the distance from the luxmeter is sufficiently high, because the sensor (se) does not absorb light uniformly at any direction. To this purpose, the measurement of illuminance E_v must be made as a function of distance, taking valid that value of luminance L_v, calculated from Eq. (5.5), corresponding to the saturation level. The so obtained luminance value L_v is correctly assigned to the source if it is at the distance higher than that for which the calculated L_v value reaches the saturation level.

The results of the luminance measurements on the monitor of Fig. 5.13 are obtained as following. The experimental data of E_v (lux) give an exponential decay as function of distance at d >10 cm (see Fig. 5.15 (a)). By applying Eq. (5.5), the function L_v shows an exponential growth with a plateau at 126 ± 2 cd/m^2 reached for distance values d > 40 cm (α_0 < 8.5°) (see Fig. 5.15 (b)).

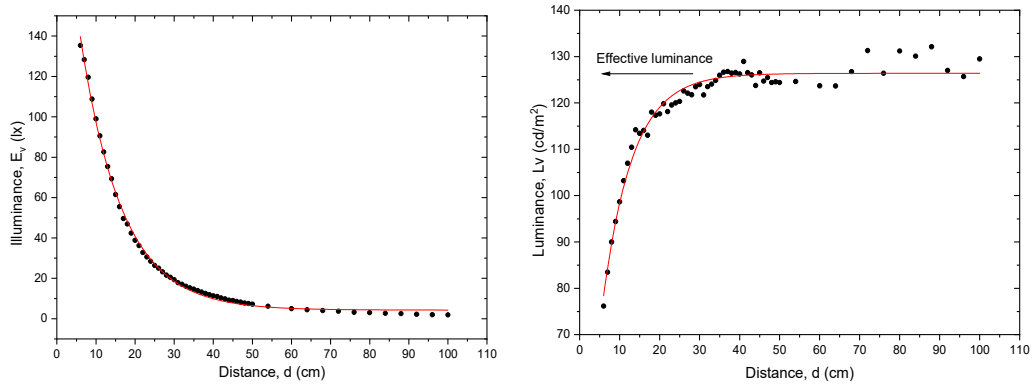

(a) (b)

Fig. 5.15. (a) Results of monitor illuminance Ev as function of distance d, as measured by the luxmeter in Fig. 5.13; (b) Results of the luminance quantity Lv, derived from Eq. (5.5), as function of distance d. For distances d > 40 cm the calculated quantity reaches the saturation at the correct luminance value.

The monitor can be approximated therefore to a Lambertian source at low angles of incidence on the detector surface ($\alpha_0 < 8.5°$) and high distances ($d > 40$ cm). This was respected by the experimental condition at which the morphoscopic VA test on monitor was conducted ($d = 2$m).

For measuring the luminance of a decimal chart printed on a white paper sheet, and with black characters in negative contrast, I used the schematic experimental apparatus shown in Fig. 5.16 (a**)**. As the decimal chart was drawn on a white paper sheet, this was covered with a black cardboard sheet (sh) with a hole of radius R = 7cm. The illumination was provided by a series of white light lamps, schematized by a single lamp (la) in Fig. 5.16(a**)**. As an alternative, I have used the LED light panel of Parko, shown in Fig. 5.16 **(**b**)** during calibration measurements, where it is visible the luxmeter (lx) and its sensor (se) placed at the end of a telescopic rod (tr), with a PL ruler used to precisely marking the distance of the sensor from the source.

The illuminance curve of the disc source, as a function of distance, shows, as for the measurements on the monitor, an exponential decay (see Fig. 5.17 (a)). From the curve of the E_v due to the source alone and applying Eq. (5.5), the curve of the source luminance, L_v, is derived, which is shown in Fig. 5.17 (b). The curve of L_v is sufficiently flat to assign an average value of 1055±56 cd/m^2.

The measurement of luminance of the white optotypes, drawn on the back of a transparent sheet, and used in the logMAR chart for the testing of morphoscopic VA with white light, was carried out using the LED light panel source provided with the setting for different lighting levels. The schematic experimental apparatus is illustrated in the photo of Fig. 5.18.

Here the white LED light source panel (pa), seen from behind, is placed at a distance of ~1m from the target (ta) and inclined of ~30° with respect to the surface normal, in order not to interfere with the movement of the sensor (se1) carried by the telescopic rod (tr). The illuminance E_v produced by the disk target (ta), of 80mm-dia, on the sensor (se1) is measured by the luxmeter (lx1) (LX-1108) as a function of distance, by moving the telescopic rod (tr) in front of (ta). The light intensity of the panel (pa) is monitored by the luxmeter (lx2) (LX-1102) by means of a second sensor (se2) dislocated near the target.

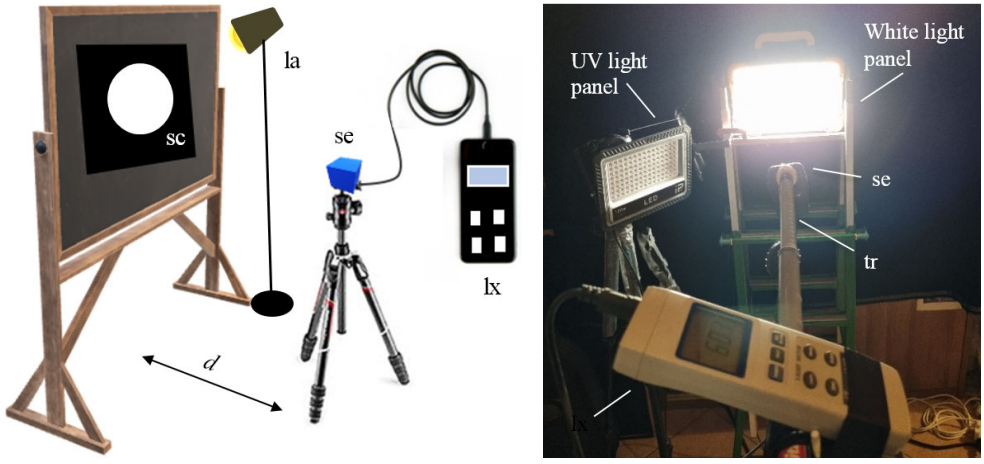

(a) (b)

Fig. 5.16. (a) Schematic experimental set up for measuring the luminance of a white chart. The lamp (la) is a white light source; (b) The white LED light panel is shown during the calibration phase.

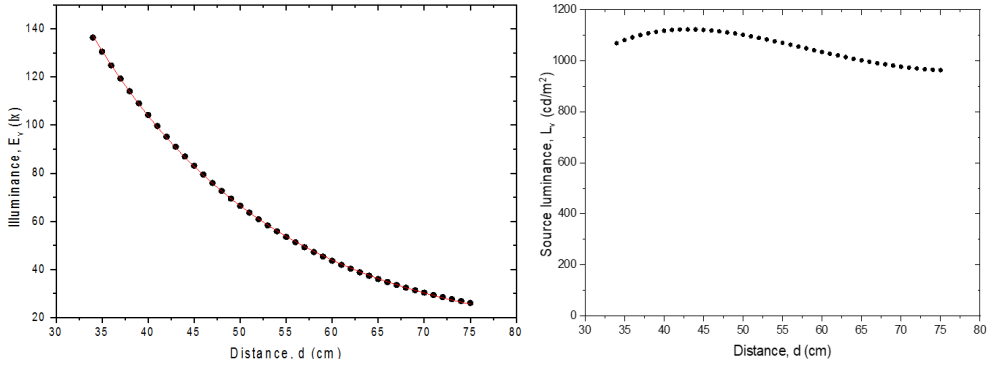

(a) (b)

Fig. 5.17. (a) Result of the illuminance measured by the luxmeter, as function of distance *d* from the illuminated disk of Fig. 5.16 (a); (b) Result of luminance of the white disk of Fig. 5.16 (a), as function of distance *d*, as derived from Eq. (5.5).

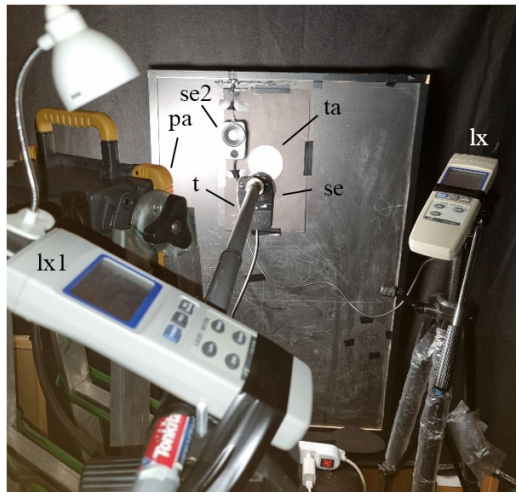

Fig. 5.18. Photo of the experimental apparatus used during the measurement of luminance of the white paint disk target (ta); (pa) is the white light LED panel source used for lighting the target (ta), whose illumination is measured by the luxmeter (lx1) through sensor (se1), moved by the telescopic rod (tr). The luxmeter (lx2), through the sensor (se2), is used to monitor the intensity of the source panel (pa).

Fig. 5.19 (a) shows the exponential decay of the illuminance E_v recorded setting the light source at 50% light level. The corresponding L_V function, calculated through Eq. (5.5), is reported in Fig. 5.19 (b). The normal distribution of the data of L_V of Fig. 5.19b gives the following values for the luminance: 110±4 nit.

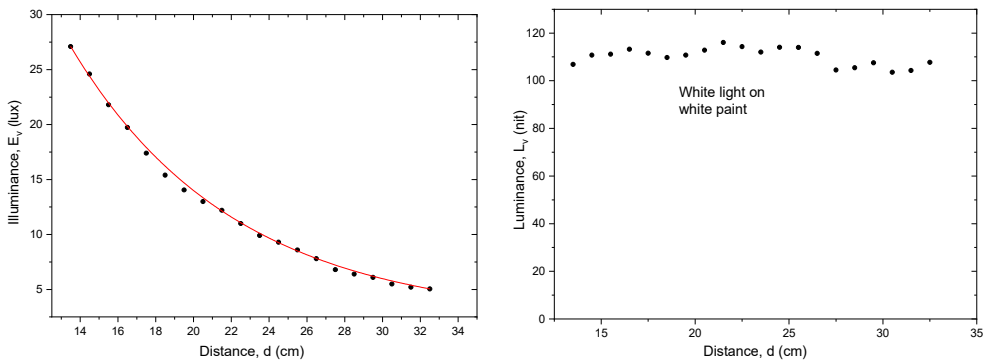

(a) (b)

Fig. 5.19. In (a) it is shown the exponential decay of the illuminance E_v, measured by the luxmeter (lx1) as function of the distance d from the disk made with white paint. In (b) it is shown the luminance L_v calculated by applying Eq. (5.5).

The L_v luminance measurements, obtained by the data of E_v illuminance, measured using the LX-1108 luxmeter, were followed by E_S illuminance measurements made directly on

the target surface, moving the sensor (se2), of the LX-1102 luxmeter, in front of the disc target (ta). Similar measurements of E_S were done by using the LX-1108 luxmeter. The number of E_S measurements ranged from a minimum of 80 to a maximum of 100. The measurements of the two luxmeters were then compared and the result is that LX-1102 provides higher values (higher sensitivity) than LX-1108 by a factor of 1.17+/-0.04.

The L_v and E_S data, these last normalized to the LX-1108 luxmeter, were obtained at the three lighting levels available for the LED panel source: 20 %, 50 % and 100 %. Two experimental setups were also chosen (see Table 5.2): in the first (a), the light source was placed at 1 m distance from the target and inclined by 30°; in the second (b) the light source was placed at 0.5m distance from the target and inclined by 40° (with respect to the surface normal). From the L_v and E_S results, the average reflectance R_S was then calculated, applying Eq. (5.6):

$$L_v = E_s \cdot R_s / \pi \tag{5.6}$$

Rosenfield & Logan [3, p. 71] report that $L_v = E_s \cdot R_s$; in reality, the correct formula is given by Eq. (5.6). The final results are summarized in Table 5.2, in terms of illuminance on the white paint target surface, luminance produced by the target, and target surface reflectance. The white paint target was illuminated with the white LED light panel at three lighting levels, and at two setup conditions: (a) source distance d = 1m; α = 30°; (b) source distance d = 0.5m; α = 40°.

Table 5.2. Summary of Optical Results obtained for the White Paint Target.

Set	Source level (%)	Illuminance E_S (lx)	Luminance L_v (nit)	Surface Reflectance R_S
a)	20	188±5	43±2	0.72±0.05
	50	490±18	110±4	0.70±0.05
	100	867±28	205±8	0.74±0.05
b)	20	780±24	165±3	0.66±0.04
	50	2078±91	461±22	0.70±0.06
	100	3766±175	799±7	0.68±0.04

Table 5.2 shows that, with these experimental conditions, it is possible to carry out AV tests with logMAR chart with white paint optotypes, on five luminance intervals (considering that setup (a) at 100 % is similar to that of (b) at 20 %), doubling the size each time from approximately 40 to 800 nits. Fig. 5.20 shows the relationship between the white light illumination on the target surface, E_S, and the luminance L_v produced by the same target. The relationship between L_v and E_S shows a near perfect linearity with the law:

$$L_v(\text{nit}) = 3.55\ (\pm 2.55) + 0.211\ (\pm 0.003) \cdot E_S\ (\text{lx}) \tag{5.7}$$

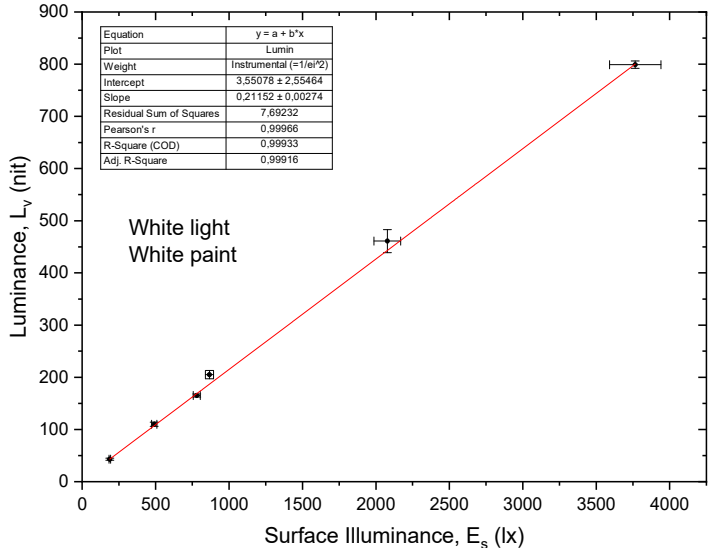

Fig. 5.20. Luminance of the target of white paint as function of the surface illumination by a white light source.

The last column of Table 5.2 reports the surface reflectance values calculated individually with Eq. (5.6) for the six lighting illuminating conditions. For the average surface reflectance of the white paint, plus the transparent sheet in front, we obtain the value of: 0.70 ± 0.05. The R_S measurements of the white paint sample are conditioned by the presence of a transparent paper sheet in front of the paint. The problem arises from the fact that, initially, it was not thought of using a mirror to carry out the VA test, as it was thought that 6m of space was available. This is the reason why the white optotypes were initially painted in the right orientation and over the transparent sheet. Subsequently, we had to work in a smaller space, compatible with half the distance, 3m, and therefore the transparent sheets with white optotypes of the logMAR chart were turned over to read the optotypes in the right orientation when seeing them through the mirror. The LED panel was placed at a distance of ~40cm and with an inclination of ~30° with respect to the target (see Fig. 5.21).

Subsequently, I decided to perform the morphoscopic AV test with the LogMAR chart with white optotypes placed in front of the transparent sheet. But, in order not to reconstruct the logMAR chart, which would involve a huge amount of work, I decided to do an alternative test using the same sheets reversed. In this way, the disturbance produced by the reflections on the transparent sheet is avoided. Of course, by reversing the sheet, also the optotypes are reversed, but this should not constitute a problem during their reading if the observer is aware of it. The measurement of luminance on the inverted optotypes was carried out as previously on a target of 8cm in diameter, illuminated with the LED panel set to 100% intensity and placed in the conditions indicated in point (b) of Table 5.2. The result was: L_v = 812 ± 20 nit, a value very close to that recorded with the presence of the transparent sheet (see Fig. 5.22).

Fig. 5.21. The logMAR chart with white optotypes lightened by the white light LED panel.

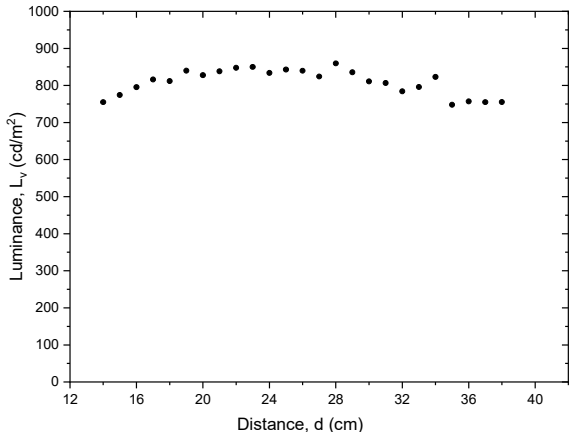

Fig. 5.22. Luminance Lv of the target of white paint sheet (free of the transparent sheet), as function of distance, derived applying Eq. (5.5).

The reflectivity of the optotypes painted with white paint on the transparent sheet was obtained from the E_S measurements on the surface of the target. We obtain: $E_S = 3615 \pm 50$ lx, from which, applying Eq. (5.6), we obtain: $R_S = 0.71 \pm 0.03$, practically the same result obtained with the presence in front of the transparent sheet (see Table 5.2). We conclude that the presence of the transparent sheet in front of the optotypes does not significantly alter the luminance measurement.

I have shown that, to get the luminance L_v of a surface reflecting source, there is an alternative way respect to its direct measurement as function of distance from the target, as illustrated in Fig. 5.16(a). In fact, when the approximation of the surface source to a Lambertian source can be admitted, and this is always valid when the angle under which

the target is seen by the (se1) sensor is small, the luminance can be expressed by the simple Eq. (5.6), when the reflectance R_S of the surface is known. Therefore, by only one measure of E_S, and knowing R_S, it is possible to get the luminance of the target. On the contrary, by measuring both E_S and L_v it is possible to obtain the target surface reflectance R_S once and for all, by applying Eq. (5.6). To obtain the surface reflectance of a white paper sheet used during the VA tests with decimal charts, a series of 24 measurements of R_S, distributed over the entire surface of the circular source of Fig. 5.16, were carried out, resulting in the following value for the illuminance: E_S = 3818±152 lx, which, combined with the value of L_v = 1055±56 cd/m^2, gave for the reflectance of the white paper sheet the value: R_S = 0.87±0.08. This value seems realistic for a white cardboard surface and in agreement with literature values [34]. The knowledge of R_S allows us to get an estimate of the luminance of a source when it is a light reflecting surface, just after some illuminance measurements on the surface itself, and the application of Eq. (5.6), without using the complicated setup of Fig. 5.16(a), requiring E_v measurements as a function of distance. Eq. (5.6) cannot be used, of course, to measure the luminance of a monitor (see Fig. 5.11 (c)) or of a PL source.

A first attempt to measure the luminance of the photoluminescent (PL) optotypes of a logMAR chart was made using a UVA torch (λ = 395nm) as a source. I adopted the same scheme shown in Fig. 5.16 (a). A circular target (D = 10cm) was realized by passing three coats of yellow/green PL paint on the transparent sheet masked by a black cardboard (bc) in order to have the same PL surface as that of the optotypes (see Fig. 5.23 (a)). The target was then illuminated with the torch lamp (la) fixed on a tripod 20 cm away and inclined of 45° (see photo in Fig. 5.23 (b)). The luminescence light decays very quickly (see next Section), so, during the measurements, the lamp was kept lit and pointed at the target. The measure of E_v as a function of distance d was made with the luxmeter (lx) placed on a second tripod (see the photos in Figs. 5.23 (b) and (c)). Applying Eq. (5.5), a luminance of L_v = 190±10 nit was finally found. The use of a UVA torch for measuring the luminance of PL optotypes is not suitable, however, for carrying out precise measurements, since the battery power supply inevitably leads to a reduction in intensity when carrying out long measurements. Consequently, two mains-powered panels were chosen as UVA light sources, which are placed laterally to the target and at a suitable distance and orientation to obtain a certain level of luminance from the target, as we will see in the description below.

The measurement of luminance of PL optotypes was carried out using the experimental apparatus illustrated in Fig. 5.24. The measurement procedure is similar to that adopted for the luminance of the white optotypes in white light (see Fig. 5.18), but the light source consisted of two UVA LED panels (see Fig. 5.9 (e)). The target, a circle with a 10cm-diameter, was made by spreading PL paint on the surface of a transparent sheet placed on a black background and masked with black cardboard. To measure the intensity of the UVA light on the surface of the target, since not having a spectrometer for the ultraviolet region, I limited myself to making a relative measurement of E_S illuminance using the same luxmeter (lx2) LX-1102, with sensor (se2), for the measurements in white light. The luxmeter (lx1) (LX-1108) was used for the E_v illuminance measurement, but the

sensor (se1) was now coupled to a high-pass filter (ft), with cut-off wavelength $\lambda = 370$ nm (see Fig. 5.25) to block the ultraviolet light.

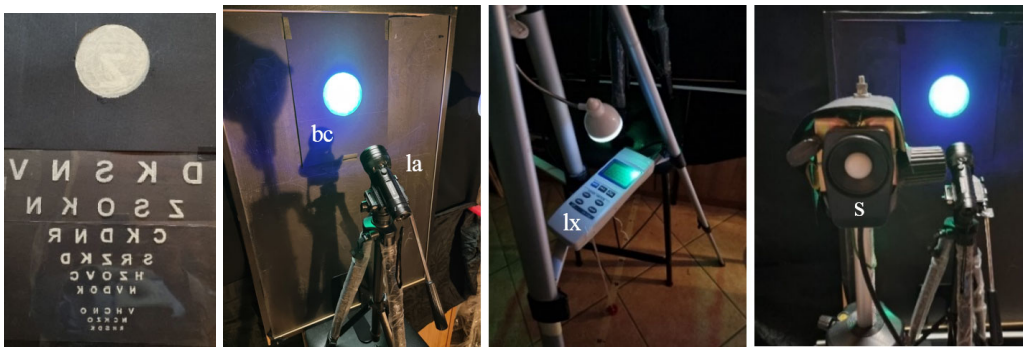

(a) (b) (c) (d)

Fig. 5.23. (a) Photo of the circular PL target, similar to the optotypes of the PL chart, used to measure the luminance; (b) Illumination of the circular PL target by a Wood torch; (c) The illuminance value on the luxmeter is read in the dark by using a small LED lamp fixed on the tripod; (d) The sensor of the luxmeter mounted on the tripod is shown.

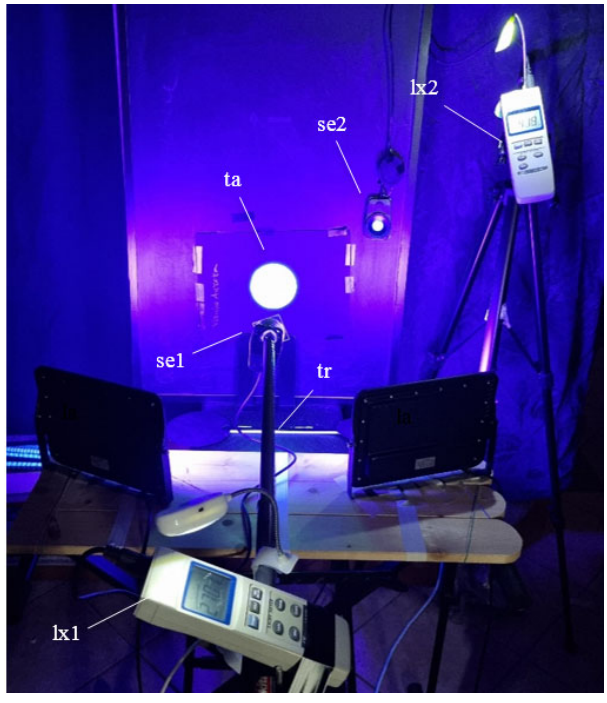

Fig. 5.24. Photo of the experimental setup for measuring the luminance of the 10 cm-diameter photoluminescent target (ta), illuminated with the two UVA LED panels.

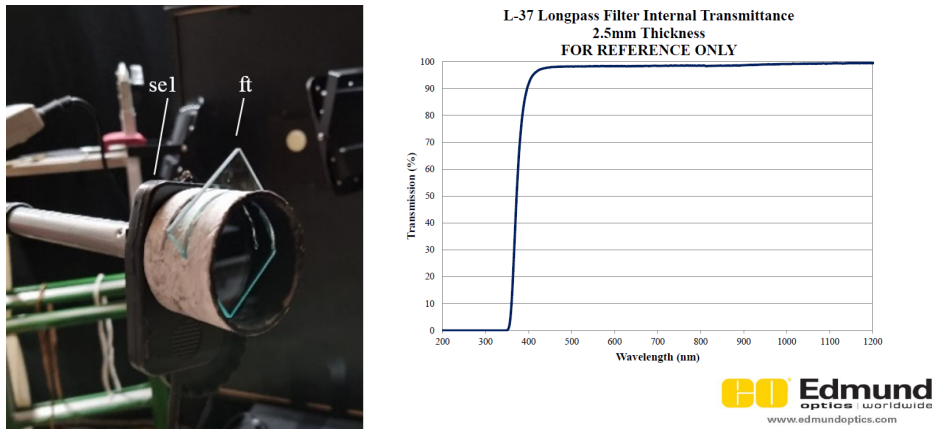

(a) (b)

Fig. 5.25. (a) Photo of the Edmund L-37 filter. (b) Corresponding optical transmittance curve.

The luminance measurements were made at different distances of the two LED panels from the target. The aim was to trace a correlation curve between the relative illuminance E_S on the target surface and the luminance L_v of the target itself. For this purpose, seven series of measurements were made in the E_S range from ~200 to ~1000 lx. The relative L_v curves, as a function of the sensor distance (se1) from the target (ta), are shown in Fig. 5.26.

By selecting the L_v values corresponding to the saturation level, the graph in Fig. 5.27 is obtained, which shows the following linear trend between L_v and E_S:

$$L_v = -5(\pm 5) + 0.59(\pm 0.01) \cdot E_s \tag{5.8}$$

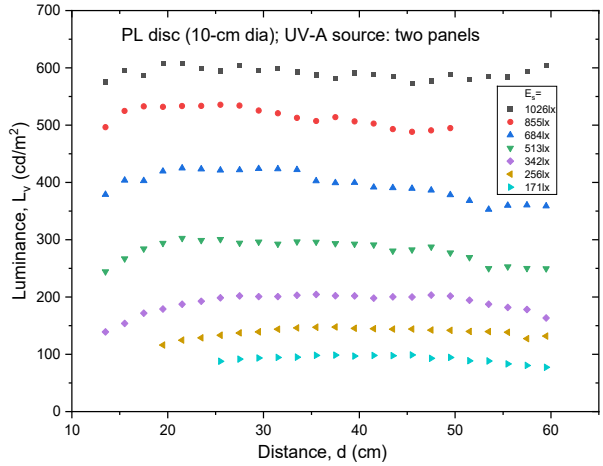

Fig. 5.26. Luminance curves E_V of the PL disk simulating the PL optotypes, as obtained from Eq. (5.5), reported for seven illuminance values E_S on the target surface.

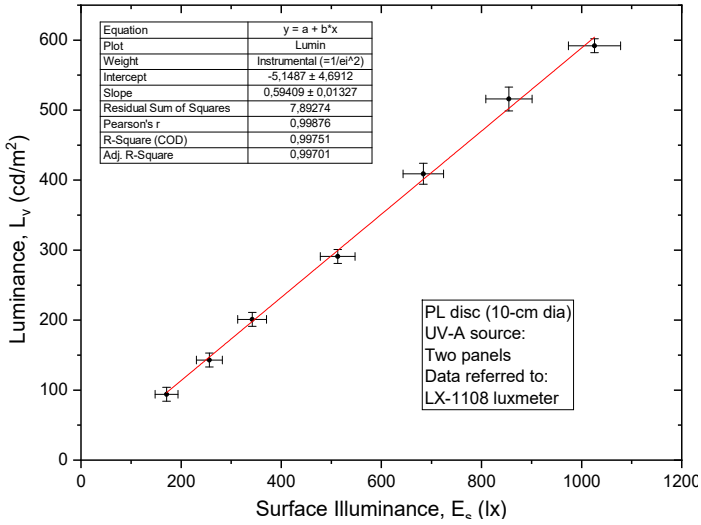

Fig. 5.27. Average luminance L_v of the PL disk simulating the PL optotypes, expressed as a function of the illuminance E_S on the target surface.

Eq. (5.8) allows us, during AV morphoscopic tests, to estimate the luminance of the optotypes on the logMAR chart as a function of the illuminance value measured with the luxmeter on the table surface. The outdoor measurements of luminance of the white characters of a logMAR chart, exposed to sunlight, were done by measuring the irradiance E_S on the surface and applying Eq. (5.6) after placing $E_S = 0.71 \pm 0.03$, and the results of illuminance were in the range $L_v \sim 1.5 \pm 6.7$ knit (see Table 5.8).

5.3.3. Luminance Decay of PL Optotypes

The measurement, or rather the estimate, of the time constant of the decay of the luminance of a PL target was necessary to evaluate the luminance level below which it is possible to perform the angle of view test. This test, in fact, is the only one that requires low luminance levels, because the conical photoreceptors, after being adapted to the dark, that is inactive, must be kept as such and not excited by the target during the test. To this end, the Becho samples (PL stickers), used specifically for the angle of view test, were characterized. The tests described in this work, which are conducted in the dark at high luminance levels, are the morphoscopic visual acuity test, for which the yellow-green PL Aurora paint was used, the Mariotte test and the minimum angle of resolution (MAR) test, for which the PL stickers from Becho were used. The other test that requires low luminance levels is, of course, the angle of view test combined with the blind spot test of Mariotte, called “Two Blind Spot Test” (TBST), since it includes the angle of view test, intrinsically linked to the dark condition. Since it is impossible to directly measure such low levels of luminance, such as those perceived during the angle of view test, without using a photomultiplier, we thought of making an indirect measurement, starting from the fact that we have an approximate idea of the time elapsed between the excitation of the

target and the moment in which it is possible to carry out the test. This time depends both on the type of target and on the excitation source.

From an experimental point of view, I noticed that the brightness of the PL target, which was excited at the beginning of the angle of view test, quickly decreased. However, it was at a level suitable for darkening the target only after about 20-30 min, that is, after the time necessary to adapt the sight to the dark. The other experimental observation made is that the target, even after a long time like 12h (one night), still maintained a minimum brightness sufficient to be able to perform the angle of view test, that is, to be darkened if seen directly. This is what was observed. Naturally, the use of the luxmeter alone to measure the decay of luminance seems inadequate to capture light signals that are already very weak after about 20-30 min, and even more so for times of the order of hours. The luxmeter allows us to evaluate the decay of luminance only for short times, on the order of a minute, and therefore what we can do is to derive a decay law for short times, hypothesizing that it remains valid also for long times, and therefore to propose an estimate of the luminance after a time of adaptation of the sight to the dark (20-30 min).

The idea was then to operate, always in the dark, on a sample of large circular targets (see Fig. 5.23(a)), in order to have the highest possible initial illumination level, to excite it and to measure the luminance as a function of time from the moment the excitation is turned off. The observed luminance decay times were very short, of the order of a second, and were measured with a stopwatch. The luminance decay measurements were made with the same instruments used for the luminance measurement, and illustrated in the previous paragraph. Considering that Eq. (5.5) establishes the direct proportionality between the luminance of the target and the illumination measured with the luxmeter facing the target at a certain distance, the luminance decay will be equivalent to the illumination decay, that is, with the same temporal law. Then it is a matter of establishing the illuminance decay function, and then of calculating the maximum luminance L_{max} starting from the measured maximum illuminance E_{max}, according to Eq. (5.5). Starting from this information, we will be able to evaluate the luminance of the target at the moment in which it is possible to darken it.

Photoluminescence, or phosphorescence, discussed in this work is the phenomenon of radiative emission by some materials following the absorption of energy through ultraviolet rays and subsequent re-emission in the form of visible light. Phosphorescent materials continue to emit light even up to many hours after the end of external illumination, as already observed. When all the accumulated energy is exhausted, the material no longer emits light. Most pigments and phosphorescent materials use zinc sulfide ZnS [35]; the one doped with copper (ZnS:Cu) shows a long-lasting greenish luminescence typical of commercial phosphorescent objects, therefore similar to that we experienced, and is also used in electroluminescent panels. Another very recent phosphorescent material, which also emits aqua-green light and whose brightness and duration are ten times greater than those of ZnS:Cu, is europium-activated strontium aluminate ($SrAl_2O_4$:Eu:Dy) [36], whose green fluorescence with a wavelength of 520 nm is the most intense. The luminance decay function of strontium aluminate is well approximated to a power law of the type $1/\sqrt{L} \propto t$:

$$L(t) = A/(t + t_0)^2 \tag{5.9}$$

The luminance decay times of this material are very long; the luminance peak decays to about a third in a time of about 200 s. For zinc sulfide of the ZnS:Cu type, the decay is instead faster in the first phase (exponential type), and is then followed by a second phase with a power law:

$$L(t) = A/(t_0 + t)^b \tag{5.10}$$

with the exponent b between 0.2 and 2. From Eq. (5.10) we deduce that the quantity $1/L^{1/b}$ is a linear function of time:

$$1/L^{1/b} = c + d\ t \tag{5.11}$$

with:

$$c = t_0 \cdot 1/A^{1/b} \qquad \text{and} \qquad d = 1/A^{1/b} \tag{5.12}$$

Our experimental luminance decay measurements first concerned the 10 cm diameter target shown in Fig. 5.24, made with layers of Aurora PL paint. The target was illuminated with the Youthink LED lamp (λ = 395 nm). Very qualitative preliminary measurements showed very fast decay times, which, if interpreted according to an exponential decay law, resulted in a time constant $\tau \approx$ 1.4 s. Decay measurements were also made on Becho adhesive PL targets, of circular shape. For them the preliminary measurements gave a very similar decay: $\tau \approx$ 1.5 s. These data refer to the first phase of luminance decay which extends for a few seconds. As we will soon see, the decay for these mentioned two materials, but also for other commercial materials examined, slows down for longer times and in a rather differentiated manner depending on the PL material [10].

Considering that the viewing angle measurements in the dark were initially made on Becho samples, it was considered necessary to make accurate measurements of luminance decay on this type of photoluminescent material. Since the measurements planned with UVA source are very long, it was not possible to use battery-powered LED torches such as Youthink or Alonefire, which would have given a significantly decreasing level of illumination over time, and therefore two LedLight UVA panels were used, with continuous power supply and of 100W each, mounted on the two sides of the target. In Fig. 5.28 two photos of the experimental apparatus are shown. The PL Becho target (ta), a 40-mm diameter disc, is illuminated by the two UV lamps (la) and the sensor (se) of the luxmeter (lx), placed at the end of the tracking rod (tr), faces the target and is very close to it, in order to have a very high initial signal and therefore to have measurable illumination levels even for decay times greater than ~1 min.

Measurements were made with the luxmeter of pairs (E_{max}, t_{stop}) at 14 fixed values of illuminance E_{stop}, from 0.1 lux to 20 lux. All E_{stop} values were then normalized by setting E_{max} = 1, and obtaining $E_{stop,norm}$. The measured illuminance values are proportional to the luminance values (see Eq. (5.5)), and therefore the trends found for illuminance should be compared with those for luminance, described by Eqs. (5.9-11). The function

$1/E_{stop,norm}{}^{1/b}$ vs. t_{stop} with $b = 2$ showed a rapid decay before 10 s, followed by a slower one, as expected for ZnS:Cu, but then a third, still rapid, trend followed (see Fig. 5.29). In reality, no satisfactory linear trend was found for $1/E_{stop,norm}{}^{1/b}$ for any value of the parameter b between 0.2 and 2.0.

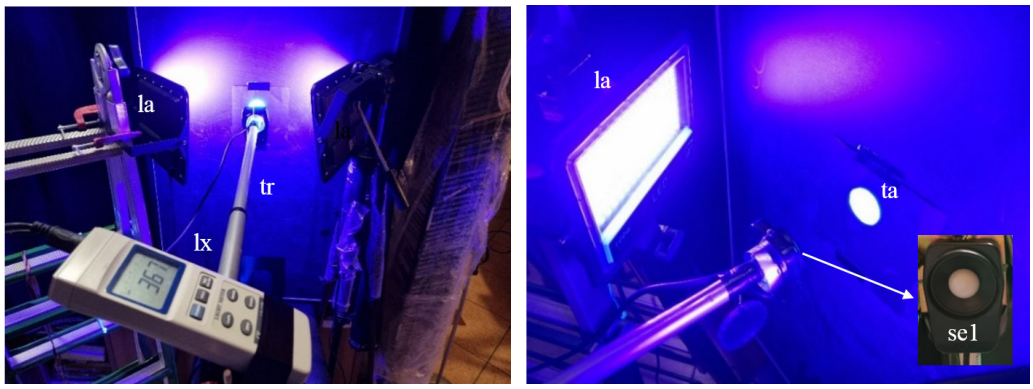

(a) (b)

Fig. 5.28. (a) Photo of the experimental apparatus for the measurement of the luminance decay of the PL target (ta); (b) The sensor (se1) of the luxmeter is put in evidence.

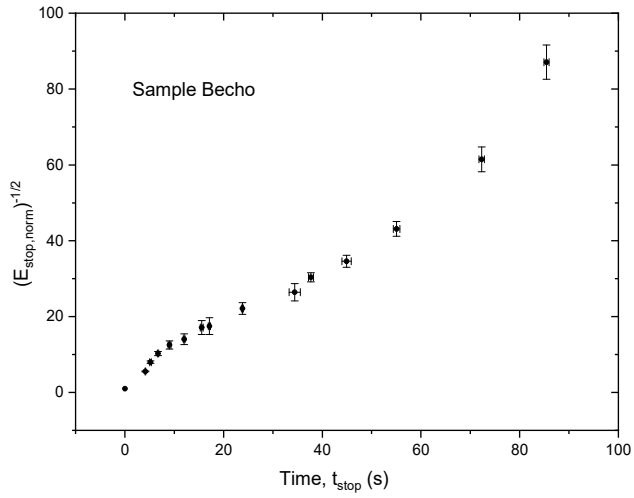

Fig. 5.29. The quantity $1/(E_{stop,norm})^{1/b}$, with $b = 2$, is shown as function of time t_{stop}. After a first fast decay, the function appears to linearize, but is followed by a second fast decay.

Alternatively, the logarithmic plot of $E_{stop,norm}$ illuminance has given an interesting result, with an initial rapid decay and a subsequent slower one whose linear fitting was maintained beyond the minute (see Fig. 5.30).

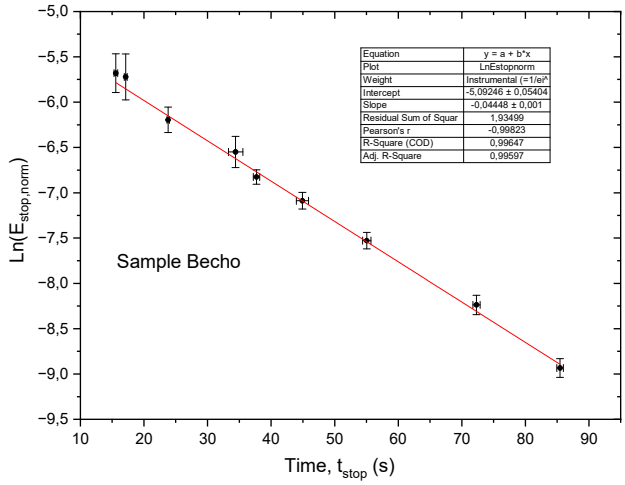

Fig. 5.30. It is shown the quantity ln($E_{stop,norm}$) as function of the time Estop, norm t_{stop} and the corresponding linear fit, with $R^2 > 99$ %.

From the linear fit of ln($E_{stop,norm}$) in Fig. 5.30, we obtain, for the illuminance with slow decay, the function:

$$\mathrm{Ln}\left(E_{stop,norm}\right) = -5.09246 - 0.04448 \cdot t \tag{5.13}$$

$$E_{stop,norm}(t) = A \cdot e^{-t/\tau} = 6.143 \cdot 10^{-3} \cdot e^{-t/22.48} \tag{5.14}$$

The function $E_{stop,norm}(t)$in Eq. (5.14) was obtained by considering the time interval t ~ 15÷85 s. If we assume that it is valid for longer times, then we can estimate the luminance for longer times, i.e. for the times required for the activation of the angle of view test, following this methodology:

i) The large PL target is illuminated with UV light, according to the scheme in Fig. 16, and, starting from the E_{max} value measured with the luxmeter, the luminance is calculated by applying Eq. (5.5), setting $E_v = E_{max}$ e $L_v = L_{max}$.

ii) The luxmeter is removed and the PL target is replaced with the set of small-sized targets (10-20 mm diameter) for the angle of view test, maintaining the same illumination conditions (same distance of the lamp to the targets and same orientation).

iii) The UV lamp is turned off and the timer starts, having already adapted the eyes to the dark.

iv) We await until the PL targets are obscured and record this time as t_{lim}.

The corresponding luminance of the PL targets will be given by:

$$L(t_{lim}) = L_{max} \cdot A \cdot e^{-t_{lim}/\tau} = L_{max} \cdot 6.143 \cdot 10^{-3} \cdot e^{-t_{lim}/22.48} \quad (5.15)$$

By applying Eq. (5.5) we finally have:

$$L(t_{lim}) = \frac{E_{max}}{\pi \cdot \{sin[tg^{-1}(R/d)]\}^2} \cdot 6.143 \cdot 10^{-3} \cdot e^{-t_{lim}/22.48} \quad (5.16)$$

For the luminance L_{max} of the Becho sample, the illuminance was measured as a function of the distance d between the sensor (se) and the target (ta), following the procedure illustrated in Fig. 5.16 and 5.18. To this end, the sensor (se) was placed at the end of the telescopic rod (tr), on which a ruler with fluorescent characters was drawn, allowing the distance to be quickly and easily adjusted in the dark, without the need to use the digital laser meter (see Fig. 5.31). The two UVA LED panels were facing the target at a distance of ~20 cm and tilted by ~45°. Fig. 5.32 shows the graph of the luminance L_v calculated by applying Eq. (5.5), starting from the data of E_v and d. Together with L_v, the data of the angle α_0 within which the target is seen by the sensor (se) are also reported (see Fig. 5.14). The signal saturation occurs for α_0 ~12°, and from the data of the saturation region we obtain for the luminance of the target: L_v = 1113±22 cd/m^2 (see Fig. 5.33).

Consequently, the luminance of the Becho target, when illuminated as above, would decay with the law:

$$L_{stop}(t) = 1113 \cdot 6.143 \cdot 10^{-3} \cdot e^{-t/22.48} = 6.84 \cdot e^{-t/22.48} \quad (5.17)$$

Eq. (5.17) leads to luminance values at the limit of visibility (in scotopic conditions) equal to $L_v \sim 10^{-6}$ cd/m^2, already after about 6 minutes, that is, after a time shorter than that necessary for vision adaptation to the dark (20-30 min) [3, p. 71; 4, p. 125].

Fig. 5.31. The telescopic rod (tr) is shown, by means of which the distance d between the sensor (se1) of the luxmeter and the PL target can be quickly changed by illuminating the rod with a UV LED lamp.

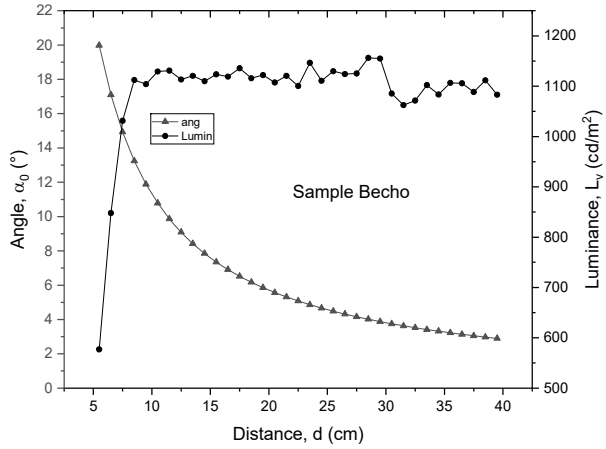

Fig. 5.32. The graph of the luminance L_V of the Becho sample as a function of the sensor-target distance is shown, calculated by applying Eq. (5.5) starting from the illuminance measurements E_V with the luxmeter. The angle α_0 subtended by the target as a function of the distance is also reported. The luminance saturation occurs for an angle of approximately 12°.

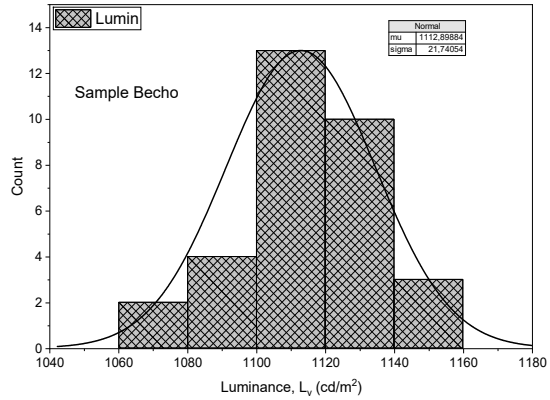

Fig. 5.33. Statistical distribution of the luminance L_V data at the saturation level in Fig. 32.

This means that the PL target, illuminated just before the start of the angle of view test, would be already ready for the test after the wait for the observer to dark adaptation. This result is not realistic, considering that the target is still visible in the dark after many hours from its activation. This means that the luminance of the PL target decays much slower than dictated by Eq. (5.17), and impossible to detect without the use of a photomultiplier. It was decided therefore to proceed with some specific experiments. But, before this, let's see how we arrive at defining the limit of visibility of the luminance at $L_v \sim 10^{-6}$ cd/m^2. In an experiment Hecht & al. [37] subjected a man to a stimulus test by illuminating a small portion of the retina rich in rods with a light beam with $\lambda = 510$nm and duration $t = 1$ms, passing through an artificial pupil of 2mm diameter. The subject, with dark-adapted

vision, was able to detect the stimulus when the energy of the light beam, measured at the entrance to the cornea, reached the level $Q_e \sim 4 \cdot 10^{-17}$ J. This energy corresponds to a radiant flux equal to $\Phi_e \sim 4 \cdot 10^{-14}$ W, which, in scotopic vision and at the peak of the luminous efficacy curve ($\lambda = 510$nm), produces a luminous flux $\Phi_v \sim 1700 \cdot 4 \cdot 10^{-14}$ W = $=6.8 \cdot 10^{-11}$ lm. Since this flux is at the limit of detectability, we will indicate it as $\Phi_{v,lim}$. In the practical case where the subject has dark-adapted vision, the pupil is dilated to about 8mm in diameter, and let ΔS_2 be its area. The limit of visible luminance will then be given by (see the Appendix):

$$L_{v,lim} = \Phi_{v,lim}/\pi \cdot \Delta S_2 = 6.8 \cdot 10^{-11}/\pi \cdot 5 \cdot 10^{-5} = 0.43 \cdot 10^{-6}\ \mathrm{cd/m^2} \quad (5.18)$$

The minimum illuminance on the retina, expressed in trolands, becomes (see the Appendix):

$$L_v(\mathrm{cd/m^2}) \cdot \Delta S(\mathrm{mm^2}) = 0.43 \cdot 10^{-6} \cdot 50 = 2 \cdot 10^{-5} \quad \mathrm{Td} \quad (5.19)$$

Let us now return to the experiments carried out to estimate the decay times of the luminance. Two black cards were prepared on which a dozen PL disks of 1cm-diameter were glued. The two identical cards were placed inside two boxes, which, before being closed and placed inside a wardrobe located in a room kept in the dark, were illuminated in two different ways. The first box (box1) was illuminated with the UVA light panel at a distance of 25 cm, which corresponded to an illuminance, measured with the luxmeter, of ≈1700 lx. The second box (box2) was instead exposed for a long time to indoor light, which corresponded to an illuminance of 20 lx. The visual inspection in the two boxes, and the observation of the two cards, took place by entering the dark room, opening the wardrobe and opening first one box and then the other. The operations carried out on the two cards are listed in sequence in Table 5.3, first their illumination and then the visual checks, and the corresponding times.

Table 5.3. Timing of the operations carried out on the PL Target.

Timing	Box1	Box2	Step
Day 1 (evening)			
0-15min		Illuminated by indoor lamp (20lx).	1
0-10min		Kept in the dark	2
Control		Slightly bright targets. They darken.	3
0-30s	Lightened by UVA LED light panel. (1720lx)		4
0-10min	Kept in the dark.		5
Control	Very bright targets. They don't darken.		6
Day 2 (morning)			
Control	Well visible targets, like step 3. They darken.	Dimly bright targets. They darken.	7
Day 3 (evening)			
Control	Dimly bright targets. They darken.	Hardly distinguishable targets.	8

From Table 5.3 the following information can be deduced: i) the illuminance of the targets does not necessarily require the use of a UVA source to perform the angle of view test; the illuminance of a commercial lamp is sufficient and the luminance of the targets is sufficiently low already after 10 min; ii) the luminance decays very slowly, more than what measurements made over short times can tell us; iii) a time of ~4h is necessary for the targets to almost completely lose their brightness and be almost invisible.

5.4. Test Methods

5.4.1. Morphoscopic Visual Acuity

The visual acuity of recognition, VA, or morphoscopic acuity, is defined by the minimum angular dimensions necessary to allow the recognition of certain symbols [3, p. 174; 4, p. 132; 20; 25; 38-42]. The capital letters of the alphabet are the most widespread ones for their ease of use. Visual acuity can be expressed in different ways: (i) the Snellen scale of 20 feet; (ii) the Snellen scale of 6 meters; (iii) the Monoyer decimal scale; (iv) the logMAR scale, where *MAR* is the minimum angle of resolution, that is the angular size of the critical detail that must be resolved by the patient to identify the optotype correctly. Fig. 5.34 shows the schematic of a morphoscopic vision acuity test. The use of a mirror in the optical path allows to double the physical distance between the subject and the chart. For example, for the tests carried out on the logMAR charts, an optical distance of d = 6m was made possible by using a mirror placed at 3m distance and the chart kept alongside the subject (see Fig. 5.34).

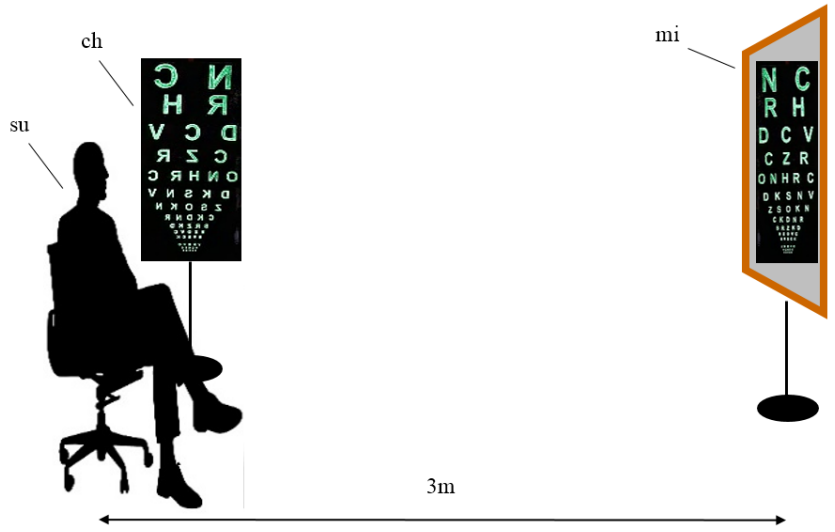

Fig. 5.34. Test of visual acuity (VA) carried out doubling the optical path to d = 6m by using a mirror (mi); (su) subject; (ch) chart; (la) lamp. For the test at dark, the PL characters are lightened by a UVA lamp (la).

Of course, since the mirror rotates the letters 180° around the vertical axis, the optotypes on the table were also drawn rotated of 180°. When the test is performed on individual eyes, the subject wears a black hood with a hole for the eye to be analyzed; this allows the not tested eye to remain open and relaxed. Furthermore, during the test, the subject, who is flanked by the light source(s), is separated from them by a black screen to prevent any direct vision of them and of the chart. In Table 5.4, the different types of tests performed to evaluate the visual acuity (VA) of a subject using Monoyer decimal or geometrical (logMAR) charts, are summarized, considering: i) the environment (E), whether lightened (L) or dark (D); ii) the type of illumination of the chart (Illum), by a lamp light, a monitor, the Sky light or UVA light; iii) the type of chart (Chart), if Monoyer decimal (Dec) or logMAR (LM); iv) the optical distance between chart and subject (d in meters); v) the background (bottom) of the chart, if white paper (WP), white screen (WS) or black paper (BP); vi) the character (Char), whether black, or white, or PL, and finally the contrast of characters, if positive or negative.

The logMAR chart was used in the light and in the dark. In the light, it was used with white characters (N = 3, 4 and 5 in Table 5.4), while, in the dark, it was used with photoluminescent characters (N = 6, 7 and 8 in Table 5.4); in both cases it was drawn for a distance d = 6m. The decimal chart was used at light in two ways: on a white cardboard with black characters (negative contrast), being printed for a distance d = 3 m (N = 1 in Table 5.4), and at a monitor with black characters (negative contrast), being drawn for a distance d = 2 m (N = 2 in Table 5.4). The tests at the light were done by illuminating the chart indoor with white light lamps or panels (N = 3 in Table 5.4), or outdoor with the skylight (N = 4, 5 in Table 5.4). The tests at dark were done by illuminating the chart in three different ways: i) with Wood's lamp (LED torch) at λ = 395 nm, ii) with Wood's lamp (LED torch) at λ = 365nm, and iii) with two Wood's lamps (LED panels) at λ = 395-405nm (N = 6, 7, 8 in Table 5.4). Table 5.4 shows the types of morphoscopic VA tests performed to assess a subject's visual acuity (VA) by using decimal or logMAR charts. (1) White light LED panel. (2) The optotypes are on the back of the transparent sheet.

Table 5.4. Summary of Morphoscopic VA Test Conditions.

N	E	Illum	Chart	*d* (m)	Bottom	Char	Contrast
1	L	Lamp	Dec	3	WP	Black	Negative
2	D	Mon	Dec	2	WS	Black	Negative
3	L	Lamp(1)	LM	6	BP	White(2)	Positive
4	L	Clear Sky	LM	6	BP	White(2)	Positive
5	L	Cloudy Sky	LM	6	BP	White	Positive
6	D	UVA torch (395nm)	LM	6	BP	PL	Positive
7	D	UVA torch (365nm)	LM	6	BP	PL	Positive
8	D	UVA panel (395-405nm)	LM	6	BP	PL	Positive

Old charts are of type Monoyer decimal. Fig. 5.36 shows the decimal optometric table with 10 lines of optotypes, calculated for a distance d = 3m. On the left column is reported the height L of characters, in mm, whereas on the right column is reported the visual acuity VA expressed in tenths $x/10=d/L$, where d is expressed in meters and L in millimeters. One of the drawbacks of the Monoyer decimal scale, as well as the Snellen scale, is that the font sizes of lines with lower visual acuity change more markedly than those of high visual acuities (see the progression of optotypes in Fig. 5.36); this prevents a good distinction between high visual acuities. The other drawback is that the number of characters is not constant in the different lines, and this makes the assignment of VA more complicated. Visual acuity is nowadays scored with reference to the logarithm of the minimum angle of resolution, *MAR*, expressed in prime degrees [39, 40, 43]. Fig. 5.35 shows the optotype E, generally taken as the example for illustrating the relationship between the angle MAR, L, the height of character, and $P = L/5$, the limb of letter E, representing the minimum distinguishable particular from which the angle MAR is derived at the distance d between the letter and the subject. The Bailey-Lovie [40] logMAR test chart with 14 lines of optotypes is shown in Fig. 5.37. The range of dimension of L is 20 times (see Table 5.5). The quantity logMAR is equal to $\log_{10}$ MAR (′). As it can be seen, the progression of characters dimension is linear with logMAR. The other advantage of the logMAR chart is that it contains only five characters per line, and this makes the assigned VA value more precise. In our case, we have simplified the chart reducing the number of characters on the first four lines, so as not to deal with excessive horizontal dimension of the chart itself, and also because the subjects who performed the test in this work showed a VA higher than x=2.5 tenths (see Table 5.5). The Bailey–Lovie [40] chart uses rectangular (5:4) alphabetic characters (see Fig. 5.35) [3, p. 174; 4 p. 135]. The values of visual acuity, expressed in Monoyer tenths, x, are given in Table 5.5 together with angle MAR, expressed in prime degrees, and the character height, L, expressed in mm, given by:

$$L(\text{mm}) = 5\cdot d(\text{m})\cdot 1000\cdot \text{tg}(1')\cdot \frac{10}{x} = 1.45\cdot d(\text{m})\cdot \frac{10}{x} = 1.45\cdot d(\text{m})/VA \quad (5.20)$$

$$\text{L(mm)} = 5\cdot d(\text{m})\cdot 1000\cdot \text{tg}(1')\cdot MAR = 1.45\cdot d(m)\cdot MAR \quad (5.21)$$

where d is the distance in meters, $10/x = MAR$ (‘), 1.45 = 5 · 1000 · tg(1′), and $x/10$ is the decimal VA.

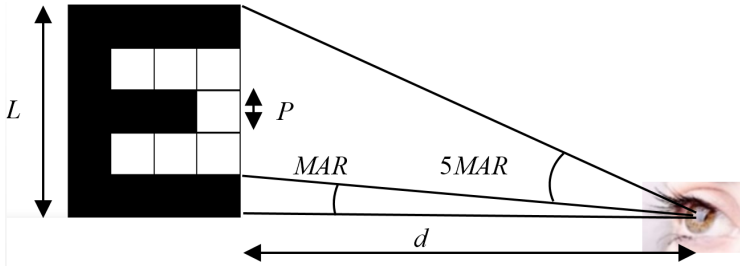

Fig. 5.35. The letter E, taken as the example to show the relationship between the quantities L, P, *MAR* and d.

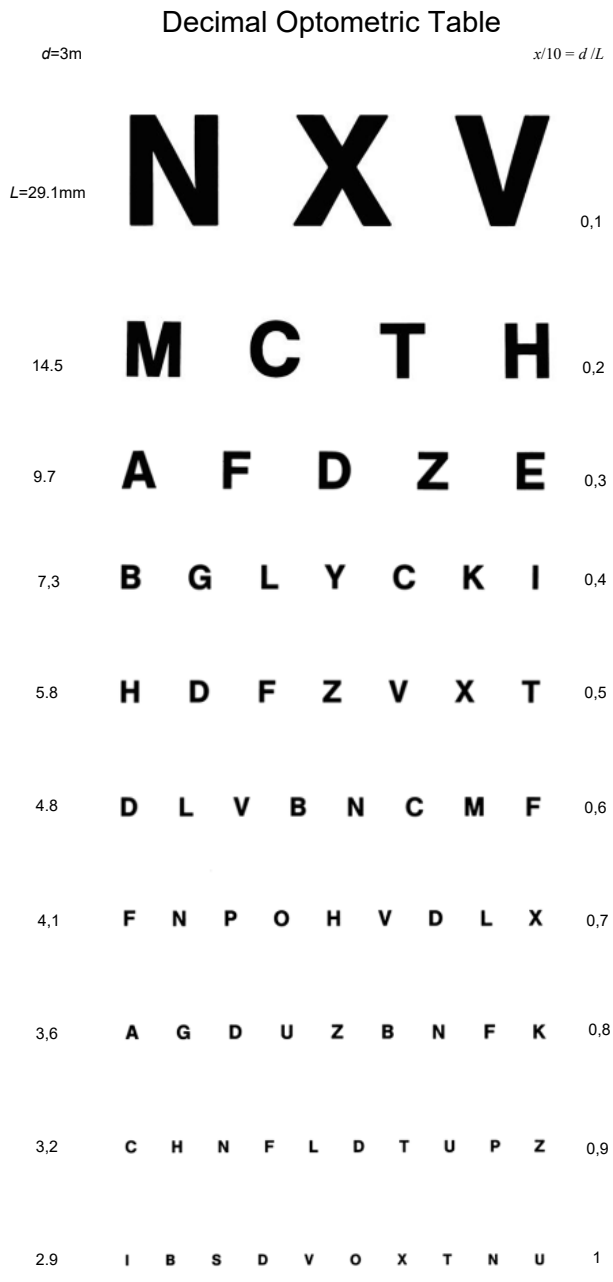

Fig. 5.36. The Decimal Optometric Table with 10 lines of optotypes. On the left column is the height *L* of characters; on the right column is the VA expressed as $x/10 = d/L$, where *d* is the distance expressed in meters and *L* is expressed in mm.

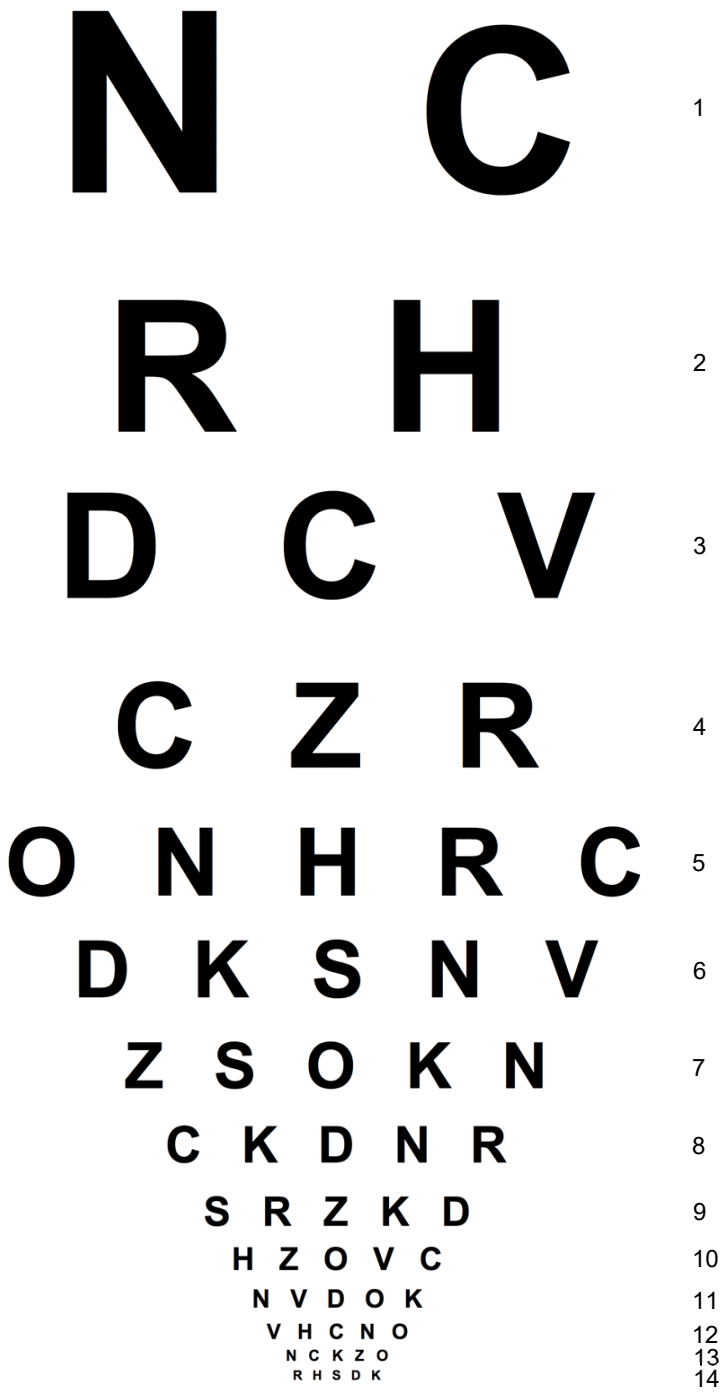

Fig. 5.37. The Bailey-Lovie logMAR test chart with 14 lines of optotypes. On the right is the line number (see Table 5.5 to see the logMAR value).

Table 5.5. Visual Acuity Conversion Table.

n **line**	***x*** **VA (tenths)**	***L*** **(mm)** ***d*****=3m**	***L*** **(mm)** ***d*****=6m**	***MAR*** **(′)**	***logMAR*** **VA**
1	1	43.6	87.3	10	1.0
2	1.3	34.6	69.3	7.94	0.9
3	1.6	27.5	55.1	6.31	0.8
4	2	21.8	43.7	5.01	0.7
5	2.5	17.3	34.7	3.98	0.6
6	3.2	13.8	27.6	3.16	0.5
7	4	11.0	21.9	2.51	0.4
8	5	8.7	17.4	1.99	0.3
9	6.3	6.9	13.8	1.58	0.2
10	7.9	5.5	11	1.26	0.1
11	10	4.4	8.7	1	0.0
12	12.6	3.4	6.9	0.79	-0.1
13	16	2.7	5.5	0.63	-0.2
14	20	2.2	4.4	0.5	-0.3

Table 5.5 shows how the quantities *MAR* (the Minimum Resolution Angle expressed in prime degrees), *L* (height of the character, calculated for 6m and 3m distance) and *x* (the visus expressed in tenths=10/MAR) vary as a function of *logMAR* (the decimal logarithm of the Minimum Resolution Angle) with steps of 0.1 from 1.0 to -0.3. From Eq. (5.20) we deduce that, for a distance d = 6m, the height of the characters becomes:

$$L(\text{mm}) = 1.45 \cdot 6 \cdot \frac{10}{x} = \frac{87.3}{x} \tag{5.22}$$

Varying x from 1 to 20, with steps of 1 (see Table 5.5), we obtain the graph in Fig. 5.38(a). For a table with a decimal scale, therefore, L is an inverse function: $L = 1 / (b \cdot x)$, and therefore varies a lot for low VA values, while it is almost flat for high VA values. For a logMAR type chart, on the contrary, always for a distance d = 6m, from Eq. (5.21) we obtain for the character height:

$$L(\text{mm}) = 1.45 \cdot 6 \cdot MAR = 8.73 \cdot 10^{logMAR} \tag{5.23}$$

By varying logMAR from 1 to -0.3 with steps of -1 (see Table 5.5), corresponding to the 1-20 interval on a decimal scale, we obtain the graph in Fig. 5.38 (b).

For a table with logMAR scale, therefore, L is an exponential function $L = A \cdot e^{-x/tl}$, and then varies in an almost linear way, and, in particular, varies appreciably in the high VA range, thus solving the problem shown by the decimal table. This changes the way to give

a value to visual acuity, as we will shortly see. Despite this, some preliminary tests have been done by us at light with this table, as specified in Table 5.4

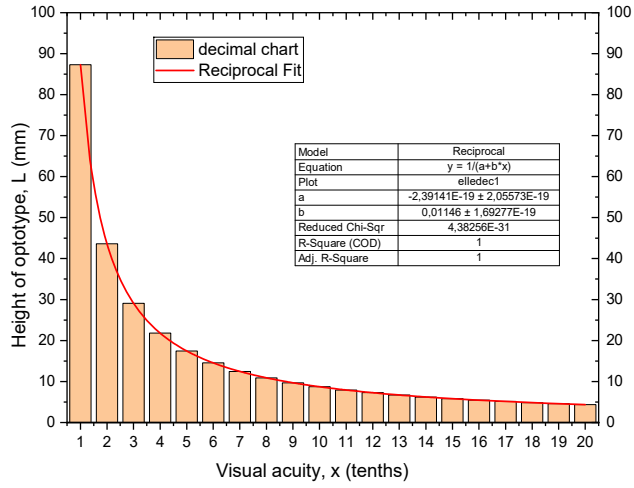

(a)

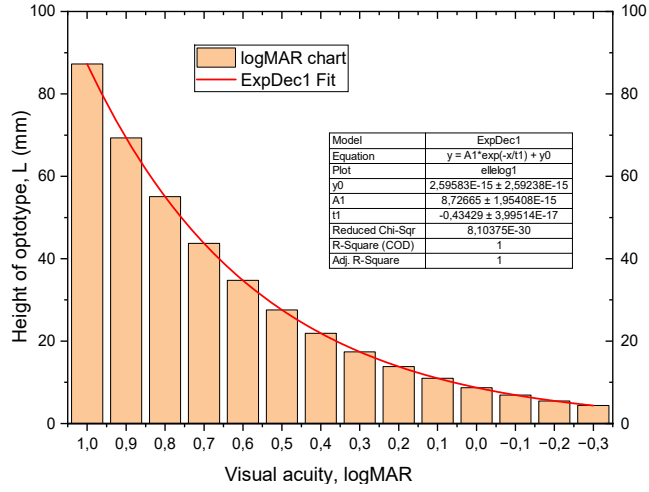

(b)

Fig. 5.38. The progression of optotypes in the Monoyer decimal chart in (a) is compared with that in the Bailey-Lovie logMAR chart in (b). While the progression of the Monoyer decimal chart is strongly non-linear, and almost flat at high x values, that of the logMAR chart is almost linear at high *x* values and not flat.

Visual acuity in tenths, *x*, varies from a minimum of 1 for the largest characters in the first line, to 10 for the smallest characters. As it can be seen, the decimal scale in Fig. 5.38 (a), with arithmetic progression, is traced linear with respect to the tenths of VA, whereas the logMAR scale in Fig. 5.38 (b), with geometric progression, is traced linear with respect

to the logarithm of the *MAR*. The curiosity of this terminology is that, although the decimal scale is arithmetic, the font size does not vary linearly, while it varies almost linearly in the logMAR scale.

The recording of visual acuity using the decimal chart follows this criterion: *x* VA = *x* value of the best line read, followed by a number of plus (+) signs of characters read in the following line, ignoring the results on the other lines below. If the subject is unable to read all of the letters on a particular line, it is a standard practice to assign a VA to the smallest line for which the patient is able to read at least half the letters. Any errors are indicated by a minus superscript, while additional letters identified correctly on the following line are shown with a plus superscript. From here we understand that in the Snellen and Monoyer decimal system, where the number of characters per line is variable, the criterion for assigning a line as read, is not consistent with the different lines, while it is so for the logMAR system, in which the number of characters per line is constant and equal to five (apart our arbitrary choice of reducing the number of characters in the first four lines, as shown in Fig. 5.37). The recording of visual acuity using the logMAR chart follows this criterion [38]: the total score for a line on the logMAR chart represents a change of 0.1 log units [11]; the score decreases as visual acuity improves. If a line contains five letters, each letter has a score value of 0.02 log units. The formula used in calculating the score is therefore:

$$logMAR \text{ VA} = logMAR \text{ of the best line read} - 0.02\,X, \tag{5.24}$$

where *X* is the number of letters read correctly in the line below. Following Rosenfield and Logan [3, p. 278], *X* is the number of letters read correctly in the lines below, irrespective of their position on the chart. A further method of scoring the VA is the *VAR* (Visual Acuity Rating) of Bailey & Lovie [43], which consists of multiplying the tenths of the best line read by 10 and adding or subtracting units for each wrong or right character, respectively. Example: Subject reads all letters of *x*/10=10/10: *VAR* score =100. If one letter is wrong, *VAR*=99; if two letters are wrong, *VAR*=98. If instead he reads a letter after 10/10, then *VAR* = 101. To assign the VA in the morphoscopic visual acuity test, we have followed the criterion expressed by Eq. (5.24), which provides the logMAR, from which we obtained the *MAR* and finally the *VA* expressed in tenths: $x = 10 / MAR(')$ (see Section 5.5.1.2).

5.4.2. Tests in an External Photometric Laboratory

The tests presented above were accompanied, for comparison, by those carried out in an external optometric laboratory. The purpose is twofold, that is, to validate the results of the common tests, and to have a more complete picture of the patient's vision acuity, considering that our tests can be slightly different from those required by the optometric protocol. The visual tests were carried out on two patients: A (the author, adult) and B (a young collaborator). External laboratory tests refer to both far (F) and near (N) distance vision; however, our attention will be limited to the visus for the far. Tables 5.6(a), (b) are the protocol tables. They are generally accompanied by two graduated lunettes reporting the angular information (from 0° to 180°) on astigmatism, as will be explained later (see Fig. 5.39).

Table 5.6 (a). Facsimile of the Tables used in the Photometric Laboratory.

	OD			OS		
D	**SPH**	**CYL**	**AX**	**SPH**	**CYL**	**AX**
F						
N						

Table 5.6 (b). Facsimile of the Tables used in the Photometric Laboratory.

Interpup. distance			Visus		
OD	**PD**	**OS**	**OD**	**OS**	**OU**

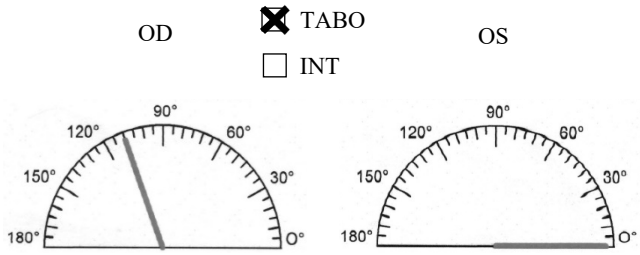

Fig. 5.39. The two lunettes represent the angular orientation system used to indicate the degree of astigmatism, for OD and OS, respectively.

The symbols on Table 5.6 are the following:

D: Distance, if far (F) or near (N).

OD: Oculus Dexter (right eye).

OS: Oculus Sinister (left eye).

OU: Oculus Uterque (both eyes).

SPH: Sphere; stands for the power of the lens that will correct the eyesight, that is, the degree (in diopters) of myopia (with the minus sign) or hyperopia (with the plus sign).

CYL: Cylinder; stands for the amount of astigmatism in the eye, and is indicated by the minus sign. The cylinder and axis appear always together and are used to correct the astigmatism.

AX: Axis; indicates, between 0° and 180°, the position of the astigmatism on the subject's visual field.

ID: interpupillary distance.

TABO or INT (International): refer to the system used for calculating the axis of the eye.

Now let's see how to interpret the information reported in Table VI. Let's consider either of the two eyes. The minus sign in the SPH box indicates that the subject is nearsighted, whereas the plus sign in the SPH box indicates that the subject is farsighted. If the SPH box is empty, then the subject is emmetrope, that is, he has no visual defects. The absolute value of SPH indicates the gradation of the lens necessary to correct the defect: the higher it is, the greater the defect. Eyeglass strength is measured in diopters. I remember that the diopter is the measurement unit of the convergence of an optical system. One diopter is equivalent to the focal length of 1m, so the convergence, in diopters, is equal to the inverse of the focal length expressed in meters. If the prescription reads -0.25, that means the eyeglasses need -0.25 diopters of strength to correct nearsightedness, that is the optical power D of the corresponding eye is diminished of 0.25 D.

Nearsightedness, or myopia, is a common refractive disorder. If the subject is nearsighted, he can see objects that are close clearly, but objects that are farther away will look blurry [4, p. 23-28]. With nearsightedness, the eye is usually elongated, with too much distance between the cornea at the front and the retina at the back. Nearsightedness can also happen if the cornea of the eye is too curved. Due to this increased distance, light rays fall in front of the retina, instead of on it. This can cause the distance vision to be fuzzy. For a nearsighted prescription, the strength of the lenses is marked with a minus sign.

Farsightedness, or hyperopia, is a refractive disorder that makes close objects harder to see than distant objects [4, p. 28]. It happens because the distance from the cornea to the retina is too short or because the cornea of the eye is not curved enough. If the subject is farsighted, light focuses behind the retina instead of squarely on it. For a farsighted prescription, the strength of the lenses is marked with a plus sign. This same refractive disorder can be attributed to presbyopia [3, p. 409], a defect attributable to age, associated with the difficulty in contracting the crystalline lens.

Now let's move on to the box marked CYL: if there is any value it means that the subject is astigmatic. This visual defect is given by a different sphericity of the cornea, which implies a different angle of the axis. The CYL section must always be filled in together with the axis field AX. The astigmatism is of myopic type if the values of SPH and CYL are both negative, while it is of hypermetropic type if the values of SPH and CYL are both positive. If the signs in the SPH and CYL boxes are different, we are in the presence of a mixed astigmatism. If the CYL box contains a digit, then there will also be a value for AX. AX indicates the obliquity of the meridian deviated by astigmatism. Generally, this is given by a slightly elongated cornea, whose correction requires the use of special lenses, called toric. This value can range from 0° to 180° and indicates the orientation that the corrective lens must have. The degrees required for the correction of astigmatism can be indicated graphically by semicircles, relating to the individual eyes.

Astigmatism is an irregular curve in either the crystalline lens or the cornea of the eye. This irregular curve can bend the light that enters the eye and affect the way it hits the retina. Astigmatism can blur both near and far objects. It can also distort the images. If the astigmatism measures 1.5 diopters or more, the subject may need to wear prescription glasses or contact lenses to see properly. The difference between TABO and INT lies in the direction of indication of the axis: in TABO, the axes of both eyes are indicated counterclockwise; in INT, the left eye is measured clockwise, while the right eye is measured counterclockwise. TABO is the universal system. If AX values are indicated with the INT system, to obtain the angle of the left eye in TABO it is necessary to subtract the INT value from 180:

$$\text{Axis TABO} = 180 - \text{Axis INT} \tag{5.25}$$

Interpupillary distance (or ID) is the distance between the pupils when looking forward. It is a necessary measure to be able to position the optical center of the lens directly in front of the pupils. It is measured in millimeters and the optimal value is between 54 and 74 mm; the average pupillary distance in Italy is 62 mm.

5.4.3. Test of the Visual Angle in the Dark

In photopic vision conditions, the concept of visual angle, or angle of view, or viewing angle, is clear. It is expressed by the symbol α, and represents the angle subtended by the object subjected to vision, of height h_0 and distant d_0 from the average nodal point, which is the distance between the object and the corneal apex added to ~7 mm, from which we obtain: $\tan\alpha = h_0 / d_0$. Knowing α, for the retinal image we obtain: $\tan\alpha = h_i / d_i$, from which we obtain h_i, the height of the retinal image, knowing the distance d_i between the retinal plane and the average nodal point (~17mm) [4, p. 14]. For example, for an angle of view ~1° and an ocular power of 63D, the height of the visual image becomes: $h_i = \tan\alpha \cdot d_i = 0.017 / 63 = 0.00028 = 0.28$ mm.

In dark operating conditions, the concept of angle of view must be redefined. In these conditions, in fact, the central region of the fovea, the one populated by the majority of cone photoreceptors, is no longer active. Scotopic vision, therefore, occurs as if using a photographic film with a central hole, corresponding, presumably, to the foveola area. Since direct vision involves precisely this region of the macula (see Section 5.2), the consequence is that, in scotopic vision, it is not possible to focus on a luminous object, in the actual case a photoluminescent target, when it is subtended by a critical angle of view (which we could define as α_D, where the suffix D stands for dark) such that $\tan\alpha_D / D$ be smaller than the size of the fovea or foveola area.

To give an example, if we establish the foveola area for the size of the region where the direct image with the highest resolution is formed, of ~ 0.35mm (see Fig. 5.4 (b)), then the critical angle of view α_D will be given by: $\tan\alpha_D = 0.00035 \cdot 60 = 1.2°$, having assumed an optical power of 60D.

As a consequence of the previous discussion, the test of angle of view in the dark is aimed to measure the critical angle α_D. The test highlights the disappearance of a light source in the dark when it is confined within the "dark cone", or "shadow cone", projected from the inner part of the fovea and with a linear divergence equal to α_D (see Fig. 5. 40).

To know exactly which part of the fovea is affected by this phenomenon, we have to wait for the test results. We will investigate this phenomenon using a circular PL sticker (PL target) as test field and measuring, in the dark, the distance at which it disappears from view. Of course, the darkening of the PL target takes place only when the subject has dark-adapted vision [3, p. 71; 4, p. 125], and the target luminance is very low (see Section 5.3.2), a necessary condition in order not to activate the photoreceptor cones. This test, "test of the angle of view in the dark", is therefore intrinsically linked to the condition of darkness, and has not an equivalent in the light. To well understand this test, it is important to have acquired the basic information on the structure of the eye (see Section 5.2) [20].

In Fig. 5.40 we still report the schematic horizontal section of the right eye of Fig. 5.3(b), in which we have added the "dark cone" projected outwards from the foveal region and whose vertex is located on the average nodal point of the eye. The aperture of this cone is the critical angle of view α_D. The axis of the cone, or rather of the two cones, the one passing through the vitreous humor and the other one crossing the lens, the aqueous humor and the cornea, before projecting outwards from the eye, is the visual axis and is oriented towards the temporal side of the head of the angle κ [3, p. 9; 25], which is around ~4° horizontally in the temporal direction and ~2° vertically, for an emmetrope eye.

We can summarize here what previously discussed, by referring to Fig. 5.40. The linear size, h_i, of the retinal image on the fovea is related to the distance between the retinal plane and the mean nodal point (~17mm), d_i, and to the critical angle of view in the dark, α_D, from the relation [4, p. 14]:

$$h_i = \mathrm{tg}\alpha_D \cdot d_i = \mathrm{tg}\alpha_D \,/\, D \tag{5.26}$$

where D is the optical power of the eye, expressed in diopters (1 diopter = 1 D = 1m^{-1}), if d_i is expressed in meters. The total optical power of the relaxed eye in humans is ~63 D, of which the cornea accounts for ~43 D and the crystalline lens for the remaining ~20 D (when the lens is compressed for near vision, the lens diopters vary in the range from +20 to +33). From Eq. (5.26) we see that, for a retinal image linear size of ~1.5 mm (the average fovea linear extension), we expect to have α_D ~ 5°; whereas for a retinal image linear size of ~0.35 mm (the average foveola extension), we expect to have α_D ~ 1.2°.

This part is dedicated to measuring the critical angle of view, α_D, in dark conditions. Being that the cones are deactivated in the dark, the consequence is that the area of the fovea that is totally depleted of active photodetectors should be the foveola (fovea centralis), rich only in cones, which should therefore become practically blind, while instead the rods remain active in the entire optical retina. The direct view of an object will then be prevented if the angular extension of its image on the foveola is smaller than the corresponding angle of view, which, in this case, should be ~1° [4, p. 77]. When the cones

of the foveola are deactivated, the sight of a source with low luminance should be made possible by the rods placed on the edges of the fovea. But we will draw conclusions on this topic only when we will present the results of the angle of view test.

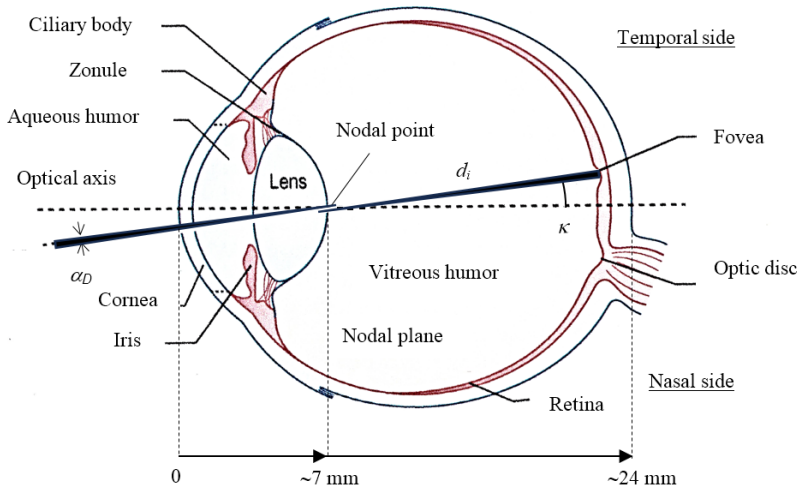

Fig. 5.40. Simple model of the horizontal section of the human right eye showing the main elements that underlie vision. The added black cones, which branch out in opposite directions from the nodal point, have a linear aperture of α_D, the angle of view in the dark, and are directed along the visual axis of the eye, forming an angle κ with the optical axis.

To measure the critical angle of view in the dark the test is organized in the following way. On a wall with a dark bottom, a photoluminescent circular sticker (a PL target), of yellow-green color and of about 1cm in diameter, is fixed at the level of the eyes of the subject (see Fig. 5.41(a)). He will remain in the dark for ~20÷30 min to make sure the cones are deactivated [3, p. 71; 4, p. 125]. Before the test, the sticker can be illuminated with a Wood's or a white light lamp. To avoid reactivating the cones, the subject will take care to keep his eyes tightly closed during this operation. The luminance of the sticker must be very low for conducting an effective test, but its intensity is unknown because impossible to be measured by us. The test was carried out both on the individual eyes, dressing shielded glasses or a hood with hole for the testing eye, and on both ones. The subject will then start from a distance of about 20 cm from the wall observing the sticker and moving away from it gradually noting the distance with a laser pointer, avoiding turning on the light during the distance measurement. The measurement of distance with the laser device must be made by approaching the device on the cornea of the eye under test (see Fig. 5.41(b)). Moving away from the sticker, the subject will notice that, at a certain distance, the PL target will tend to disappear and that it will disappear completely moving further away. At that point the subject will make distance measurements at smaller intervals, approaching and moving away from the target, in order to identify precisely the distance, $d = d_{min}$, at which the sticker disappears (see Fig. 5.41). By measuring the distance d_{min} and the PL sticker diameter D, the critical angle of view α_D will be easily determined. In conclusion, this test allows to determine the critical angle of view in the

dark, α_D, that is one of the three variables of Eq. (5.26). By knowing one of the other two variables, h_i or d_i, we would know the geometry of eye in terms of distance between the retinal plane and the mean nodal point, d_i, or of extension of the foveola area, h_i, respectively.

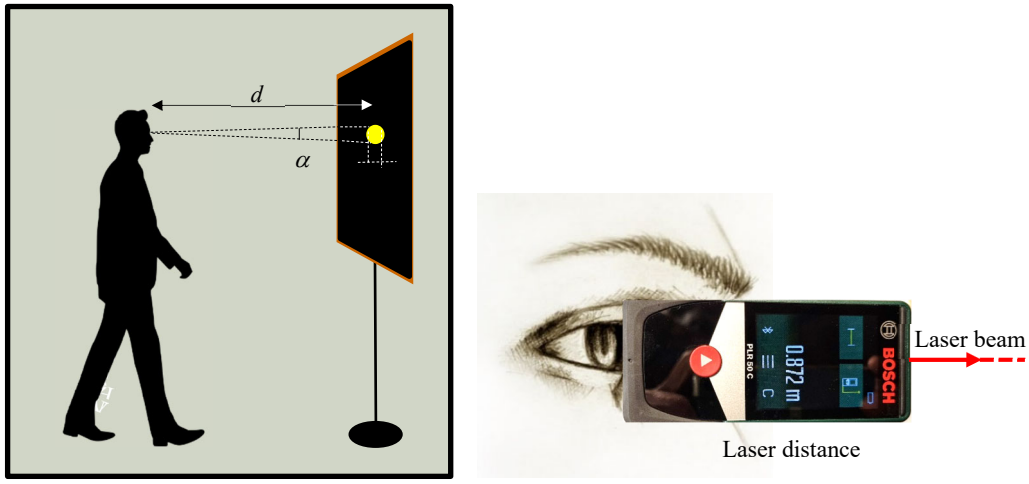

(a) (b)

Fig. 5.41. (a) The subject is shown fixing his gaze, in the dark, on the PL sticker at distance *d*. When moving away from the sticker, it will disappear, subtending an angle equal to the critical angle of view α_D. (b) The subject measures distance d by approaching the edge of the laser device to the eye's cornea.

A single Becho PL sticker, of diameter $D = 19.7 \pm 0.3$mm, previously illuminated with the Wood lamp at $\lambda = 395$ nm, was used as target for the test. The distance *d* between observer and target was measured by approaching the edge of the laser distance meter to the eye's cornea and pointing the laser beam to a point near the target. The correct distance to apply is obtained by increasing the measured distance of ~7mm, the average distance from the nodal point of the eye to the cornea (see Fig. 5.40). This small correction, however, does not change significantly the result of α_D. Referring to Fig. 5.41, we have the following critical angle of view α_D, and its error, in correspondence to d_{min}:

$$\alpha_D = 2 \cdot tg^{-1}\left(\frac{D}{2 \cdot d_{min}}\right) \tag{5.27}$$

$$\Delta\alpha_D = \left(\frac{4}{4{d_{min}}^2 + D^2}\right) \cdot (D \cdot \Delta d_{min} + d_{min} \cdot \Delta D) \tag{5.28}$$

5.4.4. The Blind Spot Test of Mariotte

The blind spot in the visual field of a human eye was discovered in 1668 by the French scientist Edme Mariotte (1620–1684), member of the Académie Royale des Sciences in Paris and famous for his experiments on vacuum that led to the famous law of Boyle and

Mariotte [8, 9, 44-46). Today, this phenomenon is also known as the Mariotte's spot in visual field. In a letter written to Pecquet in 1668, he announces the discovery of the blind spot, specifying his observation of the lack of vision which occurs when an image of an object falls solely on the optic nerve. The blind spot test refers then to a physiological phenomenon where each eye has a blind spot, an area where the optic nerve meets the retina, and there are no photoreceptors.

Fig. 5.42 shows a simplified horizontal section of the human right eye, in which the cornea (1), the aqueous humor (2) and the crystalline lens (3) are highlighted on the front. On the back are highlighted: the retina (4), the choroid (5), the sclera (6), the fovea (7) with its characteristic depression profile, the optic nerve (9) at the base of the papillary disc (8) and finally the venous (10) and arterial (11) blood vessels, which depart together with the optic nerve. This schematic representation of the human eye corresponds to what anticipated by Mariotte's works.

The eye represented in Fig. 5.42 is the right one, in which, as we see, the papilla of the optic nerve is shifted downwards, that is, towards the nose in the horizontal direction. By symmetry, the same representation for the left eye would see the papilla shifted upwards, that is, still towards the nose.

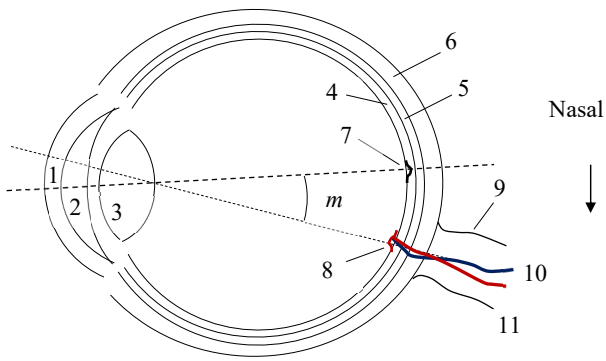

Fig. 5.42. Schematic horizontal section of the eyeball of the right eye, in which the location of the papilla (8) of the optic nerve is highlighted, which is the subject of this section.

We have already seen in the previous section how the fovea is displaced, respect to the optical axis, by about ~4° towards the temporal side. In the case of the papilla, the misalignment with respect to the visual axis, which we call angle μ in honor of Mariotte, is ~15° towards the nasal direction (see Fig. 5.42), and ~2° vertically up. The papilla is then oriented ~11° towards the nasal side with respect to the optical axis of the eye. The papilla is of about 2mm size, corresponding to ~7° vertically and ~6° horizontally. The papilla is blind, that is, devoid of photoreceptors, it therefore appears as a blind spot in the visual field (physiological scotoma or Mariotte's spot), but its presence is not felt by normal sight, because the mind implements a filling (papillary filling) of the missing visual field. In binocular vision, in fact, only one papilla is blind respect to a fixed direction, due to the symmetry of the eyes with respect to the nasal axis.

There is a simple method to highlight the presence of the Mariotte stain (blind spot test of Mariotte), and consists in fixing on a wall two small stickers at a horizontal distance H, standing in front of the left one, fixing it with the right eye and covering the left eye at the same time (see Fig. 5.43(a)). Moving away from the wall for a variable distance d, about four times H, the observer will notice that the right sticker no longer appears in the field of view, because its image falls exactly on the papilla area, free of photoreceptors (see Fig. 5.43(b)). The angle of the horizontal misalignment of the papilla, with respect to the visual axis, will then be given by $\tan^{-1}(H/d)$, and of the order of 15°.

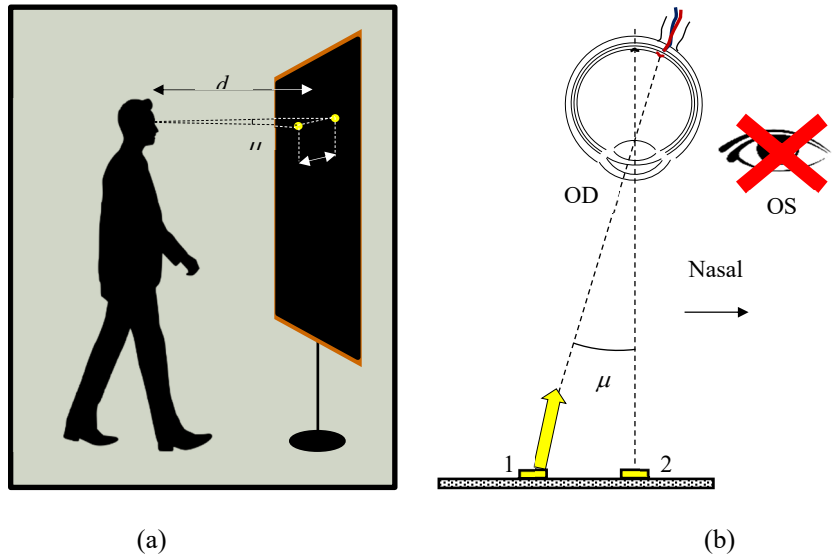

Fig. 5.43. (a) Scheme of the Mariotte's blind spot test. The observer is in front of two PL stickers in the dark. (b) Scheme of the two eyes and the two stickers seen from above. The image of sticker 1 falls on the papilla and then disappears.

Fig. 5.43(a) shows an outline of the Mariotte test. Of course, the test must also be done on the left eye by reversing the terms left / right. In this way we will have found the horizontal misalignment of the papilla for the two eyes, respect to the visual axis. The experiments have been performed both in the light, using two black disc stickers on a white wall, and in the dark using two photoluminescent disc stickers on a black wall.

In Fig. 5.43 (a), the subject is shown in front of the wall with the two stickers. Fig. 5.43(b) shows schematically the pattern of the two eyes from above on a transversal plane, with the right eye pointing at sticker (2) and the left eye blindfolded. The light emitted by sticker (2) reaches the fovea and is directly seen, whereas the light emitted by sticker (1) reaches the right eye at an angle μ and hits the blind papilla; as a consequence, the sticker (1) is not seen. The OS eye must be blinded folded because, otherwise, the target 1 would appear on that part of the retina free of the papilla.

Mariotte's blind spot test does not involve a single μ measurement, as simplified in Fig. 5.43, but an interval one on the horizontal plane, as illustrated in Fig. 5.44 [44]. In fact, at varying the distance of the subject from the target, there is a significant interval between the minimum distance d_{min} at which the target disappears and the maximum distance d_{max} at which it reappears. These two distances correspond, respectively, to the angles, μ_{max} and μ_{min}, which limit the angular range of invisibility of the papilla. The values of d_{min} and d_{max} must be corrected by adding the distance between the cornea surface and the nodal plane, which is approximately 7mm, as already discussed (see Fig. 5.40).

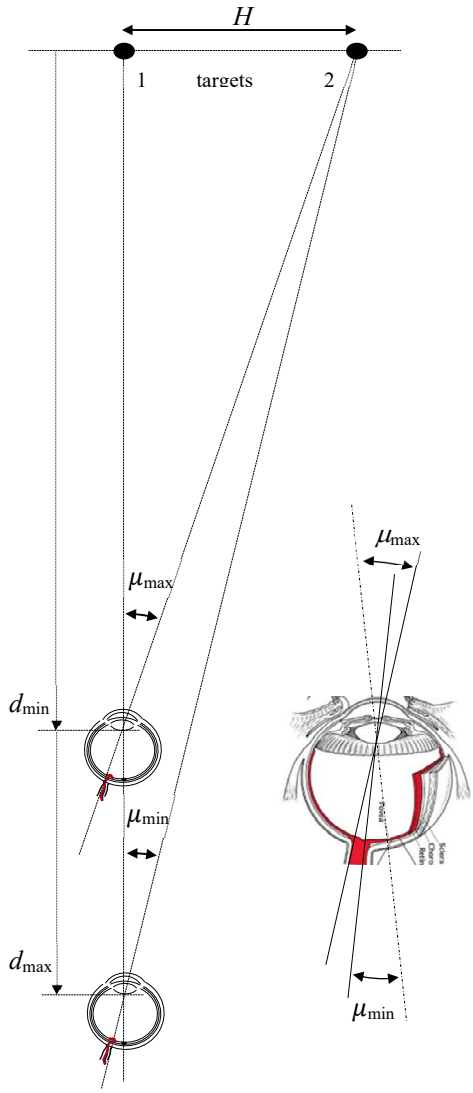

Fig. 5.44. The figure shows the origin of the angles μ_{max} and μ_{min}, associated, respectively, with the distances d_{min} and d_{max}, at which the target 2 disappears, or reappears, respectively, when the distance d of the eye from target 1 is increased.

Fig. 5.44 shows the geometry of the test. The detail on the right shows the two lines, inclined with respect to the visual axis, that define the angular limits, for an indirect view, within which there is no visibility, because the image of the object falls on the papilla. Referring to Fig. 5.44, we have the following expressions for μ_{max} and μ_{min}, and their errors, in correspondence to d_{min} and d_{max}:

$$\mu_{max} = tg^{-1}\left(\frac{H}{d_{min}}\right) \tag{5.29}$$

$$\Delta\mu_{max} = \left(\frac{1}{H^2+{d_{min}}^2}\right)\cdot(H\cdot\Delta d_{min} + d_{min}\cdot\Delta H) \tag{5.30}$$

$$\mu_{min} = tg^{-1}\left(\frac{H}{d_{max}}\right) \tag{5.31}$$

$$\Delta\mu_{min} = \left(\frac{1}{H^2+{d_{max}}^2}\right)\cdot(H\cdot\Delta d_{max} + d_{max}\cdot\Delta H) \tag{5.32}$$

5.4.5. The Combined Test of the Angle of View in the Dark and the Mariotte's Blind Spot Test

The test of angle of view and the Mariotte's blind spot test can be combined in the dark, giving rise to the new test named: Two Blind Spots Test (TBST) (see Fig. 5.45). This test must be prepared as if Mariotte's test was performed in the dark. The dark condition is necessary in this case because the angle of view test is involved. To do this, it is necessary to adjust the quantities: eye-target distance *d*, distance between the targets *H*, and diameter of the targets *D*. To combine the two tests, that is to have both targets disappeared, this procedure must be followed:

i) Measuring α_D, the critical angle of view (see Fig. 5.41);

ii) Fixing a value for $H=H_0$;

iii) From H_0 finding $\mu_{0,max}$ from the μ vs. *H* function (see Fig. 46 b);

iv) From H_0 and $\mu_{0,max}$ deriving $d_{0,min}$ (see Fig. 46 a);

v) Appling the following equation to find D_0, the targets diameter:

$$D_0 = 2\cdot\ d_{0,min}\cdot tg(\alpha/2) \tag{5.33}$$

Under these conditions, target 1 will not be visible in the range $d = d_{min} \div d_{max}$, while target 2 will not be visible at $d \geq d_{min}$. Then, the two targets will be simultaneously obscured in the range $d_{0,min} \div d_{0,max}$.

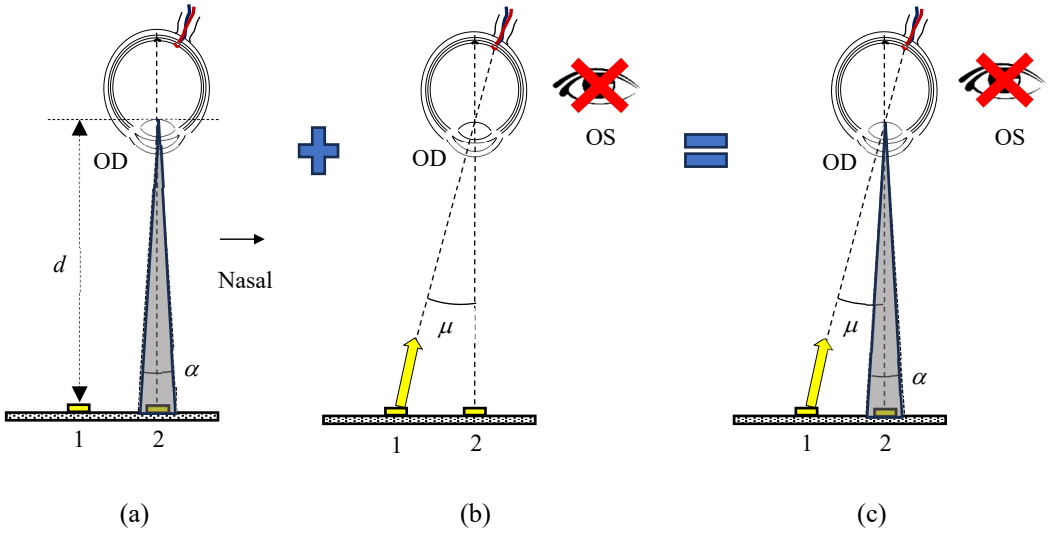

Fig. 5.45. Schematic representation of the Mariotte's blind spot test combined with the angle of view test in the dark. (a) The observer doesn't see target 2 because, in the dark, this falls within the angle of view α: (b) The observer doesn't see target 1 because of the effect of Mariotte's angle μ. (c) The observer doesn't see both targets.

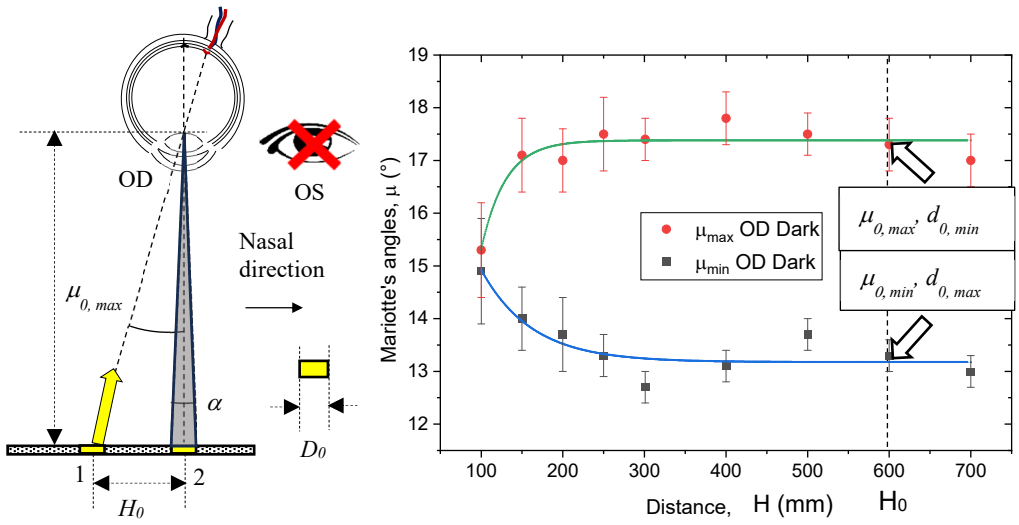

Fig. 5.46. It is shown the way to find the critical diameter D_0 of a target after having followed the procedure which includes the knowledge of α_D, the critical angle of view, the choice of H_0, the calculation of $\mu_{0,max}$ and $d_{0,min}$, and finally the calculation of D_0 from Eq. (5.33).

5.4.6. Test of Resolution Acuity or of the Minimum Angle of Resolution

The smallest resolvable angle expresses the smallest distance between two parallel lines so that they are perceived as two separate objects. The solvable minimum has values greater than the visible minimum. Theoretically, to detect distinct two lines it is necessary the activation of two photoreceptors and the presence, between them, of a deactivated photoreceptor that indicates the lack of continuity. In the normal eye (emmetrope) the resolution acuity is about 35-50 arcseconds.

Specific symbols such as Landolt's "C" can be used to quantify this type of visual acuity (see Fig. 5.47(a)) [3, p. 174; 4, p. 133]. They are circles with a rift (gap) of thickness *D* that can take different orientations. The subject is asked to locate the rift of the letter. The larger distance at which two lines are perceived as separated corresponds to the minimum angle of resolution, MAR (Minimal Angle of Resolution). For this test, the MAR is measured in arcseconds.

As an alternative to Landolt's "C" symbols, we have used simpler resolution mires in which a slit represents a lack of continuity, as shown in Fig. 5.47(b). The minimum angular resolution is the inverse of the angle of minimum resolution, considering only the thickness of the line. If grids are used instead, the angular resolution is indicated clinically in cycles per degree, that is, how many pairs of dark and light bands are present in a degree. A cycle includes both a dark and a light band.

(a) (b)

Fig. 5.47. Optotypes are single stimuli used in the quantification of visual acuity. In the case of resolution acuity, one can use a directional symbol which is Landolt's C (a), or, as an alternative, a slit (b).

5.5. Results and Discussion

5.5.1. Morphoscopic Visual Acuity

5.5.1.1. Measurements in an External Laboratory

The results of tests of morphoscopic acuity carried out in an external photometric laboratory are reported in Table 5.7 for the subjects A and B, respectively [47]. The tables are followed by the two graduated lunettes reporting the angular information *AX* (Axis),

when an astigmatism is present. In absence of an astigmatism, the *CYL* and *AX* voices are void. The results reported in Table 5.7 are compared with those found by us only for the far view (F) condition. For subject A, the older, we have hyperopia (gradation +0.75) on the right eye and a slight myopia (gradation -0.25) on the left eye; on the right eye we then have a mixed astigmatism. Vision is 9/10 in the right eye and 12/10 in the left eye [48]. Binocular vision usually coincides with that of the eye with the highest acuity, and therefore it is 12/10 [4, p. 159]. For the younger subject B, we have a slight myopia (gradation -0.25) on the right eye and a stronger myopia (gradation -1.5) on the left eye; in both eyes we register a myopic astigmatism. Vision is good, 10/10, on the right eye, poorer, 7/10, on the left eye. Binocular vision is that of right eye, 10/10. In summary, the visual acuity of the two subjects is opposite, better for the OS eye in subject A, better for the OD eye in subject B. The VA results from the external laboratory were obtained at the beginning of the experimental activity (March 2023). It is therefore possible that the VAs measured by us in the following two years of work are, at least for subject A, worsened. The dominant eye of subject A, both at light and dark, is the right one. In fact, it isn't necessarily the eye with the highest VA. Instead, it's the eye that the brain prefers to use for tasks that require precise visual input, like reading. Dominance is more about brain processing and preference, rather than just visual sharpness. Binocular vision involves both eyes working together, but the dominant eye often takes the lead in certain tasks, and dominance doesn't always correlate with the eye having higher VA. Binocular vision combines the images from both eyes to create depth perception and a wider field of view, regardless of which eye is dominant or has better acuity.

Table 5.7. Results of the Visual Acuity Tests in an External Photometric Laboratory.

	OD			**OS**		
d	**SPH**	**CYL**	**AX (TABO)**	**SPH**	**CYL**	**AX**
F	+0.75	-1.50	110	-0.25		
N	+3.25	-1.50	110	+2.25		

Interpupillary distance			**Visus**		
OD	**PD**	**OS**	**OD**	**OS**	**OU**
34.0	68.0	34.0	9/10	12/10	12/10

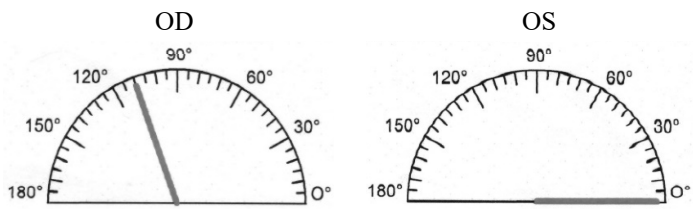

Table 5.7. Continued.

	OD			OS		
d	**SPH**	**CYL**	**AX (TABO)**	**SPH**	**CYL**	**AX**
F	-0.25	-1.25	175	-1.50	-0.50	170

Interpupillary distance			Visus		
OD	**PD**	**OS**	**OD**	**OS**	**OU**
31.3	62.5	31.3	10/10	7/10	10/10

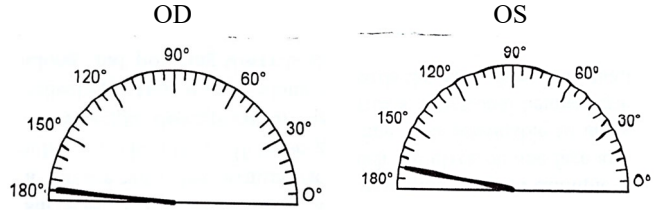

5.5.1.2. Measurements in Our Laboratory

The experimental results achieved in our laboratory on subjects A and B with the tests of morphoscopic acuity are summarized in Table 5.8. We added a column with the values of surface illuminance E_s (lux) on the chart illuminated by lamps or by skylight, or of luminance L_v (nit) for the charts projected by a monitor, or for the PL optotypes of logMAR charts used in the dark tests. The surface illuminance values E_s (lux) are associated in brackets with values of luminance calculated applying Eq. (5.6), where, for N=1, R_s = 0.87±0.08 is the reflectivity of the white paper background, whereas, for N=3 and 4, R_s = 0.70±0.05 is the reflectivity of the white optotypes with the transparent sheet on the front (see Sec. 5.3.2).

The indoor luminance data reported in Table 5.8 and carried out at a distance of 6 m (N = 3, 6, 7 and 8), must be reduced by a factor of ~0.9, equal to the average reflectivity of the mirror used. The morphoscopic VA indoor measurements on the logMAR chart with white optotypes were performed using the white light panel source set for three illuminance levels: 20 %, 50 % and 100 % (see Table 5.2). When a decimal table with VA_{max}=10/10 was used (see Fig. 5.36), scores greater than 10/10 were indicated with the >10/10 notation. To make the VA scores from the decimal and logMAR charts uniform, the logMAR data were translated into tenths *x*, using the conversion Table 5.5.

Table 5.8 shows the data of morphoscopic VA test obtained from Monoyer decimal and logMAR charts. The subjects are S=A or S=B. N gives the number of the environment reported in Table 5.4. The luminance (nit) and illuminance (lx) data are indicated in the last column. The symbol (*) means that the test has been carried out dressing the

protection glasses (type LG). The symbol (†) means that the test has been made outdoor in the night.

Table 5.8. Results of the Morphoscopic Visual Acuity Test.

S	N	OD	OS	OU	E_s/L_v
A	1	$7/10^{+4}$	$9/10^{-1}$	$9/10^{-1}$	3.8 klx (1.1knit)
A	2	$8/10^{+3}$	10/10	10/10	126 nit
A	3a	$8/10^{+2}$	$11/10^{+1}$	$11/10^{+1}$	719±54 lx (160±23nit)
A	3b	8/10	$11/10^{+1}$	12/10	1861±112 lx (414±55 nit)
A	3c	$8/10^{+1}$	$11/10^{+1}$	$11/10^{+1}$	3531±192 lx (787±99 nit)
A	4a	$10/10^{-2}$	$10/10^{+1}$	$10/10^{-2}$	8 klx (1.8knit)
A	4b	$10/10^{-1}$	12/10	12/10	30 klx (6.7knit)
A	6a	$10/10^{-2}$	$10/10^{+1}$	$10/10^{-2}$	190 nit
A	7	8/10	$11/10^{+1}$	$10/10^{-2}$	190 nit
A (*)	7	8/10	$11/10^{+1}$	$11/10^{+1}$	190 nit
B	1	$9/10^{-2}$	$5/10^{-1}$	$9/10^{-2}$	3.8 klx (1.1knit)
B	2	≥10/10	$8/10^{+4}$	≥10/10	126 nit
B	4c	12/10	$10/10^{-2}$	$10/10^{+1}$	7 klx (1.5knit)
B	4d	$12/10^{+1}$	$8/10^{-2}$	$8/10^{+2}$	20klx (4.5 knit)
B (†)	6b	$10/10^{+2}$	$12/10^{-2}$	$12/10^{-1}$	190 nit

The morphoscopic visual acuity results reported in Table 5.8 must be evaluated considering the different progression and structure of the chart, as well as the chosen lighting of it, or the luminance of the characters. Regardless of these factors, however, we find that, for subject A, the visus of the left eye is higher than that of the right one, while the situation for subject B is opposite. This agrees with what found in the private laboratory test [47]. As regards the type of chart, we find, for both subjects, a poor vision at light in reading the decimal optotypes (see the tests n. 1 and 2 in Table 5.8), evidently penalized by the negative contrast of the characters, and perhaps also by the progression of the decimal table, now out of use. The level of illumination of the chart, in the light, has a great importance on vision; in fact, it significantly increases the subject's vision, which reaches high values in conditions of strong sunlight, higher than those recorded in the private laboratory, as can be seen from Table 5.8.

Other results were obtained in the dark with logMAR charts made with photoluminescent characters (see the tests number 6 and 7 in Table 5.4), lightened by UVA torches. The PL characters were illuminated for a few seconds with UVA light and immediately read by the subject. The luminance achieved by the characters is not very high, and is comparable to that of the monitor screen in test no. 2 (see Table 5.8). Despite this, high vision acuity values are achieved. Evidently, these tests in the dark, with positive contrast characters, are optimal for distance vision. From Table 5.8 we further note that, wearing protective glasses of type LG to UVA light, does not lead to changing the visual acuity. No difference was found lightening the chart with UVA light with $\lambda = 395$ nm or $\lambda = 365$ nm.

The results of VA, taken on the logMAR chart with white optotypes in conditions of cloudy sky (N=5 in Table 5.4), are reported in Table 5.9 as function of the illuminance on the logMAR chart. In the Notes, in brackets, the corresponding luminance is indicated, calculated by applying Eq. (5.6), where $R_s = 0.71 \pm 0.03$ is the reflectivity of the white optotypes with the transparent sheet on the back. The measurements were performed by subject A (the author), and recorded by the same subject, in the form of self-tests.

Table 5.9. Results of the Morphoscopic Visual Acuity Test at Cloudy Sky.

N	OD	OS	OU	$E_S/(L_V)$
5/1	$5/10^{-3}$	$6/10^{-1}$	$4/10^{-3}$	4±0.5lx (0.9±0.1nit)
5/2	$6/10^{+1}$	$8/10^{-2}$	$10/10^{-2}$	24±0.5 lx (5.4±0.3 nit)
5/3	$6/10^{-2}$	$8/10^{-3}$	$8/10^{+2}$	32±0.5 lx (7.2±0.4 nit)
5/4	$8/10^{-2}$	10/10	11/10	43±1 lx (9.7±0.6 nit)
5/5	6/10	$8/10^{+3}$	11/10	77±2 lx (17±1 nit)
5/6	$8/10^{-2}$	$10/10^{+2}$	$11/10^{+1}$	274±4 lx (62±3 nit)
5/7	$8/10^{-1}$	$11/10^{+1}$	$11/10^{+1}$	360±12 lx (81±6 nit)
5/8	$10/10^{-2}$	$11/10^{+1}$	$12/10^{+1}$	385±5 lx (87±5 nit)
5/9	8/10	12/10	$11/10^{+1}$	455±4 lx (103±5 nit)
5/10	$10/10^{-2}$	12/10	$11/10^{+1}$	492±3 lx (111±5 nit)
5/11	8/10	11/10	12/10	574±5 lx (130±7 nit)
5/12	$10/10^{-1}$	12/10	$12/10^{+1}$	664±27 lx (150±12 nit)
5/13	$10/10^{-2}$	$11/10^{+1}$	$12/10^{+1}$	857±21 lx (194±13 nit)
5/14	$8/10^{+2}$	$10/10^{+2}$	$10/10^{+3}$	965±8 lx (218±11 nit)

Table 5.9. Continued.

N	OD	OS	OU	$E_s/(L_v)$
5/15	$10/10^{-1}$	12/10	$12/10^{+1}$	1.12±0.02klx (253±15 nit)
5/16	$8/10^{+2}$	$12/10^{+1}$	12/10	1.44±0.03klx (325±20 nit)
5/17	$10/10^{-1}$	12/10	$12/10^{+1}$	1.5±0.1klx (339±37 nit)
5/18	$10/10^{-1}$	12/10	$12/10^{+1}$	1.7±0.05klx (384±27 nit)
5/19	$10/10^{-1}$	12/10	$12/10^{+1}$	2.4±0.05klx (542±34 nit)
5/20	$11/10^{+1}$	$11/10^{+1}$	$12/10^{+1}$	2.51±0.03klx (567±30 nit)
5/21	$8/10^{+2}$	11/10	12/10	2.7±0.1klx (610±48 nit)
5/22	$10/10^{-1}$	$12/10^{+1}$	$12/10^{+1}$	3.3±0.05klx (748±43 nit)
5/23	$11/10^{+1}$	12/10	$11/10^{+1}$	4.2±0.1klx (949±63 nit)
5/24	$11/10^{+1}$	12/10	12/10	4.6±0.05 klx (1040±55 nit)
5/25	11/10	12/10	$12/10^{+1}$	5.5±0.05 klx (1243±64nit)

I realize that this procedure is not contemplated in normal optometric practice, but it was necessary to collect a large amount of data in a short time and in absence of collaborators. The VA results of Tab. 5.9 are reported as function of luminance in the graphs of Fig. 5.48.

Fig. 5.48 (a) shows the VA data in the whole luminance range explored, while Fig. 5.48(b) and 5.48 (c) show VA at smaller ranges of luminance. From Fig. 5.48 (a) we see that the visual acuity, both for OD, OS, and OU, is a function of the luminance and reaches a saturation value, VA_{sat}, different for the different visual modality, for luminance values higher than ~100 cd/m^2. The saturation values are different for the three types of vision of subject A. We have VA_{sat} ~12/10 for OS, VA_{sat} ~12.5/10=$12/10^{+1}$ for OU, while, for OD, we find VA_{sat} ~9.4/10=$9/10^{+1}$, up to a luminance of ~700 cd/m^2, whereas, for higher values of L_v, VA_{sat} tends to increase and reach around 11/10. It should be remembered that, due to the mixed astigmatism of subject A for OD, the letters appear blurred, or rather double, and this determines a clear reduction in visual acuity. In Fig. 5.48 (b), we also note that the VA of OS, OU and OD tend to decrease for luminance lower than ~75 nits. Finally, in Fig. 5.48 (c), we note that the VA of OS and OU show a clear drop below a luminance of ~10 nits. This last data will be related to what will be found by the VA tests in the dark with photoluminescent logMAR charts.

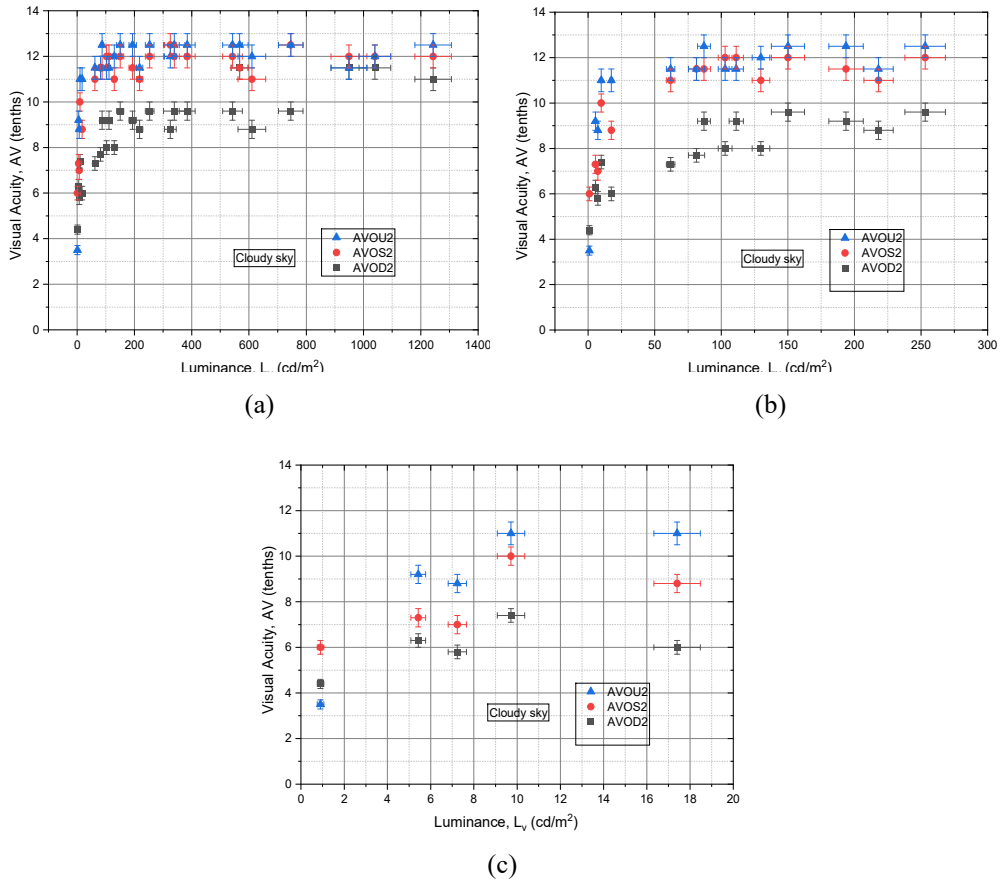

Fig. 5.48. Visual acuity VA of subject A at the light of cloudy sky, tested with the logMAR chart with white optotypes. The VA is shown as function of luminance at different luminance intervals.

As regards the VA tests in the dark and with a photoluminescent logMAR chart, some results have been already reported in Table 5.8, obtained using single LED torches as UVA light sources. Other VA results, for a total of 434, were obtained replacing the LED torches with a pair of LED panels with UVA light between 395 and 405 nm (see Tab. 5.4, N=8), as a function of the luminance of the optotypes. To vary the luminance of the optotypes, the LED panels were positioned at different distances from the logMAR chart. In this way it was possible to examine a range of luminance values between ~1 and ~800 cd/m^2. The results are reported in Table 5.10. Considering that this test is performed in the presence of UVA light in the environment, it was performed at three different experimental conditions. In the first the subject had naked eyes (NE), in the second he wore a pair of clear UV glasses (Light Glasses, LG), and finally in the third he wore a pair of dark UV glasses (Dark Glasses, DG). During the test, the subject was always shielded from direct light from the UV sources by a black cloth. As in the previous test (Table 5.9), this test was performed by subject A, and recorded by the same subject, in the form of self-test.

Table 5.10. Results of the Morphoscopic VA Test at Dark with PL LogMAR Charts.

N	E	OD	OS	OU	L_v (nit)
1	NE	8/10	$10/10^{-1}$	$11/10^{+1}$	1±1
2	LG	8/10	$10/10^{-2}$	-	
3	DG	6/10	$8/10^{-2}$	6/10	
4	NE	8/10	11/10	$11/10^{+1}$	6±5
5	LG	$8/10^{-2}$	11/10	$11/10^{+1}$	
6	DG	$6/10^{-1}$	$8/10^{+1}$	$8/10^{-2}$	
7	NE	$6/10^{-1}$	11/10	11/10	10±6
8	LG	8/10	11/10	11/10	
9	DG	$6/10^{+1}$	$10/10^{-2}$	$8/10^{-1}$	
10	NE	8/10	$11/10^{+1}$	11/10	11±6
11	LG	8/10	11/10	$11/10^{+1}$	
12	DG	$6/10^{-1}$	$10/10^{-2}$	$10/10^{-2}$	
13	NE	5/10	11/10	-	12±6
14	LG	5/10	11/10	-	
15	DG	$5/10^{-3}$	$8/10^{-2}$	-	
16	NE	$8/10^{-2}$	11/10	11/10	12±6
17	LG	$6/10^{+1}$	11/10	11/10	
18	DG	5/10	$10/10^{-2}$	$8/10^{+2}$	
19	NE	$6/10^{+1}$	11/10	11/10	15±6
20	LG	$8/10^{-1}$	11/10	11/10	
21	DG	5/10	$10/10^{-2}$	$10/10^{-2}$	
22	NE	$6/10^{+1}$	$11/10^{+1}$	$11/10^{+1}$	16±6
23	LG	8/10	11/10	11/10	
24	DG	$8/10^{-1}$	$10/10^{-2}$	$10/10^{-2}$	
25	NE	$6/10^{+1}$	11/10	11/10	18±6
26	LG	$8/10^{-2}$	11/10	$11/10^{+1}$	
27	DG	$6/10^{-1}$	$10/10^{-2}$	$10/10^{-2}$	
28	NE	8/10	$11/10^{+1}$	$11/10^{+1}$	21±6
29	LG	$8/10^{-1}$	$11/10^{+1}$	$11/10^{+1}$	
30	DG	6/10	$11/10^{+1}$	$8/10^{+2}$	
31	NE	$6/10^{-1}$	11/10	11/10	23±6
32	LG	7/10	11/10	11/10	
33	DG	$6/10^{-1}$	$8/10^{+2}$	-	
34	NE	8/10	11/10	-	25±7
35	LG	$5/10^{+1}$	11/10	-	
36	DG	5/10	$10/10^{-3}$	-	
37	NE	6/10	$11/10^{+1}$	$11/10^{+1}$	26±7
38	LG	$8/10^{-2}$	$11/10^{+1}$	$11/10^{+1}$	
39	DG	6/10	$10/10^{-2}$	$10/10^{-1}$	
40	NE	$6/10^{-1}$	11/10	11/10	29±7
41	LG	$8/10^{-2}$	$10/10^{-2}$	11/10	
42	DG	$6/10^{-1}$	$10/10^{-2}$	$8/10^{+2}$	
43	NE	$8/10^{-2}$	11/10	-	32±7
44	LG	$6/10^{-1}$	11/10	11/10	
45	DG	$5/10^{+2}$	$10/10^{+1}$	$8/10^{+2}$	
46	NE	$8/10^{-2}$	11/10	11/10	38±7

Table 5.10. Continued.

N	E	OD	OS	OU	L_v (nit)
47	LG	$8/10^{-2}$	11/10	11/10	
48	DG	6/10	11/10	11/10	
49	NE	$5/10^{+1}$	11/10	11/10	
50	LG	$5/10^{+1}$	11/10	-	40±8
51	DG	5/10	$8/10^{-2}$	$10/10^{-2}$	
52	NE	8/10	11/10	11/10	
53	LG	8/10	$11/10^{+1}$	11/10	45±8
54	DG	-	-	-	
55	NE	$11/10^{+1}$	$11/10^{+1}$	$11/10^{+1}$	
56	LG	7/10	$11/10^{+1}$	$11/10^{+1}$	50±8
57	DG	8/10	11/10	$11/10^{+1}$	
58	NE	$8/10^{-2}$	$11/10^{+1}$	11/10	
59	LG	$8/10^{-2}$	11/10	11/10	54±9
60	DG	$8/10^{-2}$	11/10	-	
61	NE	5/10	$11/10^{+1}$	$11/10^{-1}$	
62	LG	$6/10^{-1}$	11/10	9/10	62±9
63	DG	$5/10^{-2}$	$8/10^{+1}$	8/10	
64	NE	11/10	$11/10^{+1}$	11/10	
65	LG	$8/10^{+2}$	11/10	11/10	68±9
66	DG	$6/10^{+1}$	11/10	11/10	
67	NE	8/10	$11/10^{+1}$	$11/10^{+1}$	
68	LG	$8/10^{-2}$	11/10	11/10	73±10
69	DG	-	-	-	
70	NE	$8/10^{-1}$	$11/10^{+1}$	$11/10^{+1}$	
71	LG	8/10	$11/10^{+1}$	$11/10^{+1}$	79±10
72	DG	8/10	$12/10^{+1}$	11/10	
73	NE	8/10	11/10	11/10	
74	LG	$8/10^{-2}$	11/10	11/10	85±10
75	DG	$6/10^{+1}$	$10/10^{+1}$	$10/10^{-2}$	
76	NE	$6/10^{-1}$	11/10	11/10	
77	LG	$6/10^{+1}$	11/10	11/10	91±11
78	DG	5/10	11/10	9/10	
79	NE	$8/10^{-2}$	$11/10^{+1}$	11/10	
80	LG	$8/10^{-2}$	$11/10^{+1}$	12/10	111±12
81	DG	8/10	$11/10^{+1}$	11/10	
82	NE	6/10	11/10	11/10	
83	LG	$6/10^{+1}$	11/10	11/10	111±12
84	DG	-	-	-	
85	NE	$6/10^{+1}$	11/10	11/10	
86	LG	$6/10^{+1}$	$11/10^{-1}$	11/10	126±13 nit
87	DG	$6/10^{+1}$	$10/10^{+1}$	$10/10^{+1}$	
88	NE	$10/10^{-2}$	$11/10^{+1}$	$12/10^{+1}$	
89	LG	8/10	$11/10^{+1}$	$11/10^{+1}$	140±14 nit
90	DG	7/10	$11/10^{+1}$	11/10	
91	NE	$8/10^{-3}$	$11/10^{+1}$	$11/10^{+1}$	156±15 nit
92	LG	$6/10^{+1}$	$11/10^{+1}$	$11/10^{+1}$	

Table 5.10. Continued.

N	E	OD	OS	OU	L_v (nit)
93	DG	6/10	11/10	$11/10^{+1}$	
94	NE	7/10	11/10	11/10	158±15 nit
95	LG	$6/10^{+1}$	11/10	11/10	
96	DG	5/10	11/10	11/10	
97	NE	$8/10^{-2}$	12/10	$11/10^{+1}$	173±16 nit
98	LG	$8/10^{-1}$	$11/10^{+1}$	$11/10^{+1}$	
99	DG	$8/10^{-1}$	$11/10^{+1}$	$11/10^{+1}$	
100	NE	$8/10^{-2}$	12/10	-	189±17 nit
101	LG	$6/10^{+1}$	$11/10^{+1}$	$11/10^{+1}$	
102	DG	$6/10^{+1}$	11/10	$11/10^{+1}$	
103	NE	8/10	$11/10^{+1}$	12/10	210±19 nit
104	LG	8/10	$11/10^{+1}$	$11/10^{+1}$	
105	DG	8/10	$11/10^{+1}$	$11/10^{+1}$	
106	NE	$6/10^{+1}$	12/10	$10/10^{-1}$	225±20 nit
107	LG	$7/10^{-1}$	$11/10^{+1}$	11/10	
108	DG	$5/10^{+2}$	11/10	$11/10^{+1}$	
109	NE	$8/10^{-1}$	$11/10^{+1}$	$11/10^{+1}$	240±21 nit
110	LG	$8/10^{-2}$	$11/10^{+1}$	$11/10^{+1}$	
111	DG	$6/10^{+2}$	$11/10^{+1}$	$11/10^{+1}$	
112	NE	$8/10^{-1}$	$12/10^{+1}$	$12/10^{+1}$	260±22 nit
113	LG	$8/10^{-2}$	12/10	$10/10^{+1}$	
114	DG	-	-	-	
115	NE	8/10	$12/10^{+2}$	12/10	281±23 nit
116	LG	$8/10^{+2}$	12/10	11/10	
117	DG	$5/10^{-2}$	11/10	11/10	
118	NE	8/10	$11/10^{+1}$	$11/10^{+1}$	287±24 nit
119	LG	$8/10^{+1}$	$11/10^{+1}$	$11/10^{+1}$	
120	DG	$8/10^{-2}$	$11/10^{+1}$	$11/10^{+1}$	
121	NE	$8/10^{-1}$	$11/10^{+1}$	$11/10^{+1}$	328±26 nit
122	LG	8/10	$11/10^{+1}$	$11/10^{+1}$	
123	DG	$6/10^{+1}$	11/10	$11/10^{+1}$	
124	NE	8/10	$11/10^{+1}$	$11/10^{+1}$	349±28 nit
125	LG	$6/10^{+1}$	12/10	$11/10^{+1}$	
126	DG	8/10	$11/10^{+1}$	$11/10^{+1}$	
127	NE	$8/10^{-2}$	12/10	$11/10^{+1}$	369±29 nit
128	LG	$8/10^{-2}$	12/10	$11/10^{+1}$	
129	DG	$8/10^{-2}$	$11/10^{+1}$	$11/10^{+1}$	
130	NE	$6/10^{+1}$	$11/10^{+1}$	$11/10^{+1}$	398±31 nit
131	LG	$6/10^{+2}$	$11/10^{+1}$	$11/10^{+1}$	
132	DG	$6/10^{+1}$	11/10	11/10	
133	NE	$8/10^{-2}$	11/10	-	439±33 nit
134	LG	$8/10^{-1}$	$11/10^{+1}$	11/10	
135	DG	$8/10^{-2}$	$11/10^{+1}$	$11/10^{+1}$	
136	NE	$6/10^{+1}$	$8/10^{+2}$	$10/10^{-2}$	500±37 nit
137	LG	$6/10^{+1}$	$11/10^{+1}$	9/10	
138	DG	6/10	12/10	$11/10^{+1}$	

Table 5.10. Continued.

N	E	OD	OS	OU	L_V (nit)
139	NE	8/10	$11/10^{+1}$	12/10	537±40 nit
140	LG	$8/10^{-2}$	$11/10^{+1}$	$11/10^{+1}$	
141	DG	$8/10^{-2}$	$11/10^{+1}$	$11/10^{+1}$	
142	NE	8/10	$11/10^{+1}$	$11/10^{+1}$	593±43 nit
143	LG	$8/10^{-1}$	12/10	$11/10^{+1}$	
144	DG	$6/10^{+1}$	$11/10^{+1}$	$11/10^{+1}$	
145	NE	$8/10^{-1}$	$11/10^{+1}$	$11/10^{+1}$	633±46 nit
146	LG	8/10	12/10	$11/10^{+1}$	
147	DG	$8/10^{-1}$	$11/10^{+1}$	$11/10^{+1}$	
148	NE	$8/10^{-2}$	$10/10^{+1}$	-	678±49 nit
149	LG	8/10	$11/10^{+1}$	$11/10^{+1}$	
150	DG	$8/10^{-2}$	$11/10^{+1}$	$11/10^{+1}$	
151	NE	8/10	12/10	11/10	734±53 nit
152	LG	$8/10^{-2}$	12/10	11/10	
153	DG	$8/10^{-2}$	11/10	11/10	
154	NE	$8/10^{-2}$	12/10	12/10	799±57 nit
155	LG	8/10	$11/10^{+1}$	$11/10^{+1}$	
156	DG	$8/10^{-2}$	$11/10^{+1}$	11/10	

All the VA data are graphed in Fig. 5.49 as function of luminance. In this graph, since there are many points, it has been preferred not to report the errors in the luminance. Despite this, it is still difficult to clearly distinguish the various types of data, so, they are reported separately in Fig. 5.50 (a)-(c), depending on whether they were obtained with naked eyes (NE), clear UV glasses (LG), or dark UV glasses (DG). In Fig. 5.51 (a)-(c), instead, they are reported separately for the different eyes: OS, OU and OD. Fig. 5.49 shows that the VA data for OD are low, in the range between 4 and 9, and very scattered, particularly for low luminance. As we have already seen for the VA test in sunlight, due to the mixed astigmatism of subject A for OD, the letters appear blurred, or doubled, and this determines a clear reduction in visual acuity. The VA data for OS and OU, on the other hand, remain very high, between 11 and 12, although a hint of a decrease appears at luminance values close to zero.

From the Fig. 5.50 (a), (b), we see that the visual acuity data at NE and LG conditions seems almost the same. This is due to the high transmission of the clear glasses (LG) at the photoluminescent light of the optotypes, 88±3%, as reported in Tab. I, which makes the view with naked eyes and that with the light glasses almost the same. The behavior of vision is different when wearing dark glasses. In Fig. 5.50 (c), in fact, we find for the right eye a further decrease of the VA and a significant increase of the scattering. The DG-OS and DG-OU data, which have been now isolated, show a clear drop in visual acuity at low luminance values. In practice, it is thanks to the DG glasses that we can better explore the visual acuity of OS and OU at luminance close to zero. The interesting aspect of these data is that the VA of OS and OU remain virtually constant, between 11 and 12, over a very wide luminance range, starting from around 800 down to less than 50 nits, regardless of the presence or absence of glasses.

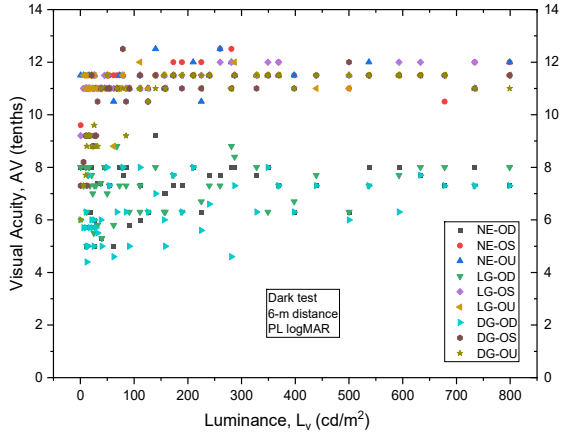

Fig. 5.49. All the 434 results of visual acuity of subject A taken at dark with the photoluminescent logMAR chart, and shown as function of luminance of the PL optotypes.

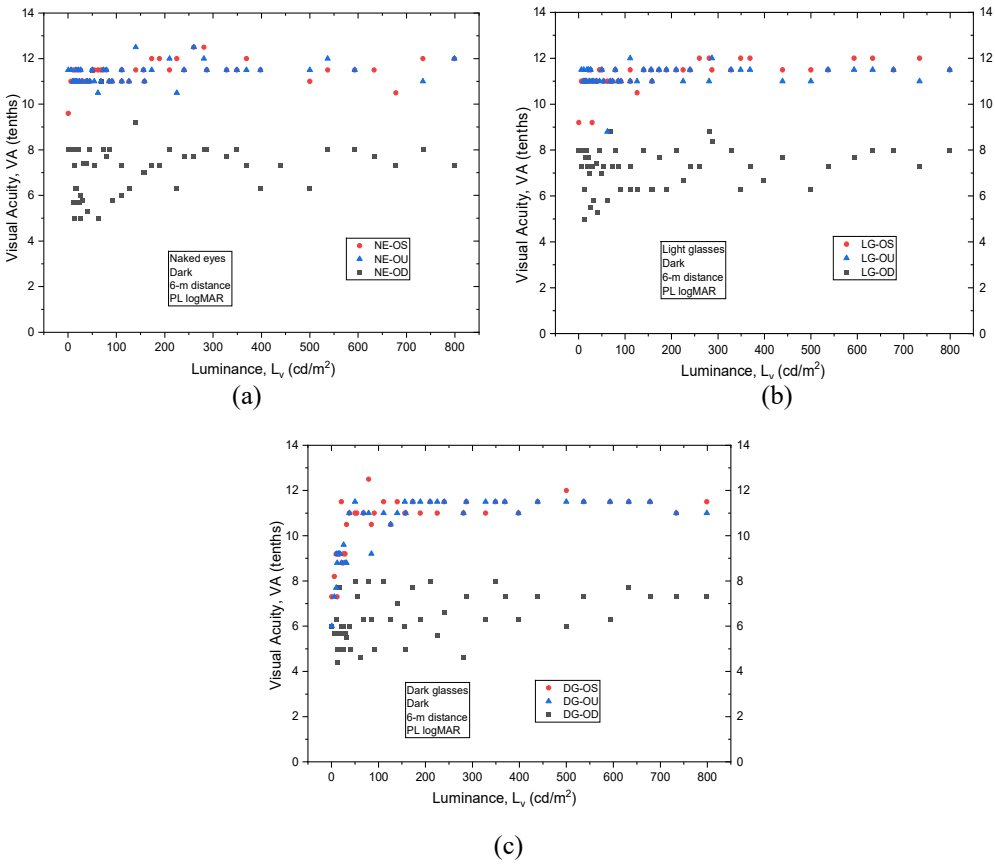

Fig. 5.50. Visual acuity of subject A at dark with the PL logMAR chart. (a) Sight with naked eyes (NE); (b) Sight with clear glasses (LG); (c) Sight with dark glasses (DG).

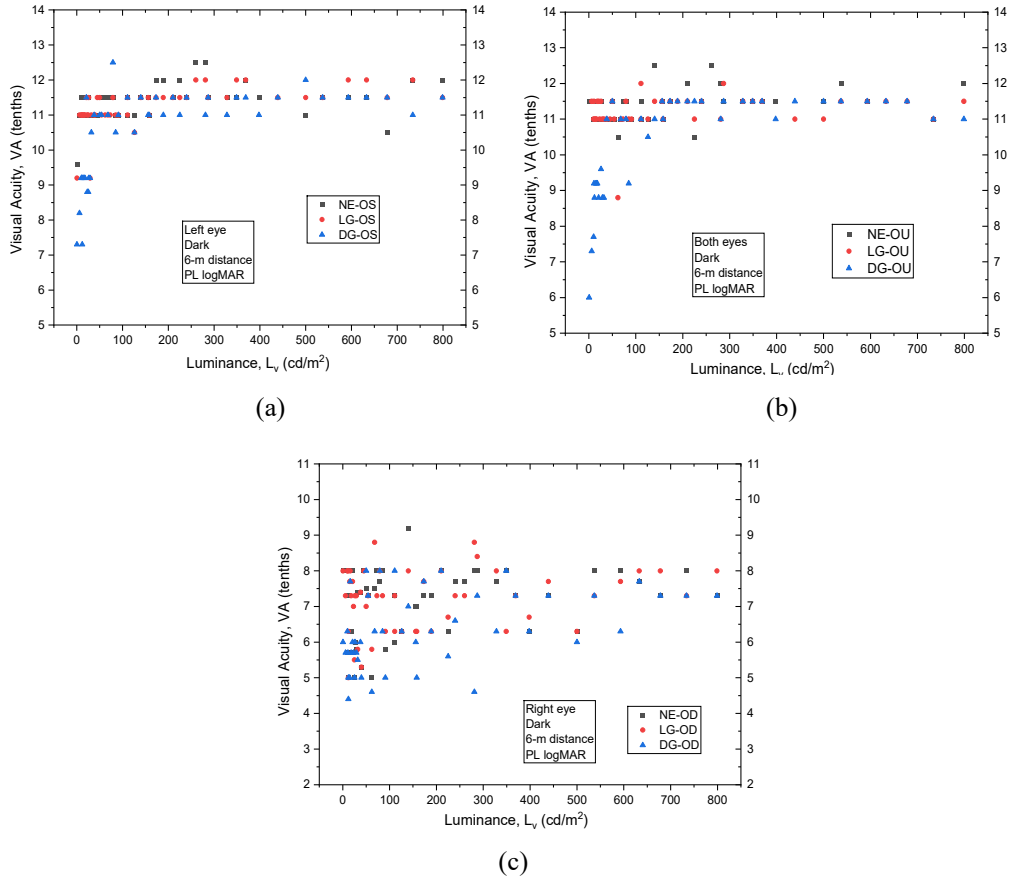

Fig. 5.51. Visual acuity of subject A at dark with the PL logMAR chart. (a) Sight with left eye (OS); (b) Sight with both eyes (OU); (c) Sight with right eye (OD).

The almost perfect superposition of the two graphs in Figs. 5.51 (a), (b) also shows that the visual acuity of OS and OU is practically the same, which confirms the fact that, in OU conditions, vision is dominated by the eye with the highest visual acuity, in this case the left eye. Figs. 5.51 (a), (b) also show the effect that dark glasses have on vision, namely a significant reduction in the VA of OS and OU towards low luminance. Fig. 5.51 (c) finally shows the high scattering of the VA data for the right eye, and that this scattering increases significantly when wearing dark glasses. Now let's look at the VA data in more detail. For high luminance values (L_v > 100nit), we find the average VA values in the different viewing conditions in Table 5.11.

Table 5.11 summarizes the VA data for luminance above 100 nits. We find what has been discussed so far, that is, very low VA values (average value around 7) and very scattered for the view with only OD, and high values, between 11 and 12, for the view with OS and OU, and a lower scattering. A different discussion must be made for the right eye, for which the VA data are scattered over the entire range of luminance examined. The results are reported in Table 5.12. From Table 5.12 we note both a reduction in the mean values of the VA of OD and an increase of their scattering.

Table 5.11. Summary of Visual Acuity of OD, OS and OU in the Range of Luminance Values higher than 100 nit.

Eyes	Conditions	Visual Acuity
OD	Naked eyes (NE)	7.4±0.7
	Light Glasses (LG)	7.3±0.8
	Dark Glasses (DG)	6.8±0.9
OS	Naked eyes (NE)	11.6±0.5
	Light Glasses (LG)	11.6±0.4
	Dark Glasses (DG)	11.3±0.3
OU	Naked eyes (NE)	11.5±0.5
	Light Glasses (LG)	11.3±0.6
	Dark Glasses (DG)	11.3±0.3

Table 5.12. Summary of Visual Acuity of OD in the Full Range of Luminance Values.

Eyes	Conditions	Visual Acuity
OD	Naked eyes (NE)	7.2±1.3
	Light Glasses (LG)	7.2±0.9
	Dark Glasses (DG)	6.3±1.0

Now let us focus on the VA data for low luminance values. In particular, we are interested in finding the threshold luminance value below which there is a significant reduction in the visual capacity of the OS and OU eyes, the only ones that show the presence of a threshold (see Figs. 5.52 (a), (b)). Let's start looking at the VA curves for OS and OU through dark glasses (DG).

The VA drop for DG-OS and DG-OU is very similar and is given, respectively, by the following equations:

$$VA_{OS} = 11.3(\pm 0.1) - 4.0(\pm 0.4)\cdot e^{-26.2(\pm 5)} \tag{5.34a}$$

$$VA_{OU} = 11.3(\pm 0.1) - 4.8(\pm 0.4)\cdot e^{-L_v/24.6(\pm 4)} \tag{5.34b}$$

We find a threshold of 26.2±5 nit for the VA of OS and a threshold of 24.6±4 nit for the VA of OU. In that case, if we now combine the threshold luminance (~25 nits) with the transmittance of the dark glasses, we should be able to predict a luminance threshold for visibility in "naked eyes" conditions. Then, calling for the threshold of OS-DG: $L_{thr,OS,DG} = 26.2 \pm 5$, and the threshold of OU-DG: $L_{thr,OU,DG} = 24.6 \pm 4$, and being the transmittance of dark glasses: $T_{DG} = 0.23 \pm 0.02$, we expect, for the OS and OU luminance thresholds in "naked eyes" conditions, respectively (here the subscript "thr" means threshold):

$$L_{thr,OS,NE} = L_{thr,OS,DG} * T_{DG} = 6.0 \pm 2\ nit \tag{5.35a}$$

$$L_{thr,OU,NE} = L_{thr,OU,DG} * T_{DG} = 5.7 \pm 2\ nit \tag{5.35b}$$

And so, we expect a luminance threshold of ~6 nit for visibility in naked eyes conditions for both OS and OU.

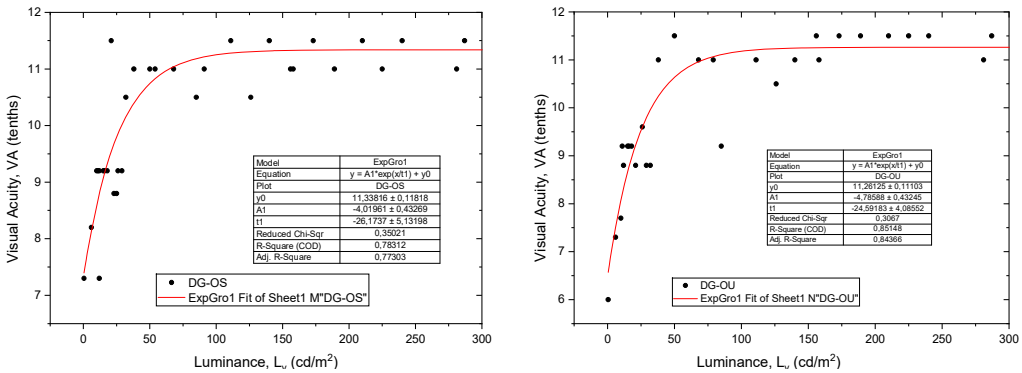

(a) (b)

Fig. 5.52. Results of visual acuity for subject A at dark with the photoluminescent logMAR chart. (a) Sight with dark glasses on OS; (b) Sight with dark glasses on OU. The luminance range has been restricted to 300 nit to better see the drop of visual acuity.

5.5.2. Test of the Angle of View in the Dark

Table 5.13 reports the results of the critical angle of view, α_D, for individual eyes and for both eyes, for the tested A and B subjects. In the notes we have included the number of measurements, the diameter *D* of target and the number of targets observed. A first series of measurements, in fact, was performed by observing a single 20mm-diameter target, while the second was performed by alternatively observing the individual targets of a group of dozens, illustrated in Fig. 5.53. The results of the angle of view test (see Table 5.13) show, for subject A, α_D values around 1°, a value considered acceptable by the literature [2, p. 14]. Subject B shows smaller values, likely associated to the myopia [49]. As regards the comparison between the left eye and the right eye, we expect the angle of view to be smaller for the eye that has greater visual acuity, and in fact this is true, even if to a minimal extent, for subject A. We do not find the same in subject B. Taking for the angle of view in the dark of subject A the value of 1°, and for a nodal point-fovea distance a value of ~17 mm, we obtain: tan1·17~0.3 mm, which corresponds quite well with the linear dimensions of the foveola (see Section 5.2). We can then definitely affirm that the angle of view test in the dark is based on the darkening of the cones located in the foveola area.

Table 5.13. Results of the Test of Angle of View in the Dark.

	a **(°)**			
Obs.	**OS**	**OD**	**OU**	**NOTES**
A	0.97 ±0.09	1.08 ±0.12	-	50 measures 20mm target 1 Target
	0.90 ±0.06	0.97 ±0.07	0.92 ±0.05	80 measures 10mm target 12 Targets
B	0.20 ±0.01	0.20 ±0.01	-	10 measures 20mm target 1 Target

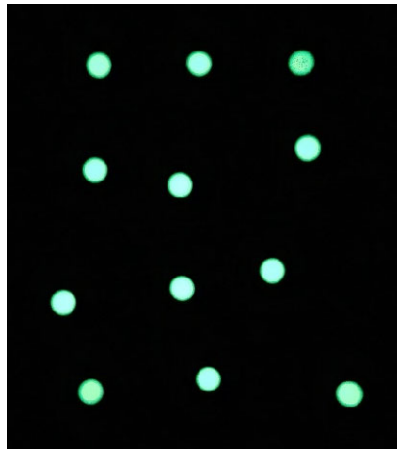

Fig. 5.53. Group of dozen 10-mm diameter targets, randomly distributed on a black card.

5.5.3. Light Sources that can be Darkened

The measures of the critical angle of view at dark, which is a consequence of the darkening of PL targets, were followed by a search for the sources showing a similar behavior. Several attempts were made to resolve this issue. Different small light sources were tested, where luminance could be controlled qualitatively by the sight, for example small LED sources of different colors. Their luminance was reduced with neutral filters in order to make it similar to that of PL targets. Despite this, the test in the dark has shown that they are not darkened. The same result was obtained by preparing a small circular window on the smartphone screen, of the same size as the PL target, having previously set a brightness of the screen such as to result in a luminance comparable to that of the PL target. Even this source could not be darkened in the dark.

The only sources that showed the phenomenon of darkening under the angle of view were: i) The phosphorescent hands of a wristwatch; (ii) Very faint white light of lamps diffused by a white wall, or by a smooth metallic surface. For example, the red ones projected on

the ceiling by digital clocks at night could not be darkened. In short, it seems that this phenomenon is complex and requires further study to be done elsewhere. Fig. 5.54 shows some examples of light sources that could be darkened, and others that could not be darkened, despite their brightness had been reduced to a minimum. Fig. 5.54 (a) shows, on the left side, a PL disk emitting very faint light. It was used as the light source in the angle of view test, and is therefore an undoubtedly darkenable light source. Fig. 5.54 (b) shows a faint white light reflected by a white diffusive wall or by a metallic smooth surface; it was observed in the house during the night and was darkened with the sight adapted to dark. Fig. 5.54 (c) shows the faint light source, of yellow-green color, from the phosphorescent hands of a wristwatch. Also, this type of light has been darkened with the sight adapted to dark.

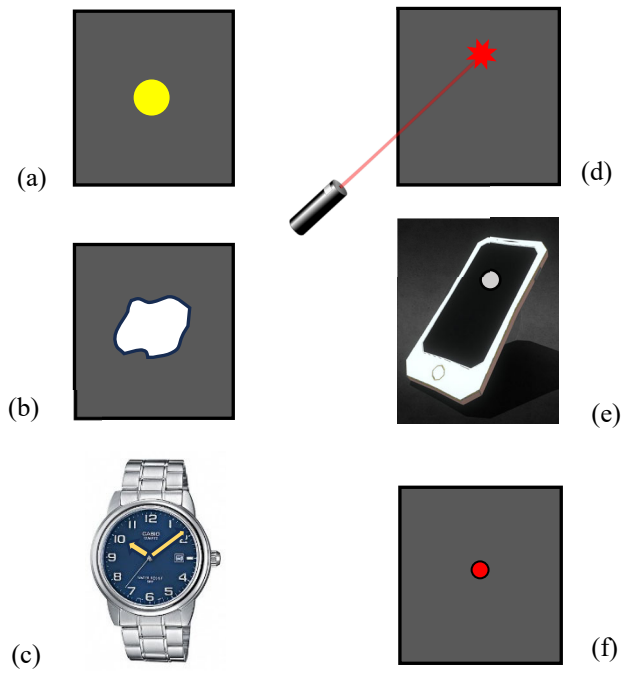

Fig. 5.54. Group of darkened (a, b, c) and undarkened (d, e, f) light sources.

These are the three conditions in which it was possible to obscure, in the dark, a weak light source, of the phosphorescent type or reflected from a surface. Fig. 5.54 (d) shows, on the right side, the spot light produced by a red laser beam incident on a white wall. It was not darkenable even at very low intensities. Fig. 5.54 (e) shows a smartphone whose screen has been shielded in such a way as to expose a small central hole. The screen has been tuned to emit light of different colors, of very low intensity. In all the cases tested, it has never been possible to obscure this tiny window of light. Finally, Fig. 5.54 (f) shows the light spot emitted by a small light source, such as that found in electronic devices to indicate the “on” or “off”, or “stand-by” status. Also, this type of light source, of any color, was not possible to be darkenable.

5.5.4. The Blind Spot Test of Mariotte

5.5.4.1. Measurements at Light

The first measurements for Mariotte's blind spot test were made using two black stickers of 17 mm in diameter placed at distance H = 149.2±0.4 mm on a white wall. An example of d_{min} measurements for the right eye of subject S=A is shown in Fig. 5.55. The distribution of d_{min} values has a good Gaussian trend. Tab. 5.14 shows preliminary results obtained for the Mariotte's test, carried out at light on the two examined subjects S (A and B), reported for the left eye (OS) and the right eye (OD). The acronym BG stands for Background The values of d_{min} and d_{max}, measured as shown in Fig. 5.41 (b), are corrected by adding the cornea-nodal plane distance (~7 mm) (see Fig. 5.40). The blind side angles μ_{min} and μ_{max} are obtained from Eqs. (5.28)-(5.31).

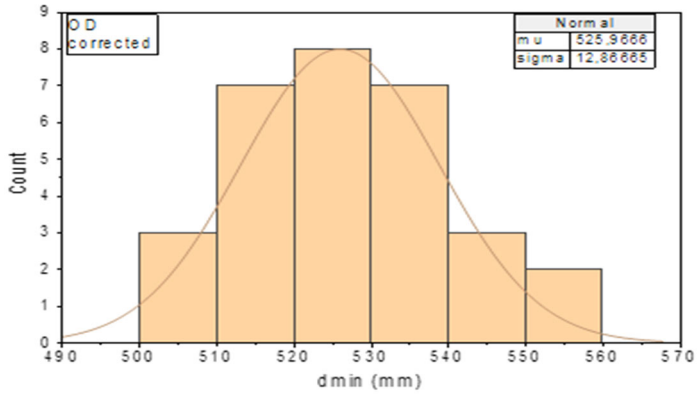

Fig. 5.55. Distribution of dmin values for the OD eye of patient A.

Table 5.14. Results of Some Tests of Mariotte at Light.

S	OS		OD		NOTES
	d_{min} (mm)	d_{max} (mm)	d_{min} (mm)	d_{max} (mm)	H = 149.2±13 (mm)
A	529 ±14	608 ±14	526 ±13	618 ±10	30 measures, black stickers, white BG
B	506 ±21	610 ±28	484 ±14	580 ±28	20 measures, black stickers, white BG
	μ_{min} (°)	μ_{max} (°)	μ_{min} (°)	μ_{max} (°)	
A	13.8 ±0.3	15.7 ±0.4	13.6 ±0.2	15.8 ±0.4	30 measures, black stickers, white BG
B	13.7 ±0.6	16.4 ±0.7	14.4 ±0.7	17.1 ±0.5	20 measures, black stickers, white BG

Other measurements, always at light, were made to study in detail the effect that the distance H between the stickers has on the aforementioned angles. The results, only for subject A, of μ_{min}, μ_{max}, $\overline{\mu}$ and $\Delta\mu$ for OS and OD, after at least 40 measurements of d_{min} and d_{max}, are given in Table 5.15. BG = Background.

Table 5.15. Results of the Tests of Mariotte at Light.

OS				OD				NOTES
μ_{min} (°)	μ_{max} (°)	$\overline{\mu}$ (°)	$\Delta\mu$ (°)	μ_{min} (°)	μ_{max} (°)	$\overline{\mu}$ (°)	$\Delta\mu$ (°)	
13.8 ±0.3	15.7 ±0.4	14.7 ±0.4	1.9 ±0.7	13.6 ±0.2	15.8 ±0.4	14.7 ±0.3	2.2 ±0.6	black stickers H=149.2 mm white BG
13.4 ±0.4	15.9 ±0.6	14.7 ±0.5	2.5 ±1.0	14.0 ±0.4	15.7 ±0.6	14.8 ±0.5	1.7 ±1.0	black stickers H=149.2 mm white BG
12.7 ±0.3	17.1 ±0.4	14.9 ±0.4	4.4 ±0.7	13.2 ±0.3	16.6 ±0.4	14.9 ±0.5	3.4 ±0.7	black stickers H=200.0 mm white BG
13.1 ±0.2	16.8 ±0.4	15.0 ±0.3	3.7 ±0.6	13.2 ±0.3	16.9 ±0.3	15.0 ±0.3	3.7 ±0.6	black stickers H=250.0 mm white BG
12.5 ±0.2	17.5 ±0.3	15.0 ±0.3	5.0 ±0.5	12.7 ±0.2	17.2 ±0.4	14.9 ±0.3	4.5 ±0.6	PL stickers H=301.0 mm black BG
12.2 ±0.2	17.3 ±0.3	14.7 ±0.3	5.1 ±0.5	13.1 ±0.2	17.4 ±0.3	15.2 ±0.3	4.2 ±0.6	black stickers H=301.0 mm white BG

Fig. 5.56 (a) shows the blind edge Mariotte's angles, μ_{min} and μ_{max}, for OS and OD, as function of the targets distance H. It was found a significant variation of the μ_{min} and μ_{max} angles at reducing H. From the graph of Fig. 5.56 (a) we note the similarity of behavior of the μ_{min} and μ_{max} angles between the OS and the OD eyes of subject A at all distances H examined, within the measurement errors. In addition, these two side angles tend to get closer (the first increasing and the second decreasing) as the distance of the targets decreases.

Fig. 5.56 (b) shows their average values $\overline{\mu}$, together with their difference $\Delta\mu$, as function of the targets distance H. As it can be seen, $\overline{\mu}$ remains almost constant (14.9±0.4°) as H decreases (it shows only a very slight decrease), while $\Delta\mu$ decreases starting from ~5°, for H=300mm, to ~2°, for H=150mm. The behavior recorded for OS and OD, as already noted, is practically the same, that is, the two eyes behave in the same way. The mean value found for $\overline{\mu}$ is in excellent agreement with what reported by Goldstein: 15° [50, p.54].

The trend shown by the side angles μ_{min} and μ_{max} as a function of targets distance reveals the tendency of their approach practically only below H=200mm, that is at only one point of the diagram of Fig. 5.56, that for H=150 mm. This fact has led us to investigate this effect further by extending the range of H values; in particular, we thought of transferring this study to dark conditions, more pertinent to the path of our work.

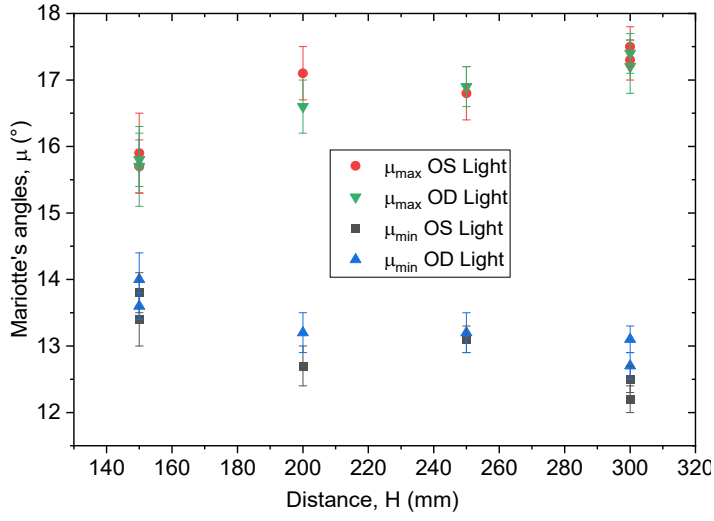

(a)

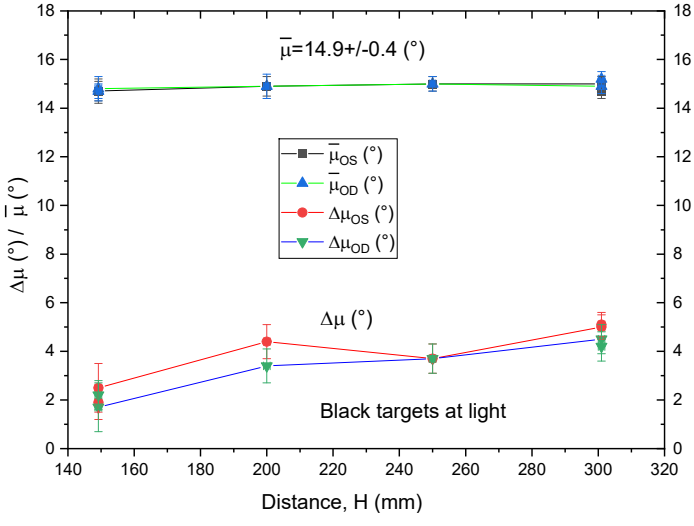

(b)

Fig. 5.56. (a) Data of μ_{min} and μ_{max} angles at light, as function of the targets distance. (b) Data of $\bar{\mu}$ and $\Delta\mu$ angles at light, as function of the targets distance. Subject A.

5.5.4.2. Measurements at Dark

Measurements on subject A have been continued in the dark, extending the range of H values, to better investigate the role played by this parameter. The results are reported in Table 5.16 and shown in the graphs of Fig. 5.57 (a) for the OS eye and in Fig. 5.57 (b) for the OD eye. In Fig. 5.57 the μ_{min} data are fitted with a decreasing exponential function and those of μ_{max} with a growing exponential function. As we saw for the measurements at light, even in the dark we see the tendency of the μ_{min} and μ_{max} angles to get closer to each other as the distance H between the two stickers decreases. It is interesting also to see that the results in the dark do not differ from those made at light. The bottom on which the stickers are placed, moreover, has no influence on the measurements, as in the dark the only bright elements are the PL stickers irradiated with UVA light.

Table 5.16. Results of the Tests of Mariotte at Dark.

OS				OD				NOTES
μ_{min} (°)	μ_{max} (°)	$\bar{\mu}$ (°)	$\Delta\mu$ (°)	μ_{min} (°)	μ_{max} (°)	$\bar{\mu}$ (°)	$\Delta\mu$ (°)	
13.8 ±0.9	15.3 ±0.9	14.5 ±0.9	1.5 ±1.8	14.9 ±1.0	15.3 ±0.9	15.1 ±1.0	0.4 ±1.9	PL stickers H=100 mm black BG
13.4 ±0.5	16.1 ±0.9	14.7 ±0.7	2.7 ±1.6	14.0 ±0.6	17.1 ±0.7	15.5 ±0.7	3.1 ±1.3	PL stickers H=150 mm black BG
13.2 ±0.4	17.4 ±0.7	15.3 ±0.6	4.2 ±1.1	13.7 ±0.7	17.0 ±0.6	15.3 ±0.7	3.3 ±1.3	PL stickers H=200 mm black BG
13.6 ±0.4	17.6 ±0.7	15.6 ±0.6	4.0 ±1.1	13.3 ±0.4	17.5 ±0.7	15.4 ±0.6	4.2 ±1.1	PL stickers H=250 mm black BG
12.2 ±0.3	17.1 ±0.5	14.6 ±0.4	4.9 ±0.8	12.7 ±0.3	17.4 ±0.4	15.0 ±0.4	4.7 ±0.7	PL stickers H=301 mm black BG
13.2 ±0.4	17.0 ±0.7	15.1 ±0.6	3.8 ±1.1	13.1 ±0.3	17.8 ±0.5	15.5 ±0.4	4.7 ±0.8	PL stickers H=400 mm white BG
12.5 ±0.6	17.3 ±0.5	14.9 ±0.6	4.8 ±1.1	13.7 ±0.3	17.5 ±0.4	15.6 ±0.4	3.8 ±0.7	PL stickers H=500 mm white BG
13.6 ±0.3	16.6 ±0.6	15.1 ±0.5	3.0 ±0.9	13.3 ±0.3	17.3 ±0.5	15.3 ±0.4	4.0 ±0.8	PL stickers H=600 mm white BG
12.8 ±0.3	17.7 ±0.4	15.2 ±0.4	4.9 ±0.7	13.0 ±0.3	17.0 ±0.5	15.0 ±0.4	4.0 ±0.8	PL stickers H=700 mm white BG

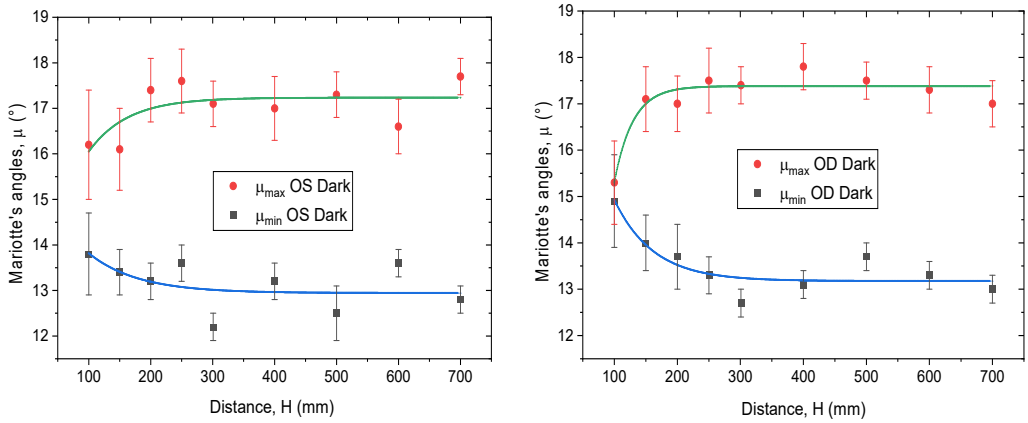

Fig. 5.57. Data of μ_{min} and μ_{max} side angles at dark, obtained with at least 40 measurements of d_{min} and d_{max}, as a function of the distance between the two PL targets, for the OS eye (a) and for the right eye (b). Subject S=A.

As we did for the measurements taken in the light, also for the dark we have calculated the average value of the side angles $\overline{\mu}$ and their difference $\Delta\mu$ as function of the targets distance H (see Fig. 5.58).

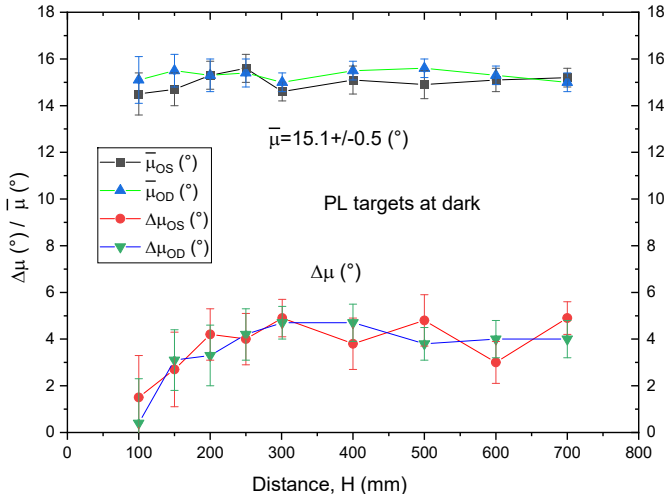

Fig. 5.58. Data of $\overline{\mu}$ and $\Delta\mu$ angles at dark, as function of the targets distance H. Subject A.

As regards $\overline{\mu}$, we get practically the same value found at dark (15.1±0.5°); for $\Delta\mu$ the behavior is now clearer, because it shows a regular decreasing trend from 4°÷5° at H~300mm to 1°÷2° at H~100 mm. The mean value of $\overline{\mu}$ is in excellent agreement with that reported by Goldstein [50, p.54] also in the dark.

Another interesting information can be drawn from the data of Table 5.16. The side angles μ_{min} and μ_{max} are similar for the two eyes and, for high H, take the values given in Table 5.17.

Table 5.17. Mariotte's Angles at High H Values in the Dark.

Eye	μ_{min} (°)	μ_{max} (°)	$\bar{\mu}$ (°)	$\Delta\mu$ (°)
OS	12.9 ±0.3	17.2 ±0.2	15.0 ±0.3	4.3 ±0.5
OD	13.2 ±0.2	17.4 ±0.2	15.3 ±0.2	4.2 ±0.4

As regards the results of Mariotte's blind spot test made on subject A, preliminary comments have already been given when presenting the results. Here we can reiterate the fact that the $\mu_{min} \div \mu_{max}$ angular interval, which we can name "blind spot angular interval", was similar, within the experimental errors, for the left and right eyes at light (see Tables 5.14, 5.15 and Fig. 5.56), for H values from H=300mm down to H=150 mm, meaning that the anatomical structure of the two eyes is practically the same. The tendency of these two angular limits to approach, in the light, as the distance H between the two targets decreases, pushed us to investigate in detail this phenomenon in the dark with photoluminescent targets.

The results (see Table 5.16 and Figs. 5.57, 5.58) show that this tendency is true; the two angular limits become even closer by reducing H down to 100 mm. Our results, as regards the blind spot angular interval on the horizontal plane, slightly differ from those reported by Lest'àk [44], which mention a blind spot size for the right visual field from 14.6±0.86° to 18.6±1.5° and a blind spot size for the left visual field from 13.2±1.5° to 16.1±2.5°. They, instead, agree quite well with what reported by Rosenfield [3, p.143, 319] which reports the following: "the physiological blind spot, corresponding to the optic disc, projects into the temporal visual field; it is usually at 15.5 degrees temporal to fixation and 1.5 degrees below the horizontal and 5.5 degrees wide and 7.5 degrees high".

The reduction of the spread of Mariotte's angles, and the constancy of their mean value, at closer H distances, might be related to the eye's accommodative response [51, p. 49], where the lens changes shape to phocus on the nearer target. This could potentially affect the perceived location and size of the blind spot. This observation suggests that the optics of the eye might be influencing the measurement in a way that is dependent on the focal distance. When the eye accommodates to phocus on a near object, the shape of lens changes due to the ciliary muscles' action. This alteration in lens shape allows the eye to phocus on objects at different distances. However, the shape of other internal parts, like the retina or the optic disc, doesn't change significantly with accommodation.

The observed effect on the blind spot's measurement might be more related to how the changing lens shape affects the image formation on the retina. As we know from the

Helmholtz's relaxation theory [30], what we can expect from the mechanism of accommodation is a change in the curvature of the lens on the anterior surface, with a consequent increase of its thickness, a reduction of its diameter and a slight shift toward the cornea (see Fig. 5.8). No other changes are expected in the other parts of the eye. A consequence of this could be a shift of the mean nodal point toward the cornea, with a consequent reduction in the angle subtended by the papilla with respect to it, which would explain the reduction in the interval between the μ_{min} and μ_{max} side angles, which has been observed experimentally. Even the constancy of the mean value observed between the two angles does not seem to be in contradiction with the modern theory of accommodation. The only difficulty in explaining what observed is given by the strong reduction of the blind spot angular interval as the distance H between the two targets diminishes, considering the reduced amplitude of accommodation expected for the eyes of the older subject (A).

5.5.5. Test of Resolution Acuity or of the Minimum Angle of Resolution

Fig. 5.47(b) shows the resolution test sight in which a slit represents a lack of continuity. The tests were carried out at both light and dark, both in positive contrast. In the light measurements, the squares are made with white card of ~90% reflectivity, illuminated with white light lamps at ~30 klux for indoor experiments, and with sunlight at ~45-50 klux for outdoor experiments. In the dark measurements, the white cardboard was replaced by PL tape, illuminated, just before each measurement, with a UVA lamp for 5 sec (luminance 190 nit). The tests were carried out individually on the two eyes, measuring the distance $d \pm \Delta d$ at which the discontinuity in the slit is no longer distinguishable. From the distance value, and the slit thickness, $D \pm \Delta D$, the minimum angle of resolution in arcseconds is then calculated as follows:

$$\alpha\ (") = \left(\frac{3600 \cdot 180}{\pi}\right) \cdot \left(\frac{D}{d}\right) \tag{5.36a}$$

$$\Delta\alpha\ (") = \left(\frac{3600 \cdot 180}{\pi}\right) \cdot \left(\frac{\Delta d \cdot D + \Delta D \cdot d}{d^2}\right) \tag{5.36b}$$

Tab. 5.18 shows the MAR results of angle α_{OS} and α_{OD}, in arcseconds, for the OS the OD eye, respectively, for subjects A and B. D is the slit thickness. The test refers to light (L) or darkness (D), and the notes indicate the illuminance E_S on the target during the test. N is the number of measurements.

The data in Table 5.18 tell us the following for subject A:

i) The MAR value, both for OS and OD, is well below 1', a value associated with a visual acuity of 10/10 (see Table 5.5).

ii) The MAR of OS is always lower than the MAR of OD, both in the light and in the dark, and this is in agreement with the fact that the morphoscopic VA measurements of OS have always given higher values than OD (see Tables from 5.8 to 5.11). The MAR worsens

significantly on the right eye due to the astigmatism, which leads to a blurring of the images.

iii) The MAR, in outdoor light, both for OS and OD, improves passing from 30 klux to 45 klux of illuminance.

iv) The transition from light to dark worsens the MAR.

v) In the dark, there is a strong drop of MAR moving from OS to OD.

Table 5.18. Minimum Angle of Resolution at Light and Dark.

S	D/L	*D* (mm)	N	α_{OS} (″)	α_{OD} (″)	Notes
A	L	1.01 ±0.03	40	22.3 ±0.9	29.5 ±1.7	E_S = 30 klux
A	L	1.01 ±0.03	40	21 ±1	26 ±2	E_S = 45 klux
A	D	1.02 ±0.05	40	34 ±3	55 ±6	Indoor
B	L	1.01 ±0.03	20	28.4 ±1.2	19.2 ±0.7	E_S = 30 klux
B	D	1.02 ±0.05	20	30 ±1.2	20.4 ±0.7	Outdoor

For subject B we have the following results:

i) Contrary to A, the MAR values improve when passing from OS to OD, both at light and dark, as the VA of OD was always better than the VA of OS (see Tables 5.7 and 5.8).

ii) Subject B has a slightly better MAR in the light than subject A, but has a significantly better MAR in the dark than subject A.

iii) Subject B shows the best overall MAR result: 19.2", which corresponds to distinguishing two points 0.9 mm apart at 10 m distance.

v) The note “outdoor” in Table 5.18 means that the measurements were performed at night outside the laboratory.

In conclusion, we can say that the trend of the MAR, for both subjects and for both eyes, is in line with what found after the morphoscopic VA tests. Furthermore, the MAR improves outdoors by increasing the level of illumination. Finally, passing from light to dark, the MAR significantly worsens for subject A, while it has only a very slight increase in subject B. As regards the absolute values of the MAR, we found the best values, for both subjects, around 20 arcseconds, a high VA, which allows to distinguish two details

1mm apart from 10m away. Average resolution acuity as high as 30 arcseconds have been reported for ideal conditions: 2.3mm-dia of the pupil and $\lambda = 555$nm [4, p. 132].

The data of Table 5.18 can be usefully compared with some of those reported in Table 5.19, obtained from the morphoscopic acuity test under similar experimental conditions, after converting the decimal tenths, $x/10$, into MAR ("), following the rules reported in Table 5.5. The results are reported in Table 5.19, where only two tests for each subject, one in the light and one in the dark, were selected. MAR values are reported in arcsec and errors have been neglected.

The MAR values obtained from the resolution test were compared with those obtained from the morphoscopic VA test, at similar experimental conditions, after converting the data $x/10$ of decimal VA into MAR (see Table 5.19). We find that the former are on average half the size of the latter, for both subjects and for both eyes. This result is not easily explained, except by attributing it to an experimental factor which makes it appear as a systematic error. One reason could be related to how the logMAR charts were designed. Since we are dealing with very low MAR values, at the limit of visibility, in the logMAR chart they correspond to very small characters (L~5mm) that were designed by hand with a small brush. This resulted in a slight roughness of the strokes which may have changed the actual MAR values of the logMAR chart.

The resolution test, on the contrary, was done by designing a slit obtained cutting a sticker by a blade, thus obtaining very clean edges free of roughness, present, instead, in the optotypes traced with the brush. We cannot find any other reason to explain the difference between the two test results.

Table 5.19. Comparison between MAR Values from Resolution Test and Morphoscopic Test.

Test Conditions		**Resolution Test**			**Morphoscopic Test (*)**			**Res/Mor**	
S	**Dark/ Light**	***MAR* (OS) (″)**	***MAR* (OD) (″)**	**Notes**	***MAR* (OS) (″)**	***MAR* (OD) (″)**	**Notes**	**OS**	**OD**
A	L	22.3	29.5	$E_S = 30$ klx	50.4	63	$E_S = 30$ klx	0.44	0.47
A	D	34	55	Indoor	57	66	Indoor	0.60	0.83
B	L	28.4	19.2	$E_S = 30$ klx	82.2	48	$E_S = 20$ klx	0.35	0.40
B	D	30	20.4	Outdoor	54.8	52.4	Indoor	0.55	0.39

5.6. Conclusions

It was just the observation of photoluminescent (PL) star stickers at night on the ceiling of my home that stimulated me to promote a study of vision in the dark using this type of light sources. After being in the dark for some time and having my vision adapted to darkness, I discovered that, focusing the sight on a single sticker of a group, it immediately

disappeared from view, while those close to it, present in the visual field of the eyes, remained visible. In addition, the sticker in question reappeared again if I moved my sight to a nearby one, which in turn became dark. The disappearance from the direct view of the PL sticker was simply due to the formation of a shadow, or dark cone, of the order of one degree, that our eye projects forward, due to the almost complete deactivation of the cone photoreceptors in the dark, and the absence of rod photodetectors in the foveal area involved by the direct view of a luminous object. The darkening of a circular PL target occurs only when it subtends to the sight of the tested eye an angle smaller than the critical angle of view, which is a parameter related to the extension of the foveal area (macula). The "test of the angle of view", or "test of the visual angle", allows therefore to know this parameter by observing the target at different distances and recording the minimum distance at which it can be darkened.

From the morphoscopic acuity tests carried out in a private optical laboratory, the results were, for subject A, the author, a +0.75 hyperopia and a mixed astigmatism on the right eye, and a -0.25 myopia on the left eye; vision is 9/10 in the right eye and 12/10 in the left eye and on both eyes. For the younger subject B, the results were -0.25 myopia on the right eye and a -1.5 myopia on the left eye; in both eyes there is a myopic astigmatism. Vision is 10/10 on the right eye and on both eyes, 7/10 on the left eye. In summary, the VA of the two subjects is opposite, better for the OS eye in subject A, better for the OD eye in subject B. These results were taken as a reference for our measurements.

The preliminary morphoscopic visual acuity tests on the two subjects, made in my laboratory, were carried out using different types of charts and different light sources. These results confirm, in broad terms, those obtained by the private laboratory, regarding the far visual acuity results, because other parameters, like myopia, hyperopia or astigmatism, could not be measured. The VA tests with the Monoyer decimal chart, no longer used and carried out at light mostly out of curiosity, resulted in a poorer vision on both subjects, penalized by the negative contrast of the characters, and also by the obsolete progression of the decimal table, which prevents a good assessment of vision for high VA values. Better VA values were obtained by using the Monoyer decimal chart projected in negative contrast by the monitor of a PC. The indoor VA tests at white light, with logMAR chart and white characters, registered higher VA values for subject A, but rather independent from the intensity of illumination in the 0.7-3.5 klx range. The VA tests at clear sky and high solar illuminances (8-30 klx), with logMAR chart and white characters, allowed to reach even higher VA values for both subjects, but little dependent on the intensity of solar radiation. The preliminary results of VA tests on logMAR photoluminescent chart were not significant, as the sources used, battery-powered UVA LED torches, did not allow to maintain a stable luminance of the optotypes during reading.

Other morphoscopic VA tests were carried out on subject A in outdoor conditions with cloudy sky, on the logMAR chart with white optotypes, and as function of the surface illuminance. We have found that the visual acuity, for both eyes, reaches a saturation value for illuminance values higher than ~450 lx, corresponding to ~100nit of luminance of the white optotypes. At lower illuminances, the VA slowly decreases, showing a clear drop at ~10 nits of luminance.

Similar morphoscopic VA tests were carried out on subject A at indoor conditions in the dark, on the logMAR chart with photoluminescent optotypes, as function of their luminance. We have found that the visual acuity, both for OD and OS, maintains constant, even at different values (~7 for OD due to the mixed astigmatism, and ~11 for OS), down to very low luminance values. Only the use of dark glasses with an attenuation factor of ~4 allowed to register a drop of visual acuity at a luminance of ~25 nit from the optotypes, corresponding to a luminance on the eyes of ~6 nit. This result is in good agreement with what found from the VA tests made outdoor at cloudy sky, apart from the possible differences due to the spectrum of light and the environment: the visual acuity at high luminance maintains high down to very low values, of the order of ~10 nit. Regarding the morphoscopic visual acuity test, it should be noted that most of the readings were performed following a self-test procedure, in the sense that subject A, the author, simultaneously acted as reader of the optotypes and as judge, deducing the visual acuity and recording it. Although this procedure is not reported in the optometric measurement protocol, which requires the distinction between the two subjects, it was adopted due to the need to compensate for the lack of collaborators and the large amount of data to be processed.

As regards the results of the angle of view test, a critical angle $\alpha_D \sim 1°$ was found for subject A, a value considered acceptable by the literature. Subject B shows smaller values, likely associated to the myopia. As regards the comparison between the left eye and the right eye, we expect the angle of view to be smaller for the eye that has greater visual acuity, and in fact this is true, even if to a minimal extent, for subject A. The test of angle of view in the dark has shown unequivocally that it is possible to obscure a PL target of very low luminance (but not known in absence of a photomultiplier) after adapting the eyes to the dark (~20 min) and staying at a suitable distance.

The measurements of the angle of view, which led to the darkening of the PL targets, were carried out by a search for the light sources that showed the same behavior. Among these we mention the phosphorescent hands of a wristwatch and the weak diffuse reflections of a white light bundle by a white, diffusive wall or by a smooth metallic surface. All other sources tried, from the small LED lights, to laser spot on a wall, or small light windows from the screen of a cellular, were impossible to be darkened even by reducing drastically their intensity.

The Mariotte's blind spot test was carried out initially at light on both subjects, founding that the angular interval within which is possible to obscure a target, the blind angular interval, is the same for the left and right eyes within the experimental errors, for a distance between the targets of about 150mm, meaning that the anatomical structure of the two eyes is practically the same. Other measurements were also done at light on subject A by increasing the distance between the targets up to about 300mm. The result was a blind spot angular interval which reduces at reducing the target distance. This phenomenon was investigated also in the dark on subject A by using photoluminescent targets, and we have found similar results; the two angular limits become even closer by reducing the target distance down to 100mm. The way in which this blind spot angular range narrows could be attributed to a variation in the distance of the papilla from the nodal plane of the eye,

due to the displacement of the nodal plane after the changing of the focus status of the crystalline lens. This, for shorter distances on the object plane, should contract and move the nodal plane towards the cornea side, ultimately increasing its distance from the papilla and thus reducing the blind spot angular interval. In this way, however, we do not take into account possible deformations of the eye when the optical power of the crystalline lens varies. Our results were more precise than those reported by Lest'àk, which mention a blind spot size for the right and left visual field, without studying the effect of distance of the two targets.

The eye's resolving acuity test had the aim to find the minimum angle of resolution (MAR). It was addressed at light and dark cutting a slit from white or PL stickers, respectively. We expected to find a resolution visual acuity parameter in tune with what found from the results of the morphoscopic acuity test and the angle of view tests. We find in fact a resolution acuity better for the left eye for subject A, and a resolution acuity better for the right eye for subject B. As regards the absolute values of the minimum resolution angle, we find the best values, for the two subjects, around 20 arcseconds, a high VA, which allows to distinguish two details 1mm apart from 10m away. It improves as the intensity of the light illumination increases, and, for subject A, it worsens significantly on the right eye due to the astigmatism, which leads to a blurring of the images. In the transition from light to dark, the minimum angle of resolution (MAR) remained very low in subject B, while it worsened significantly in subject A.

In the last part of this work, we compared the MAR values obtained from the resolution test with those obtained from the morphoscopic VA test at similar experimental conditions, converting the data $x/10$ of decimal VA into MAR. This comparison showed that the former are, on average, half the size of the latter, for both subjects and for both eyes. This result is not easily explained. One reason could be related to how the logMAR charts were designed. Since we are dealing with very low MAR values, at the limit of visibility, in the logMAR chart they correspond to very small characters (L~5mm) that were designed by hand with a small brush. This resulted in a slight roughness of the strokes which may have changed the actual MAR values of the logMAR chart. The resolution test, on the contrary, was done by making a slit by cutting a sticker, whose edges are free of roughness. We cannot find other reasons to explain the difference between the two tests.

In conclusion, with this work we have shown that the use of PL targets in the dark reveals interesting aspects in the field of optometry. The use of PL targets allowed us to measure the critical angle of view in the dark in a simple way. We were also able to deepen the phenomenon of Mariotte's blind spot test in the dark and with PL targets, combining it with that of the angle of view, thus finding a way to simultaneously obscure two PL targets, promoting in this way a new blind spot method: the two blind spots tests (TBST). Using a slit with PL stripes, we were finally able to measure the minimum resolution angle in the dark. This work can be carried out by using commercial materials and devices of limited cost, so it could be useful for educational purposes, making simple experiments in the field of optometry and thus stimulating the study of vision in secondary school students.

Acknowledgments

The author sincerely thanks Mrs. Irene Mazza of the Le Mura Optics Laboratory (Ferrara, FE, Italy) and Eng. Achille Monegato, of Favini S.r.l. (Rossano Veneto, VI, Italy) for helpful discussions on optometry and optical properties of materials. The author also thanks the young student Enrico Cheng, for his help in some experimental measurements and for his enthusiasm in participating. Special thanks go to my wife Antonietta, who allowed me, for more than two years, to take care exclusively of the preparation of this work.

References

[1]. S. Huo, Y. Li, Phosphorescent Materials, *American Chemical Society*, Washington, DC, 2023.
[2]. K. A. Franz, W. G. Kehr, A. Siggel, J. Wieczoreck, W. Adam, Luminescent Materials in: Ullmann's Encyclopedia of Industrial Chemistry, *Wiley-VCH*, 2002.
[3]. M. Rosenfield, N. Logan, Optometry: Science, Techniques and Clinical Management (2nd ed.), *Butterworth Heinemann Elsevier*, 2009.
[4]. A. Rossetti, P. Gheller, Manuale di optometria e contattologia (2nd ed.), *Zanichelli*, Bologna, 2003 (in Italian).
[5]. R. H. Daw, Johann Heirich Lambert (1728-1777), *Cambridge University Press*, 2012.
[6]. A. Huxley, L'arte di vedere (19th ed.), *Adelphi*, Milano, 1989 (in Italian).
[7]. H. Andreade, Edmé Mariotte--born 350 years ago. *Die Quintessenz*, Vol. 21, Issue 11, 1970, pp. 153-155.
[8]. A. Grzybowsky, P. Aydin, Edme Mariotte (1620-1684): Pioneer of Neurophysiology, *Survey of Ophthalmology*, Vol. 52, Issue 4, 2007, pp. 443-451.
[9]. K. Watanabe, On the Achromatic Zone around the Spot of Mariotte, *The Tohoku Journal of Experimental Medicine*, Vol. 67, Issues 2-3, 1958, pp. 235-243.
[10]. Parretta, A., work in preparation.
[11]. H. Helmholtz, Helmholtz's treatise on physiological optics, Trans. J. P. C. Southall*, Optical Society of America*, Vol. 1, 1924.
[12]. H. Helmholtz, Helmholtz's treatise on physiological optics, Trans. J. P. C. Southall, *Optical Society of America*, Vol. 2, 1924.
[13]. H. Helmholtz, Helmholtz's treatise on physiological optics, Trans. J. P. C. Southall, *Optical Society of America*, Vol. 3, 1925.
[14]. H. Helmholtz, Helmholtz's treatise on physiological optics, Trans. J. P. C. Southall, *Thoemmes*, 2000.
[15]. N. J. Wade, A natural history of vision, Vol. 30, Issue 4, *MIT Press*, Cambridge Mass., 1998.
[16]. N. J. Wade, The vision of Helmholtz, *Journal of the History of Neurosciences*, Vol. 30, Issue 4, 2021, pp. 405-424.
[17]. G. Berkely, An essay toward a new theory of vision, *Pepyat*, Dublin, 1709.
[18]. D. C. Lindberg, Theories of vision from Al-Kindi to Kepler, *University of Chicago Press*, Chicago, 1996.
[19]. D. Park, The fire within the eye, *Princeton University Press*, Princeton, New Jersey, 1997.
[20]. P. Artal, Optics of the eye and its impact in vision: a tutorial, *Advances in Optics and Photonics*, Vol. 6, Issue 3, 2014, pp. 340-367.
[21]. I. Bekerman, P. Gottlieb, M. Vaiman, Variations in eyeball diameters of the healthy adults, *Journal of Ophthalmology*, Hindawi Publishing Corporation, Vol. 2014, Article ID: 503645.

[22]. N. Cuenca, I. Ortuño-Lizarán, I. Pinilla, Cellular characterization of OCT and outer retinal bands using specific immunohistochemistry markers and clinical implications, *Ophthalmology*, Vol. 125, Issue 3, 2018, pp. 407–422.
[23]. C. A. Curcio, K. R. Sloan, R. E. Kalina, A. E. Hendrickson, Human photoreceptor topography, *The Journal of Comparative Neurology*, Vol. 292, Issue 4, 1990, pp. 497-523.
[24]. E. B. Goldstein, Sensation and Perception (9 edn.), *Cengage Learning*, 2013.
[25]. Y. LeGrand, S. G. ElHage, Physiological Optics, *Springer*, Berlin, Heidelberg, 2013.
[26]. G. O. Ovenseri-Ogbomo, O. A. Oduntan, Mechanism of accommodation: A review of theoretical propositions, *African Vision and Eye Health*, Vol. 74, Issue 1, 2015, pp. 1-6.
[27]. T. Young, Observations on vision, *Philosophical Transactions of the Royal Society*, Vol. 83, 1793, pp.169-181.
[28]. F. C. Donders, On the anomalies of accommodation and refraction of the eye, with a preliminary essay on physiological dioptrics, *The New Sydenham Society*, London, 1864.
[29]. C. Scheiner, Oculus hoc est: Fundamental Opticum, *Oeniponti: Apud Danielem Agricolam*, 1619.
[30]. H. Helmholtz, Uber die Akkommodation des Auges. *Archiv für Ophthalmologie*, Vol. 1, 1855, pp. 1–74.
[31]. H. Helmholtz, Popular lectures on scientific subjects, *D. Appleton & Co*, New York, 1881.
[32]. H. Helmholtz, Helmholtz's treatise on physiological optics, (Trans. from the 3rd German ed.) (J. P. C. Southall, Ed.), *Optical Society of America*, 1924.
[33]. D. M. Pipe, L. Rapley, Ocular Anatomy and Hystology (2nd edn.), *Association of Dispensing Opticians*, 1997.
[34]. Monegato, A. Favini Srl (Rossano Veneto, VI, Italy, www.favini.com), private communication.
[35]. PhysicsOpenLab (2019a, February 6). Fosforescenza del Solfuro di Zinco (in Italian). https://physicsopenlab.org/2019/02/06/fosforescenza-del-solfuro-di-zinco/.
[36]. PhysicsOpenLab (2019b, February 5). Brillando nel Buio (in Italian). https://physicsopenlab.org/2019/02/05/fosforescenza/.
[37]. S. Hecht, S. Shlaer, M. H. Pirenne, Energy, quanta and vision, *Journal of General Physiology*, Vol. 25, 1942, pp. 819-840.
[38]. N. B. Carlson, D. Kurtz, Clinical Procedures of Ocular Examination (4th edn.), *McGraw-Hill Education*, 2016.
[39]. I. L. Bailey, Visual acuity, in: W.J. Benjamin (ed.) Borish's clinical refraction (2nd edn). *Butterworth-Heinemann*, 2006, pp. 217-246.
[40]. I. L. Bailey, J. E. Lovie, New design principles for visual acuity letter charts, *American Journal of Optometry and Physiological Optics*, Vol. 53, Issue 11, 1976, pp. 740-745.
[41]. J. H. Levenson, A. Kozarsky, Visual Acuity, in: Clinical Methods: The History, Physical, and Laboratory Examinations (3rd edn.) (Ch. 115), H. K. Walker, W Dallas Hall, & J.W. Hurst (Eds.), *Butterworths*, Boston, 1990.
[42]. A. Adams, J. Lovie-Kitchin, Ian L. Bailey, *Clinical and Experimental Optometry*, Vol. 87, Issue 1, 2004, pp. 37-41.
[43]. I. L. Bailey, J. E. Lovie, Visual acuity testing. From the laboratory to the clinic, *Vision Research*, Vol. 90, 2013, pp. 2-9.
[44]. J. Lest'ák, Mariotte's spot, *Czech and Slovak Ophthalmology*, Vol. 49, Issue 6, 1993, pp. 394-398 (in Czech).
[45]. M. D. Grmek, An exemplary scientific debate: Mariotte, Pecquet and Perrault in search of the site of visual perception, *History of Philosophy of the Life Sciences*, Vol. 7, Issue 2, 1985, pp. 217-255.
[46]. A. Dubois-Poulsen, Mariotte's spot in binocular vision, *Archive d'Ophthalmology Revue Général d'Ophthalmologie*, Vol. 29, Issue 6, 1969, pp. 487-490.

[47]. Visionottica Beltrami, Galleria C.C. Le Mura, Via Copparo 132, 44123 Ferrara (FE), Italy, https://www.visionottica.it
[48]. C. Owsley, Vision and Aging, *Annual Review of Visual Science*, Vol. *2*, 2016, pp. 55–71.
[49]. B. Mohd-Ali, Y. C. Low, M. M. Shahimin, N. Arif, H. A. Hamid, W. H. W. A. Halim, S. S. Mokri, A. B. Huddin, N. Mohidin, Ocular Dimensions, Refractive Error, and Body Stature in Young Chinese Children with Myopia in Kuala Lumpur, Malaysia, *Clinical Optometry*, Vol. 14, 2022, pp. 101–110.
[50]. E. B. Goldstein, Blackwell Handbook of Perception, *Blackwell*, 2001.
[51]. F. H. Adler, P. L. Kaufman, L. A. Levin, A. Alm, Adler's Physiology of the Eye, *Elsevier Health Sciences*, 2011, ISBN: 978-0-323-05714-1.
[52]. L. N. Thibos, N. Lopez-Gil, A. Bradley, What is a troland? *Journal of the Optical Society of America A*, Vol. 35, Issue 5, 2018, pp. 813-816.

Appendix

Some Notes on the Flux through the Pupil Area

Let us consider the experimental conditions illustrated in Fig. 5.58. The target PL, of area ΔS_1, emits light with a luminance L_v within the solid angle $\Delta\Omega$, which is collected by the eye placed at a distance d, and with pupil area ΔS_2.

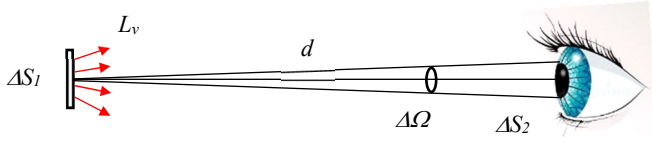

Fig. 5.58. The scheme for measuring the luminous flux produced by a source surface of area ΔS_1 and luminance L_v, entering the pupil of area ΔS_2, is shown.

The flux collected from the pupil, Φ_v, is approximately given by:

$$\Phi_v = L_v \cdot \Delta S_1 \cdot \Delta\Omega = L_v \cdot \Delta S_1 \cdot \Delta S_2 / d^2 \qquad (5.A1)$$

As we will see soon, Eq. (5.A1) is valid when the target is seen by the eye within a small linear angle. As it can be seen from Eq. (5.A1), the flux depends on the luminance of the surface, on the areas ΔS_1 and ΔS_2 projected in the direction of observation, and on the distance d. Let us now imagine that the eye is faced with an extended, theoretically unlimited environment, of constant luminance L_v, placed at a distance d, and let us now calculate the flux, Φ_v, collected by the pupil under these conditions (see Fig. 5.59).

Let us begin by calculating the elementary flux $\mathrm{d}\Phi_v$, emitted by the circular crown of radius r and thickness $\mathrm{d}r$, seen by the eye under the angle α.

$$d\Phi_v = L_v \cdot (dS_1 \cdot \cos\alpha) \cdot d\Omega = L_v \cdot (2\pi r \cdot dr \cdot \cos\alpha) \cdot [\Delta S_2 \cdot \cos\alpha / (d/cos\alpha)^2] \quad (5.A2)$$

By expressing r as function of α, we obtain:

$$d\Phi_v = 2\pi \cdot L_v \cdot \Delta S_2 \cdot \sin\alpha \cdot \cos\alpha \cdot d\alpha \quad (5.A3)$$

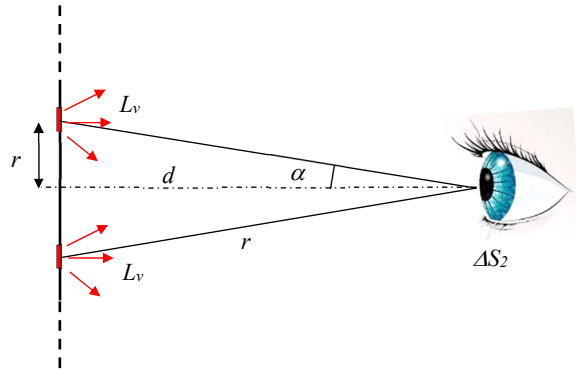

Fig. 5.59. The scheme for measuring the luminous flux entering the pupil of area ΔS_2, produced by a surface of unlimited area and uniform luminance L_v, is shown.

To have the total flux, we integrate on α from 0° to 90°:

$$\Phi_v = \int_{\alpha=0}^{\pi/2} 2\pi \cdot L_v \cdot \Delta S_2 \cdot \sin\alpha \cdot \cos\alpha \cdot d\alpha = \pi \cdot L_v \cdot \Delta S_2 \quad (5.A4)$$

From Eq. (5.A4) we deduce that the total flux on the pupil no longer depends on the distance between the source and the eye. The total transmitted flux, therefore, is not simply the product of luminance and area of interest, as sometimes found in the literature [3], but is also multiplied by π. When we are dealing with an extended light source like this, we speak of "scene luminance" [3, p. 8]. If the source is not extended to ∞, but up to a subtended angle $\pm\alpha_0$, as illustrated in Fig. 5.60, the total collected flux will be in this case:

$$\Phi_v = \int_{\alpha=0}^{\alpha_0} 2\pi \cdot L_v \cdot \Delta S_2 \cdot \sin\alpha \cdot \cos\alpha \cdot d\alpha = \pi \cdot L_v \cdot \Delta S_2 \cdot \sin\alpha_0{}^2 \quad (5.A5)$$

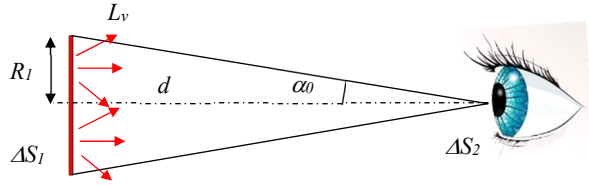

Fig. 5.60. Scheme for measuring the luminous flux entering the pupil of area ΔS_2, produced by a surface of ΔS_1 area and uniform luminance L_v.

The collected flux will be reduced by a relative quantity equal to ($\sin^2\alpha_0$), reported as a percentage in the graph of Fig. 5.61. It is easy to demonstrate that Eq. (5.A5) gives the same result of the Eq. (5.A1) for small values of the angle α_0. Calling as R_1 the radius of the circular area ΔS_1, we have in fact (see Fig. 5.60):

$$\Phi_v = L_v \cdot \Delta S_1 \cdot \Delta S_2 / d^2 = L_v \cdot \pi \cdot {R_1}^2 \cdot \Delta S_2 / d^2 = \pi \cdot L_v \cdot \Delta S_2 \cdot \tan{\alpha_0}^2 \quad (5.A6)$$

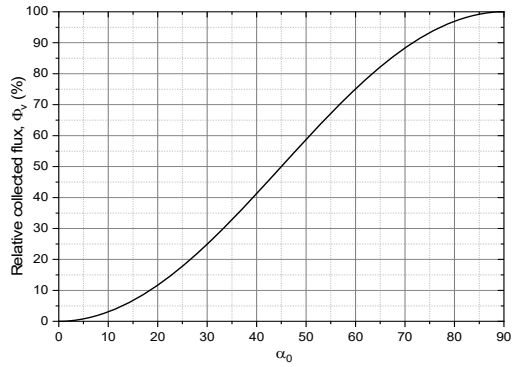

Fig. 5.61. The relative percentage flux transmitted to the eye by a surface limited to a subtended angle $\pm\alpha_0$.

Eq. (5.A6), for small angles α_0, is equivalent to Eq. (5.A5), but the correct formula for the flux is given by Eq. (5.A5). Eq. (5.A5) suggests a simple way to calculate the luminance of a surface. It is sufficient to measure the flux collected by a luxmeter placed at a distance d from the source (see Fig. 5.62):

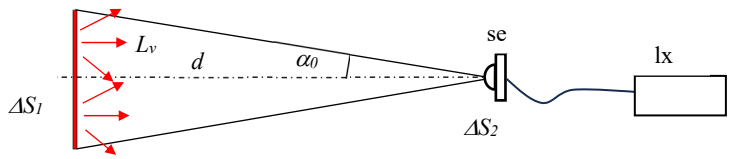

Fig. 5.62. Scheme for measuring the luminance L_v of a source surface of ΔS_1 area, by using a luxmeter (lx) with a sensor (se) of area ΔS_2.

If ΔS_2 is the area of the sensor (se) of the luxmeter (lx), Φ_v the measured flux, measuring the angle α_0, the luminance of the surface will be given by:

$$L_v = \frac{\Phi_v}{\pi \cdot \Delta S_2 \cdot \sin{\alpha_0}^2} \quad (5.A7)$$

There is one other unit occasionally used in relation to the eye. When viewing a surface source with uniform luminance and unlimited area, the illuminance on the retina is dependent on the source luminance and the pupil area, as we know from Eq. (5.A4). This

new unit is called troland, and 1 troland is the retinal illuminance produced by a surface with 1 cd/m^2 luminance, through a pupil area of 1mm^2 [3, p. 71; 4, p. 109; 52]:

$$1\ \text{troland} = 1\ \text{Td} = 1\ \frac{\text{cd}}{\text{m}^2} \cdot 1\ \text{mm}^2 \tag{5.A8}$$

In this way, the troland has the same dimension of a luminous intensity (lm/sr), but is 10^6 times lower:

$$1\ \text{troland} = 1\ \text{Td} = 1\ \frac{\text{cd}}{\text{m}^2} \cdot 1\ \text{mm}^2 = 1\ \frac{\text{cd}}{\text{m}^2} \cdot 10^{-6}\ \text{m}^2 = 10^{-6}\text{cd} = 1\mu\text{cd} = 1\mu\,\text{lm/sr} \tag{5.A9}$$

The correct interpretation of the troland unit has been the subject of a critical work of Thibos et al. [52]. As reported by Thibos, trolands are a widely used measure of retinal illuminance in vision science and visual optics, but disagreements exist for the definition and interpretation of this photometric unit. In his communication, Thibos wants to resolve the confusion by providing a sound conceptual basis for interpreting trolands as a measure of angular flux density incident upon the retina. Using a simplified optical analysis, he shows that the troland value of an extended source is the intensity in micro-candelas of an equivalent point source located at the eye's posterior nodal point that produces the same illuminance in the retinal image as does the extended source (see Fig. 5.63).

This optical interpretation of trolands reveals that total light flux in the image of an extended object is the product of the troland value of the source and the solid angle subtended by the source at the first nodal point, independent of eye size.

We have therefore, for the total luminous flux (in μlumen) in the image of an object, extended

$$\Phi\,(\mu\text{lumen}) = Td \cdot \Delta\Omega\ ((\text{cd}|\text{m}^2) \cdot \text{mm}^2 \cdot \text{sr}) \tag{5.A10}$$

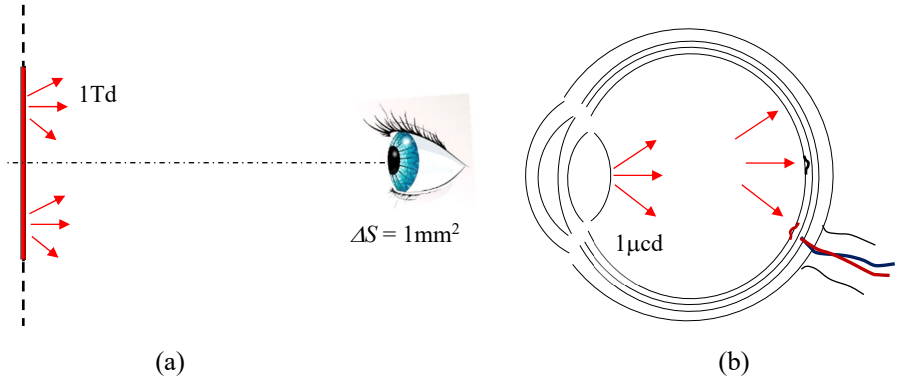

Fig. 5.63. An extended surface source with 1Td, illuminating a 1mm^2 pupil (a), has the same effect (is equivalent to) of a point light source with luminous intensity of 1μcd, located at the eye's posterior nodal point (b), in the sense that it produces the same illuminance in the retinal image as does the extended source.

Index

G

H

I

L

M

Advances in Optics, Volume 7

Sergey Y. Yurish, Editor

Advances in Optics, Vol. 7 presents a rich collection of current research exploring the frontiers of optical science and technology. The volume reflects the interdisciplinary nature of modern optics—bridging photonics, biomedical applications, materials science, and optical metrology—through contributions from leading academic and research institutions.

This book features innovative work on microstructured optical fibers, holographic imaging, diffractive optics, and advanced methods in bio-optical detection and optometry. The chapters provide not only in-depth theoretical foundations but also emphasize practical implementations, experimental validation, and potential applications—making this volume especially valuable for academic researchers seeking both new insights and technical guidance.

Designed for a scholarly audience, Advances in Optics, Vol. 7 serves as a reference for professors, PhD candidates, postdoctoral researchers, and advanced graduate students in optical engineering, photonics, applied physics, biomedical optics, and related disciplines. It also provides inspiration for cross-disciplinary collaboration and the development of new lines of inquiry in sensor-based optical systems.

With its focus on emerging topics and open-access format, this volume contributes to the ongoing exchange of ideas and advances in the optics research community. It will find a welcome place in university libraries, research laboratories, and academic courses dedicated to optical science and technology.

ISBN 978-84-09-57871-9